Bell Telephone Laboratories
Research and Development Unit of the Bell System

EFFECTS OF RADIATION ON SEMICONDUCTOR MATERIALS AND DEVICES

by
D. K. Wilson
J. F. Mitchell
J. D. Cuthbert
H. S. Lee

Bell Telephone Laboratories, Incorporated
on behalf of Western Electric Company, Incorporated
83 Maiden Lane, New York, New York 10038

Contract No. F19(628)-67-C-0147
Project No. 4608 Task No. 460801

FINAL REPORT

Period covered: 1 January 1967 thru 31 December 1967
30 April 1968

Contract Monitor: Henry M. DeAngelis
Solid State Sciences Laboratory

Prepared for
AIR FORCE CAMBRIDGE RESEARCH LABORATORIES
OFFICE OF AEROSPACE RESEARCH
UNITED STATES AIR FORCE
BEDFORD, MASSACHUSETTS 01730

1404

DISCLAIMER NOTICE

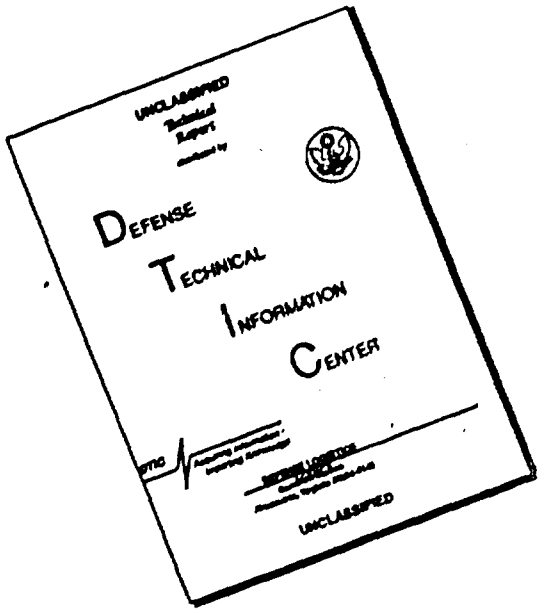

THIS DOCUMENT IS BEST QUALITY AVAILABLE. THE COPY FURNISHED TO DTIC CONTAINED A SIGNIFICANT NUMBER OF PAGES WHICH DO NOT REPRODUCE LEGIBLY.

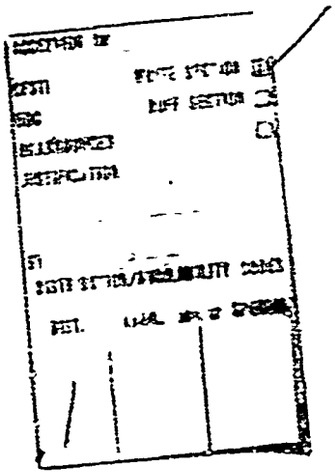

Qualified requestors may obtain additional copies from the Defense Documentation Center. All others should apply to the Clearinghouse for Federal Scientific and technical information.

EFFECTS OF RADIATION ON SEMICONDUCTOR MATERIALS AND DEVICES

D. K. Wilson, et al

Bell Telephone Laboratories, Incorporated
New York, New York

30 April 1968

68-0250

AFCRL-[redacted]

Bell Telephone Laboratories

Research and Development Unit of the Bell System

EFFECTS OF RADIATION ON SEMICONDUCTOR MATERIALS AND DEVICES

by

D. K. Wilson
J. P. Mitchell
J. D. Cuthbert
H. S. Lee

Bell Telephone Laboratories, Incorporated
on behalf of Western Electric Company, Incorporated
83 Maiden Lane, New York, New York 10038

Contract No. F19(628)-67-C-0147
Project No. 4608 Task No. 460801

FINAL REPORT

Period covered: 1 January 1967 thru 31 December 1967
30 April 1968

Contract Monitor: Henry M. DeAngelis
Solid State Sciences Laboratory

Prepared for
AIR FORCE CAMBRIDGE RESEARCH LABORATORIES
OFFICE OF AEROSPACE RESEARCH
UNITED STATES AIR FORCE
BEDFORD, MASSACHUSETTS 01730

ABSTRACT

Results of investigation on the effects of nuclear radiation on semiconductor materials, device surface layers, and devices are discussed.

Optical studies revealed that low-temperature red luminescence in GaP doped with (Zn,O) or (Cd,O) arises either from recombination of electrons at neutral Cd-O (or Zn-O) complexes with holes trapped at Cd (or Zn) acceptors, or from decay of excitons at Cd-O (or Zn-O) complexes. The temperature dependence of intensity and time-resolved spectra of the red luminescence was investigated and showed that bound-exciton emission becomes dominant between 60° and 120°K. An explanation is offered for the accompanying large changes in the spectral and time-decay characteristics.

An analysis of the model for radiation-induced positive space-charge buildup in SiO_2 layers is presented and the predictions compared with results obtained on commercial MOS-FETs. Trap levels in SiO_2 layers were investigated using thermoluminescence and thermally stimulated glow curve techniques. Co^{60}-gamma radiation introduces five trap levels in SiO_2 layers. Oxide layers in commercial MOS-FETs showed a high density of inherent electron traps. Platinum-silicide/silicon Schottky barrier diodes with "guard-rings" were found to be unaffected by up to 10^8 rads of ionizing radiation and 10^{15} n/cm^2.

Recombination and trapping mechanisms in neutron-irradiated silicon diodes were studied using open-circuit forward-voltage recovery and reverse-bias capacitance-voltage characteristics. The results are interpreted in terms of isolated defect and clustered damage models.

The effects of fast neutrons on the dc and microwave characteristics of "nearly-abrupt" X-band avalanche diodes are reported. Above 10^{15} n/cm^2 significant improvement in device behavior was observed.

CONTENTS

CONTENTS (continued)

CONTENTS (continued)

CONTENTS (continued)

*This appendix supplements Section II.
†This attachments supplements Section I.

ILLUSTRATIONS

ILLUSTRATIONS (continued)

ILLUSTRATIONS (continued)

ILLUSTRATIONS (continued)

ILLUSTRATIONS (continued)

ATTACHMENT I

NEW RED PAIR LUMINESCENCE FROM GaP

ILLUSTRATIONS (continued)

ILLUSTRATIONS (continued)

TABLES

EFFECTS OF RADIATION ON SEMICONDUCTOR MATERIALS AND DEVICES

1. INTRODUCTION

The studies discussed in this report were carried out in three general areas:

1. Recombination mechanisms at defects in compound semiconductors through the use of optical spectroscopy.
2. Radiation-induced space-charge buildup in the SiO_2 layers of planar devices and trap levels in these layers using glow-curve techniques.
3. Effects of fast neutrons on silicon junction devices.

The work discussed in this report is, in many respects, a continuation of the work reported in the final report of contract AF19(628)-4157 (AFCRL-67-0068).

In the study of recombination in semiconductors, we have employed optical luminescence to determine defect properties and recombination mechanisms operative at defects. This report contains the results of investigations on p-type, Zn- and Cd-doped GaP materials which promise to be important red phosphors. This luminescence was originally chosen for study because initial observations strongly suggested that the center responsible for the luminescence involved a natural vacancy in GaP. This model was not confirmed by later studies, but the work did lead to the first reported observations of a new recombination mechanism involving interimpurity recombinations between a neutral acceptor and a charged inert trap. The research on p-type GaP was divided into two parts: the first part was aimed at establishing an understanding of the low-temperature luminescence properties, the second part aimed at extending this understanding for temperatures up to 300°K. A wide range of techniques was brought to bear on the problem including: the study of luminescence time decay and time-resolved spectra as functions of temperature; the temperature and doping dependencies of the intensity spectra; Zeeman splitting and isotopic substitution experiments; and luminescence excitation experiments. Section I of this report describes these studies and the conclusions that can be drawn about recombination mechanisms in p-type GaP.

Section II of this report deals with surface effects of radiation on semiconductor devices; in particular, the problem of radiation-induced space-charge buildup in the SiO_2 layers of silicon planar devices. An analysis of the charge buildup process is presented which predicts the dependence of this buildup on radiation dose, dose rate, and the bias applied across the oxide layer during irradiation. The predictions are compared with results found on commercial MOS-FETs.

Experiments were performed to study trap levels in SiO_2 layers in an attempt to gain a more fundamental understanding of the charge buildup process. The technique of thermoluminescence glow curves was used to study the effects of Co^{60}-gamma radiation on trap levels in thermally grown SiO_2 layers. The effects of high-temperature annealing on these traps were also investigated. The results were compared with those from a study on commercial MOS-FETs using thermally-stimulated current-glow curves and have lead to a better understanding of the space-charge buildup process and of the thermal annealing of this space-charge as well. A model is proposed which explains the thermally stimulated current observed to flow through an irradiated MOS structure.

The effects of ionizing radiation and fast neutrons on a new type of Schottky-barrier device are described. This new structure has a P-N junction guard ring to eliminate the "edge effects" which degrade device characteristics in a radiation environment. The effect of ionizing radiation on the density of surface states at the metal-semiconductor interface is also described.

Section III of this report is concerned with the effects of fast neutrons on silicon junction devices. The first part of this section describes some preliminary experiments to characterize recombination and trapping mechanisms in neutron-radiated silicon PνN, PπN, and PIN diodes using two techniques: (1) open-circuit forward-voltage recovery and (2) reverse-bias capacitance-voltage measurements. Measurements of devices irradiated over a wide range of temperatures are described and their results are interpreted in terms of isolated defect and clustered damage models.

The second part of Section III is devoted to a study of neutron effects on "nearly abrupt" X-band avalanche diodes. These microwave oscillators and amplifiers are being widely employed in military systems and their radiation sensitivity is of much interest. Both dc and microwave measurements were made to a total neutron fluence of 10^{16} n/cm^2. Surprisingly enough, microwave-device behavior was found actually to improve at high neutron fluences. The improvement in device behavior in terms of device structure is discussed.

I. OPTICAL PROPERTIES OF ZN-O AND CD-O COMPLEXES IN GAP

2. INTRODUCTION

The observation of luminescence arising from the recombination of electrons and holes at defects in semiconductors offers the experimenter the possibility of deducing many important characteristics of defects. Although most of the research in this direction has been concerned with chemical impurities, it has become apparent with the discovery of radiation-induced defect luminescence that the properties of such recombination centers may also be obtained. The recent work of Yuknevich et al.,[1]* and Spry and Compton,[2] who have studied the radiation-induced luminescence from the A center in silicon, exemplifies this possibility. However, the precise recombination mechanism which is operative in this case is not yet clear. In a previous paper[3] we demonstrated that this information is crucial to the proper interpretation of experiments which are based on the use of semiconductor statistics appropriate to the model of the recombination. The optical studies described there also showed that significant data on the properties of nonradiative radiation damage centers can be obtained through their perturbation of the recombination spectra due to other luminescence centers in the same crystal.

Closely allied to radiation-induced defects are natural defects involving vacancies which are incorporated during the growth of crystals. Luminescence associated with such defects is also well known. For a time, it was believed that the red luminescence in p-type GaP containing Zn or Cd acceptors was related to an intrinsic defect, possibly the phosphorus vacancy in GaP. Other investigators of this luminescence had suggested that it arose from donor-acceptor pair recombination involving isolated Zn or Cd and O; however, proof that O was involved was never convincing. For example, crystals grown without the deliberate addition of O to the melt usually exhibited the red luminescence. On the other hand, much of the initial data was consistent with a model for the recombination center of an uncharged electron trap formed by an acceptor and nearest neighbor phosphorus vacancy.

The studies reported here showed that the luminescence mechanisms were complex and that the red band was actually composed of two bands. The high-energy band has a very striking series of phonon peaks which strongly suggest a vibrational local mode of a heavy atom. Zeeman splitting experiments, lifetime measurements,

*References are listed on page 128

and the observation of a Cd isotopic shift in the zero phonon line of spectrum all pointed to a complex defect containing an acceptor with an axis of symmetry along the <111> direction. Prompted by the work of Morgan et al.[4] who were performing similar studies, further experiments were done which confirmed their finding of an O isotope shift in the sharp lines of the high-energy band. This forced us to conclude that complexes formed by nearest neighbor Zn-O and Cd-O pairs were instrumental in causing the red luminescence so that the acceptor-vacancy model had to be abandoned.

3. SUMMARY OF RESEARCH

The study of the red luminescence in GaP divided naturally into two parts: (1) The identification of the centers and recombination mechanisms operative at low temperatures (≤20°K) (described in detail in Attachment I); (2) The study of these mechanisms at higher temperatures (described in detail in Attachment II). Brief summaries of these studies are given below.

At high excitation levels (or short delay times in time-resolved spectroscopy), a high-energy, bound exciton red luminescense band is observed in GaP(Zn,O) and GaP(Cd,O). In Cd-doped GaP, the bound-exciton band displays a no-phonon doublet line replicated at 7-meV intervals to lower energies by a distinctive series of sharp phonon sidebands. A similar though less distinctive series of phonon replicas is seen in Zn-doped material but the zero phonon line is not visible. At weak excitation levels (or long delay times in time-resolved spectroscopy), a low-energy pair band is observed. In neither material does this band show any structure. The bound-exciton and pair bands are shown in Figure 1(a) of Attachment I. The fine structure present in the bound-exciton spectrum in Cd-doped GaP made possible a wide range of experimental observations.

The doublet nature of the no-phonon line and the temperature dependence of the relative intensities of its member lines are immediately reminescent of the spectrum from isoelectronic traps.[5] In these, a doublet arises from an exciton, bound at an uncharged trap, decaying out of two states; the more energetic transition corresponds to an allowed transition while the lower energy transition corresponds to a forbidden transition. The exact analog to the present case was confirmed by Zeeman splitting experiments on the no-phonon doublet. The symmetry of the Zeeman splitting also showed that the defect has an axis of symmetry in the <111> direction. Decay-time measurements showed an exponential decay and a temperature dependence of the decay time which was consistent with the model of an exciton bound at an inert trap. Isotopic substitution experiments, first involving Cd^{114} and Cd^{110} and later O^{18} and O^{16} showed that both Cd and O are present near the trapping center.

The low- and high-energy red-luminescence bands always occur together and have similar shapes; this result indicates an intimate relationship between the two. Decay-time measurements and time-resolved spectroscopy proved very valuable in investigations of the low-energy pair band. They showed that while this band has a very long, non-exponential decay, it does not, like regular donor-acceptor pair spectra, shift to longer wavelengths with increasing time delay. These measurements, by separating the low- and high-energy bands completely, provided an accurate value for the energy separation of the bands in both Zn- and Cd-doped crystals.

This experimental data suggested the following model. [Refer to Figure 1(c) of Attachment I.] Electron traps are envisaged to arise from the formation of complexes consisting of nearest neighbor Cd-O or Zn-O pairs. When electron-hole pairs are created, the electrons become trapped in the short-range attractive potential of these complexes. The holes are either trapped in the resulting coulomb field or on any (compensated) ionized acceptors. The bound-exciton band arises from the decay of the electron-hole pairs bound at the Cd-O or Zn-O complexes, while the pair band arises from the recombination of electrons at Cd-O or Zn-O complexes with holes on distant Cd or Zn acceptors. There is no coulomb interaction energy term involved in this transition, which explains the absence of any change in shape of the low-energy band as the red luminescence decays. The variable separation and consequent variable overlap of the hole and electron wave functions are entirely analogous to regular donor-acceptor pair spectra, so that the overall time decay is non-exponential and long. The model accounts very satisfactorily for the relative energy positions of the bands.

The luminescence decay-time measurements of the bound exciton, when combined with absorption measurements in Cd-doped GaP, established that the concentration of Cd-O complexes is a few times $10^{16}/cm^3$. Later experiments showed that the concentration of these complexes could only be explained by a preferential pairing of donors and acceptors. The residual concentration of oxygen in GaP is $10^{17}/cm^3$ and deliberate doping with oxygen through the addition of Ga_2O_3 to the melt does not greatly increase the O content of crystals.

When an understanding had been obtained of the low temperature properties of the red luminescence in Zn- and Cd-doped GaP, experiments were performed which were designed to provide an understanding of the red luminescence at higher temperatures.

In this study, the spectral positions of the bound-exciton and pair bands and their time decays were determined as functions of temperature. The positions of the overlapping bands were determined by time-resolved spectroscopy and changes were correlated with corresponding changes in the decay-time characteristics.

These measurements showed unequivocally that at high temperatures the bound-exciton transition dominates over the pair emission.

A theory which accounts both qualitatively and quantitatively for the high temperature results in Zn-doped material was developed. The theory gives only qualitative agreement for Cd-doped material, for reasons which are explained. The theory was based upon the assumption of a thermal equilibrium distribution of holes. The dominance of the bound-exciton transition at high temperatures is basically due to the much larger transition probability of this transition along with the consequences of thermal equilibrium, which maintains the population of holes in the exciton-hole state at high temperatures. The theory also accounts for the various complicated sample- and excitation-dependent effects which are observed.

Absorption and luminescence measurements in Zn-doped GaP show that the concentration of Zn-O complexes continues to rise as the acceptor concentration is increased above that corresponding to maximum luminescence efficiency. However, concentration quenching of the luminescence eventually occurs offsetting any large increase in the luminescence efficiency.

In the higher temperature studies, we required that samples be strongly excited by an electron beam at intermediate temperatures between 4.2° and 300°K. Many samples had to be appraised and usually these samples were irregularly shaped, brittle, and small. No commercially made dewar presently available is suitable for such studies. A dewar was designed specially with the present optical studies in mind.* It is a single-refrigerant dewar employing the forced convection of cold gas to obtain sample temperatures in the range 12° to 300°K. It features quick cool-down time, the option of fast thermal cycling, the efficient removal of heat from small irregularly shaped samples mounted strain free, the ability to change samples easily, and thermometry isolated from the sample irradiation chamber.

*The design and construction of this dewar was funded by another contract. Because of its use in these studies, the description of it is included in this report as Attachment III.

II. RADIATION-INDUCED SURFACE EFFECTS

4. RADIATION-INDUCED SPACE-CHARGE BUILDUP IN MOS STRUCTURES

a. Introduction

Ionizing radiation causes a positive space-charge accumulation in the SiO_2 layer commonly used in Si planar devices. These devices, which employ SiO_2 layers as a means of surface passivation, suffer degradation as a result of this space-charge buildup — h_{FE} and I_{CBO} degradation for bipolar transistors and turn-on voltage shifts for unipolar MOS-FETs.[1] Recently there has been a considerable effort made to understand the radiation-induced charge-buildup process with the result that we now have a reasonably good semiquantitative understanding of the phenomenon.[2-7]

The interest in this problem stems from the combination of the need for devices that are suitably radiation tolerant and the increasingly widespread use of planar devices and techniques — particularly in the area of integrated circuits. Increased use of planar integrated circuits means, of course, an increased use of surface passivation layers such as SiO_2. The purpose of this portion of the report is to analyze the presently accepted model of the space-charge buildup process to determine how various factors will affect this buildup, and then to compare the analysis with observations made on the SiO_2 layers found in commercial MOS-FETs.

b. The Space-Charge Buildup Process

1. Qualitative Discussion. Zaininger[5] has proposed a simple model which explains qualitatively some of the observed features of the space-charge buildup. As shown in Figure 1 the oxide layer is part of a metal-oxide-semiconductor (MOS) structure across which a potential difference, V_G,* is applied. (V_G is considered positive when the metal is positive with respect to the Si.) Ionizing radiation passing through the oxide creates hole-electron pairs. The holes are assumed to be relatively immobile and are thus trapped or recombine with electrons before they can leave the oxide. The electrons, on the other hand, are mobile and, as a result, drift toward the positive electrode. Some electrons are thus removed from the oxide and, since the Si is unable to supply electrons to the SiO_2 (because of a large potential barrier at the Si-SiO_2 interface), a net positive space-charge, Q_R, builds up near the Si-SiO_2 interface. As the positive space-charge grows, the electric

*A glossary of terms for Section II is included in Appendix A.

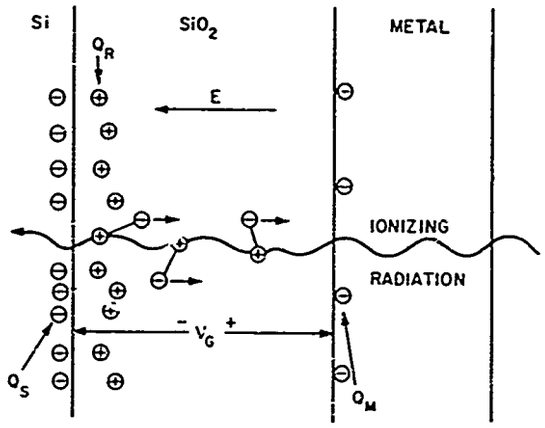

Figure 1. Model of space-charge buildup process in an MOS structure exposed to ionizing radiation.

field, E, in the oxide between the space-charge and the positive electrode decreases. When the field in this region is reduced to zero, no further charge will accumulate unless V_G is increased. It is apparent then that Q_R is positive, that it saturates with increasing dose, and that the saturation value, $Q_R(\text{sat})$, will depend on V_G. Q_R will induce negative charges in both the Si and metal electrodes. When the irradiation ceases and the electrodes are shorted ($V_G = 0$) the net charge in the Si surface, Q_S, and the net charge in the metal, Q_M, will both be negative and their sum equal in magnitude to Q_R, i.e.,

$$Q_R + Q_S + Q_M = 0 \qquad (1)$$

Speth and Fang[3] and Grove and Snow[4] have proposed similar models which relate quantitatively $Q_R(\text{sat})$ to the bias applied across the oxide during irradiation, V_G. These models do not, however, explicitly discuss the charge buildup process in a quantitative way.

2. Quantitative Analysis. The model for the charge buildup process presented in the previous section is a rather simple one and may, for this reason, yield to a straightforward analysis. In this section an expression will be derived for Q_R (or what is more useful, ΔV, the voltage shift of the capacitance-voltage (C-V) curve for an MOS capacitor, which is the quantity actually observed) as a function of radiation dose. It will be assumed that the oxide layer is uniform in all necessary

properties and initially free of any space-charge. Factors such as contact potential difference and the effect of radiation on the fast states at the SiO_2-Si interface will be ignored.

Consider the situation illustrated in Figure 2. The potential V_G across the oxide gives rise to an electric field, E, which is uniform throughout the oxide and of magnitude V_G/X_o. The effect of ionizing radiation is to generate hole-electron pairs uniformly throughout the oxide at a rate of g pairs cm^{-3} s^{-1}. The effect of the electric field will be to drive electrons toward the metal and holes toward the Si. Goodman[8] has shown that the mobility-lifetime product for holes in SiO_2 layers is approximately an order of magnitude smaller than for electrons and thus we will assume that a significant concentration gradient will be set up only for the electrons. It is shown in Appendix B that the free electron concentration gradient, n(x), will reach an equilibrium given by

$$n(x) = g\tau\left[1 - \exp\left(\frac{-ax}{X_o}\right)\right] \tag{2}$$

where

$$a = \frac{X_o^2}{\mu\tau V_G}$$

provided diffusion is neglected and there has been no appreciable accumulation of space-charge to alter the field E.

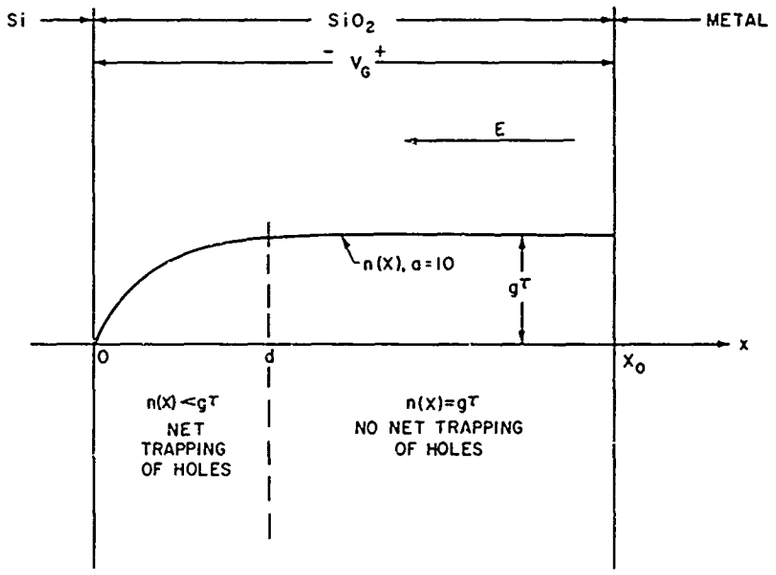

Figure 2. Initial conditions in the SiO_2 layer of an irradiated MOS structure.

The form of the expression for n(x) is shown in Figure 2 for a = 10. The quantity a is the ratio of the thickness of the oxide to the distance an electron will drift in time τ. If $V_G = 0$ then $a = \infty$ and $n(x) = g\tau$ everywhere in the oxide. Experimentally, it is observed that some space-charge accumulates when $V_G = 0$, presumably as the result of diffusion of electrons out of the oxide or as the result of a built-in field in the oxide. However, the amount of space-charge accumulated when $V_G = 0$ is relatively small so it will be assumed that the net trapping rate is proportional to $g\tau - n(x)$, i.e., there is no net trapping of holes in the region in which $n(x) = g\tau$. Since n(x) is least at x = 0, the net trapping rate will be greatest near the SiO_2-Si interface. Furthermore, since it is observed experimentally that the space-charge accumulates almost entirely in the small fraction of the oxide adjacent to this interface,[4,9] it appears that 10 is a reasonable estimate for a, i.e., that $n(x) = g\tau$ throughout most of the oxide. As a result, no charge is accumulated in the bulk of the oxide and the electric field is uniform in this region (the region between the space-charge and the anode) at all times. As the space-charge builds up, the field in the bulk of the oxide decreases. When sufficient charge collects, E vanishes and no more electrons drift out of the oxide into the metal electrode.

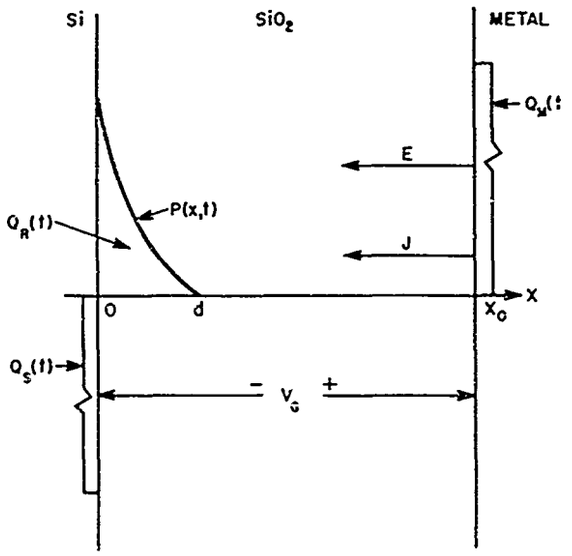

Figure 3. Situation in the SiO_2 layer at any time during irradiation.

At any time, t, the density of trapped holes in the oxide, P(x,t), is greatest at x = 0 and decreases to zero at some distance d from the SiO_2-Si interface, see Figure 3. We may write

$$Q_R(t) = q \int_0^d P(x,t)dx \tag{3}$$

$$Q_S(t) = -q \int_0^d \frac{X_o - x}{X_o} P(x,t)dx \tag{4}$$

$$Q_m(t) = -q \int_0^d \frac{x}{X_o} P(x,t)dx \tag{5}$$

The expressions for $Q_S(t)$ and $Q_M(t)$ are valid when the irradiation has ceased and $V_G = 0$. We may also write

$$Q_R(t) = - \int_0^t J\,dt \tag{6}$$

where J is the current density due to electrons crossing the SiO_2-metal interface.

$$J = qg\mu\tau E(X_o) \tag{7}$$

It is shown in Appendix C that

$$E(X_o) = -\frac{V_G}{X_o} + \frac{q}{\epsilon\epsilon_o} \int_0^d \frac{x}{X_o} P(x,t)dx \tag{8}$$

Combining (3), (6), (7), and (8) we have

$$\int_0^d P(x,t)dx = \int_0^t \left[A - B \int_0^d xP(x,t)dx \right] dt \tag{9}$$

where

$$A = \frac{g\mu\tau V_G}{X_o}$$

and

$$B = \frac{qg\mu\tau}{\epsilon\epsilon_o X_o}$$

Differentiating (9) with respect to time and rearranging we have

$$\int_0^d \left[\frac{\partial P(x,t)}{\partial t} + BxP(x,t) - Am(x)\right] dx = 0 \tag{10}$$

where m(x) is an arbitrary function of x subject to the restriction

$$\int_0^d m(x)dx = 1 \tag{11}$$

For (10) to be true in general the integrand must be identically zero. It may easily be shown that the equation obtained by equating the integrand of (10) to zero yields

$$P(x,t) = \frac{V_G \epsilon\epsilon_o}{q}\frac{m(x)}{x}\left[1 - \exp\left(\frac{-q\mu\tau xgt}{\epsilon\epsilon_o X_o}\right)\right] \tag{12}$$

The voltage shift, $\Delta V_{\pm}(t)$, for $V_G > 0$ of the MOS C-V curve is given by

$$\Delta V_{\pm}(t) = \frac{Q_S(t)}{C_{ox}} = \frac{-qX_o}{\epsilon\epsilon_o}\int_0^d \frac{X_o - x}{X_o} P(x,t)dx \tag{13}$$

or using (12)

$$\Delta V_{\pm}(t) = -V_G \int_0^d \left(X_o - x\right)\frac{m(x)}{x}\left[1 - \exp\left(\frac{-q\mu\tau xgt}{\epsilon\epsilon_o X_o}\right)\right] dx \tag{14}$$

From (14) it is immediately apparent that since the generation rate, g, appears only in the product gt, $\Delta V_{\pm}(t)$ will be the same for a given number of hole-electron pairs (gt) regardless of the rate at which the pairs were generated (g); in other words, $\Delta V_{+}(t)$ is dose-rate independent.

It is also apparent from (14) that $\Delta V_{+}(t)$ will saturate for large values of t:

$$\lim_{t\to\infty} \Delta V_{+}(t) = \Delta V_{+}(sat) = -V_G\left[X_o\int_0^d \frac{m(x)}{x}dx - 1\right] \tag{15}$$

We have postulated that the space-charge is due only to the trapping of holes and hence, for (12) to be physically meaningful, we must have $m(x) \geq 0$ for $0 \leq x \leq d$.

When this restriction is coupled to (11) it is apparent that $\int_0^d \frac{m(x)}{x}\,dx$

will have its minimum value when $m(x) = \delta(x-d)$, i.e., when the space-charge occurs in the form of a sheet of charge at $x = d$. Under these conditions

$$\int_0^d \frac{m(x)}{x}\,dx = \int_0^\infty \frac{\delta(x-d)}{d}\,dx = \frac{1}{d}$$

and

$$\Delta V_+(\text{sat})_{\min} = -V_G\left(\frac{X_o}{d} - 1\right)$$

Hence, for the general case we may write

$$\Delta V_+(\text{sat}) = -V_G\left(\frac{nX_o}{d} - 1\right), \quad n \geq 1 \tag{16}$$

Since we know from experiment that $X_o \gg d$, (16) predicts that the magnitude of the voltage shift at saturation will be greater (in general much greater) than the bias applied across the oxide during irradiation.

For $V_G < 0$ the same basic charge buildup process should occur except that the accumulation will take place close to the metal-SiO_2 rather than the SiO_2-Si interface. In this case the space-charge is further removed from the Si electrode and hence will have less effect upon it. The net result should be a smaller voltage shift for the same amount of space-charge accumulation. We can develop an expression for the voltage shift for $V_G < 0$, $\Delta V_-(t)$, quite simply by imagining the Si and metal electrodes to be interchanged in the case discussed above. Hence,

$$\Delta V_-(t) = \frac{Q_M(t)}{C_{ox}} = -\left[\frac{Q_R(t) + Q_S(t)}{C_{ox}}\right]$$

or

$$\Delta V_-(t) = -\frac{q}{C_{ox}}\int_0^d P(x,t)\,dx - \Delta V_+(t) \tag{17}$$

where we have used (1) and (3). By combining (12), (14), and (17), and remembering to change the sign of V_G to conform to our convention of signs, we have after simplification:

$$\Delta V_-(t) = V_G\int_0^d m(x)\left[1 - \exp\left(\frac{-q\mu\tau x g t}{\epsilon\epsilon_o X_o}\right)\right]dx \tag{18}$$

It is apparent that the space-charge buildup for $V_G < 0$ is also dose-rate independent and that $\Delta V_{-}(t)$ is negative and saturates with increasing irradiation.

At saturation, (18) yields

$$\Delta V_{-}(sat) = V_G \int_0^d m(x)dx = V_G \tag{19}$$

It is interesting to note that $\Delta V_{-}(sat)$ is independent of the actual space-charge distribution in the oxide.

There is a special case worth discussing which arises if we assume that the density of trapped holes at every point in the oxide has the same dependence on irradiation time. Such an assumption is clearly an oversimplification but it leads to a simple and rather useful result. Under this assumption we may write

$$P(x, t) = f(x) \cdot h(t) \tag{20}$$

and then (10) becomes

$$\frac{dh(t)}{dt} + kgh(t) = rg \tag{21}$$

where

$$k = \frac{q\mu\tau \int_0^d xf(x)dx}{\epsilon\epsilon_o X_o \int_0^d f(x)dx}$$

and (22)

$$r = \frac{\mu\tau V_G}{X_o \int_0^d f(x)dx} \tag{23}$$

The general solution of (21) is

$$h(t) = \frac{r}{k}\left[1 - \exp(-kgt)\right]$$

Combining (13), (20), and (23), we obtain for this case

$$\Delta V_+(t) = -V_G\left[1 - \exp(-kgt)\right]\left\{\frac{X_o\int_0^d f(x)dx}{\int_0^d xf(x)dx} - 1\right\} \tag{24}$$

The voltage shift for $V_G < 0$ can be found from (17) to be

$$\Delta V_-(t) = V_G\left[1 - \exp(-kgt)\right] \tag{25}$$

If we assume a specific form for f(x) then (24) can be simplified further. Snow et al.[7] have shown that at saturation the space-charge density should decrease exponentially with distance into the oxide from the SiO_2-Si interface. We will assume (as an approximation) that the density has this form at all times and choose $f(x) = e^{-x/c}$. Under this assumption (24) becomes

$$\Delta V_+(t) = -V_G\left(\frac{X_o}{c} - 1\right)\left[1 - \exp(-kgt)\right] \tag{26}$$

where

$$k = \frac{q\mu\tau}{\epsilon\epsilon_o}\frac{c}{X_o}, \quad X_o \gg c \tag{27}$$

c. Experimental Procedure

As implied earlier the most convenient way to monitor the space-charge buildup in an SiO_2 layer is to observe the voltage shift of the capacitance-voltage (C-V) curve of the MOS structure of which the SiO_2 layer is a part. A very convenient MOS structure is found in commercial MOS-FETs. These devices are available with different oxide types and with both n- and p-type Si substrates. For the studies reported here the Raytheon RN-1030 and Fairchild FI-100 MOS-FETs were found to be the most suitable. The RN-1030 is a p-channel enhancement mode device with a Au-Cr gate 1200Å thick, 1600Å of deposited SiO_2, and an n-type substrate. The source and drain are arranged in an interdigitated geometry. The FI-100 is also a p-channel enhancement mode device. It has an Al gate with 1200Å of thermally grown SiO_2 on an n-type substrate. Both devices have a gate-to-substrate capacitance of a few picofarads.

The (C-V) curves of the MOS-FETs were obtained with an automatic curve tracer (employing a Boonton 71A L-C meter) at a measuring frequency of 1 MHz. The source and drain connections to the devices were left open during measurement.

It was found experimentally that there is a variation in radiation sensitivity among devices. It is, therefore, not generally possible to make a meaningful quantitative comparison between the results obtained from two devices even though they are the same type and made by the same manufacturer. The procedure followed in these experiments was to irradiate a device under one set of conditions, anneal the device, then irradiate it again under a new set of conditions. For the RN-1030 devices an anneal at 300°C for one hour at zero bias was found to be sufficient to remove virtually all the radiation-induced space-charge even in devices which had received doses of several megarads of Co^{60}-gamma rays. Furthermore, devices irradiated a second time under the same conditions used in the first irradiation showed good reproducibility of results, i.e., after an anneal a device has no memory of a previous irradiation. In most cases the FI-100 MOS-FETs did not anneal completely in one hour at 300°C. Generally these devices were annealed for longer times at somewhat higher temperatures.

The C-V curves of the irradiated MOS-FETs showed both hysteresis and distortion which increased with increasing radiation dose but which appeared to be relatively independent of the bias used during irradiation. Both phenomenon indicate the creation by the radiation of fast interface states at the SiO_2-Si interface. These states are not part of Q_R and are not included in the analyses discussed in b. of this section. It was observed experimentally that if the C-V curve tracer was stopped at any voltage value the capacitance value decayed with time to a value midway between the two branches of the C-V curve. Furthermore, the same equilibrium value of capacitance was reached from either branch of the C-V curve. Accordingly the voltage shift of a C-V curve was measured using a point midway between the two branches.

The distortion of the C-V curves was greatest in the inversion regime. At the flat band condition, where ΔV was measured, the distortion was not large enough to cause appreciable error and was therefore ignored.

d. Experimental Results

1. Space-Charge Buildup as a Function of Radiation Dose. The voltage shift of the C-V curves of both an RN-1030 and FI-100 MOS-FET as a function of dose is shown in Figure 4 for devices irradiated at +2.5V bias, and in Figure 5 for devices irradiated at -2.5V bias. All irradiation were performed using Co^{60}-gamma rays at a dose rate of approximately 10^2 rads/s. In order to make a quantitative comparison between the results shown in Figures 4 and 5 and the analysis discussed earlier we will make the most realistic assumptions we can consistent with mathematically tractable equations; namely, we assume $P(x, t) = f(x) \cdot h(t)$ and that

f(x) is of the form $e^{-x/c}$. It is more convenient to work with radiation dose than time, t, or number of hole-electron pairs, gt, and hence we will rewrite (26) and (25) as

$$\Delta V_+(D) = -\alpha V_G\left(1 - e^{-\beta D}\right) \tag{28}$$

$$\Delta V_-(D) = \gamma V_G\left(1 - e^{-\beta D}\right) \tag{29}$$

D is the dose in Mrads. We have seen that in general γ should be unity. From (26)

$$\alpha = \left(\frac{X_o}{c} - 1\right) \tag{30}$$

If it is assumed that ~25 eV (approximately 3 times the energy gap of SiO_2) are required to create a hole-electron pair in SiO_2 then using the definition of the rad (100 ergs absorbed per g) it may be shown that the number of hole-electron pairs, gt, created by a dose D is given by

$$gt\left(\text{pairs/cm}^3 \text{ in } SiO_2\right) = 6.7\text{x}10^{24}\ D(\text{Mrads})$$

Using this conversion factor and (27) we have

$$\beta = 6.7\text{x}10^{24}\,\frac{q\mu\tau}{\varepsilon\varepsilon_o}\,\frac{c}{X_o}\ , \qquad c \ll X_o \tag{31}$$

α and γ in (28) and (29) may be obtained directly from the saturation values of ΔV in Figures 4 and 5. The values so obtained are listed in Table 1. As expected from (16), $\alpha \gg 1$. However, $\gamma < 1$ in contradiction to (19). This point will be discussed in more detail later. From (30) it is possible to obtain the ratio c/X_o and subsequently the value of c since X_o is known for the devices used. Values of c/X_o and c are included in Table 1. The values of c given in the Table are consistent with the finding of Snow et al.[4] and Zaininger[9] who find the space-charge is located within $\lesssim$200 Å of the SiO_2-Si interface. Since $c \ll X_o$ we are justified in using (31) for β.

TABLE 1

Oxide Parameters for Space-Charge Buildup

	V_G = +2.5V					V_G = -2.5V		
	α	c/X_o	c (Å)	β (Mrad^{-1})	$\mu\tau$ (m^2/V)	γ	β (Mrad^{-1})	$\mu\tau$ (m^2/V)
RN-1030	12.5	0.074	120	0.10	$5\text{x}10^{-16}$	0.79	21	$9\text{x}10^{-15}$
FI-100	21.0	0.045	54	0.125	$1\text{x}10^{-16}$	0.37	31	$2\text{x}10^{-14}$

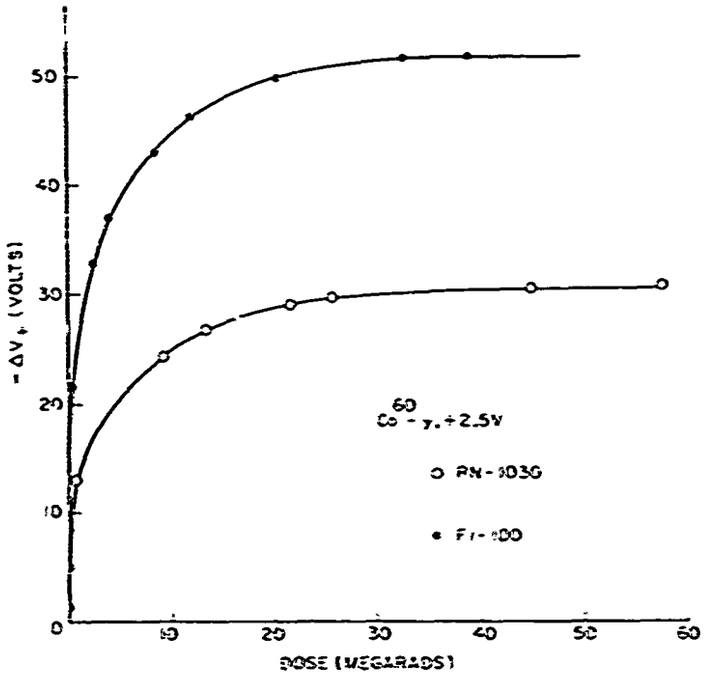

Figure 4. Voltage shift as a function of dose for an RN-1030 and FI-100 MOS-FET irradiated at -2.5V bias.

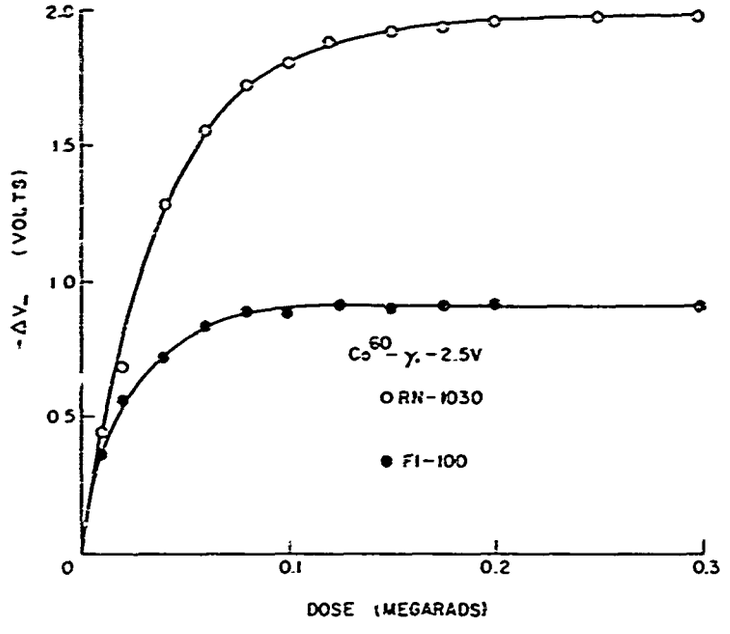

Figure 5. Voltage shift as a function of dose for an RN-1030 and FI-100 MOS-FET irradiated at -2.5V bias.

For $V_G = +2.5V$, β may be obtained from a semilog plot of (28) rewritten in the form

$$1 - \frac{\Delta V_+(D)}{\alpha V_G} = e^{-\beta D} \tag{32}$$

β for $V_G = -2.5V$ may be obtained in a similar way from (29). The semilog plots for +2.5V and -2.5V bias are shown in Figures 6 and 7 respectively. For both polarities of bias, the graphs are not straight lines; β is initially large then

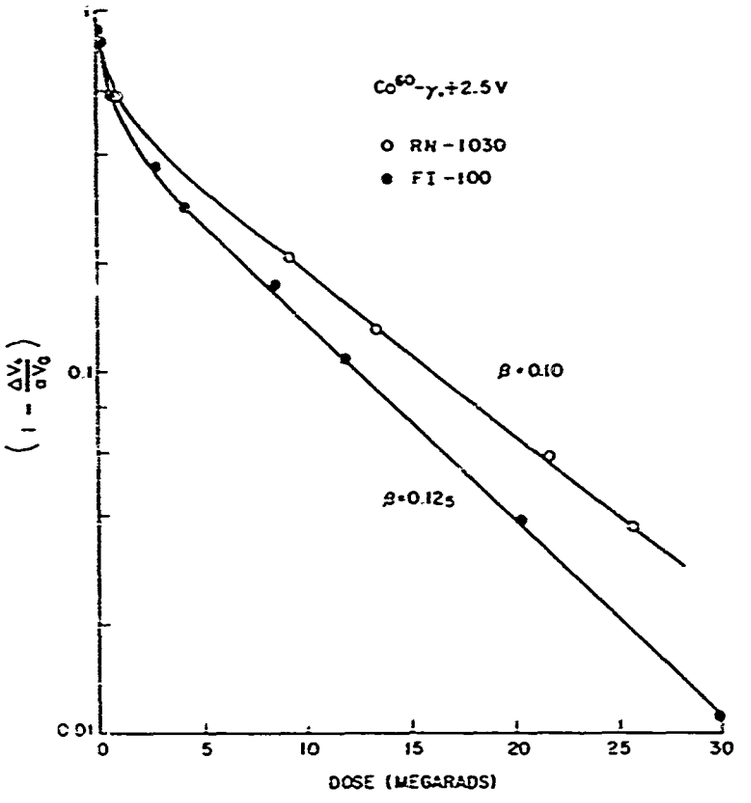

Figure 6. Semilog plot of $\left[1 - \frac{\Delta V_+(D)}{\alpha V_G}\right]$ as a function of dose for an RN-1030 and FI-100 MOS-FET irradiated at +2.5V bias.

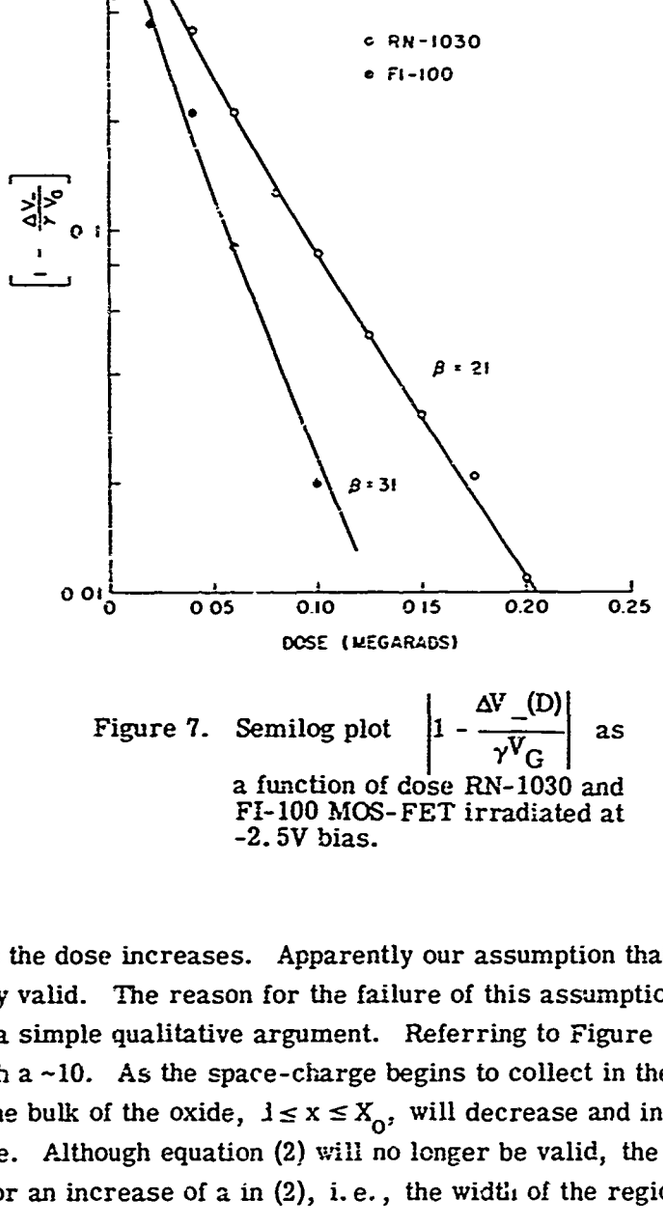

Figure 7. Semilog plot $\left|1 - \frac{\Delta V_{-}(D)}{\gamma V_G}\right|$ as a function of dose RN-1030 and FI-100 MOS-FET irradiated at -2.5V bias.

decreases as the dose increases. Apparently our assumption that $P(x,t) = f(x) \cdot h(t)$ is not strictly valid. The reason for the failure of this assumption may be made apparent from a simple qualitative argument. Referring to Figure 2, n(x) is initially as shown with a ~10. As the space-charge begins to collect in the region $0 \leq x \leq d$ the field in the bulk of the oxide, $d \leq x \leq X_0$, will decrease and in so doing cause n(x) to change. Although equation (2) will no longer be valid, the result will be similar to that for an increase of a in (2), i.e., the width of the region in which $n(x) < g\tau$ will decrease. Succeeding increments in the space-charge will occur closer and closer to the SiO_2-Si interface. Thus, the center of gravity of the space-charge will move closer to the SiO_2-Si interface with increasing dose. In terms of our postulated exponential form for the space-charge, c/X_0 and, hence, β should decrease

with increasing dose. In (32), α is also a function of c/X_o while γ which appears in the corresponding equation for $\Delta V_{-}(D)$ is not. For this reason, the departure from linearity is more pronounced for +2.5V bias than for -2.5V bias. The values of β obtained from the straight line portions of the curves in Figures 6 and 7 are listed in Table 1.

Substituting the values of c/X_o and β from Table 1 into (31) yields the values indicated in the Table for the $\mu\tau$ product. For V_G = -2.5V the value of c/X_o for +2.5V was assumed and this assumption may be responsible, at least in part, for the very large difference between the $\mu\tau$ values for the two bias polarities. c/X_o may, in fact, be considerably larger for $V_G < 0$ in which case (31) would yield a smaller value for $\mu\tau$. There is no way of determining c/X_o from the measurements discussed here; etching experiments for $V_G < 0$ similar to those referred to earlier[4,9] may show whether c/X_o is larger for this case. However, it is unlikely that c/X_o is ~200 times greater for space-charge accumulation at the SiO_2-metal interface. and part of the discrepancy must arise from a real difference in the properties of the oxide at the two interfaces. The $\mu\tau$ product as calculated from (31) should reflect the properties of the oxide in the region of space-charge accumulation, and hence $\mu\tau$ must be smaller at the SiO_2-Si interface than at the SiO_2-metal interface. One might intuitively expect this to be the case since the mismatch between the Si and SiO_2 and, hence, the disorder responsible for lowering the $\mu\tau$ product will be greater than that between the metal and SiO_2. The values of $\mu\tau$ given for V_G = -2.5V are probably closer to, although somewhat less than, the value for bulk oxide. The values are thus consistent with the value ~10^{-13} m^2/V reported by Goodman[8] for much thicker oxides.

2. Dependence of Charge Buildup on Bias. The analysis of the charge build-up model presented earlier predicts that ΔV should depend strongly on the bias applied across the oxide during irradiation. Figures 8 and 9 show the voltage shift of MOS capacitance for a single RN-1030 device irradiated with Co^{60}-gamma rays at ~10^2 rads/s for bias values between +10V and -15V. For $V_G < 0$ a relatively small dose was required to reach saturation at each bias value. For $V_G > 0$, on the other hand, the dose required to reach saturation is very large. (See Figure 4.) Because of the long irradiation times involved and the small chance that a device would survive several irradiations to such high dose levels and the subsequent anneals, it was decided to stop the irradiations for $V_G > 0$ at ~4 Mrads. For this dose level, β has become reasonably constant (Figure 6) and hence we may employ (28).

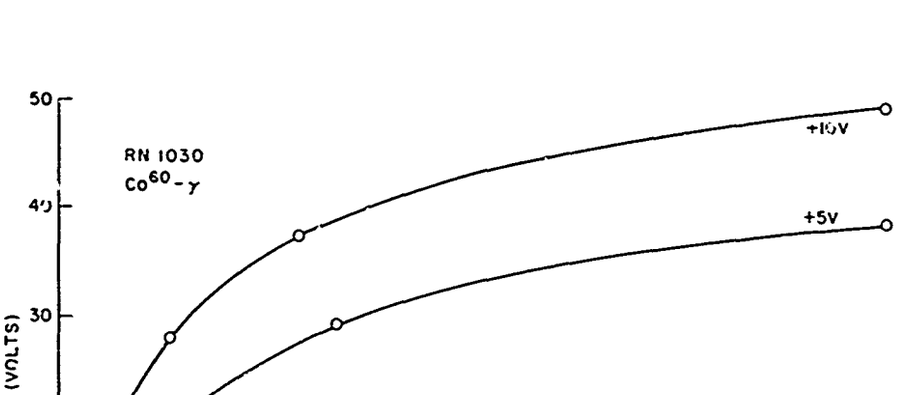

Figure 8. Voltage shift as a function of dose for an RN-1030 MOS-FET for positive bias values.

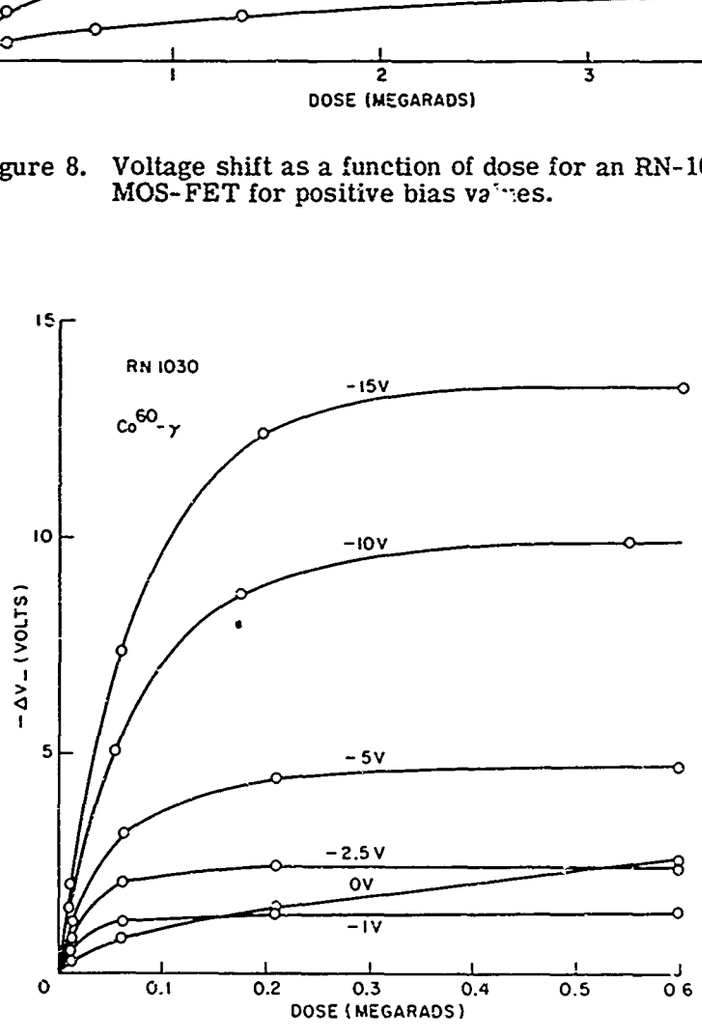

Figure 9. Voltage shift as a function of dose for an RN-1030 MOS-FET for negative bias values.

From Figure 8 it is observed that a charge buildup occurs at OV bias. This buildup may result either from a built-in bias across the oxide as might arise from the contact potential difference between the metal and Si electrodes or from diffusion of the electrons out of the SiO_2. The analysis presented earlier ignores both these effects and is thus not valid for $V_G = \sim OV$. The curve for OV is shown in both Figures 8 and 9 and a comparison shows that this curve clearly belongs with the set for $V_G > 0$, indicating perhaps that a built-in voltage corresponding to positive polarity on the gate is responsible. For the FI-100 the curve for OV bias is more of a compromise between the sets for the two polarities; this compromise suggests a smaller built-in potential than for the RN-1030.

Figure 10 shows the voltage shift at saturation for $V_G < 0$ and at 4 Mrads for $V_G > 0$ as a function of V_G for the curves shown in Figures 8 and 9. At 4 Mrads, $\Delta V_+(4)$ should be $\sim 2/3 \Delta V_+(sat)$. (See Figure 4.) The curve for $V_G > 0$ thus has $\sim 2/3$ the slope of the curve for saturation but should have the same shape. $\Delta V_+(4)$ appears to be linear with V_G for smaller values of V_G in agreement with (28). (The slope should be $\sim 2/3 [(X_o/c) - 1]$.) This linearity implies that at saturation, c is not a function of V_G - a fact which has been tacitly assumed in using (28). At higher values of V_G the slope decreases; this indicates a reduction in X_o/c. Such behavior is not unexpected. As V_G increases, $Q_R(sat)$ will increase causing an increase in both the density of electrons in the Si surface and the electric field at the SiO_2-Si interface. This electric field can be extremely large - possibly large enough to cause significant field-assisted tunnelling of electrons into the trapped-hole sites close to the Si. This effect will change the shape of the distribution of $Q_R(sat)$ in such a way that the effective value of c will increase causing X_o/c to decrease. (See Figure 11.)

Figure 10 also includes some points for FI-100 MOS-FETs. The points shown were obtained from several different devices and hence may only be used to indicate the general behavior of this type of device compared to the RN-1030. For $V_G > 0$ the curve seems to be similar to that for the RN-1030 but with a steeper slope. The same change in the shape of the $Q_R(sat)$ distribution for larger values of V_G probably occurs in this device as well.

For $V_G < 0$, $\Delta V_-(sat)$ appears to be linear with V_G for the RN-1030 with a slope close to unity as expected from (19). For the FI-100, on the other hand, the slope of the curve is considerably less than unity. This observation cannot be explained as the result of a variation of c since we have seen from the analysis given earlier that $\Delta V_-(sat)$ does not depend explicitly on the shape of the space-charge distribution. It can be explained very simply, however, if we follow Stanley[6] and assume that, in this case, electrons as well as holes are trapped in the oxide. For

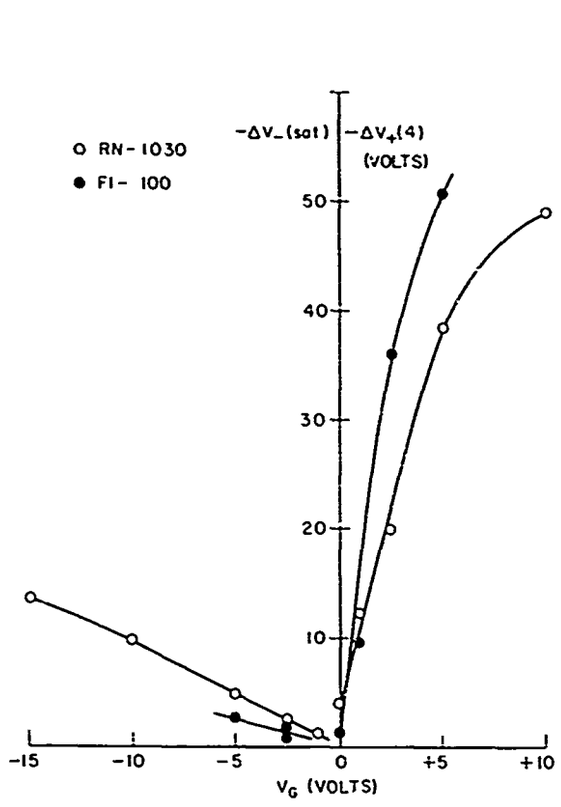

Figure 10. Voltage shift at saturation for $V_G < 0$ and 4 Mrads for $V_G > 0$ for an RN-1030 and FI-100 MOS-FET.

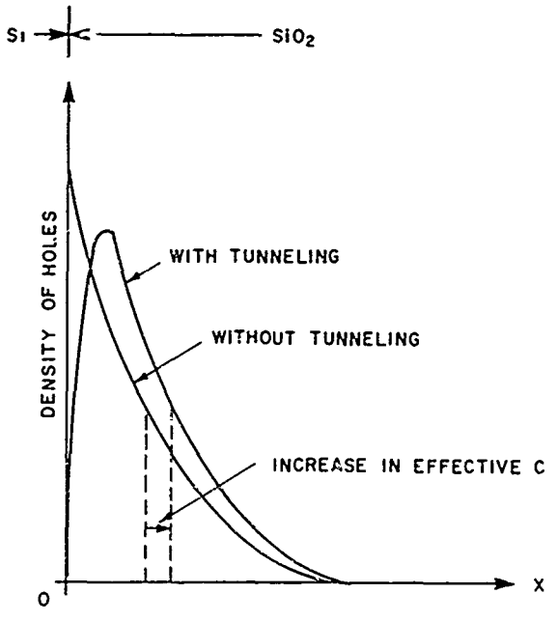

Figure 11. Distribution of radiation induced space-charge in SiO_2 with and without tunnelling at the SiO_2-Si interface.

the simple situation shown in Figure 12 in which holes are trapped uniformly over a distance d_2 at the SiO_2-metal interface and electrons are uniformly trapped over a distance d_1 at the SiO_2-Si interface it may be shown[6] that

$$\Delta V_{-}(sat) = V_G \left(1 - \frac{2Q_{R_-} d_1}{Q_{R_+} d_2 + Q_{R_-} d_1} X_o \right) \tag{33}$$

From (33) it is apparent that a slope of unity for $\Delta V_{-}(sat)$ vs V_G is a limiting case which occurs for $Q_{R_-} = 0$, i.e., no electrons trapped in the oxide. For all other cases the slope is less than unity. Using (33) it is possible to estimate the amount of negative charge required to produce the observed reduction in slope for the FI-100 devices. If we substitute $\Delta V_{-}(sat) = 1/2\ V_G$ and $d_1 \sim d_2 \sim X_o/10$ in (33), we obtain $Q_{R_-} \approx Q_{R_+}/40$. Thus a very small amount of negative charge trapped at the SiO_2-Si interface will greatly reduce the voltage shift for $V_G < 0$.

3. Location of Space-Charge in the SiO_2 Layer. It was mentioned earlier that it has been shown experimentally that the space-charge accumulates in a narrow region very close to SiO_2-Si interface for $V_G \geq 0$ during irradiation.[4,9] For $V_G < 0$ during irradiation, it was postulated that the space-charge accumulated next to the SiO_2-metal interface. The results presented in the previous sections appear to agree quite well with predictions derived from this assumption. Nevertheless, this agreement does not constitute conclusive proof. More direct evidence of the correctness of the model was obtained by the method illustrated schematically in Figure 13.

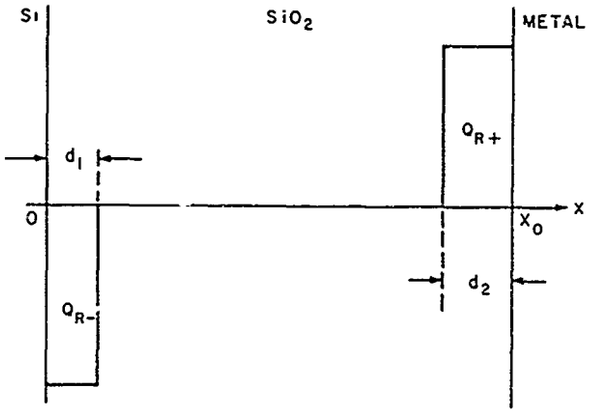

Figure 12. Simplified model of space-charge buildup at saturation when electron trapping occurs at the SiO_2-Si interface.

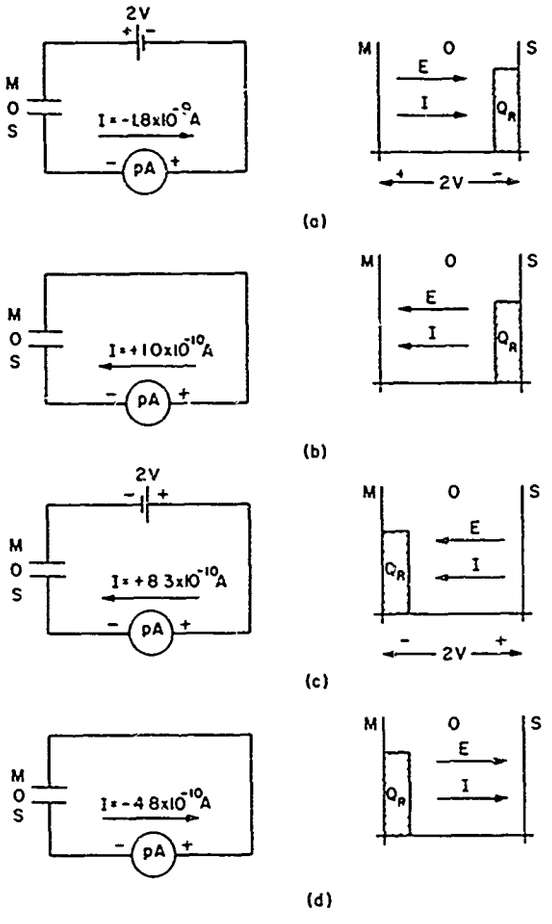

Figure 13. Location of space-charge in SiO_2 layer: (a) and (b) $V_G > 0$, (c) and (d) $V_G < 0$.

The gate-to-substrate MOS structure of an RN-1030 MOS-FET was connected in series with a 2V bias and a Keithley 610A electrometer (ammeter) as illustrated in Figure 13(a). The MOS structure was then exposed to Co^{60}-gamma radiation at a dose rate of $\sim 10^2$ rads/s. The conventional current flow observed in the circuit was -1.8×10^{-9}A (corrections were made for leakage currents in leads, etc.). Note the polarity of the meter. The situation in the MOS structure is also illustrated in Figure 13(a). The space-charge buildup, Q_R, occurs near the SiO_2-Si interface when the applied electric field, E, is as shown. After an exposure of ~40 minutes ($\sim 2.4 \times 10^5$ rads) the bias source was removed from the circuit, see Figure 13(b). The field in the oxide is now controlled by Q_R and will thus be reversed. As

expected the current in the circuit reversed. The direction of current flow through the oxide thus appears to be a sensitive indicator to the general location of the space-charge.

The experiment was repeated this time with the bias reversed, see Figure 13(c). The current flow was in the direction expected. After an exposure of approximately 40 minutes the bias was removed and the current was observed to reverse indicating a positive space-charge buildup near the SiO_2-metal interface, see Figure 13(d).

4. Dependence of Space-Charge Buildup on Radiation Dose Rate. RN-1030 MOS-FETs were irradiated at bias values of +4.6V, $\pm$2.5V, and OV at a high- and low-dose rate. The devices were first irradiated at a dose rate of $\sim 10^2$ rads/s using Co^{60}-gamma rays. After irradiation, the devices were annealed and then irradiated again, each device at the same bias as before, this time at a dose rate of $\sim 10^{10}$ rads/s using 20 keV electrons. It was estimated, using the dose-depth curves of Schumacher and Mitra[10], that each incident electron deposited 4.6×10^{-8} rads in the SiO_2 layer of the MOS-FET. (The electrons stopped in the SiO_2 layer have a negligible effect on Q_R.)

The voltage-shift curves as a function of dose are shown in Figures 14 and 15. For bias values of +4.6V and +2.5V the curves at the two dose rates coincide within experimental accuracy for doses up to 1 Mrad, the maximum dose used in these experiments. This result is in agreement with the predictions made from Equation (14). The prediction of dose-rate independence was based on the assumption that g increased linearly with dose rate. This assumption is probably reasonable although at high dose rates a situation may be reached in which the fraction of the incident electron energy used to create hole-electron pairs will change because other mechanisms by which the electrons lose energy may become important.

Dose-rate independence also requires that the $\mu\tau$ product be constant with dose rate. At very high dose rates the quasi-Fermi levels in the SiO_2 may shift sufficiently to influence the density of effective recombination centers and unfilled traps in the oxide and hence alter the lifetime or the mobility of the carriers. Both holes and electrons could be affected and without a detailed knowledge of the recombination centers and traps present in the oxide it is impossible to predict the effect of high dose rates. However, neither of these two effects seems to occur for $V_G > 0$ and dose rates up to $\sim 10^{10}$ rads/s.

At $V_G = 0$ the situation is quite different. For a given dose the voltage shift is approximately twice as large for the higher dose rate. The analysis which predicts the dose-rate independence is not applicable to this case, however, since it is based on the drift of electrons through the oxide and neglects diffusion. A possible

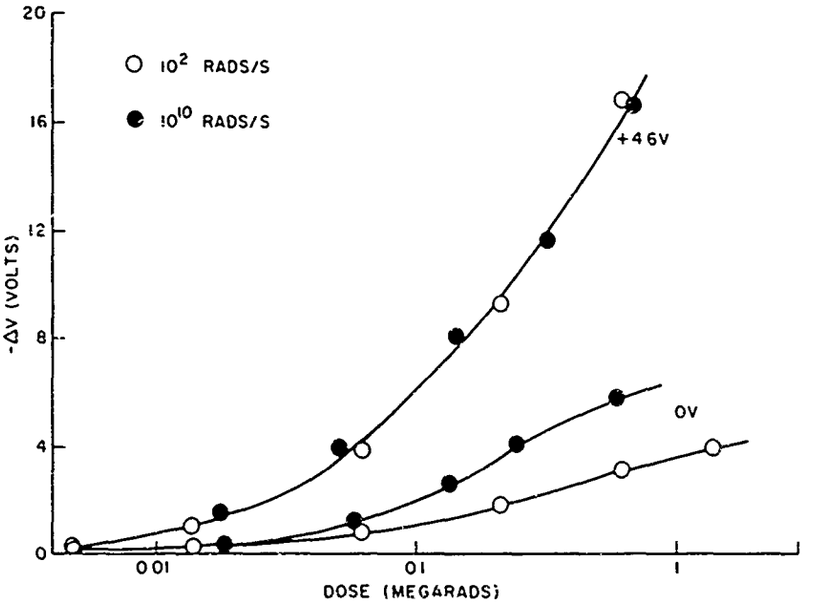

Figure 14. Voltage shifts as a function of dose for low and high dose rates for bias values of +4.6V and OV.

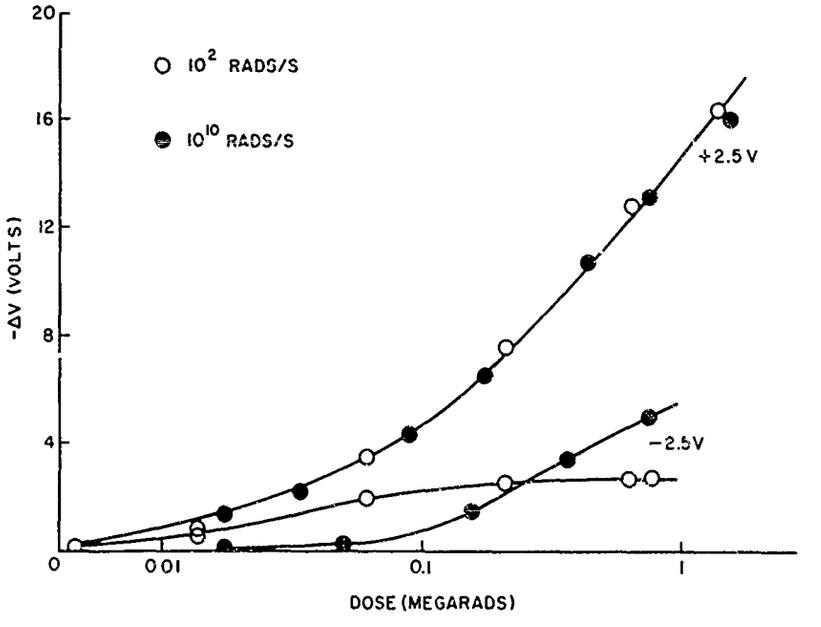

Figure 15. Voltage shifts as a function of dose for low and high dose rates for bias values of $\pm$ 2.5V.

mechanism for space-charge accumulation for $V_G \sim 0$ is diffusion of electrons out of the oxide. This process will increase with an increase in the density of free electrons in the oxide, $g\tau$, i.e., with an increase in the dose rate.

For V_G = -2.5V the voltage shift saturates at $\sim$-2.5V at the low dose rate as predicted by (19). At the high dose rate, on the other hand, the voltage shift is small for low doses but increases to a value considerably greater than -2.5V as the dose approaches 1 Mrads. This anomolous behavior cannot be explained in terms of the model discussed earlier. A comparison of the curves for OV and -2.5V bias at a high dose rate shows that these two curves are almost identical. The similarity suggests that the cause of the anomolous behavior may be diffusion. Thus, at high dose rates there may be enough diffusion of electrons across the SiO_2-Si interface to create a significant positive charge near the Si. This space-charge, even though it may be considerably smaller than the space-charge at the other interface, would be much closer to the Si and would have virtual control of the voltage shift. At high dose rates then, the voltage shift at negative bias values may be approximately the same as for OV bias.

Dose rates approaching 10^{11} rads/s were investigated, also using 20 keV electrons. At these dose rates it was found that the conductivity of the oxide becomes large enough that V_G may drive appreciable current through the oxide. If V_G is a high impedance source ($\geq 10^6$ ohms) the potential difference across the oxide may drop significantly with the result that less space-charge is accumulated.

e. Summary

The simple model used for the positive space-charge buildup assumes that the holes produced by ionizing radiation are trapped in the oxide while some of the corresponding electrons drift out of the oxide under the action of the applied potential difference. The analysis of this model predicts (1) the charge buildup should saturate with dose, D, approximately as $(1 - e^{-\beta D})$, (2) that the buildup at saturation should increase linearly with bias for both polarities of bias, (3) the buildup should depend on the dose absorbed but be independent of the radiation dose rate. The agreement between the predictions of the analysis and the experimentally observed buildup in SiO_2 layers in commercial MOS-FETs is generally quite good. However, to obtain quantitative agreement it was necessary to assume a much lower value for the mobility-lifetime product for electrons in the oxide for $V_G > 0$ than for $V_G < 0$. Furthermore, for some experimental observations it was necessary to postulate that a small amount of electron trapping also occurred in the oxide, and for others that diffusion of electrons at high dose rates may be important. The model appears to be of general validity since the results for two oxides prepared by quite different methods (deposited for the RN-1030 and thermally grown for the FI-100 MOS-FETs) are quite similar.

The general applicability of the model is due to the fact that it does not require a detailed knowledge of the hole (or electron) trapping process. Conversely, the experimental results can tell us little about the traps themselves. However, if we are to reduce or eliminate the radiation-induced space-charge buildup in surface passivation layers such as SiO_2 it is important that we obtain a more detailed knowledge of the traps. Such knowledge will require that new techniques be employed in conjunction with those discussed here.

5. RADIATION-INDUCED TRAP LEVELS IN SiO_2 LAYERS

a. Introduction

The model for space-charge buildup presented in the previous section assumed the presence of hole traps in the SiO_2 layer. Fortunately, an understanding of this buildup process did not require a detailed knowledge of these traps. However, if this type of space-charge accumulation is to be fully understood and ultimately controlled we will need to have more information about these traps. In particular, we should like to know the depth, capture cross section, location, density and origin of such traps.

The C-V technique by itself can at most tell us the magnitude and location of a net space-charge in the oxide layer. Other techniques are required to obtain the additional information. Thermoluminescence glow curves and the closely related thermally stimulated current glow curves have been used extensively to study traps in many materials including quartz. This technique is, in principle at least, relatively straightforward and can be made to yield quantitative results for trap depth and capture cross section.

The purpose of the experiments described here was twofold. (1) To determine whether this method could, in fact, be used with thin insulation layers such as the thermally grown SiO_2 used in planar devices and (2), if the method was successful, to study the effect of Co^{60}-gamma radiation on SiO_2 layers.

b. Thermoluminescence Glow Curves

The basic physical processes involved in thermoluminescence glow curves are illustrated in Figure 16 for a simple case of a single electron-trap level situated E_t below the conduction band and a set of recombination centers containing trapped holes[11]. The probability, p, that a trapped electron will escape and enter the conduction band is given by

$$p = f \exp\left(-\frac{E_t}{kT}\right) \tag{34}$$

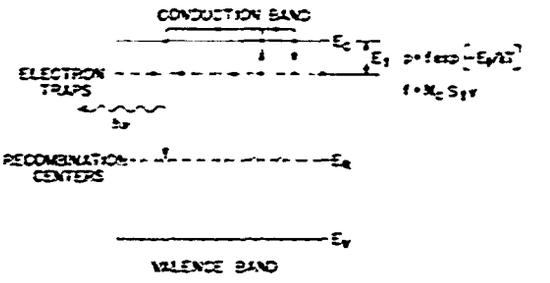

Figure 16. A simple model to illustrate the processes involved in thermoluminescence glow curves.

An electron which enters the conduction band will either be retrapped or recombine with a trapped hole. The extent of retrapping will depend on the relative cross sections of the traps and recombination centers. If a photon is emitted during the recombination process the emptying of a trap can be observed via the accompanying luminescence. Furthermore, the intensity of the luminescence can be used as a measure of the rate at which the traps are emptying.

According to Equation (34) the probability of escape can be increased by increasing the temperature. In glow-curve work, it is customary to increase the temperature linearly with time. Since p depends exponentially on T, the rate of trap emptying will increase with increasing temperature, giving a corresponding increase in luminescence. However, the population of trapped electrons will be steadily decreasing and, therefore, at some temperature the trap emptying rate (and, hence, the luminescence) will reach a maximum value; thereafter, the rate will decrease toward zero as the number of trapped electrons is exhausted. The curve of luminescence intensity, I(T), as a function of temperature is referred to as a glow curve.

If the traps empty with negligible retrapping of electrons then the recombination kinetics are monomolecular and it can be shown[12] that I(T) is given by

$$I(T) = C\, n_{t_0}\, f \exp\left[-\frac{E_t}{kT} - \int_{T_0}^{T} \frac{f}{b} \exp\left(-\frac{E_t}{kT}\right) dT\right] \qquad (35)$$

The form of this expression is illustrated in Figure 17. Note that the curve is not symmetrical about the peak temperature, T^*, but has a tail to the low temperature side.

If, for an electron in the conduction band, there is an equal probability for retrapping and recombination, probability for retrapping the kinetics become bimolecular and the expression for I(T) becomes[11]:

$$I(T) = \frac{C\, n_{t_o}^2\, f \exp\left(-E_t/kT\right)}{N_t \left[1 + \frac{n_{t_o}}{N_t} \int_{T_o}^{T} \frac{f}{b} \exp\left(-E_t/kT\right) dT \right]} \qquad (36)$$

This expression is also illustrated in Figure 17. For bimolecular kinetics, the shape of the curve depends on the initial amount of trap filling (n_{t_o}/N_t) and tends to be more symmetrical about the peak temperature. For the case in which retrapping is much more likely than recombination (the so-called fast retrapping case) an expression for I(T) can be also derived.[11] However, this situation is seldom observed in practice and will not be discussed further.

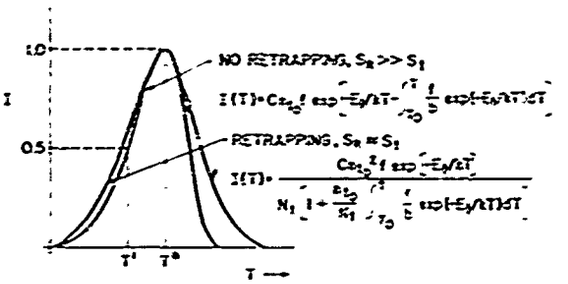

Figure 17. Shape of glow curves for cases of no retrapping (monomolecular kinetics) and retrapping (bimolecular kinetics).

If glow curves such as those shown in Figure 17 could be obtained, then in principle it should be possible to obtain the values of E_t and f (and hence S_t) for the corresponding electron traps. In practice, the glow curves obtained experimentally are not isolated peaks which can be described by Equation 35 or 36. Rather, they are composed of several overlapping peaks to which it is difficult to assign a specific type of recombination kinetics. Various methods have been proposed for extracting information from these curves: Two of the simpler methods will be discussed briefly.

For both Equations 35 and 36, it is easily seen that for small values of $(T-T_o)$ the integral in each equation may be neglected and I(T) is then proportional to $\exp(-E_t/kT)$. Hence, for the initial portion of a glow peak the slope of a plot of log I(T) against 1/T yields the value of E_t. This method of "initial rise" proposed by

Garlick and Gibson[12] has the advantages that it is simple to use and is valid regardless of the recombination kinetics involved. Furthermore, it does not involve a knowledge of f. The method has its limitations, however,[13] and is difficult to use in cases of several overlapping glow peaks.

A second method due to Grossweiner[14] is valid for the case of monomolecular kinetics. Grossweiner showed that to a good approximation E_t is given by

$$E_t = \frac{1.51\, kT^*T'}{T^*-T'}, \quad E_t > 20\, kT^* \tag{37}$$

T' = temperature at half peak $[I(T^*)/2]$ on the low temperature side of the peak, see Figure 17.

The same approximation yields

$$f = \frac{3}{2}\frac{T'b\exp\left(E_t/kT^*\right)}{T^*(T^*-T')}, \quad \frac{f}{b} > 10^7 \tag{38}$$

Note that f depends exponentially on E_t and hence a 10% error in E_t will lead to an error of an order of magnitude in f.

The above discussion has been based on the situation illustrated in Figure 16 in which it was assumed that electrons were released from traps to recombine with more deeply trapped holes. It should be pointed out that the roles of the electrons and holes could be interchanged with no changes required in the preceding discussion. Furthermore, there is no way of telling, on the basis of glow curves alone, whether holes or electrons are released during the thermoluminescence.

c. Experimental Procedure

The glow curves to be presented in the following sections were all obtained using a Harshaw model 2000A thermoluminescence dosimeter in conjunction with a Harshaw model 2000B picoammeter. This instrument will plot a glow curve directly on an X-Y recorder over the temperature range 300° to 700°K. The heating rate is linear and adjustable from 2° to 25°C/s.

The SiO_2 samples studied were all in the form of ~6000Å layers on one side of 0.24 in. square Si chips. The samples included both wet and dry thermally grown SiO_2, deposited SiO_2, and thermally grown SiO_2 which had purposely been contaminated with Na.

Co^{60}-gamma radiation [dose rate ~3.5×10^5 rads/hr(C)] was used in the experiments for two purposes. In one case, it was used as ionizing radiation to generate hole-electron pairs to fill the traps and recombination centers; it was also used to introduce damage into the SiO_2 layers and thus increase the trap density.

The first step in obtaining a glow curve is to remove any trapped charge in the sample by heating to a temperature above the range in which the glow curve is to be taken. In these experiments, this step was accomplished by heating the sample to the maximum temperature attainable with the Harshaw dosimeter (~700°K). Next a background curve was generated on the X-Y plotter over the temperature range of the glow curve (~300° to 575°K). This curve showed only a small background light output for the sample and planchet in the range 500° to 575°K. The sample was then exposed to sufficient Co^{60}-gamma radiation to fill a significant portion of the traps, generally a 10-minute exposure. This dose is not large enough to alter appreciably the density of traps in the samples. If the glow curve was to be compared with other glow curves then the same excitation dose was used throughout. Finally a curve was obtained for the irradiated sample and the background curve subtracted to yield the desired glow curve.

d. Experimental Results

1. Radiation-Induced Traps in SiO_2. Co^{60}-gamma radiation in sufficient doses can create defects in solids. It was decided, therefore, to investigate the effects of Co^{60}-created defects on the glow curves of SiO_2 layers. A previously unirradiated thermally grown dry oxide specimen was investigated first. Glow curves for this sample were obtained as described previously using an excitation dose of 5.8×10^4 rads and a heating rate of 10 °C/s. The glow curves, shown in Figure 18, were taken after accumulated doses of 0.058, 0.69, 4.7, and 8.8 Mrads. It should be kept in mind that at each of the accumulated dose levels the SiO_2 layer was annealed to remove any trapped charge. The glow curve was then taken using an excitation dose of 5.8×10^4 rads to fill the traps - the same excitation dose was used for all glow curves. At lower accumulated doses, the glow curve is a broad almost structureless peak. With increasing Co^{60}-defect concentration, the curve grows until at 8.8 Mrads five distinct peaks appear.

The growth of the glow curve shown in Figure 18 is typical of the results found for the other oxide samples. Samples that were steam grown, deposited, and steam grown with Na contamination all exhibited the same five peaks although the dose at which the peaks occurred and the relative heights of the peaks varied from sample to sample. The sample with Na contamination did not show any additional peaks in the temperature range 300° to 550°K. After a sufficient dose, typically a few Mrads, the glow curves stopped growing, perhaps indicating either a saturation of the density of filled traps or a reduction of the luminescence efficiency. However, the shape of the glow curves continued to change with the individual peaks becoming less and less distinct. More will be said about this point later.

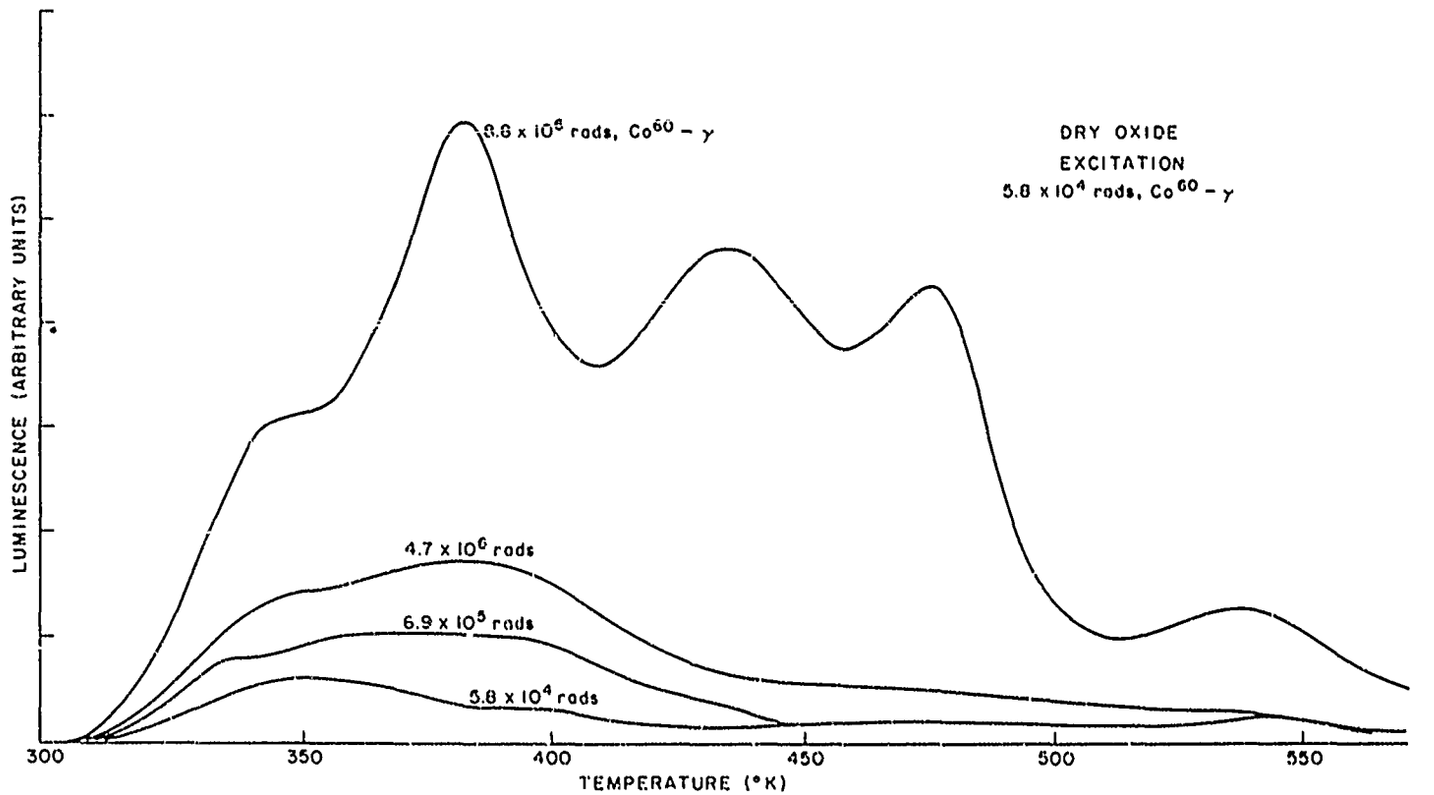

Figure 18. Glow curves for a thermally-grown dry oxide after various accumulated doses of Co^{60}-gamma radiation. Excitation dose = 5.8×10^4 rads Co^{60}-gamma.

It was pointed out previously that glow curves alone cannot determine whether trapped holes or electrons (or in this case both) are released during the heating cycle. This question remains unanswered at present. There are, however, two conclusions which can be reached at this point. First, the Co^{60}-gamma radiation does, in fact, introduce traps into the oxide, as opposed to merely increasing the luminescence efficiency, by creating additional luminescence recombination centers. If only the luminescence centers were changed by the radiation, the shape of the glow curve would not be altered, i.e., the five peaks would be present in all glow curves of Figure 18. Second, since the relative heights of the peaks vary with dose during the growth of the glow curve and from sample to sample, the five peaks do not represent five levels of the same trap structure. However, two or more peaks may belong to the same trap structure: Sufficient data is not available to permit further comment.

2. Resolution of the Glow Peaks. Before any quantitative information can be obtained about the trap levels corresponding to the peaks in the SiO_2 glow curve, it is necessary to resolve the glow curve into its components - presumably five separate peaks. This resolution was accomplished for the steam-grown oxide glow curve shown in Figure 19 using a "partial cleaning" technique.[11] The first step in the process is the isolation of the peak at the highest temperature -- peak 5. The sample is first given the usual excitation dose of Co^{60}-gamma radiation but, before the glow curve is plotted, the oxide is heated in the glow-curve apparatus to a temperature corresponding to the fourth peak and then immediately cooled to room temperature. This heating cycle empties the first four peaks and partially empties the fifth. Subsequently, the glow curve is recorded in the usual way and reveals only the fifth peak. The process is then repeated, this time emptying the first three peaks. The subsequent glow curve then contains two peaks (4 and 5) which may be resolved since the shape of the peak 5 is known. Repeated application of the process yields the other peaks. The method of partial cleaning is tedious and at best only moderately accurate in cases where there are several overlapping peaks such as the case presented here. Nonetheless, the glow curve did resolve rather straightforwardly into the five peaks shown in Figure 19.

The trap depth was estimated for each of the peaks using Grossweiner's formula, Equation (37). The condition $E_t > 20\ kT^*$ is satisfied in each case. The trap depths were also estimated for a different steam-grown oxide by resolving the component peaks and using the method of initial rise discussed earlier. The results for the two methods are listed in Table 2. Except for peak 1 the trap depths as determined by the two methods agree reasonably well. For peak 1 the accuracy of the initial rise method was poor and only the value estimated using Equation (37) is shown.

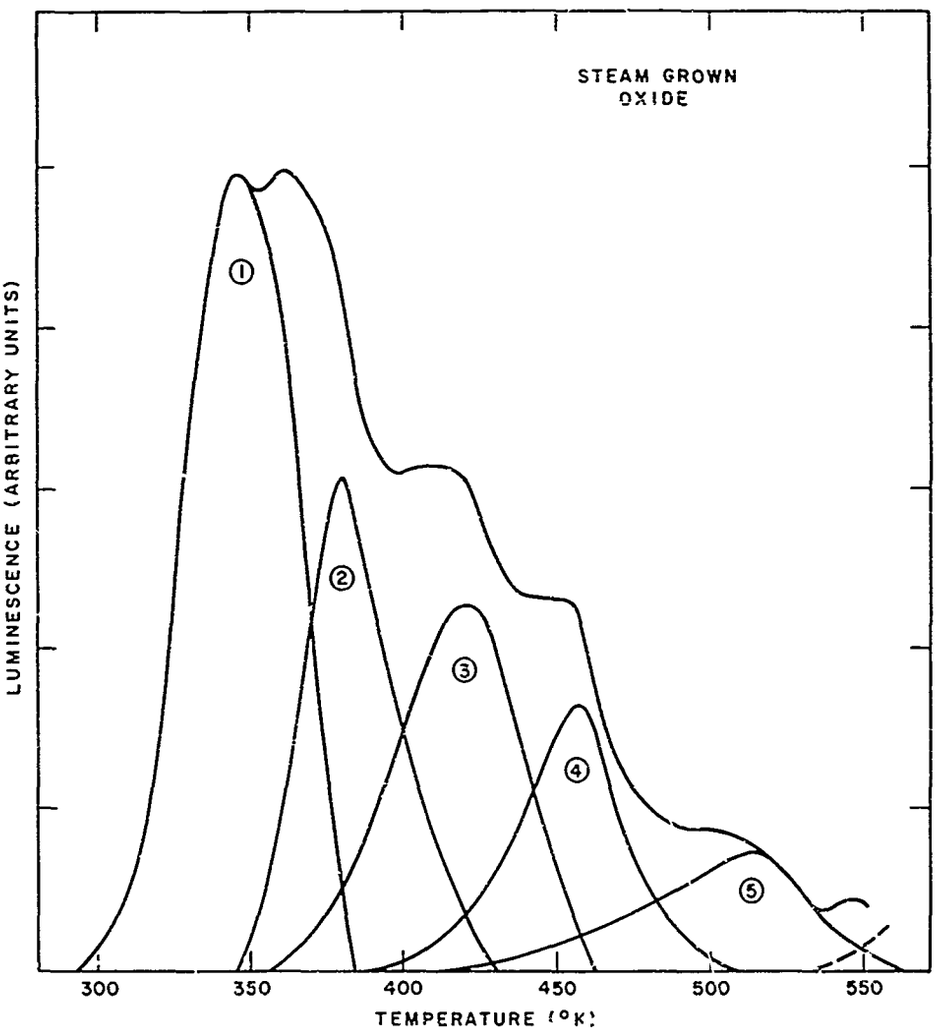

Figure 19. Resolution of glow curve for a steam-grown oxide into five component peaks.

TABLE 2

Trap Depths and Capture Cross Sections

Peak	E_t(eV) Grossweiner	E_t(eV) Initial Rise	f s^{-1}	S_t cm^2
1	0.8		$1x10^{11}$	$3x10^{-16}$
2	1.1	1.2	$3x10^{14}$	$7x10^{-13}$
3	0.8	0.9	$2x10^{9}$	$3x10^{-18}$
4	1.4	1.4	$9x10^{14}$	$1x10^{-12}$
5	0.9	1.0	$3x10^{8}$	$3x10^{-19}$

The attempt-to-escape-frequency values shown in Table 2 were estimated using Grossweiner's formula, Equation (38). The condition $f/_b > 10^7$ was fulfilled in each case. The accuracy of the values for E_t is ~10% and so the values of f are correct to the order of magnitude. The values of f for peaks 2 and 4 are unreasonably large. The upper limit on f is the frequency of vibration of the atoms of the SiO_2 lattice, $\sim 10^{14} s^{-1}$. Values of f are usually observed to be considerably smaller than this upper limit. It is possible that for these two peaks the recombination kinetics are not monomolecular in which case Equation (38) would not be applicable. Comparison of Figures 17 and 19 reveals that peaks 1. 3, and 5 (in Figure 19) have the low-temperature tail expected for monomolecular kinetics while peaks 2 and 4 more closely resemble the curve for bi-molecular kinetics. The method of initial rise does, however, confirm the larger values of E_t found for peaks 2 and 4.

Capture cross sections for the trap levels were estimated from the values of f in Table 2 using the relations

$$f = N_c S_t v$$

$$N_c = 2\left(2\pi m^* kT/h^2\right)^{3/2}$$

$$v = \sqrt{\frac{3kT}{m^*}}$$

For the values of S_t in Table 2, m^* was taken as the rest mass of the electron and $T = T^*$.

The values of S_t for peaks 2 and 4 are very large because of the correspondingly large values of f. If peaks 2 and 4 do have much larger capture cross sections than the other trap levels this fact should be apparent in the filling of trap levels during exposure to ionizing radiation. More will be said about this point later.

3. Filling of Trap Levels. Figure 20 shows the glow curves obtained for a thermally-grown dry-oxide sample for seven different values of excitation exposure

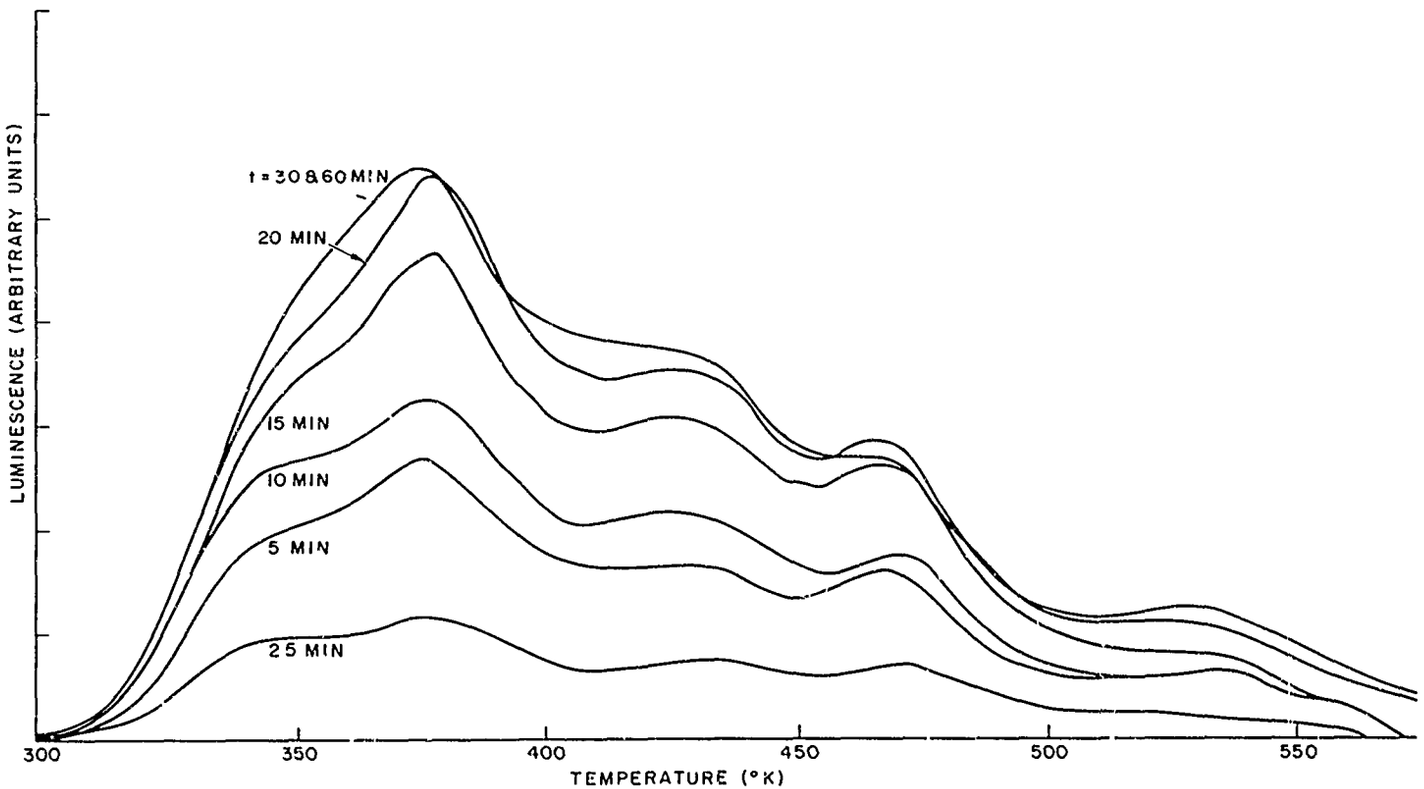

Figure 20. Glow curve of a thermally grown dry oxide for various excitation exposure times.

time. This sample had previously been exposed to sufficient Co^{60}-gamma radiation to saturate the trap density so that differences among the glow curves should reflect only differences in the fraction of traps filled by the radiation. Figure 21 shows the integrated light output from each curve as a function of the exposure time. The traps apparently saturate after a 20- to 30-minute exposure.

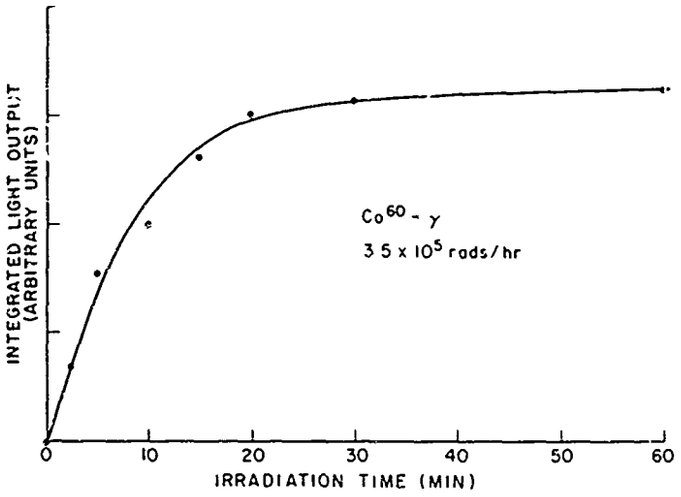

Figure 21. Integrated light output for the curves of Figure 5 as a function of exposure time.

If any of the five trap levels had a much larger capture cross section than the other levels, the peak corresponding to this level should increase more quickly with dose and saturate at a lower dose level. Within experimental accuracy, however, the five individual peaks all saturated at the same rate, i.e., the same rate as the integrated light output shown in Figure 21. This observation is inconsistent with the capture cross-section values shown in Table 2. Even if the values for peaks 2 and 4 are disregarded peak 1 has a capture cross section three orders of magnitude larger than peak 5. Such a large difference should be observable in Figure 20.

There is no obvious explanation at present which can reconcile the discrepancy between the greatly different capture cross sections and the observed filling of the trap levels. Further experiments may, however, uncover the cause.

4. Effects of High-Temperature Prebaking. It was mentioned earlier that the glow curves (i.e., the area under the curves) saturate with increasing Co^{60}-gamma radiation dose. It was also observed that with increasing radiation the five peaks tend to become less and less distinct; the glow curve becomes a

single broad peak with a maximum near 350°K (compare the glow curves of Figures 18 and 20). The effect of high-temperature baking of the SiO_2 layers prior to taking a glow curve was investigated for samples which had shown glow-curve saturation. Figure 22 shows glow curves for a steam-grown oxide prebaked in air at the various temperatures indicated (all glow curves in this figure were obtained with an excitation dose of 5.8×10^4 rads). The glow curve obtained after a large radiation dose is labelled 400°C since at this stage the maximum temperature to which the oxide has been heated is ~400°C. A three-hour prebake at 670°C resulted in a substantial increase in the glow curve at all temperatures. Subsequent prebakes at 818°C and 953°C also enhanced the luminescence. However, three hours at 1070°C was found to reduce the glow-curve peak and increase the high-temperature tail somewhat.

A similar behavior, namely enhancement of luminescence for anneals at temperatures up to 900°C and a decrease for higher temperatures, has been reported for crystalline quartz[15]. The effect was ascribed to an increase in luminescence efficiency in the quartz resulting from an increase in crystallinity. The effect observed here may be due also to an increase in luminescence efficiency. This possibility is indicated by the fact that a previously unirradiated oxide showed a substantial increase in luminescence output when prebaked at high temperatures even though it had not received sufficient radiation to increase the trap density significantly.

The effect of the high-temperature prebaking on the trap levels themselves was investigated next using the technique of partial cleaning discussed earlier. Figure 23 shows the results for a steam-grown oxide (an excitation dose of 5.8×10^4 rads was used for the curves of this figure). The complete glow curve has a single peak with a maximum at 353°K. The sample was precleaned to this peak temperature before the second glow curve, labelled 353°K, was taken. As shown, the peak of the second glow curve is shifted to ~380°K with no indication of a peak at 353°K. This result indicates that the original glow peak is due to a continuum of trap levels rather than to discrete levels. Precleaning in a similar way to the temperatures indicated in the curves of Figure 23 indicates that the continuum of states exists which empty throughout the temperature range 300° to 550°K.

Since the entire glow curve arises from a continuum of trap levels, the shape of the original glow curve must reflect the variation of trap density with trap depth. It may be concluded then that the density of traps decreases with increasing depth. Nothing can be said regarding the density of traps below depths corresponding to ~353°K, since these traps will normally be empty at room temperature and therefore contribute nothing to the glow curve.

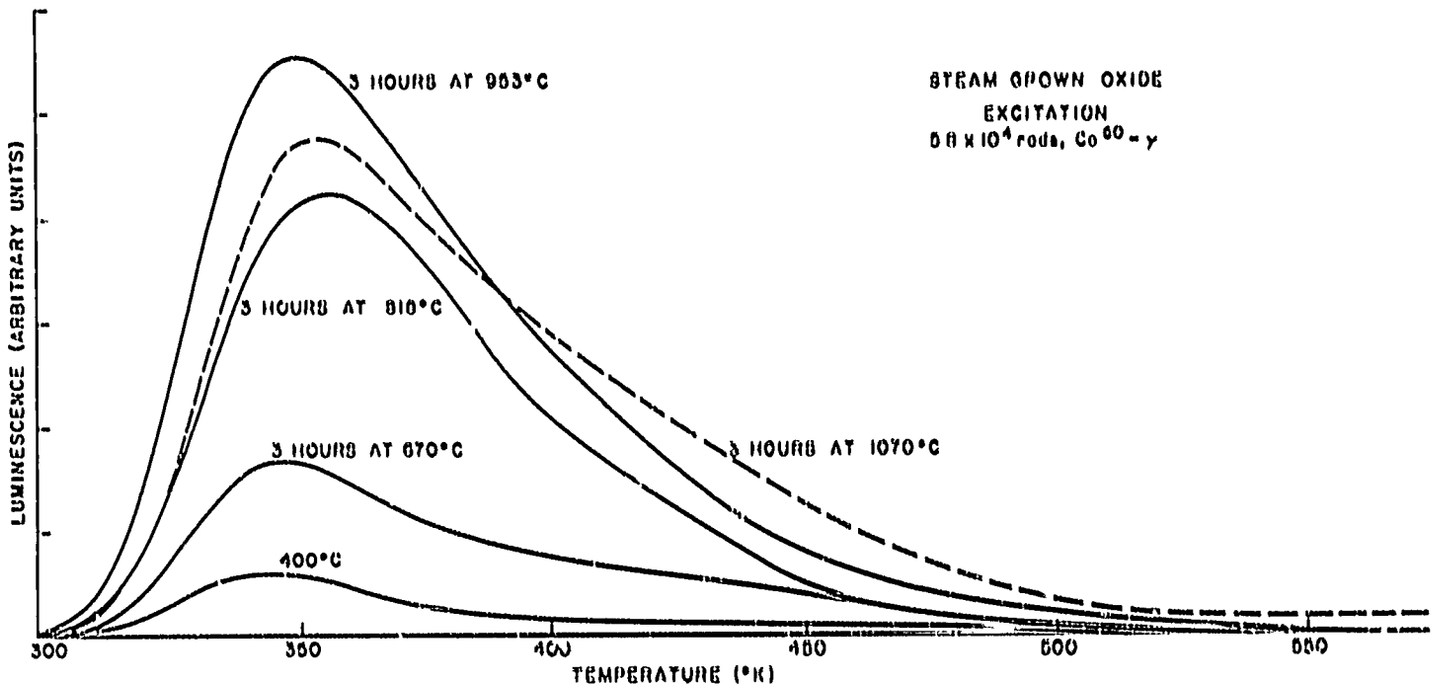

Figure 22. Glow curves for a steam grown oxide after various high temperature prebakes in air. Excitation dose 5.8×10^4 rads.

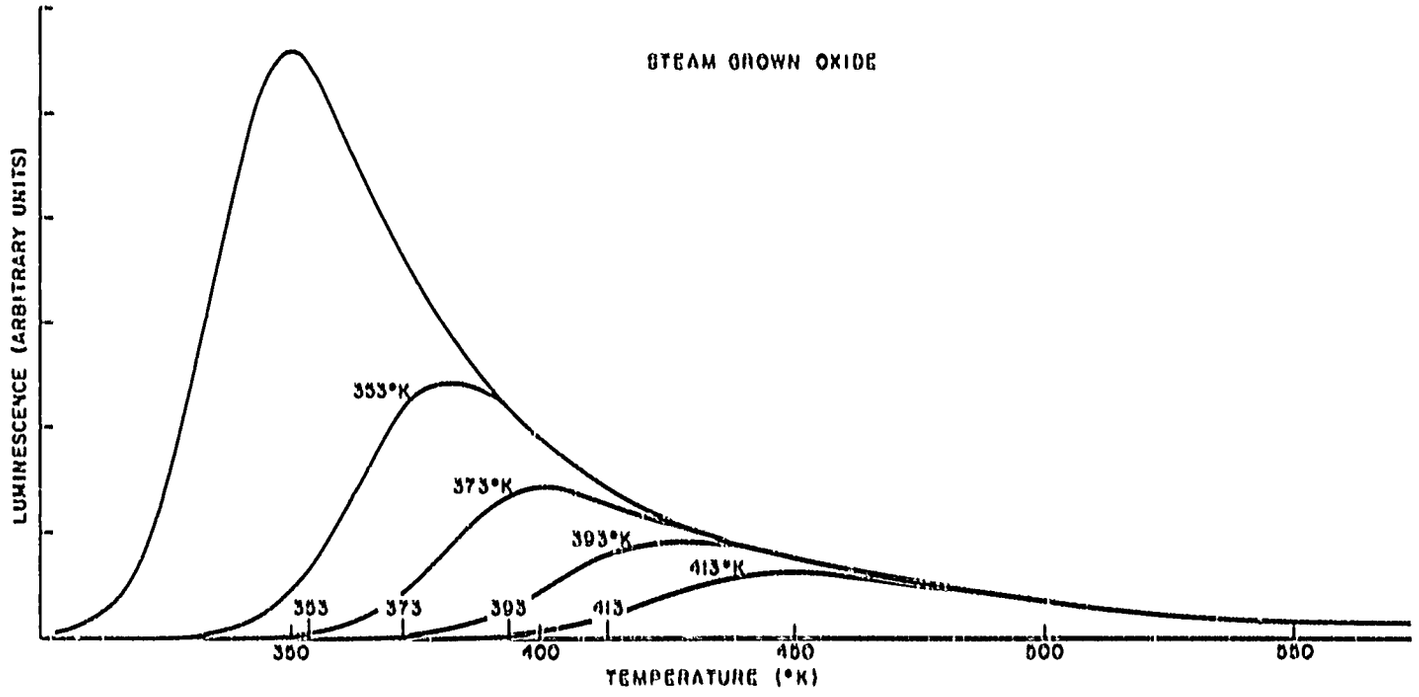

Figure 23. Effect of partial cleaning on glow curves of a steam grown oxide which has been annealed at high temperatures.

e. Discussion

The technique of thermoluminescence glow curves appears to be sufficiently sensitive to study trap levels in thin SiO_2 layers. (It may, therefore, be useful in the study of thin films of other materials.) The results have shown that "fresh"* SiO_2 layers do not have a great many traps corresponding to the temperature range 300° to 550°K, (i.e., prior to irradiation, the apparatus used did not detect any thermoluminescence). However, radiation capable of introducing defects, (such as Co^{60}-gamma radiation), can introduce a substantial number of trap levels. In particular, Co^{60}-gamma radiation introduces five discrete levels with depths ~1 eV. With increasing radiation dose, the density of filled traps saturates and the discrete levels change to a continuum of levels with a high-temperature bake. Baking at temperatures up to ~980°C does not anneal out the radiation-induced traps.

There has been no report in the literature of thermoluminescence work on SiO_2 layers although there have been numerous papers dealing with thermoluminescence and optical absorption in various kinds of quartz.[15-22] The results are confusing and often contradictory, due in part, no doubt, to the large number of sources of natural quartz and the variety of methods of preparing synthetic quartz. Much of the work on the trap levels of quartz employed optical absorption measurements (a review of this work is given in Ref. 19). Others used thermoluminescence glow curves[15, 16, 17, 19, 20, 21] and found glow peaks in the temperature range used in these experiments. None of these peaks was found to be associated with any impurity present in the quartz[15]; unspecified defects were usually postulated as the cause of the associated trap levels. No author reported observing five peaks as observed for the SiO_2 layers; however, some investigations have reported peaks near 350°K due to a band of trap levels.[15,16]

Several important questions remain to be answered regarding the SiO_2 layers. The glow curves should be investigated for oxide layers of various thicknesses to determine what role, if any, is played by the SiO_2 - Si interface. If the trap levels exist in the bulk of the oxide then the magnitude of the glow curves should increase directly with the volume of the oxide layer. The glow curves should be investigated for lower temperatures, i.e. 77°K to 300°K. Some quartz shows trap levels with peaks ~150°K.[23] These trap levels have been attributed to the glassy state of quartz[24] since they do not appear in crystalline quartz. Low-temperature glow curves may, therefore, give some indication of the order present in SiO_2 layers. The spectrum of the thermoluminescence should also be determined. For quartz, the spectrum has a peak at ~3.3 eV with a tail to lower energies and a cutoff at ~3.7 eV.[15,12]

*"Fresh" in this context implies that the SiO_2 layers have not been subjected to the processing steps used in fabricating commercial devices.

The most important question here is the extent to which the results obtained for fresh oxide layers can be applied to the oxide layers found in planar devices. The fact that prebaking can alter a glow curve very drastically would imply that processing steps in device manufacture would alter the trap structure of oxide layers significantly. It would be a relatively simple matter to expose fresh oxides to these steps and take the glow curve after each step. Such a program may prove very instructive.

6. THERMALLY STIMULATED CURRENTS IN MOS STRUCTURES

a. Introduction

It was shown in Part 5 of this section that thermoluminescence glow curves can be useful in the study of trap levels in SiO_2 layers. The SiO_2 layers of prime interest are those found in planar Si devices. Unfortunately, the thermoluminescence glow-curve technique cannot be used on these layers. It is necessary, therefore, to show that device oxides exhibit a similar behavior under irradiation before results obtained on the simple oxidized chips can be applied to device oxides.

Fortunately, there is a technique very closely related to the thermoluminescence glow-curve technique which can be used for oxides in MOS structures and which can be made to yield similar information about the traps. In place of observing the light emitted when a carrier released from a trap recombines, the increased electrical conductivity of the material is observed when the carrier enters the conduction band while passing from the trap to the recombination center. The conductivity (in the form of a current at fixed applied potential) as a function of temperature is referred to as the current glow curve.

b. Procedure

The apparatus used for obtaining current glow curves from commercial MOS-FETs is shown schematically in Figure 24. The device under test is connected in series with a potential source V and a Keithley 610A electrometer (ammeter). The output of the ammeter is connected to the Y input of an X-Y recorder. The TO-18 can of the MOS-FET slip-fits snugly into a copper heating block which contains a 100W Vulcan cartridge heater. The temperature of the device is measured with an iron-constantan thermocouple. This thermocouple is mounted in a TO-18 can which slip-fits into the copper heater block as does the device under test. The thermocouple and device are symmetrically placed with respect to the heater and should be at the same temperature. The output of the thermocouple is connected to the X input of the X-Y recorder. The apparatus was used in the temperature range 25° to 200°C. In this range the heating rate was constant at 3.6°C/s.

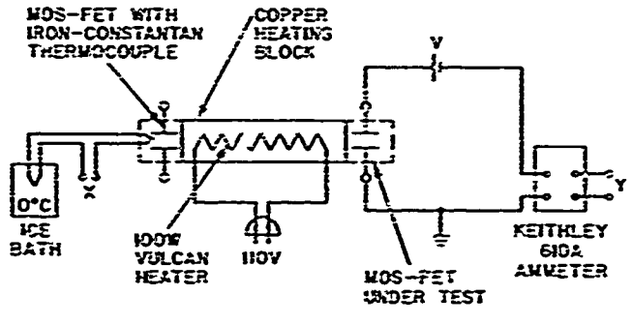

Figure 24. Apparatus used to obtain current glow curves from MOS-FETs.

The first step in obtaining a glow curve is to determine the background current over the temperature range required with the applied bias to be used. A background curve for an RN-1030 with a bias of +1V (i.e., gate positive with respect to the substrate) is shown in Figure 25. The next step is to irradiate the device to the desired dose at the gate bias value selected and then obtain a second curve, the uncorrected glow curve. The uncorrected curve for an RN-1030 exposed to 3.5×10^5 rads at $V_G = 0V$ is shown in Figure 25. Finally the glow curve is obtained by plotting the difference between the two previous curves. The glow curve is also illustrated in Figure 25.

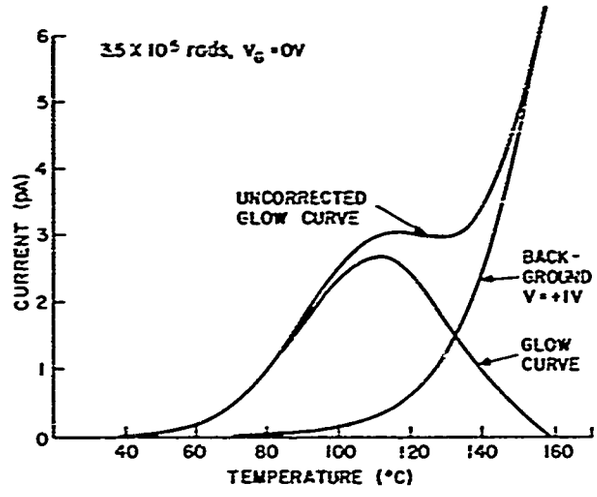

Figure 25. Background, uncorrected glow curve, and glow curve for an RN-1030 MOS-FET.

c. Experimental Results

1. Dependence of Glow Curves on Applied Bias. The background and uncorrected curves for glow-curve bias values of 0 and ±1V are shown in Figure 26 for an RN-1030 MOS-FET exposed to 3.5×10^5 rads in $V_G = 0V$. The device was annealed at 300°C for at least one hour between glow curves to remove any space-charge buildup remaining from previous exposures. The background currents for ±1V have opposite signs, as expected, while for 0V the background current is positive and tends to saturate above ~180°C. The corrected glow curves are shown in Figure 27.

Two interesting facts are revealed in Figure 27. First, regardless of the sign of the bias applied, the glow-curve current is always positive, i.e., conventional current flows out of the gate of the MOS-FET. Second, within experimental accuracy, the integrated current flow (represented by the area under the glow curve) is independent of the bias value used. In connection with this second point, it should be mentioned that it was difficult to compare accurately the integrated current for the three cases. As may be seen in Figure 26 for 0 and -1V the two curves do not meet at high temperatures as they do for +1V. In some cases, however, the curves did meet for these bias values, even crossing occasionally. The inconsistency of the background curves makes quantitative measurements difficult.

It is thus apparent that the current flow in the glow curve is not controlled by the applied bias. Attempts to increase the glow-curve current with larger bias values were unsuccessful. For significantly larger bias values, the background current greatly increased making it very difficult to observe the glow-curve current which was not increased.

2. Effect of Bias During Irradiation. Figure 28 shows three glow curves taken for an RN-1030 MOS-FET for three different values of bias during irradiation, namely $V_G = 0$ and ±2.5V. For each curve the device was irradiated to a dose of 3.5×10^5 rads and the glow-curve bias used was 0V. The C-V shifts for the device were -0.6V, -6.6V, and -1.6V for bias values of 0V, +2.5V, and -2.5V respectively.

The glow curves are quite similar for the three bias values with the 0V curve being perhaps slightly larger in area. The current flow is in the same direction for all three glow curves despite the fact that the field in the oxide due to Q_R is in opposite directions for ±2.5V bias. The glow curves, therefore, do not appear to be controlled by the positive space-charge in the oxide. Again the current flow is positive for all three curves. The positive space-charge in the oxide is much greater for $V_G = +2.5V$ than for $V_G = 0V$. However, there is no correspondingly large difference between the areas of the two glow curves. It may be concluded, then, that the glow curve is not directly related to the radiation-induced space-charge.

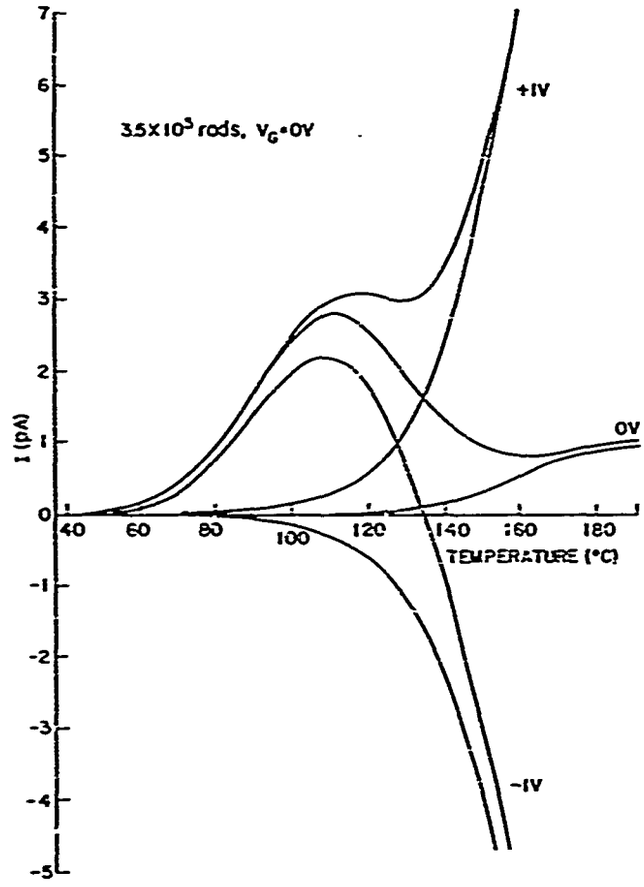

Figure 26. Background and uncorrected glow curves for an RN-1030 MOS-FET using bias values of 0 and ±1V.

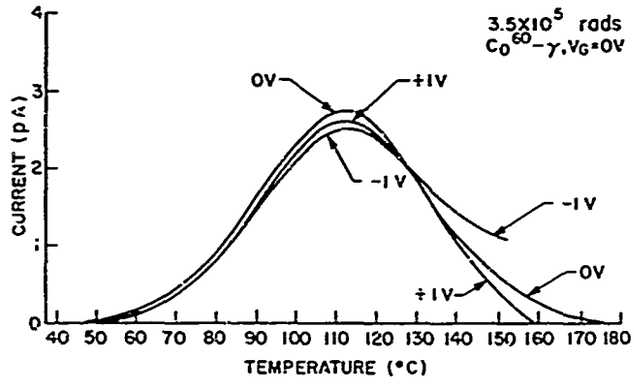

Figure 27. Corrected glow curves for results shown in Figure 26.

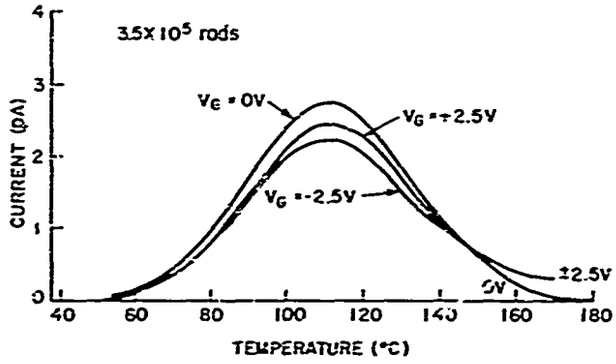

Figure 28. Corrected glow curves for an RN-1030 exposed to 3.5×10^5 rads at bias values of $V_G = 0$ and ±2.5V and glow curve bias of 0V.

It is instructive to compare the charge represented by the area under a given current glow curve with the radiation-induced space-charge in the oxide as measured by the C-V curve shift. For the $V_G = 0V$ curve in Figure 28, the area under the curve corresponds to 4.2×10^{-11} coulombs. The voltage shift, ΔV, of the corresponding C-V curve was -0.6V. When we use $C = C_{ox}\Delta V$, the density of positive space-charge is found to be $\sim 1 \times 10^{-8}$ coulombs/cm^2 for an oxide layer 1600Å thick. The gate area of the RN-1030 MOS-FET is $\sim 8 \times 10^{-5}$ cm^2 and, hence, the radiation-induced space charge is 8×10^{-13} coulombs — a very much smaller charge than that represented by the area under the glow curve. It is quite possible, however, that the glow current originates in the oxide under the entire metallized area of the SiO_2 surface, i.e., including the drain, source, and gate contact areas as well as the active gate area. For this situation, a comparison requires an estimate of the fraction of the glow current collected by the gate itself. It is estimated from the geometry of the RN-1030 that $\sim 8 \times 10^{-12}$ coulombs of the total 4.2×10^{-11} coulombs were collected by the gate. Account has been taken of the fact that the oxide under the contact areas is much thicker (~5000Å) than under the gate area (~1600Å).

The charge represented by the glow curve is for both estimates much greater than the positive space-charge. Since the glow-curve charge is much larger than that which causes a shift of the C-V curve, it must exist in the oxide as a compensated charge.

3. Energy Distribution of Trap Levels. The technique of partial cleaning used in the previous experiments with the SiO_2 layers was applied to the current glow curves for MOS-FETs to determine the type of energy distribution for the

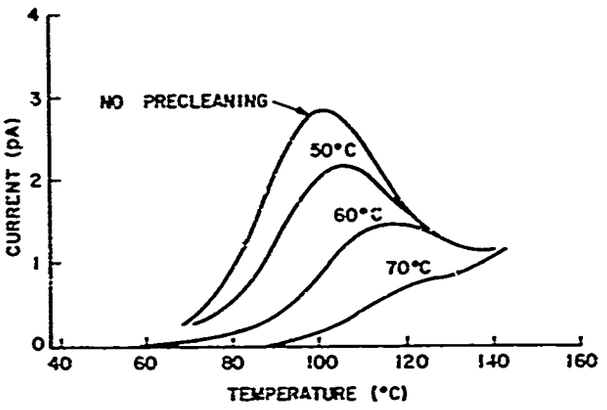

Figure 29. Uncorrected glow curves for an RN-1030 MOS-FET showing the effect of precleaning at 50°, 60°, and 70°C.

traps involved. The results are shown in Figure 29. Four glow curves were obtained from a single RN-1030 MOS-FET using a radiation dose of 3.4×10^5 rads with $V_G = 0V$ and a potential of 0V in the glow-curve circuit. As indicated, one curve was obtained with no precleaning. The other three curves were precleaned for 5 minutes at the temperatures indicated in the figure.

The curves shown in Figure 29 are actually uncorrected glow curves. The background curves for this device behaved very erratically making it impossible to obtain meaningful corrected curves. The vertical scale for each curve was arbitrarily adjusted to give consistent behavior at the high-temperature end of the curves. The point to notice, however, is the shift of the glow-curve peak to higher temperatures with increased precleaning. This shift will not be affected by adjustments in the vertical position of the curves. It may be concluded, therefore, that the current glow curve arises from a continuum of trapping levels rather than a discrete level or levels.

It is interesting to compare a current glow curve for a MOS-FET with a thermoluminescence glow curve for a prebaked SiO_2 layer. The prebaked SiO_2 layers also exhibit a continuum of trap levels. Figure 30 shows the glow curve for the oxide layer of Figure 23 and the current glow curve shown in Figure 28 for the irradiation bias $V_G = 0V$. The curves have been normalized to the same peak height. Before any comparisons are made, it should be recalled that the heating rate for the SiO_2 layer was 10°C/s compared to 3.6°C/s for the MOS-FET. If the heating rate for the MOS-FET were 10°C/s, the current glow curve would be displaced to slightly higher temperatures (~15°C higher for the trap parameters reported earlier).

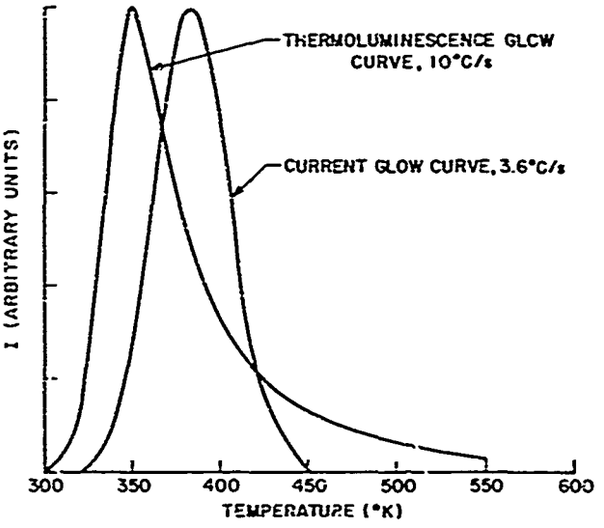

Figure 30. Thermoluminescence glow curve for an annealed SiO_2 layer and a current glow curve for an RN-1030 MOS-FET.

Both the temperatures of the glow-curve peaks and the shapes of the glow curves are different indicating differences in trap depths and distribution of trap density with depth. The shapes and peak temperatures of glow curves depend on the recombination kinetics involved and on the capture cross sections of the traps (see Equations 35 and 36). A meaningful comparision between glow curves is thus impossible unless the kinetics and capture cross sections are known. If for the curves of Figure 30 the recombination kinetics and capture cross sections are, in fact, the same, then it may be concluded that for the MOS-FET the trap levels tend to be somewhat deeper with a narrower spread of trap depths than the traps in the SiO_2 layer.

The traps in the MOS-FET oxide layer are not radiation induced but are present inherently in all devices presumably as a result of the treatment received by the oxide during the manufacture of the MOS-FET. It would be surprising, therefore, if the two glow curves revealed exactly the same trap levels. Nevertheless, there is a continuum of trap levels in both cases with depths in the region of 1 eV.

4. Buildup of Current Glow Curves with Radiation Dose. The growth of a glow curve as a function of radiation dose was investigated using an RN-1030 MOS-FET. The device was irradiated to various dose levels with $V_G = 0V$, and the glow curves taken with no applied bias. The device was annealed at 300 °C for one hour before each irradiation. The glow curves are shown in Figure 31.

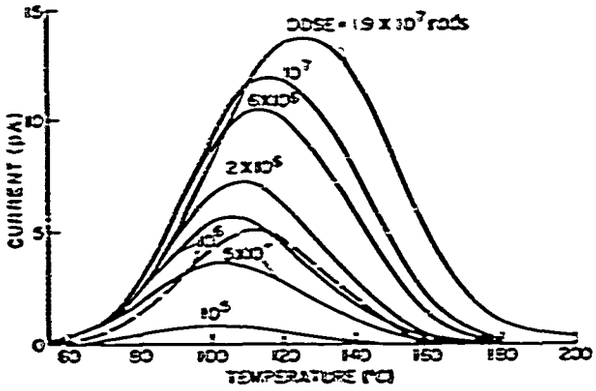

Figure 31. Corrected current glow curves for various dose levels for an RN-1030 MOS-FET.

The family of glow curves clearly shows a shift of the glow-curve peaks to higher temperatures with increasing radiation dose. This shift indicates that deeper and deeper traps are filled as the amount of trapped charge increases. Such behavior may be explained in terms of retrapping. During irradiation, any occupied trap level may be emptied either thermally or by the ionizing radiation. The shallowest traps will be emptied most frequently, the deepest least frequently. As a result there will be a tendency for the carriers in the shallowest traps to be released and then retrapped in deeper levels. The counterflow of carriers from deep to shallow traps will be much smaller and the net result will be a higher proportion of filling of the deeper traps with increasing radiation dose. The effect will be observed as a shift of glow-curve peak to higher temperatures.

The glow curves were taken in the order of increasing dose. Thus, after the curve for 1.9×10^7 rads, the device had received an accumulated dose of almost 3.9×10^7 rads. The curve for 10^6 rads was repeated (dashed glow curve) to determine whether this large accumulated dose had altered the trap levels in any way. The second curve for 10^6 rads is slightly smaller in area than the first and the peak is shifted to a slightly higher temperature (8 °C higher). The difference in area is probably not significant but the shift of glow peak indicates some increase in the density of deeper states. However, considering the rather large dose of Co^{60}-gamma radiation absorbed, it is surprising that the trap levels showed such a small change. This result may imply that the density of trap levels is already so large that it cannot be increased. This was certainly not true for the fresh SiO_2 layers.

Figure 32 shows the area under the glow curves of Figure 31 plotted as a function of radiation dose. The area under the glow curves increases rapidly at first then more slowly as the dose level passes 5 Mrads. At 19 Mrads it is still increasing,

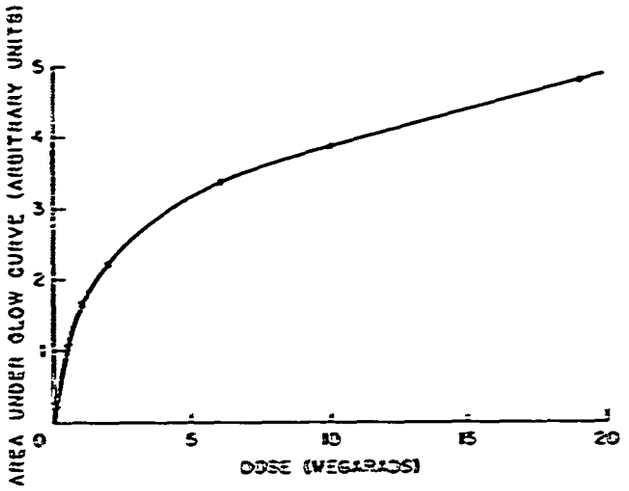

Figure 32. Buildup of current glow curves as a function of irradiation dose for the curves of Figure 8.

however, with no indication of saturation. The space-charge buildup, on the other hand, saturates in the range of 10 to 20 Mrads (see, for example, Figure 20).

5. Glow Curves for Other MOS-FETs. In addition to the Raytheon RN-10 two other commercial MOS-FETs were investigated briefly. These devices wer the Fairchild FI-100, a p-channel device described in Part 4d. of this section, and the Motorola 2N3797. The 2N3797 is a star geometry, n-channel device employing a phosphorous treated SiO_2 layer (1200Å thick) and a 12,000Å Al gate.

Both devices yielded current glow curves similar to those obtained for the RN-1030. The background current for the FI-100 with no applied bias was found to be negative while that for the 2N3797 was positive as reported previously for the RN-1030. Current glow curves for the three devices are shown in Figure 33 for a radiation dose of 3.4×10^5 rads at $V_G = 0V$. The glow-curve bias was 0V for all curves. The glow curves are all positive and approximately of the same shape and area. The temperatures of the peaks, however, are different indicating that each oxide has a slightly different distribution of trap levels. Such a behavior is not surprising since the oxides for the devices were prepared in quite different ways. Although the FI-100 and 2N3797 were not investigated as thoroughly as the RN-1030, the results indicate that they exhibit the same behavior as the RN-1030. The process responsible for the glow-curve current is thus independent of the method of preparation of the SiO_2, the device geometry, the metal used for the gate electrode (i.e., Cr or Al), and the conductivity type of the MOS-FET substrate.

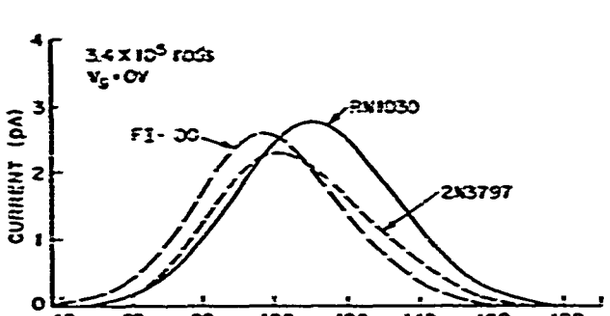

Figure 33. Corrected current glow curves for an RN-1030, FI-100, and 2N3797 MOS-FET.

6. Annealing of Positive Space-Charge During Current Glow Curves. In a previous report,[25] isochronal annealing studies on radiation-induced positive space-charge in MOS structures were reported. The effect of bias both during irradiation and during annealing was investigated. Briefly, it was found that a substantial fraction of the space-charge could be annealed rather easily by raising the temperature to ~200°C. Complete removal of the space-charge, however, required annealing at temperatures ≥300°C for periods of one hour or longer. The annealing process could not be described in terms of a single activation energy. Furthermore, annealing with negative gate potential produced less recovery than anneals with zero or positive bias.

When the current glow curves discussed in the previous sections were obtained, the devices showed a partial annealing of the positive space-charge in the oxide layer as measured by voltage shifts of the C-V curves. Recoveries ranged from ~80 percent for devices with small space-charge buildup to ~30 percent for devices with larger space-charge accumulations. The amount of recovery did not appear to depend significantly on the bias used while taking the glow curve.

The correlation between the current glow curves and the annealing of the positive space-charge, Q_R, was studied in more detail using a technique which obtained a glow curve for the space-charge annealing process. The method is based on the fact that changes in the turn-on voltage of a MOS-FET, V_T (qualitatively defined as the minimum voltage at which a channel is destroyed for a p-channel or created for an n-channel device), follow the space-charge accumulation in the oxide in much the same manner as the voltage shift of the MOS C-V curves. Hence monitoring V_T provides another method of observing Q_R — a method which is useful for our purposes since changes in V_T may be used directly in a circuit which contains the device itself as an active element. The circuit used in these experiments,

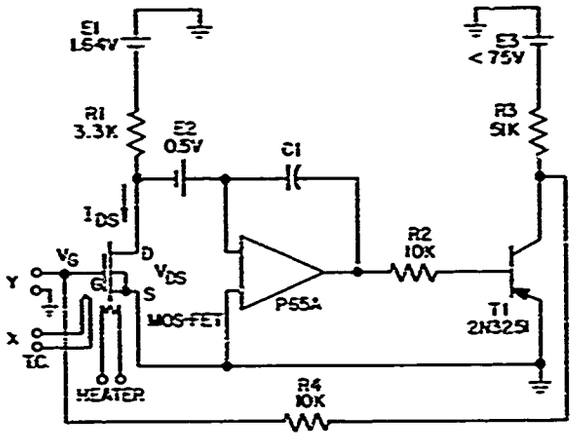

Figure 34. Circuit used to obtain a glow curve for annealing of Q_R.

shown in Figure 34, consists of three major elements, the MOS-FET under test, a P65A Philbrick operational amplifier (connected in the inverted mode), and a 2N3251 PNP transistor (T1). The operational amplifier and the transistor form a feedback loop which controls the gate voltage (V_G) of the MOS-FET. V_G can be controlled over the range $0 \leq V_G \leq E_3$.

For the experiments discussed here, we want $V_G = V_T$. It is necessary, therefore, to have a quantitative definition of V_T. In such circumstances V_T is customarily defined as that value of V_G at which the drain-to-source current, I_{DS}, achieves a predetermined value (usually very small) for a stated value of the drain-to-source voltage V_{DS}. In the circuit of Figure 34, $V_{DS} = E_2$ since at equilibrium the potential drop across the operational amplifier input is essentially zero. I_{DS} is selected through the choice of E_1 and R_1. The feedback loop will maintain V_G at the turn-on voltage defined by I_{DS} and V_{DS}.

As an irradiated MOS-FET is heated, the space-charge will anneal and V_T will change. V_T and the temperature (i.e., thermocouple output) of the MOS-FET are recorded as a V_T-versus-T plot using an X-Y recorder as indicated in Figure 35.

The heater element used was a standard 60-watt GE soldering iron with the tip replaced by a copper fitting into which the MOS-FET can (TO-18) was slip-fitted. The temperature was measured with an iron-constantan thermocouple mounted in the copper fitting as close to the device as practicable. In the temperature range 50° to 225°C, the heating rate was found to be 2.2 ± 0.2°C/s.

The Raytheon RN-1030 MOS-FET was chosen for use in these experiments. The turn-on voltage of a typical unirradiated device is ~-1.5V at $V_{DS} = -5.0$V and

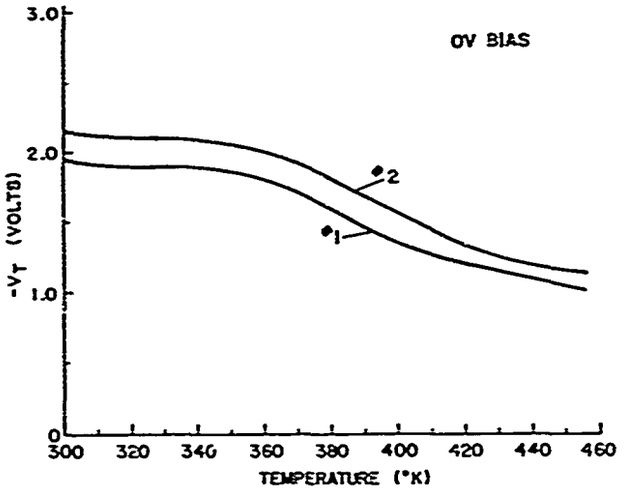

Figure 35. Turn-on voltage as a function of temperature for 0V irradiation bias.

I_{DS} = 10 μa. For these experiments V_T was defined as the value of V_G for which I_{DS} = 0.35 ma at V_{DS} = 0.5V. This value of I_{DS} is considerably larger than normally used in defining V_T but the choice was dictated by the requirement that I_{DS} be large compared to the drain-to-source leakage currents at the highest annealing temperatures used (~500°K).

Prior to irradiation, a V_T-versus-T curve was obtained for each device used so that the temperature dependence of V_T could be removed from the V_T-versus-T curves of the irradiated device. The MOS-FET was then irradiated under the desired gate bias condition using Co^{60}-gamma radiation at a dose rate of ~4 x 10^5 rads/hr. Next, the device was annealed using the circuit of Figure 34 and the V_T-versus-T curve obtained. The V_T-versus-T curve for the unirradiated condition was then subtracted from this curve to obtain the dependence of V_T on T due to the annealing of the space-charge. The slope of the resultant curve, dV_T/dT, was obtained as a function of T by manually differentiating the V_T-versus-T curve. A plot of dV_T/dT versus T yields the desired "glow" curve for the annealing process.

Two RN-1030 MOS-FETs were irradiated under a total of three different bias conditions. The irradiation information is summarized in Table 3. The curves of V_T as a function of temperature are shown for both devices in Figure 35 for a bias during irradiation of 0V. The curves are slightly displaced from each other but within experimental accuracy have the same shape. The derivative (dV_T/dT) of these curves as a function of T is plotted in Figure 36, a single curve (solid line) is drawn through the two sets of points. There is clearly a pronounced peak at ~380°K.

TABLE 3

Positive Space-Charge Annealing Glow-Curve Data

Device	Dose Co^{60}-γ (rads)	Bias (V)	T* (°K)
1	2.0×10^5	0	380
1	2.0×10^5	-2.5	370
1	2.0×10^5	+2.5	355
2	2.0×10^5	0	380
2	2.0×10^5	+2.5	355

Glow curves were obtained for bias values of $\pm$2.5V in the same way and are shown in Figure 37. The voltage shifts for these irradiation bias values are much larger than for the 0V bias case. A single curve is drawn through the two sets of points for the positive bias condition. Again the glow curves show a large single peak but at somewhat lower temperatures than was observed for the 0V-bias case. The temperatures of the peaks, T*, are listed in Table 3.

The method used to obtain the glow curves for the space-charge anneal has the drawback that the bias applied to the SiO_2 layer during the anneal is constantly changing to keep $V_G = V_T$. The glow curves will, therefore, likely be somewhat distorted, particularly for the larger radiation-induced shifts of V_T such as occurred for $V_G = +2.5V$. The glow curves least affected and hence most suitable for

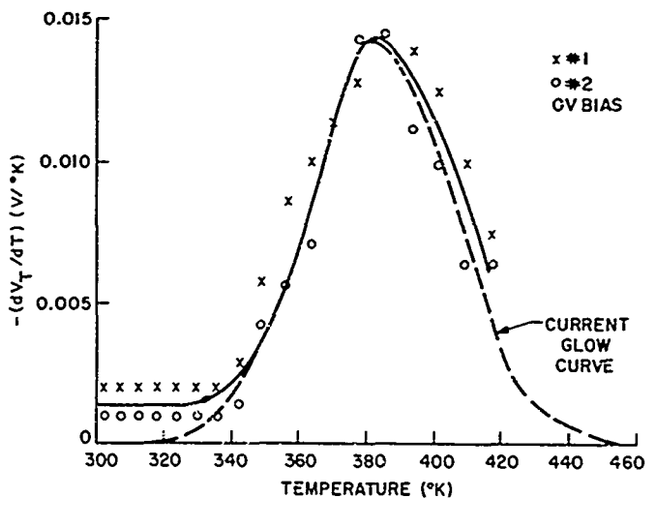

Figure 36. Glow curve of the turn-on voltage for 0V irradiation bias.

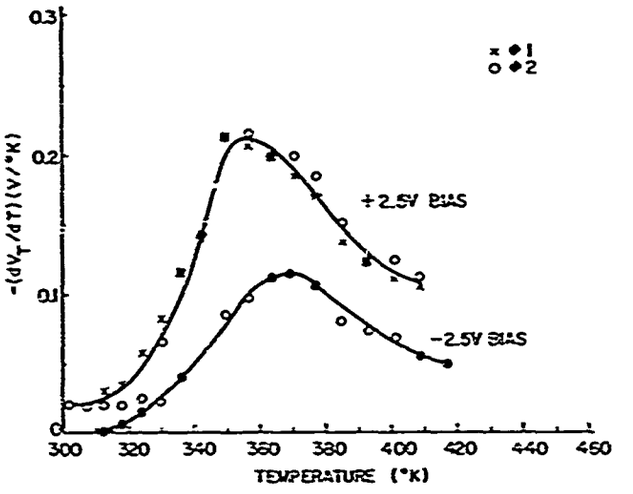

Figure 37. Glow curves of the turn-on voltage for ±2.5V irradiation bias.

comparison with the current glow curves are those for which V_G = 0V during irradiation (Figure 36). The current glow curve for V_G = 0V shown in Figure 28 is included in Figure 36 (dashed curve) for comparison purposes. The agreement between the curves is excellent and indicates that the partial annealing of Q_R and the current glow curve are closely related. The slightly different heating rates for the two curves should have very little effect on the agreement.

d. Model for Glow-Curve Current and Annealing of Positive Space-Change

From the experiments described in the previous sections, the following facts regarding the current glow curve and the accompanying partial anneal of Q_R have become clear:

(1) In addition to the positive space-charge, a much larger compensated charge is trapped in the SiO_2 layer.

(2) One of the carriers of the compensated charge is trapped in a band of levels ~1 eV from the appropriate band-gap edge.

(3) When the large compensated charge is released thermally the positive space-charge is partially annealed.

(4) The complete annealing of the positive space-charge requires longer annealing times and/or higher temperatures than those used to anneal the compensated charge.

The model proposed here is illustrated schematically in Figure 38. In this case, an MOS structure has been irradiated so that Q_R accumulates next to the SiO_2-Si interface (i.e., $V_G \geq 0V$). In the remaining neutral portion of the oxide there exists a large compensated trapped charge. It will be assumed that the electron traps (shown schematically as a single level) are shallower than the hole traps (also shown as a single level). This assumption is based on the following argument: If the holes resided in the shallower levels then during the glow-curve annealing all the positive charge should be released and the annealing of the positive space-charge should be complete. It is observed, however, that the annealing is not complete implying either a second deeper band of hole traps or that the electrons are trapped in the shallower band with all the holes more deeply trapped. The two-level-hole trap model will be dropped in favor of the simpler model shown in Figure 38.

When the irradiated MOS structure is heated, the trapped electrons enter the conduction band whereupon they either recombine with trapped holes or diffuse out of the SiO_2 into the metal or Si electrode. The current which is observed to flow through the MOS structure requires that electrons be injected into the SiO_2 layer through or over the metal-SiO_2 barrier. This barrier is several electron-volts high and, therefore, thermal excitation over the barrier may be discarded because of the relatively low temperatures used. If the SiO_2 bands are bent severely because of the presence of a large space-charge in the oxide near the metal-SiO_2 interface then tunnelling would be a possible injection mechanism. However, for irradiations in which $V_G \geq 0$ there is no appreciable space-charge buildup near the metal-SiO_2 interface and no corresponding band bending. Tunnelling may, therefore, be ruled out.

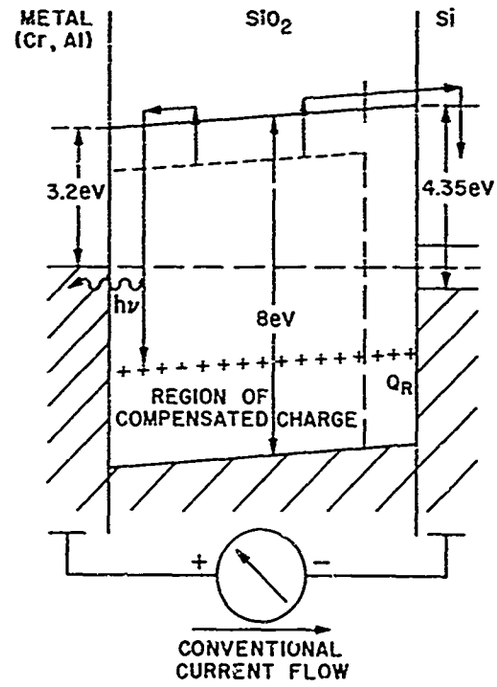

Figure 38. Schematic illustration of model to explain glow-curve current and partial annealing of positive space-charge.

If the recombination process in the SiO_2 layer is a radiative one, as it was found to be for the simple SiO_2 layers discussed in Part 5 of this section, then photoelectric emission may be considered as the injection mechanism. Thermoluminescence in quartz has a continuous spectrum in the range 3200 to 7000Å.[15,22] The bulk of the luminescence lies in the range 3200 to 4500Å with a peak at ~3800Å ($h\nu = 3.3$eV). If it is assumed that the SiO_2 layer produces similar luminescence then each of the SiO_2 interface regions will receive approximately half the light output of the SiO_2. The two interfaces are not symmetrical, however. As shown in Figure 38, the barrier height for the metal-SiO_2 interface is 3.2 eV for Cr[28] (RN-1030) and 3.2 eV for Al as well,[28,29] (FI-100 and 2N3797). The barrier heights quoted here are for the zero field condition. A barrier height of 3.05 eV has been observed[30] for a heavily degenerate n-type Si surface corresponding to photoemission from the Si conduction band. The combination of luminescence spectrum and interface barrier height appears to favor rather strongly photoemission from the metal rather than the Si into the SiO_2.

Photoemission from the metal is also favored by the quantum yields, i.e., the number of electrons emitted per absorbed photon, found for metals as compared with Si. The photoelectric yield for electrons from Si into SiO_2 has been reported as $(5 \pm 3) \times 10^{-5}$ electron/photon for photon energies of 5.38 eV, i.e., ~1 eV above the barrier height.[31] In comparison, quantum yields from Cr into BaO over a barrier height of 1.7 eV have been reported as $\sim 10^{-3}$ for photon energies of ~5 eV.[32] For energies ~1 eV above the threshold, the yield was $\sim 3 \times 10^{-4}$ electron/photon. The photoelectric yield for Cr (and presumably for Al as well) is thus significantly larger than for Si, again tending to make the metal electrode much more efficient at injecting electrons into the SiO_2 layer. The net transfer of electrons across the metal-SiO_2 and SiO_2-Si interfaces will thus be as shown in Figure 38. The conventional current flow in the external circuit will be from metal to silicon in agreement with observation.

Electrons will continue to be injected into the oxide only as long as trapped electrons are released. The current should, therefore, reflect the emptying of the electron traps; in other words, the current-vs-temperature curve is a true glow curve. While the current is flowing, more electrons will enter the SiO_2 than leave and hence there will be a partial annealing of Q_R. However, once all the trapped electrons have been released further neutralization of the space-charge must take place by some other process such as tunnelling of electrons from the electrodes into the positive trap sites. These other processes are much slower and account for the difficulty in annealing the space-charge completely.

The annealing process, according to this model will be almost entirely independent of the polarity of V_G used during irradiation and the bias used during the glow-curve anneal. For a negative bias during irradiation, the space-charge will be close to the metal-SiO_2 interface. However, the electrons will still be injected by the metal electrode and, as observed, the glow-curve current will flow in the same direction as for the case $V_G \geq 0$. Furthermore, for the same radiation dose, the same amount of compensated charge will be trapped and hence essentially the same glow curve should be observed in both cases.

The glow curve may depend to some extent on the magnitude of Q_R. Consider two cases with the same radiation dose, one with $V_G = 0V$, the other with $V_G = +2.5V$. Q_R will be much larger in the second case but, because the dose is the same, the larger value of Q_R will be the result of fewer trapped electrons rather than more trapped holes. Hence when the two glow curves are taken, the curve for the larger Q_R value ($V_G = +2.5V$) should show a smaller area under the curve. Reference to Figure 28 indicates that this prediction is fulfilled. For $V_G = -2.5V$, the area under the curve is also smaller; this fact indicates that Q_R for this bias value is also larger than for $V_G = 0V$ as expected. The difference between the curves in Figure 28 is small, however, and this point should be investigated further for confirmation.

e. Density of Electron Traps

By using the model presented above, it is possible to make a rough estimate of the density of trapped electrons in the SiO_2 layer. For a typical glow curve, we have seen that the area under the glow curve represents $\sim 4 \times 10^{-11}$ coulomb or $\sim 2.5 \times 10^{8}$ electrons injected photoelectrically into the SiO_2 layer. If the photoelectric process is ~0.1-percent efficient[32] then $\sim 10^{3}$ times as many electrons ($\sim 2.5 \times 10^{14}$) must be trapped in the SiO_2 as are injected over the metal-SiO_2 barrier. The uncertain quantity in the estimate is the volume of SiO_2 in which the electrons are trapped. If only the SiO_2 under the gate area is involved then the density is 10^{20} cm^{-3}. If, however, the active volume also includes the SiO_2 under the electrode contact areas then the density is $\sim 10^{19}$ cm^{-3}.

For both cases the density of trapped electrons appears to be very large. In contrast, an electron trap density of $\sim 3 \times 10^{14}$ cm^{-3} with a trap depth of ≥ 2 eV has been reported for thermally grown SiO_2 layers in Au-SiO_2-Si structures.[31] The thermoluminescence experiments discussed earlier revealed that the density of traps in fresh SiO_2 layers is low but that exposure to Co^{60}-gamma radiation significantly increased the density. Thus, the relatively low density of 3×10^{14} cm^{-3} mentioned above is likely valid for fresh oxides but probably much too low for oxides which have been irradiated or subjected to other treatments such as those used in the fabrication of planar devices. For the oxide layers in commercial devices, the

results of Figure 31 indicate that large doses of Co^{60}-gamma radiation have very little effect on the trap density. One explanation may be that processed oxide layers contain such a high density of inherent trap levels that irradiation cannot cause a significant increase in the density.

f. Summary

The results reported in this part of the report have clarified the process of radiation-induced space-charge buildup in SiO_2 layers. Both holes and electrons generated by radiation are trapped and the positive space-charge is the excess of trapped holes over trapped electrons. The electrons are trapped in a band of trap levels ~1 eV below the SiO_2 conduction band, while the holes are more deeply trapped. This model is considerably different from that proposed by Snow et al.[7] in which only the trapping of holes is postulated.

When an irradiated MOS structure is heated, the trapped electrons are released into the SiO_2 conduction band and, subsequently, drift out of the oxide or recombine with trapped holes. It is postulated that luminescence accompanying the recombination causes photoemission of electrons from the metal electrode into the SiO_2 layer allowing a current to flow through the MOS structure and resulting in a reduction of Q_R. Complete removal of Q_R usually requires further annealing at higher temperatures for longer periods of time. The processes by which the remaining portion of Q_R is annealed have not been identified.

It should be mentioned that the trapping of both holes and electrons in the SiO_2 layer of an MOS structure will not alter the space-charge buildup process or the analysis of this process presented in Part 4 of this section.

7. EFFECTS OF RADIATION ON SILICON SCHOTTKY BARRIER DIODES

a. Introduction

As Schottky barrier diodes are majority carrier devices, their operation does not depend upon injection, decay, and transport of excess minority carrier densities; thus, the diodes are not subject to the effects of the degradation of excess carrier lifetime due to nuclear radiation. However, in a previous study of irradiated Schottky barrier devices, severe degradation of the device characteristics was found to occur because of space-charge buildup in the peripheral metal-oxide-semiconductor (MOS) region with consequent "edge" breakdown and leakage.

It has been demonstrated recently that improved Schottky barrier diodes with nearly ideal current-voltage (I-V) characteristics can be made with the use of a clean junction between the metal and the semiconductor, with improved oxide passivation, and by the addition of a p-n guard-ring structure, diffused around the

metal-semiconductor junction.[31,32] These improved Schottky barrier diodes have extremely "hard" reverse characteristics, i.e., high breakdown voltage and low-leakage currents; they are comparable to the best p-n junction diodes. These guard-ring structures should eliminate the edge effects from nuclear radiation which have been observed in devices without guard rings.

Guard-ring Schottky barrier diodes are of interest not only for applications in devices such as high-frequency rectifiers, microwave oscillators, and logarithmic converters but also for studies of bulk-material characteristics and the nature of the metal-semiconductor interface. As an example, capacitance-voltage (C-V) measurements on Schottky barrier diodes can be used to determine introduction rates, energy levels, and capture rates of radiation-induced defects in the bulk semiconductor material. For normal p-n junction devices, such measurements are far more difficult to interpret because of the large impurity concentrations present near the junction.

Of interest during the study described here were the effects of radiation on the metal-semiconductor interface since the I-V characteristics of the Schottky barrier diodes are partly determined by the density of interface states. In nonirradiated devices, the surface states have a density of the order of 10^{14} states/cm^2.[23] Since the thickness of the interface region is only a few angstroms, these defect concentrations are large compared to those which would be produced in the bulk material at typical radiation exposure levels. However, it has been suggested that nuclear-radiation defect production rates at the surface may be much greater than those in the bulk because the surface would serve as a sink for vacancies and interstitials. Therefore, in this study, a specific effort was made to deduce changes in the interface states by nuclear radiation from both I-V and C-V characteristics of irradiated, nearly ideal structures. In addition, some effort was directed toward understanding changes in the characteristics of nearly ideal Schottky diodes resulting from a space-charge buildup in the MOS region surrounding the junction guard-ring region.

b. Results of Experiments on Device Parameters in a Radiation Environment

1. Devices and Exposures. The devices used in this study were fabricated, by planar processes, on n-type 0.8 ohm-cm silicon substrates (thickness ~100μ) and had platinum-silicide contacts and diffused p-n junction guard rings. Each diode thus consisted of three parts in parallel: a Schottky diode, a p-n junction guard ring, and a MOS guard ring. The area ratio of the constituent parts in the 20-mil device was 25:1:11 respectively. The thickness of the thermally grown oxide was about 5000Å. The junction depth of the guard ring was 1 to 2μ.

Cross sections of this device and of a conventional planar Schottky diode without a guard-ring structure are shown in Figure 39. Also shown in this figure are the electric-field line distributions and the expected shape of the depletion region. In the conventional Schottky barrier diode without a guard ring (Figure 39a), highly localized fields occur at the electrode edge. As a result of these fields, the conventional Schottky diode exhibits excess leakage current and low breakdown voltage. If under an ionizing radiation environment trapped positive charges build up at the SiO_2-Si interface in the vicinity of the corners of the metal-semiconductor junction, the electric-field lines, originating in the trapped positive charges, must end on the edge of the metal-semiconductor interface. Thus, the edge field is further intensified. This increase of the edge field drastically lowers the breakdown voltage and increases the leakage current. This serious degradation in characteristics is reduced in the new device (Figure 39b). The p^+ diffused guard ring, overlapping both the platinum-silicide electrode and the MOS region, together with the metal overlay on top of the device virtually eliminate the edge effect inherent in conventional Schottky diodes. In this structure the widths of the depletion region under MOS, guard ring, and Schottky junction become roughly the same. The electric-field intensity near or at the corners is therefore greatly reduced, while the metal overlay also serves to prevent the formation of an inversion region under the oxide layer.

Schottky barrier diodes with three different area-to-periphery ratios were exposed. In addition, devices with only p-n junction and MOS guard ring and with MOS structure alone were fabricated and irradiated.

The devices were exposed with and without reverse bias during radiation. The Co^{60}-gamma-ray tests were performed at Bell Telephone Laboratories. The dose

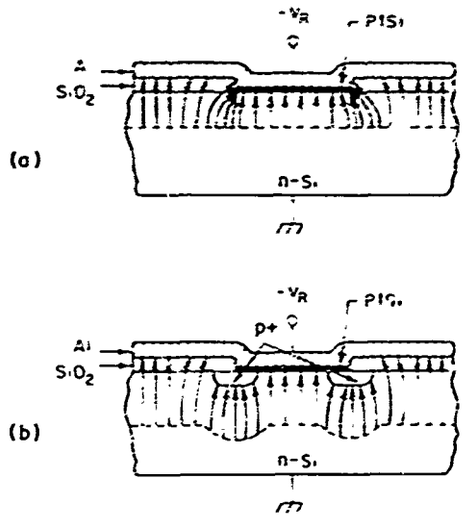

Figure 39. Cross-section of Schottky diodes. (a) without a guard ring, (b) with a guard ring.

rate was approximately 100 rads/s. The neutron irradiation tests were conducted in the nuclear reactor at Pennsylvania State University. The neutron fluences ($E > 10$ keV), were established by sulfur-foil activation methods, and were accurate to ± 10 percent.

2. Current-Voltage Characteristics. The I-V characteristics of platinum-silicide diodes before-and-after Co^{60}-gamma radiation, both with and without p-n junction guard rings, are compared in Figure 40. Before irradiation, the device without a guard-ring structure shows less than ideal characteristics in both the forward- and reverse-current directions. In the forward direction, the n factor (a measure of the slope of the log I versus V characteristic) of the diode equation[34]

$$I_f = I_s \left[\exp\left(\frac{qV_f}{nkT}\right) - 1 \right] \tag{1}$$

where

$$I_s = A^{**}T^2 \exp\left(-\frac{q\phi_{Bn}}{kT}\right)$$

varies from 1.2 to 1.5 for the unprotected device, compared to its value of 1.02 for the device with a guard-ring structure. Since both the effective Richardson constant and the barrier height are voltage-dependent, n is approximately 1.01 for an ideal Schottky barrier in silicon.

In the reverse direction, the I-V characteristics show a "soft" breakdown for the Schottky diode without guard ring, whereas, the breakdown is "hard" for the corresponding guard-ring device.

Following an irradiation of 10^8 rads, the reverse current of the device without guard ring increases by three orders of magnitude. A comparable degradation occurs in the low current region of the forward-current characteristics. The mechanism giving rise to this severe degradation is a radiation-induced positive-charge buildup at the peripheral oxide layer, with a consequent decrease in the depletion width under the MOS part and a corresponding intensification of the electric field at the junction edge. Tunnelling or avalanche breakdown occurs at the edge; this is evidenced by the small temperature dependence of the degraded reverse current[25] rather than by the large temperature dependence expected for a thermal-generation process.

The devices with a guard-ring structure show a very small degradation of the reverse- and forward-current characteristics, even after a 10^8-rad gamma dose. The n factor of the forward characteristic for a guard-ring structure increased to 1.2. However, the "hard" reverse characteristic was preserved.

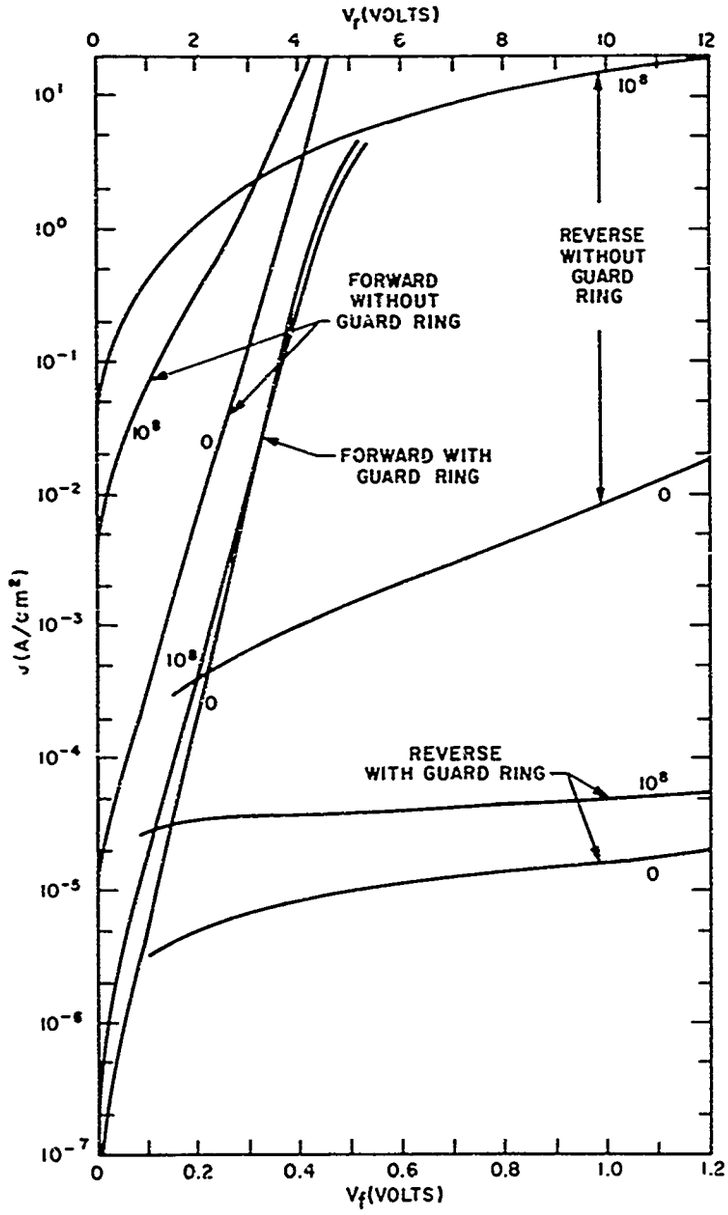

Figure 40. Gamma-dose effects on the I-V characteristics of Schottky diodes.

Figure 41 shows the variations in the forward I-V characteristics with gamma dose and, for comparison, the forward characteristics of the p-n junction guard ring alone. The degradation of the latter's characteristics in the low current region is due to the electron hole recombination at fast surface states.[4,7] These are located at the surface of the depletion region which is induced under the MOS part

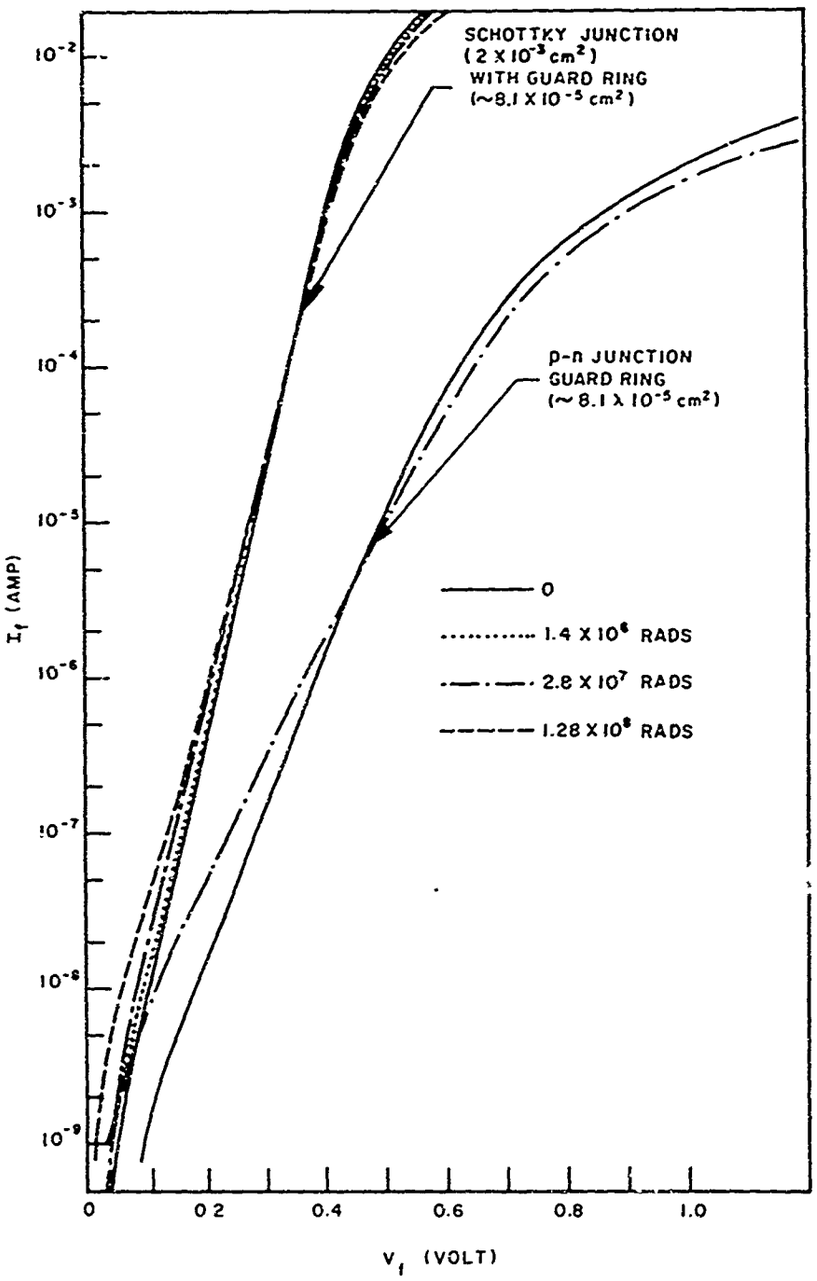

Figure 41. Variations in forward I-V characteristics with gamma dose.

in the vicinity of the p-n junction. By comparing the forward characteristics of the Schottky diode with and without a guard-ring structure (Figure 40) with those of the p-n junction guard ring (Figure 41), one notices that the junction guard ring helps to suppress the edge leakage current of the diode.

When the characteristics in Figure 41 are compared with the diode equation, it becomes apparent that they follow the equation very closely, indicating nearly ideal Schottky barrier behavior. Below 10^{-3} A, the characteristics follow the equation over six orders of magnitude, with $I_s \approx 10^{-10}$A; i.e., nearly the entire current is carried by electrons injected into the platinum silicide. Above 10^{-3}A, the characteristics deviate from the exponential dependence on voltage, as a result of bulk series resistance. The series resistance increases slightly with radiation.

Figure 42 shows the changes in the forward characteristics produced by fast neutron bombardment. Generally, the same comments apply to these results as to the gamma irradiations. At the 10^{15}n/cm^2 neutron fluence and above 10^{-3}A, a large increase in the forward voltage results from the large decrease in the majority carrier concentration. In the low current region, below 10^{-7}A, the current increases with an increase in dosage. This is due partly to an increase in the Schottky saturation current and partly to an increase in the recombination current.

By extrapolating the I-V characteristics in the 10^{-4} to 10^{-6}A range, which is free of excess current and series resistance, to 0 voltage, one obtains the saturation current and the corresponding barrier height. The variations in the barrier height, φ_{Bn}, and the slope, n, with gamma dose and with neutron fluence are given in Figures 43 and 44 respectively. A slight decrease in φ_{Bn} (from 0.83 to 0.79eV) and a corresponding increase in n (from 1.02 to 1.19) occurred with an increase in radiation. At 10^8 rads or at 10^{15} n/cm^2, the barrier height decreases a few percent. Since the Schottky current is a sensitive exponential function of the barrier height, the Schottky saturation current increases by about one order of magnitude. However, the results indicate that the changes in interface state density are small up to a very high dosage.

Figure 45 gives the comparison between the reverse characteristics of a neutron-irradiated 20-mil-diameter platinum-silicide Schottky diode with guard ring and of a corresponding diffused p-n junction guard ring alone. The reverse current of the entire Schottky diode is given by the sum of the generation current contributions from the depletion regions under the Schottky, guard-ring, and MOS parts. Thus,

$$I_r = \left\{ A^{**}T^2 \exp\left(\frac{q}{kT}\right)\left[-\phi_{Bn} + \sqrt[4]{\frac{q^3 n_D\left(V + V_D - \frac{kT}{q}\right)}{8\pi^2\epsilon^3}} \right]\right\} A_s$$

$$+ \frac{qn_i}{2}\left\{ \sum_i \left(\frac{W_i}{\tau_i} A_i\right) + S_0 A_0 \right\} \qquad (2)$$

with

$$\frac{1}{\tau_i} = K\phi$$

$$W_i = \sqrt{\frac{2\epsilon}{qn_D}\left(V_i + V_D - \frac{kT}{q}\right)}$$

A_s, A_i, and A_0 are the areas, W_i is the depletion width of the corresponding parts, τ_i is the effective lifetime, S_0 is the surface recombination velocity. The first component is due to the Schottky saturation current modified by image-force lowering by the reverse voltage. The slope of the I-V characteristic due to this factor is less than 1/2. The pre-irradiation characteristic, Figure 45, indicates that the Schottky current dominates the reverse characteristics before avalanche breakdown. As additional recombination centers are introduced by fast-neutron bombardment, the generation current components become dominant through the decrease in the effective lifetime.

At 10^{15}n/cm^2 fluence, there is a significant decrease in the effective doping and a corresponding increase in the width of the space-charge depletion region. These changes are reflected by an increase in the breakdown voltage (Figures 45 and 46) as well as by an increase in the forward voltage (Figure 42).

These changes are reflected by an increase in the breakdown voltage (Figures 44 and 45). The pre-irradiation breakdown voltage of 62V corresponds to a doping level of $8.7\text{x}10^{15}/\text{cm}^3$. At 10^{15}N/cm^2, the breakdown voltage increases to 65V, characteristic of a doping level of $8\text{x}10^{15}/\text{cm}^3$. One concludes that approximately 0.7 donors/N-cm are removed. Similar values of the compensation of a majority carrier dopant were deduced from the displacement in the capacitance data. The changes also are reflected in an increase in the forward voltage (Figure 42). This increase, above 10^{-3}A, can be attributed to the decrease in conductivity as a result of both the carrier removal effect and carrier mobility changes.[35]

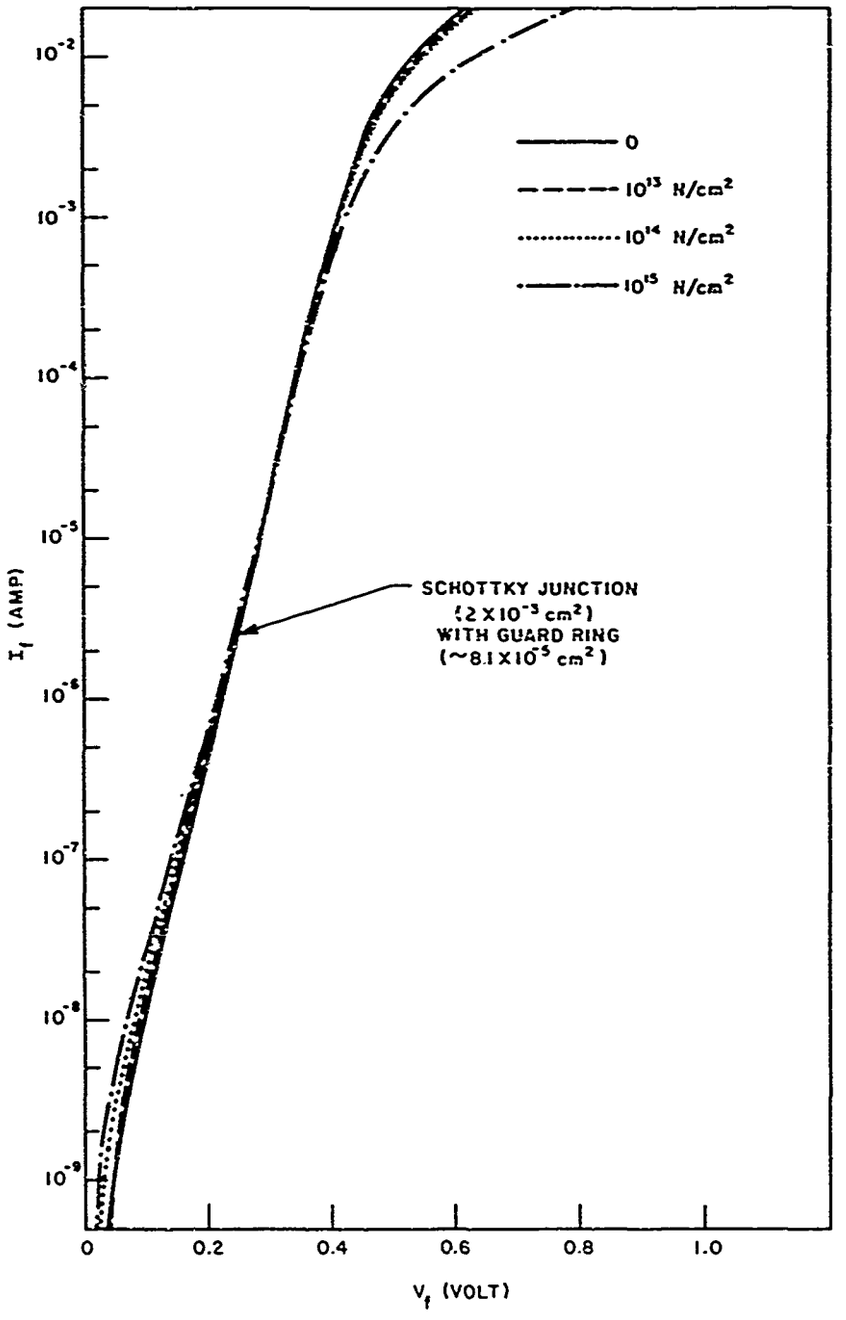

Figure 42. Variations in forward I-V characteristics with neutron fluence.

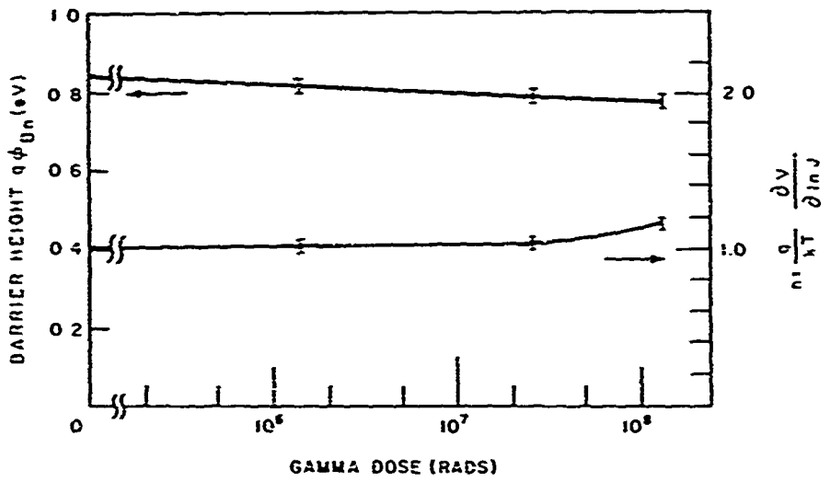

Figure 43. Variations in "n" value and Schottky barrier height with gamma dose.

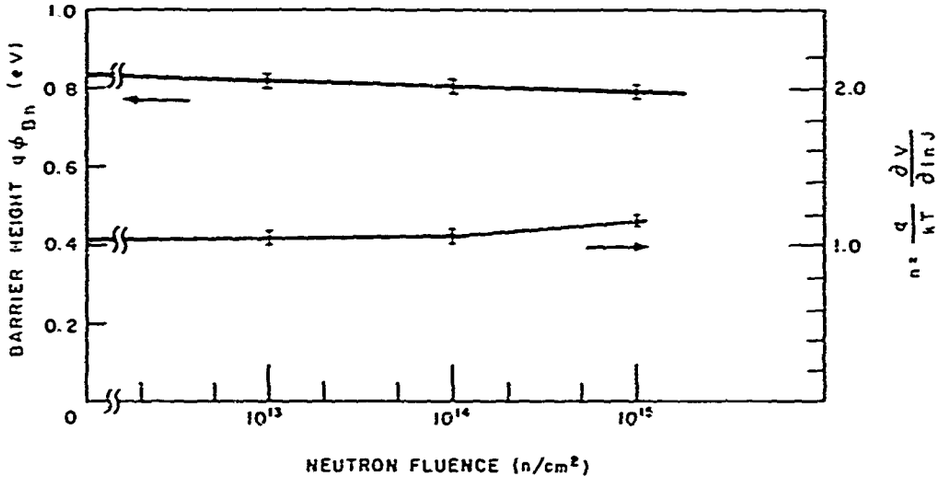

Figure 44. Variations in "n" value and Schottky barrier height with neutron fluence.

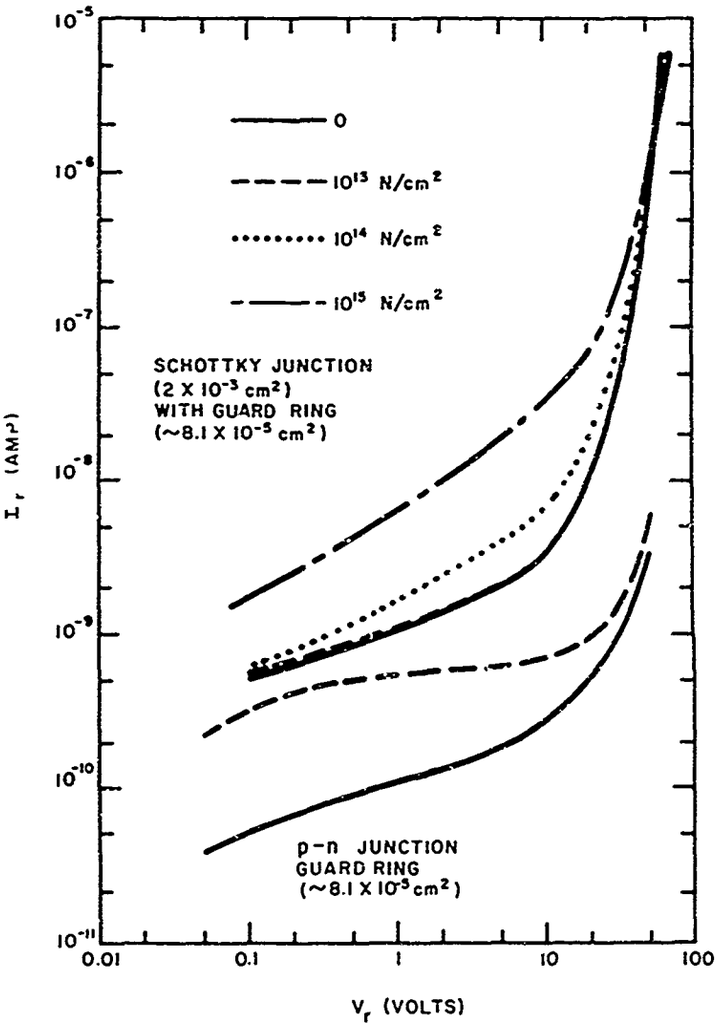

Figure 45. Variations in reverse I-V characteristics with neutron fluence.

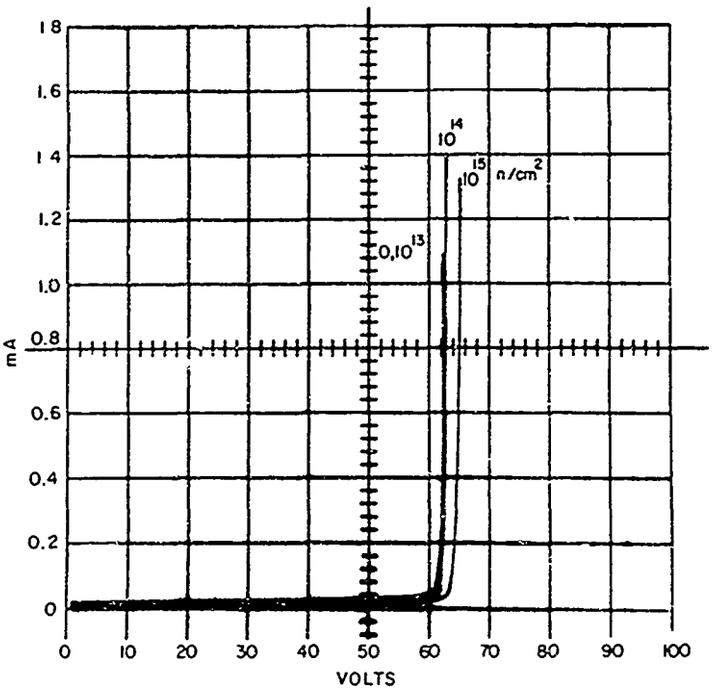

Figure 46. Variations in reverse-current breakdown characteristics with neutron fluence.

The order-of-magnitude increase in the reverse current of a p-n junction guard-ring structure at 10^{13}n/cm^2 fluence can be attributed to the channel formed[7] by the inversion of the surface of the p^+ region. This inversion is caused by the radiation-induced positive space-charge within the oxide.

3. Capacitance-Voltage Characteristics. It has been demonstrated that differential capacitance measurements can be used to characterize the properties of junction devices and to investigate the characteristics of surface space-charge regions.[36,37] Possible sources of errors and the factors which affect the interpretation and validity of the measurements on metal-semiconductor barriers have been discussed by Goodman.[38]

In view of the composite structure of the guard-ring type Schottky diodes, decomposition of the total capacitance of the diode is necessary. The effective capacitance per unit area caused by Schottky junction, MOS, and p-n junction guard-ring components was determined by solving simultaneous equations for total capacitances (subtracting header capacitance) of 20-, 8-, and 3-mil devices of known areas (three equations for three unknowns) for a given reverse voltage and a given radiation dose. Figure 47 shows the variations in the C-V characteristics of a 20-mil

device for several neutron fluences. The capacitance was measured at 1 MHz. An example of the decomposition of the total device capacitance at zero dose into capacitances of the inherent components is also shown in the illustration. Generally, at high reverse voltage, the total device capacitance increases with an increase in the neutron fluence. This is due mostly to the shift of the MOS C-V characteristic toward the higher reverse voltage; this shift is caused by the radiation-induced positive-charge buildup in the SiO_2-Si interface. The amount of shift is larger for devices which have been reverse-biased (at -45V) during irradiation. In the case of gamma radiation, the voltage shift saturates at the same voltage as the reverse-bias (-45V) voltage.

At a 10^{15}n/cm^2, displacement damage decreases the concentration of the majority carriers. This decrease causes some decrease in the total capacitance in the low-voltage range and an increase in the breakdown voltage.

The variations in the effective capacitances for the Schottky junction and for MOS under gamma radiation are summarized in Figure 48. The values of the

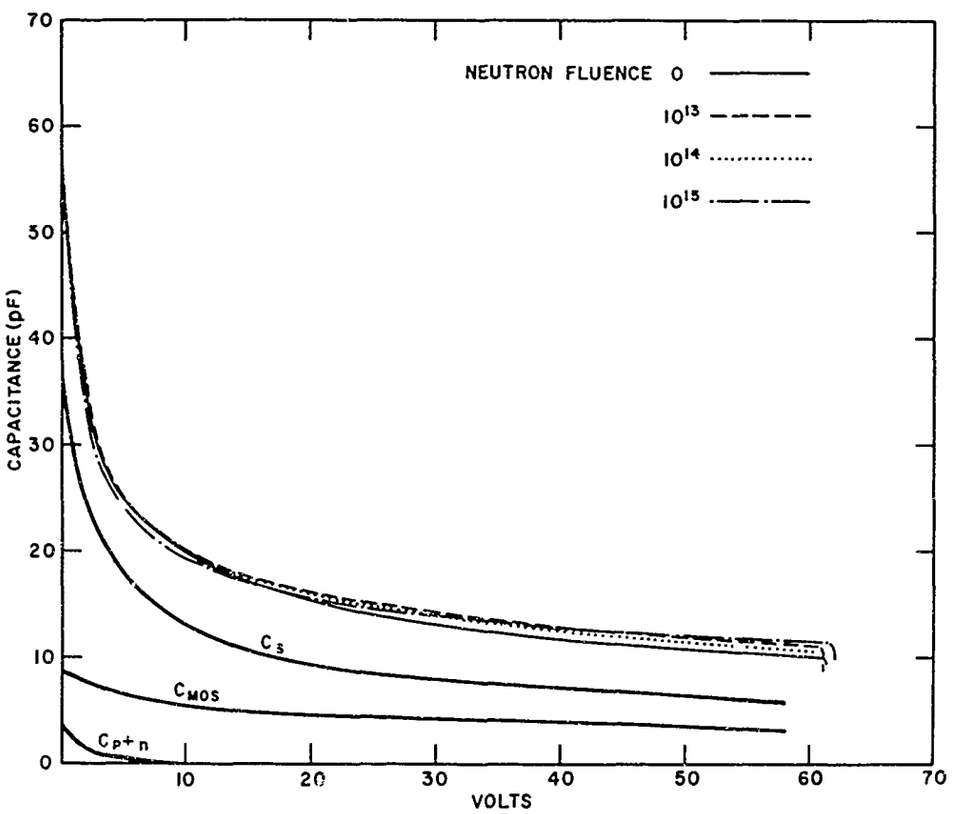

Figure 47. Effect of neutron irradiation on C-V characteristics.

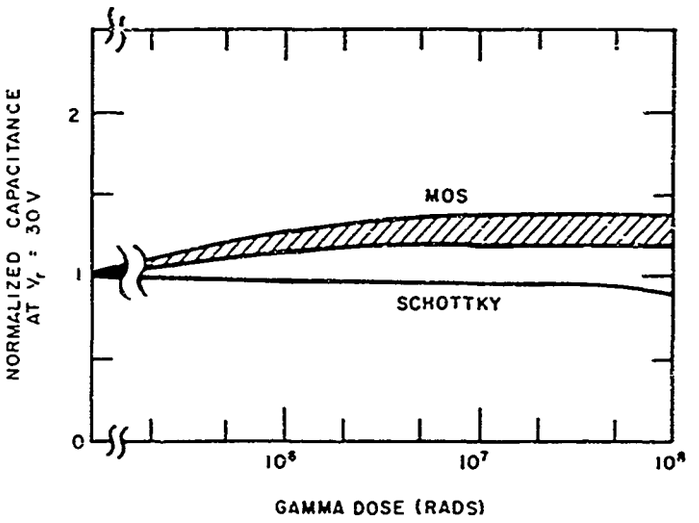

Figure 48. Normalized Schottky junction and MOS capacitances, variation with gamma dose (V_r = 30V).

capacitances, taken at 30V reverse bias, are normalized to the capacitance values before irradiation. Notice that the effective capacitance of the Schottky junction is virtually independent of radiation up to nearly 10^8 rads and that the same is true for neutrons up to 10^{15}n/cm^2, as shown in Figure 49. The intercept of a $1/C^2$-versus-V plot on the voltage axis yields $V_D - (kT/q)$. The value of the diffusion potential, V_D, was found to vary, from 0.55 to 0.60V and show a slight decrease as the dosage increased, again confirming that no appreciable change in surface state density occurs. In Figure 49, the effective capacitance of the MOS part increases with an increase in dosage but saturates above 10^6 rads or 10^{14}n/cm^2 fluence. The shaded area covers the range of uncertainty in the MOS data.

The effective capacitance of the p-n junction guard ring also increases with an increase in the ionizing radiation dose through the formation of channels. However, the p-n junction guard ring has the smallest area in the device structure and there is a much larger scatter in the data.

In order to investigate further the effects of space-charge buildup in the MOS part, devices with the same junction guard-ring structure but with an additional MOS part replacing the Schottky junction and with a metal overlay covering the top of the entire diode were made. These were then subjected to gamma radiation. Figure 50 gives the result of this experiment. Also shown in the figure are plots of the theoretical capacitances for the p-n junction guard ring and of the MOS capacitance based on the depletion approximation. By comparing the addition of the

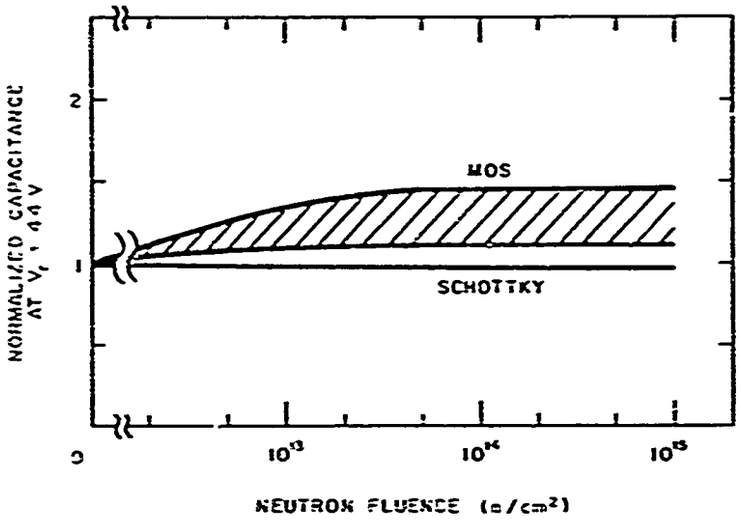

Figure 49. Normalized Schottky junction and MOS capacitances, variation with neutron fluence $V_r = 44V$.

two capacitances with the experiment results, one finds that, during irradiation, the voltage shift due to the MOS C-V characteristic increases with an increase in the gamma dose but saturates at the same voltage as the reverse bias. Some increase in capacitance is also observed in the low voltage region, close to zero bias, because of channel formation.

c. Summary

Platinum-silicide silicon Schottky barrier diodes with a guard-ring structure exhibit a high degree of radiation resistance. The improved Schottky barrier diodes have near-ideal forward characteristics and "hard" reverse characteristics comparable to the best p-n junction diodes with the same background doping. These improvements are preserved up to a gamma dose of 10^8 rads and to a high neutron fluence of $10^{15} n/cm^2$. By the use of a low resistivity substrate and a thin epitaxial layer, one may expect that the exponential current range of the guard ring Schottky diode could be extended from one to two orders of magnitude higher. The behavior of such a device under irradiation should be similar to that of the device which was investigated. Such devices would be of value as ordinary rectifiers and switches in severe radiation environments.

From both the forward-current zero-voltage intercepts and the C-V characteristics, we find that the surface state density at the platinum silicide silicon interface is unaffected up to 10^8 rads or $10^{15} n/cm^2$.

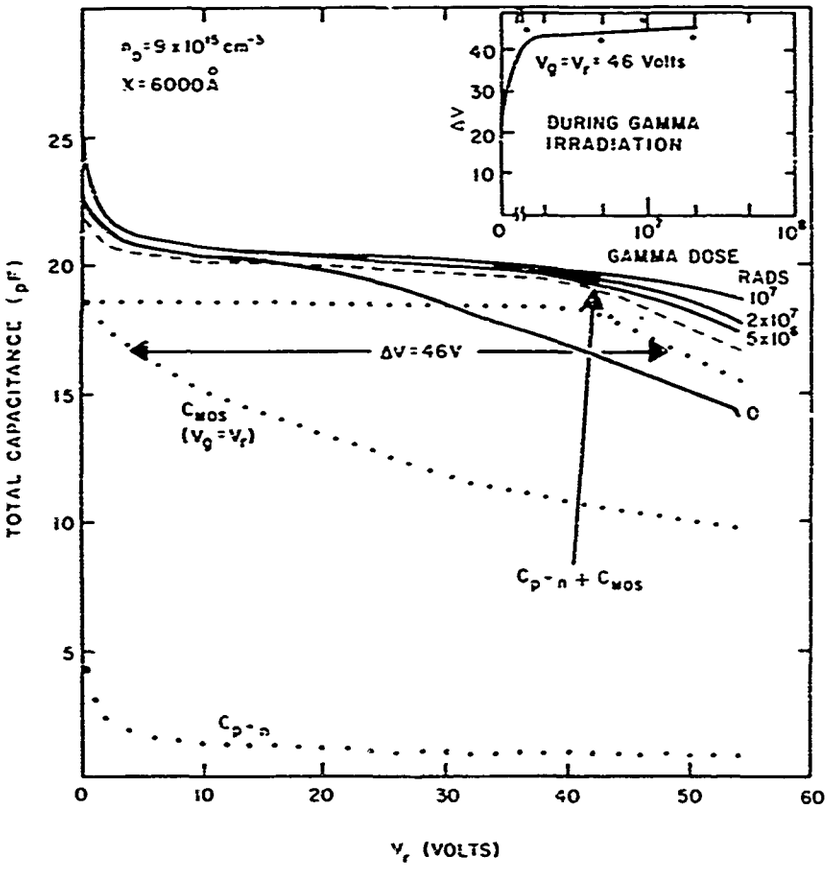

Figure 50. Guard-ring and MOS capacitances versus voltage (gamma dose as the parameter). Insert shows the voltage shift ΔV of the C-V characteristic as a function of gamma dose.

The measurement of capacitance changes in Schottky barrier devices to characterize bulk or surface charges is complicated by capacitance changes in the shunting MOS structure and p-n junction guard ring. The MOS structure shows large and somewhat unpredictable space-charge buildup effects. These effects may be partially eliminated by minimizing the MOS capacitance associated with the aluminum overlay and by increasing the area ratio of Schottky junction to an MOS guard ring.

BLANK PAGE

III. RADIATION EFFECTS ON DEVICE STUDIES

8. EFFECTS OF FAST NEUTRONS ON PIN, PπN, PνN SILICON DIODES

a. Introduction

In the study of radiation effects on semiconductors, junction device structures have often been used because of the wide range of minority carrier levels that can be obtained. Of all the structures that have been employed probably the most desirable is the PXN diode (X = I, π, ν) for the following reasons:

(1) The electrical behavior of the device is largely determined by the width, doping, and lifetime of the X region. These parameters can be varied over a wide range without altering the basic device analysis.

(2) It is the best understood junction device in several respects:

(a) The current flow is essentially one dimensional.

(b) Surface effects can be neglected provided the perimeter/width ratio of the X region is large.

(c) The relationships of external electrical behavior and fundamental physical parameters have been extensively analyzed.[1,2]

(3) Both high-injection and low-injection level regimes can be studied. Furthermore the open-circuit voltage across the structure is a measure of the relative positions of the hole and electron quasi-Fermi levels. Thus it is conceptually possible to do Fermi-level spectroscopy in such devices without changing the temperature.

(4) PXN devices are of interest as radiation hardened devices and as detectors of ionizing radiation. The increased understanding of radiation effects in these devices should lead to improved structures.

A program was started under this contract to study the effects of fast neutrons on PXN silicon diodes with the following aims;

(1) To establish the presence of clustered damage regions and the degree to which such regions control the electrical behavior of the bulk material.

(2) To determine the magnitude of isolated defect recombination and to identify, if possible, the defect concentrations, energy levels, recombination mechanisms, and capture cross sections.

(3) To determine the nature of the fast "recovery" process in neutron-irradiated silicon devices.

In the course of this program it was planned to expose a wide variety of specially prepared PXN diodes at liquid-nitrogen and room temperatures to a source of 14-MeV neutrons. Before these irradiations were undertaken some preliminary irradiations with commercially available silicon diodes were done at the White Sands Fast Burst Reactor (WSFBR), and the results of these experiments will be given in this report.

In these preliminary experiments, two types of device measurements were explored:

(1) A transient measurement of the open-circuit forward-voltage recovery (OCFVR) of junction voltage following abrupt termination of forward bias.

(2) Steady state measurement of reverse bias junction capacitance (RBC).

An analysis was made using Shockley-Read[3,4] recombination statistics to predict the shape of the OFCVR curve and to deduce defect parameters. These results are compared with experimental measurements done at temperatures from -100° to +25°C on fast neutron-irradiated PIN silicon diodes. OCFVR measurements of PIN diodes were also made as a function of time following a burst of neutrons in order to study the fast recovery process.

RBC measurements were made at 77°K and 295°K, both before and after minority carrier injection. The recovery effects due to injection are discussed and a model for recovery in terms of clustered damage is presented.

b. Open-Circuit Forward-Voltage Recovery (OCFVR)

1. Theory. The use of PIN structures in investigations of transient recombination from high-injection levels in semiconductors has been examined by Davies.[5] He employed a technique, originally introduced by Gossick,[7] in which the current flow is abruptly terminated and the open-circuit transient voltage across the structure is observed. Wilson[8] has shown experimental results of the effect of high-injection level and temperature on the recombination process. He also indicated the advantages of the open-circuit carrier decay method over the "junction-recovery" method of measuring lifetime.

The purpose of the present study was to examine the feasibility of applying the open-circuit carrier decay method as a possible probe for characterizing various recombination and trapping processes, in particular, those due to radiation-produced defects.

Consider, first, a forward-biased PIN diode. As the I region is inundated by holes and electrons injected from the P^+I and IN^+ junctions, the electron and hole quasi-Fermi levels move away from the thermal equilibrium Fermi level toward their respective band edges. If the PIN structure is abruptly open circuited, the excess free-carrier densities decay toward zero. As the carrier densities decrease by recombination, their quasi-Fermi levels recede from band edges and approach each other — relaxing back to the thermal equilibrium value of the Fermi level. As the quasi-Fermi levels pass through defect energy levels, states that were recombination centers during a steady high-level injection period now become trapping states and empty their carriers via the respective free bands.

Since the open-circuit forward voltage is a measure of the separation of the quasi-Fermi levels, the decay of this voltage will be linear in time with a slope given by $2kT/q\tau_h$ where $2kT/q = 0.05V$ at room temperature and τ_h is the high-injection-level lifetime. For a single dominant Shockley-Read type recombination center, this slope is expected to change as the appropriate quasi-Fermi level moves through the Shockley-Read level, giving rise to an inflection in the recovery curve.

The effect of a single Shockley-Read-Hall (SRH) recombination level position within the forbidden band on the steady-state lifetime, τ, of nonequilibrium carriers may be seen from the following expression for the case of low-trap concentration such that $\Delta n = \Delta p$ (neglecting Δn_t associated with the trap level).

$$\tau = \tau_\ell \left\{ \frac{1 + \left(\tau_h/\tau_\ell\right)\left[\Delta n/\left(n_o + p_o\right)\right]}{1 + \Delta n/\left(n_o + p_o\right)} \right\}$$

where $\tau_h = \tau_{po} + \tau_{no} = \dfrac{1}{\sigma_p v_p N_t} + \dfrac{1}{\sigma_n v_n N_t}$ = high injection-level lifetime

$$\tau_\ell = \tau_{po}\left(\frac{n_o + n_i e^{m}}{n_o + p_o}\right) + \tau_{no}\left(\frac{p_o + n_i e^{-m}}{n_o + p_o}\right) = \text{low injection-level lifetime}$$

$$m = \frac{E_t - E_i}{kT} = \text{normalized trap position with respect to intrinsic level}$$

The variation of lifetime with injection level based on an SRH model indicates a monotonic increasing or decreasing function depending on the ratio τ_h/τ_ℓ.

If the spatial distribution of excess carriers in the base region is neglected, the time dependence of the excess carrier concentration can be shown as

$$\left(\tau_h - \tau_\ell\right) \ln\left[\frac{\Delta n_o + n_o + p_o}{\Delta n(t) + n_o + p_o}\right] - \tau_\ell \ln\left[\frac{\Delta n(t)}{\Delta n_o}\right] = t$$

The open-circuit voltage is approximately related to the excess carrier density by

$$V(t) = \frac{kT}{q} \ln \left\{ \frac{\left[n_o + \Delta n(t)\right]\left[p_o + \Delta n(t)\right]}{n_i^2} \right\}$$

Preliminary results were obtained using the above results for the open-circuit decay of a PIN structure assuming various energetic positions of the Shockley-Read level. These results are shown in Figure 51. It is evident that no sharp inflection points appear in these solutions. Instead, the decay curve has a smooth change in slope in which curvature is concave upward, straight, or concave downward according to whether

$$\left[n_o + p_o + 2\Delta n(t)\right]\left[p_o + \Delta n(t)\right]\left(n_o + p_o\right)\left(\tau_h - \tau_\ell\right)$$

is less than, equal to, or greater than

$$\left(p_o - n_o\right)\left[n_o + p_o + \Delta n(t)\right]\left[\left(n_o + p_o\right)\tau_\ell + \tau_h \Delta n(t)\right]$$

The absence of inflection points in the solution is attributed to the fact that slow equilibration of the Shockley-Read states smears out the transition over many kT/q in open-circuit voltage.

In order to cope with the more realistic situation where spatial distribution of excess carriers injected from both ends of the base region becomes important, a computer solution (Scharfetter-Gummel time-evolution program) of the entire open circuit-voltage process was attempted.

Analytical results were obtained using this computer program for the transient behavior of electron and hole concentrations and for the corresponding quasi-Fermi levels in the lightly-doped central I region following a switch from forward bias to open-circuit condition. It was determined that the quasi-Fermi levels were virtually constant within the order of kT/q across the I region for times greater than one lifetime after the initiation of the open-circuit condition. By choosing a PIN structure with a base-width to diffusion-length (W/L) ratio appropriate for the range of excess carrier lifetimes, a constant quasi-Fermi level across the base region may be obtained, and a uniform relaxation of excess carriers with respect to the trap level is possible. Thus, investigation of the effect of the relative position of trap level with respect to the Fermi and quasi-Fermi levels becomes meaningful.

Figure 52 shows the time decay of the hole and electron quasi-Fermi levels for a PIN structure with W/L ratio equal to 6 and acceptor doping of 10^{13} cm^{-3} in the π region. The forward current is assumed to be 10 A/cm^2, and unequal hole

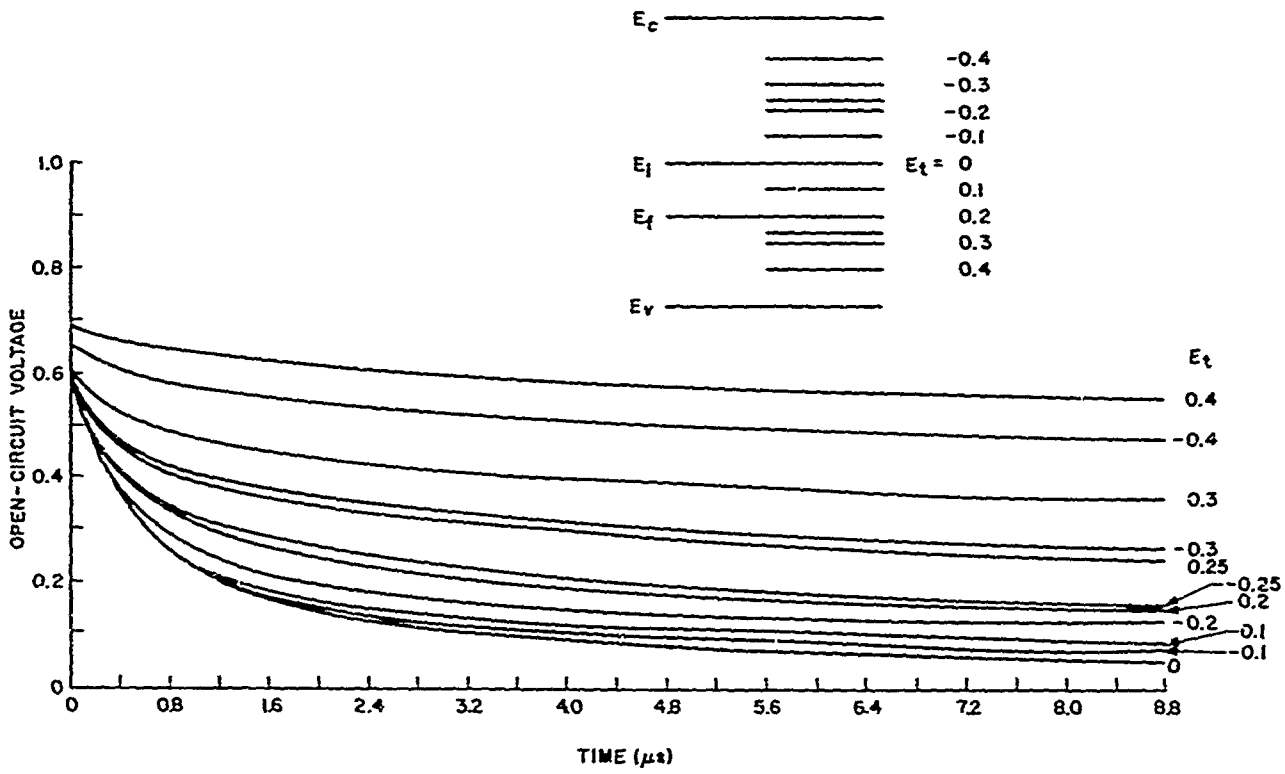

Figure 51. Effect of a single trap level on the open-circuit voltage decay of a PIN structure assuming various energetic positions of the Shockley-Read level.

and electron mobilities are taken into account. The corresponding decay in open-circuit voltage is shown in Figure 53. From Figures 52 and 53, the following information is obtained:

1. The decomposition of the voltage decay curve into its constituent junction voltages, $V_{p\pi}$ and $V_{\pi n}$ (shown in Figure 53) reveals that an inherent change in the slope will occur if the base region is not strictly intrinsic. This change occurs because the difference in contributions from the $P\pi$ and πN junctions depends strongly on the base doping. This change in slope in voltage decay occurs at 0.35V for doping of 10^{13} cm^{-3}. This is the terminal voltage at which the minority carrier transition goes from a high- to a low-injection condition with accompanying decrement (approximately 1/2) in slope of the voltage-decay curve.

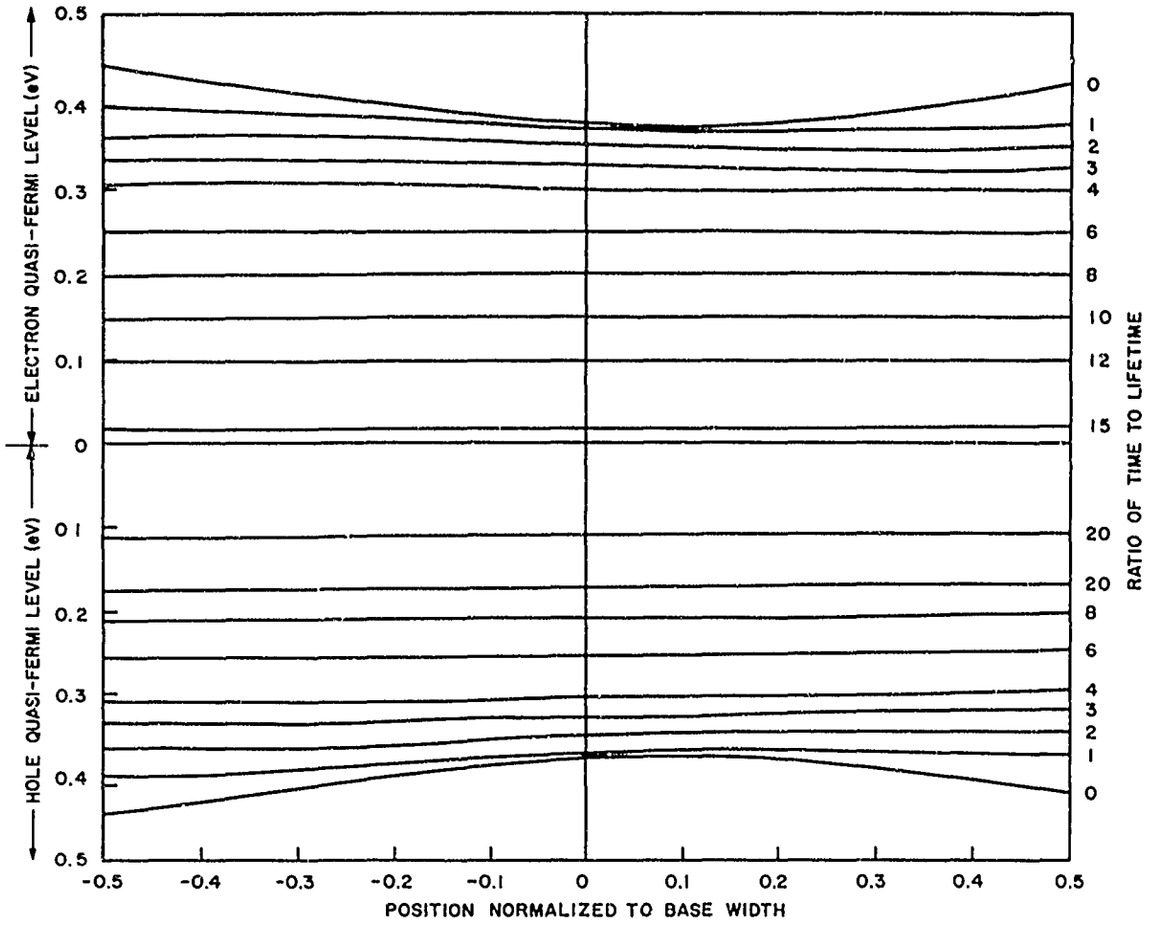

Figure 52. PIN electron and hole quasi-Fermi levels as functions of position and time for W/L = 6.

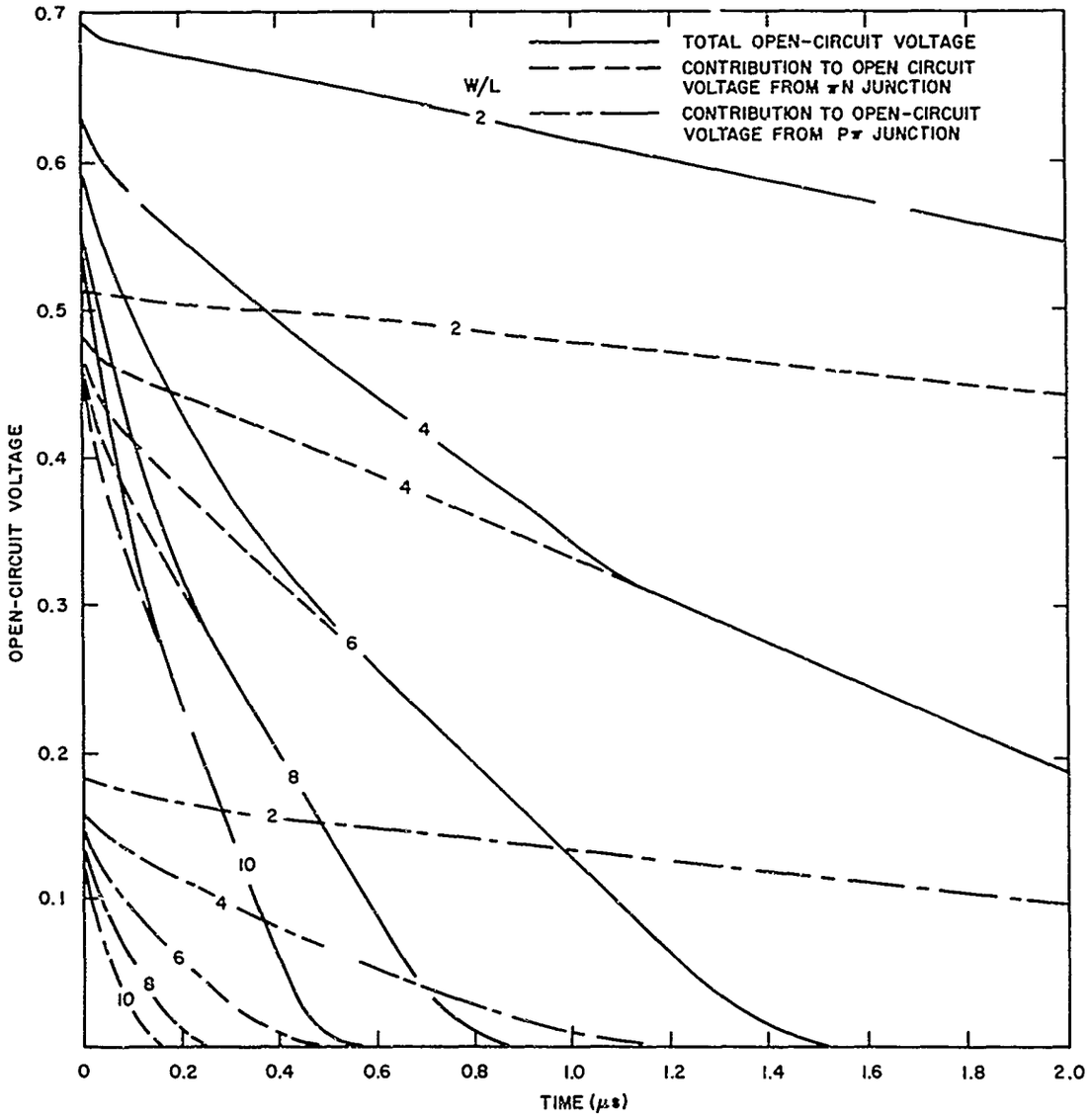

Figure 53. OCFVR for PπN, Pπ, and πN junctions.

2. The initial rate of decay is very rapid for PIN diodes with a large W/L ratio. The voltage-decay curves correspond respectively to W/L of 2, 4, 6, 8, and 10.

These theoretical considerations indicate that the recombination of electrons and holes may be observed over high- to low-injection levels by the above technique, especially when the base region is as near to intrinsic as possible and W/L ratio

is close to unity. By varying the temperature and the initial injection level, it may be also possible to identify other recombination processes, such as Auger and radiative recombinations.

In the future, it would be desirable to include in the analysis such nonlinear properties of the device material as: (1) mobility as a function of defect density and electric field, (2) multilevel trapping and recombination centers with arbitrary energy levels and cross sections, and (3) simulation of neutron radiation effect by a space-charge screened SRH model.

2. Measurements. Measurements of the open-circuit recovery were made using the method described by Wilson.[6] Forward current pulses, 30 mA in amplitude and a few μseconds in length, were supplied by a Rutherford pulse generator through a Schottky barrier diode to the diode under study. The open-circuit voltage was measured with a Tektronix sampling scope. The diodes were usually shunted with a 0.1-megohm resistor. When the dynamic resistance of the diode exceeds 0.1 megohm, open-circuit conditions no longer hold and a rapid exponential decay follows. The instrumental inflection which results has been related mistakenly to bulk recombination levels by several experimenters.[5,7]

At the cessation of the forward current pulse, an instantaneous drop of forward voltage occurs. This voltage step is due to the voltage drop across the central region and depends exponentially on the ratio of the width of the region to its ambipolar diffusion length. The voltage step is also a measure of the density of injected carriers in the central region.

Measurements were made at various temperatures of unirradiated and neutron irradiated (5×10^{12} n/cm^2) PπN silicon diodes with a central region doping of approximately 10^{14}/cm^3 and a central region width of 100μ. Typical results are shown in Figures 54 and 55. The bulk high-level lifetime before irradiation is $\approx$5 μs and it drops to $\approx$0.3 μs after 5×10^{12} n/cm^2. Figure 54 shows an inflection in the recovery curve of the unirradiated sample of $V_0 \cong 0.50$V at 25°C. This inflection occurs as the quasi-Fermi level for holes reaches its equilibrium position at $E_i - 0.25$ eV. Thereafter only the minority carrier density is changing and the slope decreases. More than two orders of magnitude in injection level are covered in the linear parts of these decay curves. Assuming that the high-level slope is given by $\tau_{po} + \tau_{no}$ and the low-level by τ_{no} alone, we conclude that $\tau_{po} << \tau_{no}$. The lower temperature recovery curves show the inflection point moves to $V_0 = 0.62$V at -25°C and to 0.75V at -75°C. These values correspond to the equilibrium Fermi-level position at these temperatures for an impurity concentration of 10^{14} cm^{-3}

Figure 55 shows that after irradiation there is no evidence of an inflection point although the recovery curve still overlaps with high- and low-injection level

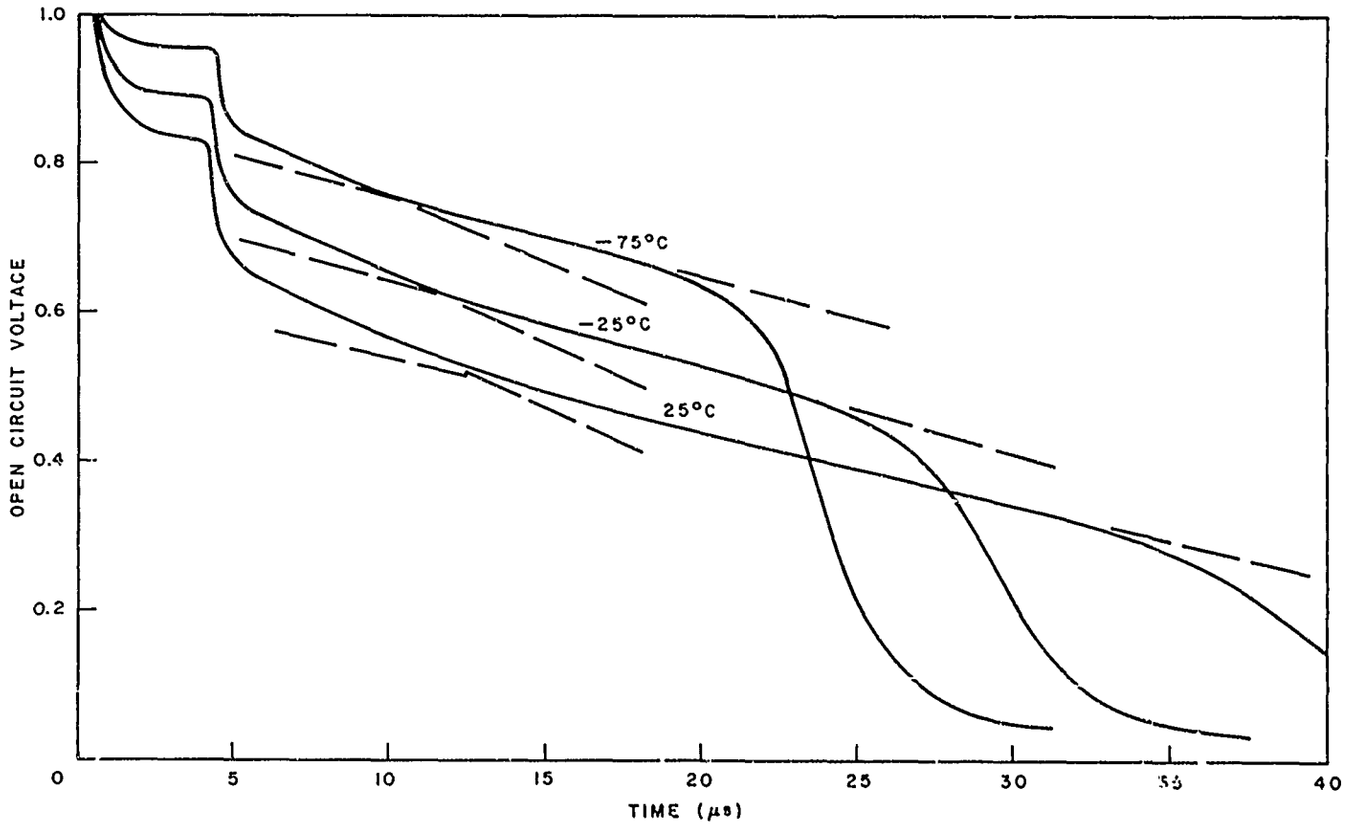

Figure 54. Open-circuit voltage recovery of unirradiated PπN diode for 30 mA pulse.

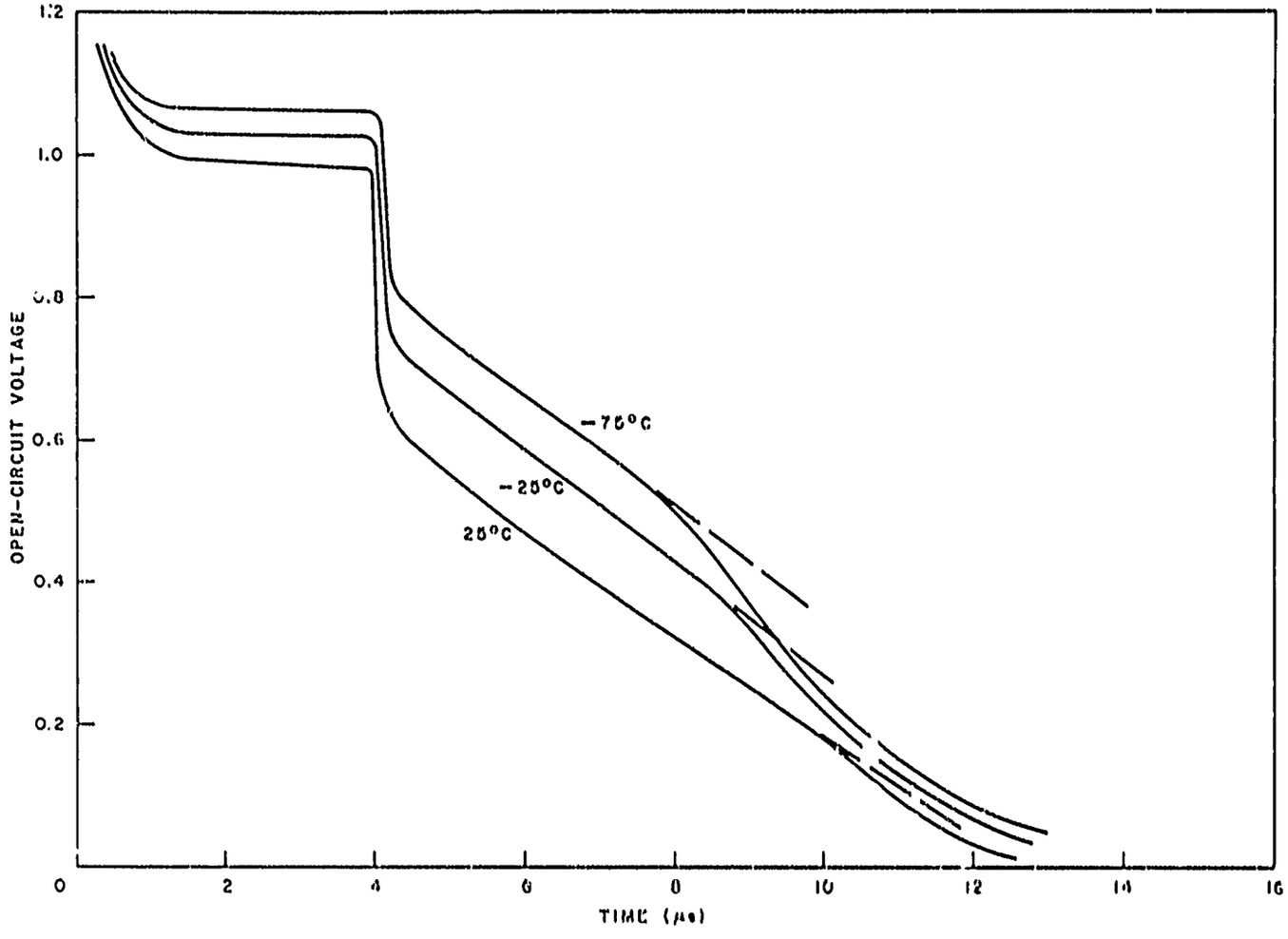

Figure 55. Open-circuit voltage recovery of P#N diode after 5×10^{12} n/cm^2 for 30 mA pulse.

regions. We can explain this result if we assume $\tau_{po} = \tau_{no}$. Then the slope in both regions would be the same. This result might have been expected since lifetime damage constants and carrier removal rates by fast neutrons are roughly equal for n and p silicon. Using typical values for both, we conclude that capture cross sections for both holes and electrons of neutron-induced centers are of the order of 10^{-13} cm^2.

The high-injection-level lifetime is not found to change markedly with temperature. This also is expected since the temperature dependence of τ_h is determined by the temperature dependence of the capture cross section which is small. Low-injection lifetimes were found from reverse current measurements to be roughly an order of magnitude shorter than those determined by the open-circuit recovery technique at high-injection levels.

In the above discussion, we have assumed that the neutron-produced recombination centers are isolated Shockley-Read type defects. If we alternatively suppose that the dominant recombination occurs at clustered defects rather than isolated defects we would be led to expect a very different open-circuit recovery characteristic.

O. L. Curtis et al.[5] have experimentally measured high-injection level recombination in neutron-irradiated bulk-silicon samples and found a pronounced injection-level dependence which they were able to explain using a clustered defect model based on Gossick's assumption[6] that the damaged region becomes intrinsic and is surrounded by a large space-charge region. In this model, the lifetime increases with injection level until the injected carrier concentration is equal to the bulk equilibrium major-carrier concentration. Above this level, the lifetime again decreases. The magnitudes of the lifetime changes in the experiments of Curtis et al. are such that significant curvature in the recovery curve of the irradiated PxN diodes should have been observed.

We observe no such curvature in a wide variety of fast neutron irradiated silicon PXN diodes. The discrepancy may be due to the fact that Curtis et al. used steady state photoconductivity amplitude to determine lifetime. Moreover, their results may depend on trapping rather than recombination effects.

It might be well to point out that a strong injection-level dependence of recombination at clustered damage is expected if one assumes that the quasi-Fermi level of minority carriers is flat across the clustered damage region. On the other hand, if one assumes the clustered region has a very high recombination rate so that in the clustered damage region the minority carrier quasi-Fermi level could not be shifted far from the intrinsic Fermi level, then no strong injection-level dependence of lifetime should be expected.

3. PIN Diode Open-Circuit Recovery After Neutron Bursts. PIN diode OCFVR following exposure to a pulse of fast neutrons also was measured to determine "transient annealing" behavior of the central region lifetime τ_h and the hole mobility μ_p. Lifetime is measured from the slope dV/dt of the diode open-circuit voltage decay following application of forward bias. Diffusion length in the intrinsic region is determined from the voltage step at the forward-bias to open-circuit transition. From the diffusion length and lifetime the mobility was then determined.

To date it has been presumed that the transient annealing changes following neutron bursts are due to lifetime recovery alone. This experiment was intended to show whether or not mobility changes were also of importance.

In these experiments the PIN diode under test was given a succession of brief forward-current pulses at a low-repetition rate to minimize recovery due to current during observation. A Schottky barrier diode in series with the device under test assured rapid current turnoff at the end of each pulse. The tendency of cable capacitance to prolong diode turnoff time was eliminated by driving the sheath of the cable to the diode with an emitter follower.

In order to obtain repeated information on the OCFVR characteristic, the scope display of the characteristic was intensified at three different times: (1) at a time shortly before forward current is interrupted, (2) immediately after forward current is interrupted and (3) several μseconds later. The voltage step is determined by the vertical displacement of intensified spots 1 and 2, the slope from the spacing of spots 2 and 3, and their known time interval. Using very slow sweep speeds the intensified spots become virtually solid lines showing the time dependence of transient annealing. These measurements were made at several temperatures using the variable temperature mount described in a preceding report.[10]

The OCFVR decay for 295°K and 173°K before, immediately after, and five minutes following the burst are shown in Figure 56. The precipitous change in slope following the neutron burst ($\approx 10^{13}$ n/cm^2) is caused by the order of magnitude reduction in lifetime (from a few μseconds to tenths of μseconds). An abrupt increase also occurs in the voltage step at the termination of the forward pulse. Subsequently both the step and slope slowly decrease.

The calculated lifetime and mobility changes with time from these results are shown in Figure 57. Lifetime increases by a factor of roughly 2 at 173°K, 2.8 at 295°K, and 1.5 at 373°K. Following a burst, mobility changes were small at 173°K and 373°K and decreased by roughly 10 percent at 295°K. The mobility values at all three temperatures are in good agreement with expected values for a doping level of 10^{14} N_A/cm^3. Thus mobility changes following the burst are small.

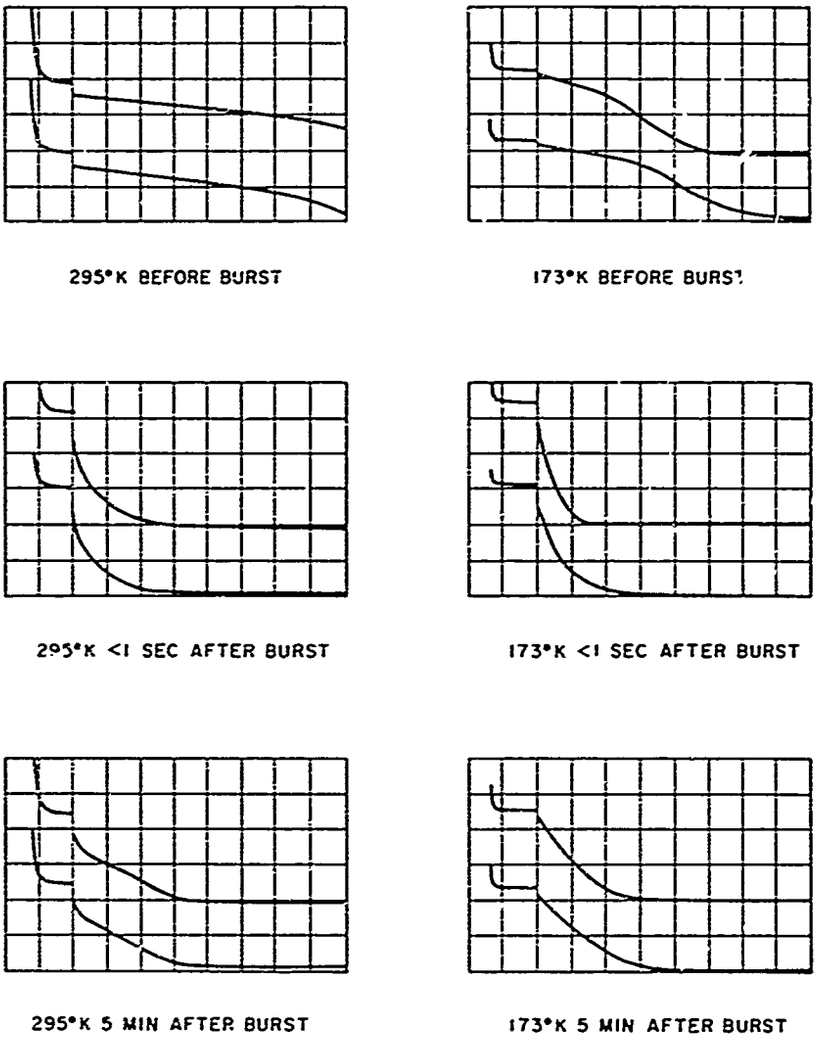

Figure 56. OCFVR at 295°K and 173°K for 10 mA pulse. Vertical scale — 0.5 v/division. Horizontal scale — 2 μs/division. Characteristics of two devices are shown at each temperature.

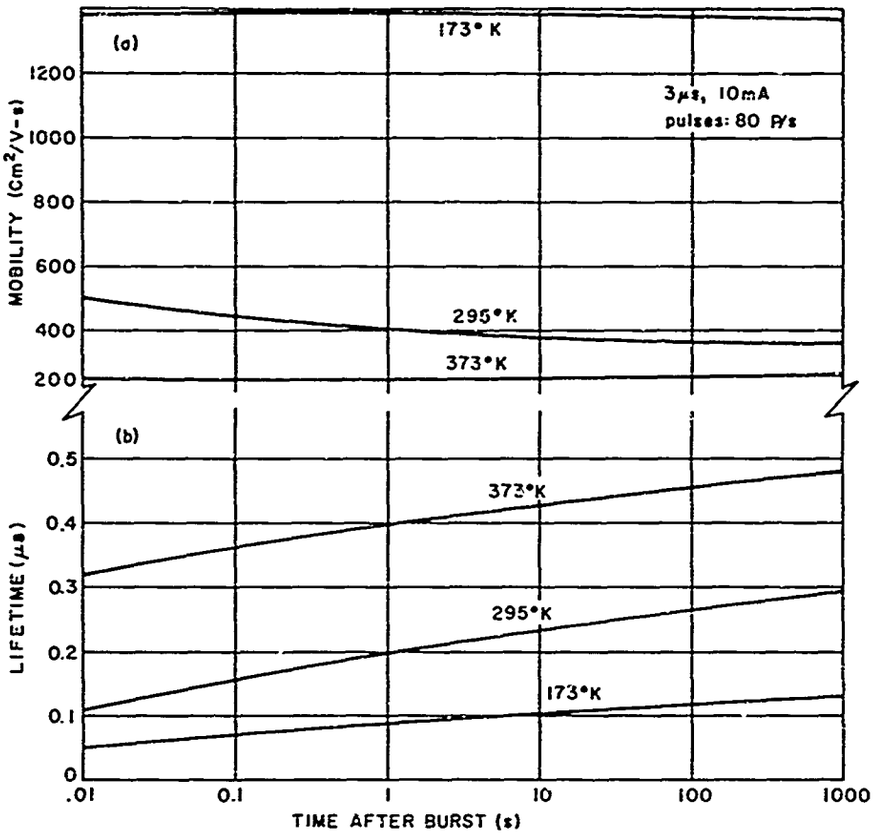

Figure 57. Recovery in PIN diodes after a burst of fast neutrons (10^{13} n/cm^2). (a) Mobility. (b) Lifetime.

Large clustered damage regions might be expected to reduce drastically mobility as well as lifetime. In this experiment, however, no significant mobility changes or recovery of mobility were observed in the neutron irradiated diodes. Therefore, recovery of transistor gain must be concluded to result almost entirely from lifetime changes.

In Figure 57 it should be noted that immediately following the neutron burst the slope of the open-circuit decay is not constant but indicates a decreasing lifetime with increasing injection level. This is in agreement with measurements of O. L. Curtis et al.[8] for the high-injection level behavior. After recovery, however, the slope again is constant. This result suggests that lifetime immediately after a burst of neutrons may be dominated by Gossick-type damage regions but ultimately is controlled either by isolated defects or by clustered damage regions within which it is not possible to change significantly the minority carrier population.

c. Reverse Bias Capacitance Under Neutron Irradiation

1. Introduction. In a preceding report[10] we described transient recovery of the reverse bias junction capacitance of commercial PπN silicon diodes following exposure to a burst of fast neutrons. We observed that the carrier removal rates immediately after the neutron burst were roughly four times as large as the post-recovery rate. We also observed an exponential recovery of the capacitance with a time constant of 325s. A more careful analysis of the data showed an additional exponential component with a time constant of 4s as well. Similar measurements were made at -100°C, and again two exponential decays were resolved, one with a time constant of 8s and the other with a time constant of 0.5s.

In the measurement of reverse bias junction capacitance Sah and Reddi[11] have described the effects of deep traps on the measurement. In effect, if the capacitance measurement is made at very low frequency the trap populations will follow the up and down movement of the quasi-Fermi level produced by the oscillating measuring signal. In this case, the junction capacitance is determined primarily by the shallow inpurity concentration, N_D. At high measurement frequencies the trapped charge does not follow the motion of the quasi-Fermi level and the capacitance drops to a value determined by $N_D - N_t$. If the trap population were suddenly changed in N-type material by exposure to a burst of nuclear radiation, majority carrier traps will equilibriate with a time constant in the space-charge region (n = p = o)

$$\tau_n = \frac{1}{\sigma_n V_n N_c} \exp\left(\frac{E_c - E_t}{kT}\right)$$

where σ_n is the electron capture cross section, V_n is the thermal velocity of electrons, N_c is the density of states in the conduction band, and $E_c - E_t$ is the position of the trap with respect to the conduction band edge. Obviously, if either the temperature or capture cross section is low or if the trap level is far below the band edge, the trap equilibration time will be very long.

Assuming that the capacitance changes, given above, are due to the slow filling of isolated defect traps in the space-charge region, we obtain from the above data two trap levels one at $(E_c - 0.46)$ eV and the other at $(E_c - 0.26)$ eV. The trap cross sections were also estimated from these data and were $\sigma_n \approx 5 \times 10^{-15}$ cm^2 and 2×10^{-16} cm^2 respectively. Thus, very reasonable trap depths and cross sections would account for the recovery of junction capacitance after a burst of neutrons. Rupprecht and Klein,[12] using a pulsed field-effect technique, obtained trap levels in neutron irradiated N type silicon of $(E_c - 0.37)$ eV and $(E_c - 0.15)$ eV with electron cross sections of 2×10^{-18} cm^2 and 1.5×10^{-15} cm^2 respectively.

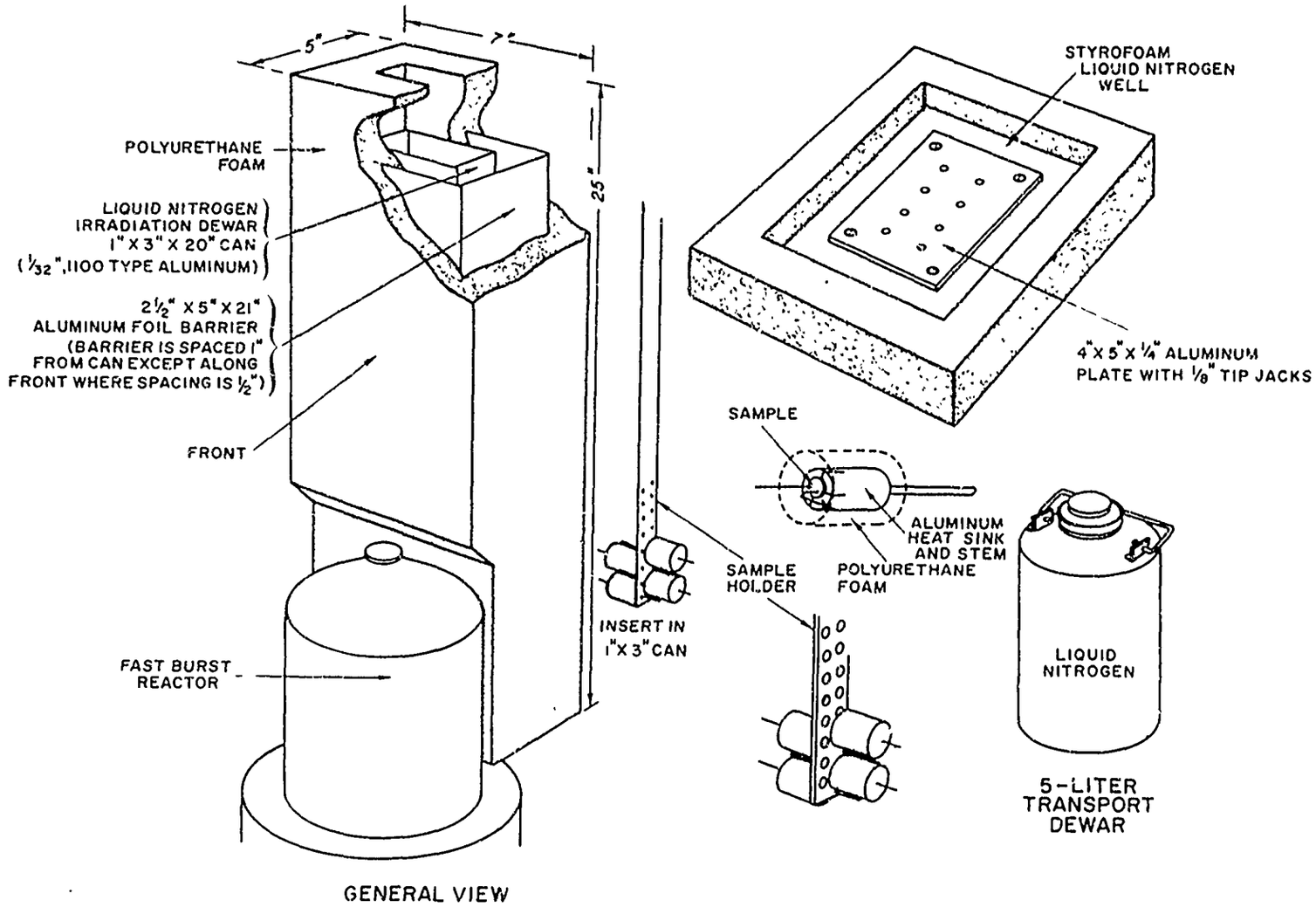

Figure 58. Low-temperature radiation equipment.

From the above results, we expect that at 77°K the recovery of either the deep or shallow trap will be essentially indefinite. However, should the traps be filled by other than the normal generation process, say by forward biasing the diodes and injecting minority carriers, then rapid filling of the traps would take place.

2. Measurements. To verify this result we exposed silicon PπN and PνN diodes with impurity concentrations from 2×10^{14} cm^{-3} to 10^{15} cm^{-3} to fast neutrons at 77°K. The devices were irradiated at the WSFBR and transported back to Bell Telephone Laboratories, Whippany, N. J., for measurements using the low-temperature irradiation equipment shown in Figure 58. Carrier concentrations were determined by reverse bias junction capacitance measurements at 1 MHz. Capacitance measurements were also made as a function of frequency from 1 KHz to 100 MHz to see if any very fast traps were also present. Trap time constants at 77°K were all much slower than 10^{3}s, and at room temperature the time constants were greater than 10^{-5}s so that the 1-MHz measurement frequency was sufficiently high. Following the initial measurements, forward current of 5A/cm^2 was passed through the diodes. In all devices the electrically-active radiation-defect concentration decreased by a factor of roughly 3 after injection. The defect concentrations as functions of neutron fluence deduced from the capacitance measurements before and after forward bias are shown in Figure 59 for bulk impurity concentrations of 10^{14} cm^{-3} donors and 2×10^{14} cm^{-3} acceptors. For bulk impurity concentrations of 10^{15} cm^{-3} donors and 2×10^{15} cm^{-3} acceptors similar results were obtained. However, the carrier removal rates both before and after injection were somewhat smaller. In the absence of forward bias, reverse-bias junction capacity at 77°K for all impurity concentrations showed no change over a two-month period.

Junction capacity also was measured as a function of reverse bias voltage for some of the irradiated diodes. Then the diode was slightly forward biased. The C-V curves, after successively increased levels of forward bias, are shown for a PνN silicon diode in Figure 60. It can be seen that the principal recovery of carrier concentration after low forward bias is at low reverse bias, i.e., close to the metallurgical Pν junction. After increased forward bias, carrier recovery extends further and further away for the metallurgical interface. The abrupt break in the capacitance presumably corresponds to the minority carrier diffusion length in the ν region which in this case increases from roughly 1μ to several μ after the largest forward bias. Similar results were obtained on PπN diodes. Other evidence for marked increase in diffusion length after injection was obtained from the voltage drop across the ν or π region for low forward bias. This voltage drop which increases exponentially with the W/L ratio of the ν or π region decreases abruptly in irradiated diodes following strong forward bias. The diffusion length deduced

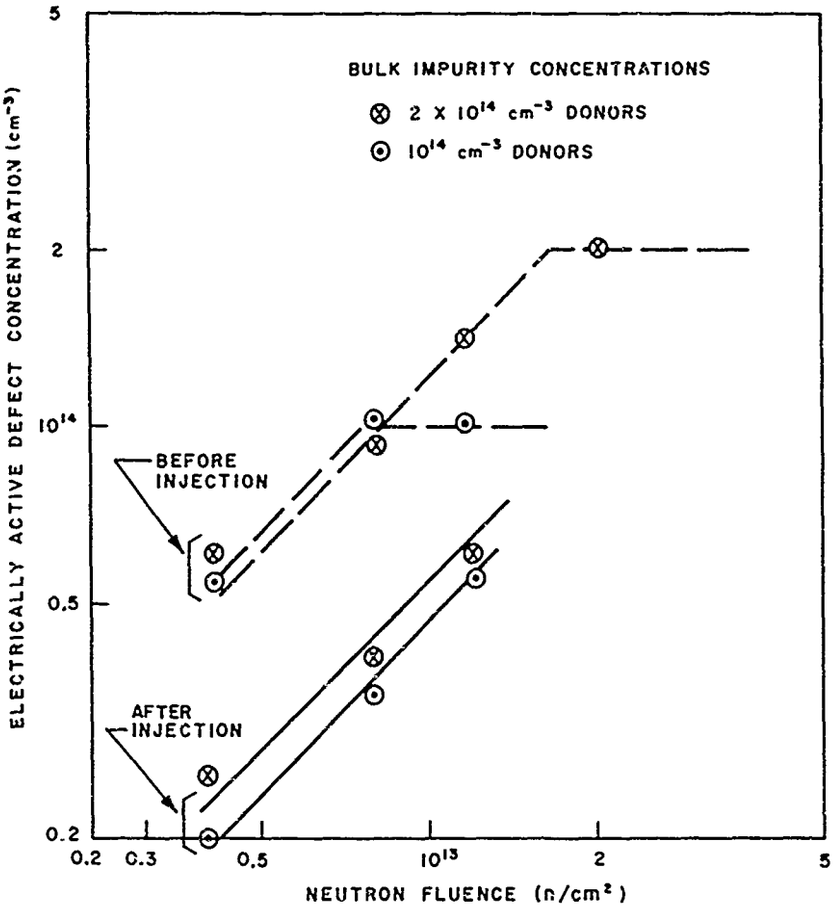

Figure 59. Defect concentration versus neutron fluence at 77 °K.

from this voltage drop has been found to increase fourfold at 77 °K after forward current is passed. This corresponds to a change in lifetime of a factor of 16. These results strongly support the model that both capacitance and lifetime recovery are the result of slow carrier trapping by radiation produced defects.

3. Discussion. The results obtained on capacitance recovery are in agreement with the qualitative model that was previously suggested for transient annealing effects,[10] i.e., transient recovery is due to slow charge equilibration of traps located within the clustered damage regions. The charge on these traps is believed to control the recombination kinetics of other defects also located in the clustered damage region. The preceding experiments suggest a slight modification of the model as follows: We assume as in Gossick's model[9] that, after a disordered region is created, majority carriers are trapped within this disordered region and these are initially compensated by ionized impurity atoms outside the disordered region. During injection, however, we suggest that minority carriers become

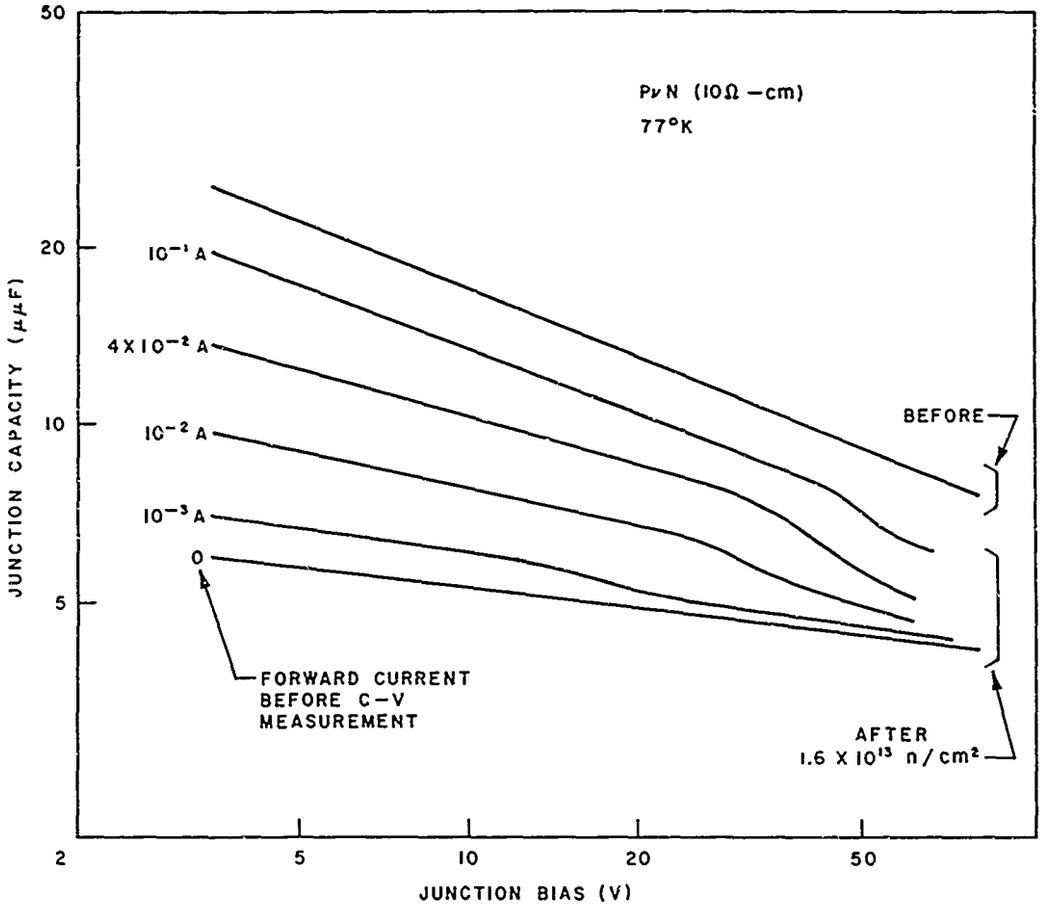

Figure 60. C-V characteristics of neutron irradiated PνN diode before and after minority carrier injection.

trapped at the perimeter of the disordered region and substitute their charge for that of the ionized impurity atoms. Thus, after injection of minority carriers, the disordered region is largely selfscreened; that is, the trapped majority carriers are entirely compensated by trapped minority carriers also within the disordered region. In other words, upon injection, the potential hill around the disordered region gradually shrinks in diameter to the size of the disordered region alone. During shrinkage, the ionized impurity-atom and free-carrier concentrations gradually recover. In addition, the lifetime and mobility of minority carriers should increase, while the trap release time of minority carriers should decrease. Any of these effects would give rise to an increase in diffusion length.

In this picture, the trapping process in the absence of injection is trapping of minority carriers at the edge of disordered damage space-charge region. The trapped minority carriers would free majority carriers and the capacitance would recover. Thus the trap parameters given previously for majority carriers,

assuming an isolated defect model, could also apply to the minority carriers (with $E_c - E_t - E_t - E_v$) assuming the clustered damage model.

To account for the subsequent failure to observe effects of slow trapping after the initial recovery, it is necessary to require that the recombination defect concentrations toward the center of the cluster are so large that significant displacements of the electron and hole quasi-Fermi levels from the intrinsic level are not possible. As we have pointed out previously, this result suggests that clustered damage should behave very much like an internal surface having large surface recombination velocity. A further consequence of this model is that strong injection-level dependence of the lifetime in clustered damaged material would not be observed (as we have reported) since it is impossible to significantly alter the quasi-Fermi levels within the clustered damage regions.

d. Summary

Open-circuit forward-voltage recovery (OCFVR) measurements were made on neutron-irradiated PπN and PνN silicon diodes. No large dependence of lifetime on injection level was observed in contrast to results obtained on bulk semiconductor samples. In the absence of injection-level dependence, these studies are not useful in characterizing the recombination mechanism. OCFVR measurements made on diodes exposed to bursts of fast neutrons show that diffusion length recovery after fast neutron irradiation is solely due to lifetime recovery and does not involve changes in carrier mobility.

C-V measurements on silicon diodes exposed to neutrons at 77 °K show carrier removal rates several times greater than room-temperature irradiations. Following minority carrier injection, the carrier removal rates are reduced to the room-temperature values. The capacitance recovery, following injection, appears to be due to minority carrier trapping at the edges of clustered damage regions. Recovery effects in depleted junction devices, such as junction field-effect transistors, are expected to be much larger than in strongly injecting devices.

9. RADIATION EFFECTS IN SILICON AVALANCHE DIODES

a. Introduction

Silicon junction diodes operating in the reverse avalanche mode exhibit at microwave frequencies a negative resistance which has been employed to make oscillators, amplifiers, etc. When a PN junction is operated in breakdown, the junction space-charge region subdivides into a narrow avalanche region and an adjoining avalanche-free drift region. A negative resistance occurs at microwave frequencies as a consequence of phase shifts between the voltage and current produced in both the avalanching region and in the adjoining saturated-carrier-velocity drift region.

A large number of silicon, germanium, and gallium arsenide junction structures have been shown to exhibit this negative resistance. They have been called by various authors avalanche diodes, IMPATT (impact avalanche and transit time) diodes, and Read diodes. These bulk negative devices have many potential applications particularly in the radar field. Present oscillator efficiencies are of the order of 5 percent. A maximum theoretical efficiency of 30 percent has been predicted. Power outputs at X-band of several watts of power have been achieved.

Radiation effects in these devices are of interest in many applications. Since carrier recombination and trap release times, even in severely irradiated semiconductors, are long compared to the period of oscillation in most avalanche diodes, radiation effects on trapping and recombination times are not expected to degrade the device behavior at microwave frequencies as they would the performance of normal bi-polar devices. Furthermore, the effects of damage centers on the avalanche process or on the scattering limited velocity of holes and electrons are expected to be minor because the associated mean-free paths are small compared to the distances between radiation produced defects. On the other hand, carrier removal effects due to radiation and consequent changes in the width and field profile of the junction space-charge region could alter the device behavior.

In this study, we subjected "nearly-abrupt" epitaxial P^+NN^+, X-band, silicon avalanche diodes which have been described by Misawa[13] to bombardment by fast neutrons with integrated fluxes up to 10^{16} n/cm^2. The structures studied have a 7-μm-thick epitaxial N layer with 10^{16} cm^{-3} donors deposited on a heavily doped N^+-type substrate. Into this epitaxial layer a 3-μm-thick P region was diffused. At breakdown the total junction space-charge width of this structure is 3 μm and the avalanche region extends over approximately one third of this width. These particular structures were chosen because they exhibit fairly high power output and efficiency at low operating current densities. Low current densities are necessary to minimize the temperature of the devices and the possibility of annealing of radiation damage during the microwave testing.

Microwave measurements were made of the oscillation threshold, power output, frequency, FM noise, and AM noise to determine the effects of neutrons on the high-frequency negative resistance behavior. The changes in RF parameters were correlated with changes produced in the field profile of the depletion region by radiation defects.

In addition to the RF measurements, extensive dc measurements were made of forward, reverse, and breakdown V-I characteristics. The dc measurements were made for two reasons: (1) to correlate dc changes with changes in the RF parameters and (2) to evaluate the behavior of the narrow-base epitaxial devices as radiation-hardened diodes.

b. Theory

Read,[14] in 1958, suggested that microwave negative resistance could be obtained in a PN junction biased to reverse breakdown. His structure used an abrupt P⁺N junction to produce a thin avalanche region of width ℓ_a. Adjoining the N region was a wide intrinsic region of width ℓ_d. In this region the avalanche injected carriers would drift at scattering limited velocity v_d. In the avalanche region, it is the rate of change of the avalanche current rather than current itself which depends on the field. Therefore, a change in current does not follow instantaneously a change in field but requires a definite time to develop. The resulting carrier current lags behind the field and hence the voltage across the region. Thus, the avalanche region behaves like an inductance at high frequencies. The phase delay at microwave frequencies can approach 90 degrees.

Additional phase delay is associated with the transit time of carriers across the drift region because of a finite carrier velocity, which is of the order of 10^7 cm/s for electrons. Thus, by making the drift region of suitable length, the current will be delayed 180 degrees behind the voltage and microwave power gain can be realized.

In 1965, operating avalanche diodes of the Read type were demonstrated as well as avalanche diodes of very different structures.[15] In general, all of the negative resistant structures resemble the Read device in having an avalanche region and a drift region. However, in many of the structures the demarcation between these two regions is not evident. In addition to these two regions there is usually present a third region arising from inactive bulk semiconductor material which adds undesirable parasitic series resistance R_s. It has been shown by a number of authors that the parameters of all three regions have profound effects on the operation of the avalanche diode. We will use the analysis of Gilden and Hines[15] to illustrate their relative importance. Gilden and Hines show that the total impedance of a Read device of cross-sectional area A has the following form provided the transit time in the drift region, ℓ_d/v_d, is small compared to the period of oscillation:

$$Z = R_s + \frac{\ell_d^2}{2\epsilon v_d A} \cdot \frac{1}{1 - (\omega/\omega_c)^2} - \frac{1}{j\omega C} \cdot \frac{1}{1 - (\omega_c/\omega)^2} \qquad (1)$$

The first term in this expression arises from the parasitic series resistance. The second term is the active resistance which is negative for $\omega > \omega_c$ and is positive for $\omega < \omega_c$. It approaches a finite value at zero frequency, a quantity which is called the space-charge resistance. The third term is reactive and corresponds to a parallel resonant circuit which includes the diode capacitance and a shunt inductor.

C is the capacitance of the total depletion zone and ϵ is the dielectric constant. In this expression ω is the angular frequency of operation and ω_c is the critical resonance frequency of the parallel resonant circuit formed by the equivalent inductance of the avalanche region and its parallel depletion capacitance. It is given by the expression

$$\omega_c = \sqrt{\frac{2Jv_d}{\epsilon} d\alpha/d\epsilon} \qquad (2)$$

According to the Gilden and Hines analysis, the operating frequency must exceed the critical frequency in order to obtain negative resistance. In non-Read type structures with diffuse avalanche regions, this criterion is not necessary. The critical frequency varies significantly with the details of the structure because of its dependence upon the derivative of the ionization coefficient. For the nearly-abrupt structure used in this study (which resembles the Read structure) the variation of ω_c with current density is shown in Figure 61. Although ω_c does not depend explicitly on the width of the avalanche region l_2, analysis has shown that an increase in l_2 will reduce ω_c. Note that the variation of ω_c with current density permits the frequency of operation of the device to be electronically tuned. The nearly-abrupt structures exhibit useful negative resistance at X-band frequencies with current densities of the order of 500 A/cm^2.

From Equation (1) it should be evident that the space-charge resistance which is positive at zero frequencies and negative for $\omega > \omega_c$ increases with the length of the drift region. Thus, it is desirable that the transit time across the drift region should be comparable to the period of oscillation. This result means that the Gilden and Hines expression (Equation 1) is only approximate. The optimal length of the drift region is an open question at present since it depends critically on field profile. In the nearly-abrupt structures examined in this study the ratio of drift time to the period is roughly 1, which was believed to be close to optimum. We will show later that the changes in field profile after neutron radiation may have produced a more nearly optimum structure.

From Equation (1) it is also evident that a minimum parasitic resistance R_s is desirable. Hence, the amount of epitaxial layer not penetrated by the space-charge region (the "unswept" epitaxial region) should be a minimum. The importance of the parasitic resistance has been demonstrated for germanium avalanche diodes by Koval and Gibbons[17] who found that 3 μm of unswept material could reduce the efficiency by a factor of 10.

The reactive component in Equation (1) increases with frequency and becomes strongly inductive just below the critical frequency. Above the critical frequency, the diode becomes capacitive.

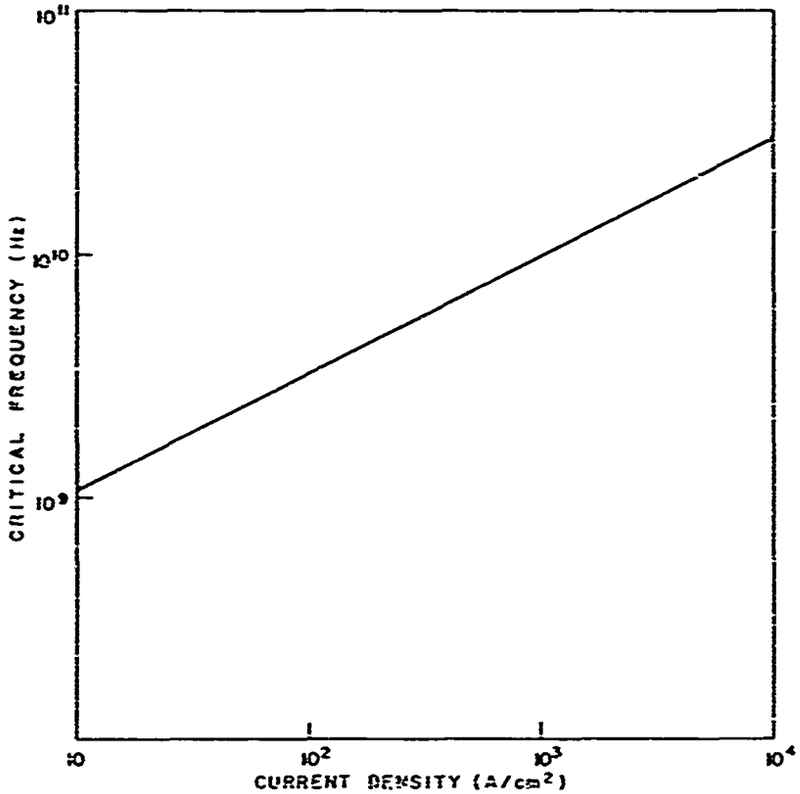

Figure 61. Critical frequency versus current density for nearly-abrupt P^+NN^+ silicon diode for $N_d = 10^{16}\ cm^{-3}$

The avalanche diode is quite similar to a klystron in its operation since they both depend on transit-time phase shifts. High Q cavities are generally employed with both devices in order to reduce the noise spectrum associated with their respective mechanisms. A high Q cavity may be undesirable, however, if one wants to take advantage of the electronic tunability of the avalanche diode. As an oscillator, the avalanche diode is normally operated above the critical frequency so as to resonate with the series inductance of a high Q cavity operated below its resonant frequency. The microwave output can be obtained provided the negative active resistance of the avalanche diode exceeds the sum of the external cavity series resistance, the load resistance, and the parasitic resistance.

Avalanche diodes have been made which operate at frequencies from less than 1 GHz to more than 100 GHz. As the frequency of operation increases, the available power from an avalanche diode decreases since, at higher frequency, the depletion region thickness is reduced as $1/\omega$. This depletion width reduction decreases the

permitted applied voltage: the available power from such a device is in turn reduced with increasing frequency as $1/\omega^2$.

c. Effects of Radiation on Avalanche Diodes

Transit times across the junction space-charge regions of the avalanche diodes are less than 10^{-10} s. In heavily irradiated semiconductors, recombination or trap release times are generally greater than 10^{-10} s. Thus, during one period of oscillation, the contributions of recombination or trapping would not be expected to have any significant bearing on the transit-time negative resistance of the avalanche diode. Large numbers of generation centers in the space-charge region will reduce the field required for breakdown and also will reduce the statistical fluctuations in the avalanche process. Since noise in the avalanche diode arises primarily from such statistical fluctuations, radiation damage might be expected to reduce the noise figure.

Radiation damage centers have been shown to affect the mobility of carriers in a semiconductor; however, little is known about the effect of damage centers on the scattering limited velocity or upon the avalanche process. In either case, the effects of radiation are expected to be small because the mean-free paths involved in either the avalanche or scattering-limited-velocity process are of the order of 100Å. The maximum radiation fluences employed in this study were 10^{16} n/cm^2 and at this dose the distance between scattering centers is of the order of 300Å. Hence, the effect on either of these processes should be small.

Radiation damage centers can affect the field profile in the avalanche diode by compensation of the bulk impurity doping. As the majority carrier concentration decreases, the junction space-charge region widens. Consequent changes in the critical frequency ω_c, the space-charge resistance R_{sc}, and the total depletion capacitance C will result. However, the effects of changes in these parameters on the microwave performance of the avalanche diode will depend critically on the particular device structure.

d. Measurements

1. Devices. The devices studied were silicon avalanche diodes with nearly-abrupt junctions which have been described by Misawa.[13] The junction is formed by diffusing boron 3-μm deep and a surface concentration of 10^{18} cm^{-3} into a uniformly doped n-type epitaxial layer with a doping of 10^{16} cm^{-3} and a thickness from the junction to the substrate of 4.5 μm. The diameter of the diodes is approximately 100 μm. The wafer is mounted upside down for good thermal contact to a copper stud and inserted in a microwave pill package. Ten devices supplied by B. C. De Loach, Jr., of Bell Telephone Laboratories. Murray Hill, N. J., were studied.

2. DC Measurements. DC measurements of forward and reverse I-V characteristics were made with a North Hills CS-111 constant current source and a

digital voltmeter. Lifetime measurements were estimated using a B-Line Stored Charge meter. In addition to the dc measurement of avalanche breakdown characteristics, a pulse measurement of the incremental avalanche resistance was made using the circuit shown in Figure 62. The diode is reverse biased into the breakdown region and a 50-ns wide pulse is applied. The incremental voltage and current are read with a sampling oscilloscope. Junction capacitance measurements were made as a function of reverse bias with a Boonton Electronics model 75H bridge operating at a 1 MHz. Measurements were also made as a function of frequency. The variable frequency measurements showed that the 1-MHz measurements were suitable for determining electrically-active defect concentrations and their influence on the field profile in the space-charge region.

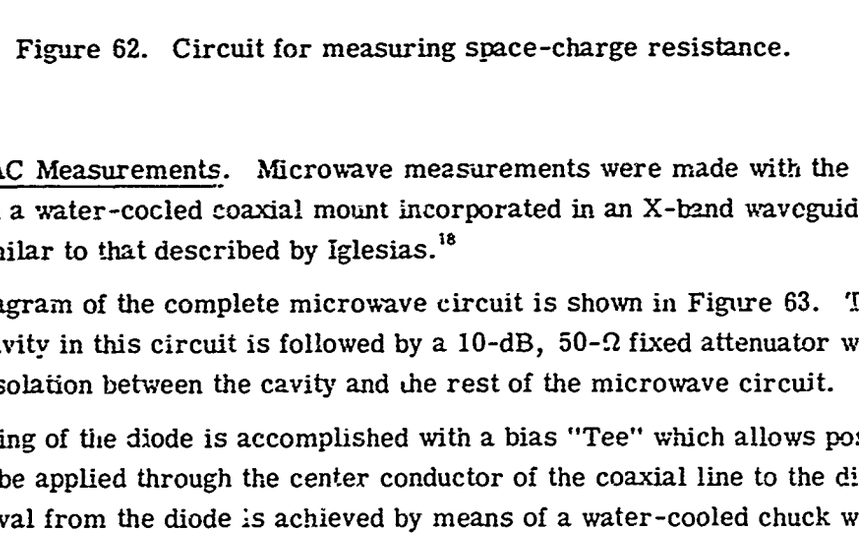

Figure 62. Circuit for measuring space-charge resistance.

3. AC Measurements. Microwave measurements were made with the diode mounted in a water-cocled coaxial mount incorporated in an X-band waveguide test circuit similar to that described by Iglesias.[18]

A diagram of the complete microwave circuit is shown in Figure 63. The diode test cavity in this circuit is followed by a 10-dB, 50-Ω fixed attenuator which provides isolation between the cavity and the rest of the microwave circuit.

Biasing of the diode is accomplished with a bias "Tee" which allows positive dc bias to be applied through the center conductor of the coaxial line to the diode. Heat removal from the diode is achieved by means of a water-cooled chuck which provides a high-pressure metal-to-metal contact with the diode.

The output of the bias "Tee" is connected to a coax-to-waveguide transition. Further isolation is obtained by means of a 20-dB ferrite waveguide isolator. A 20-dB directional coupler is used to sample a portion of the main power. The

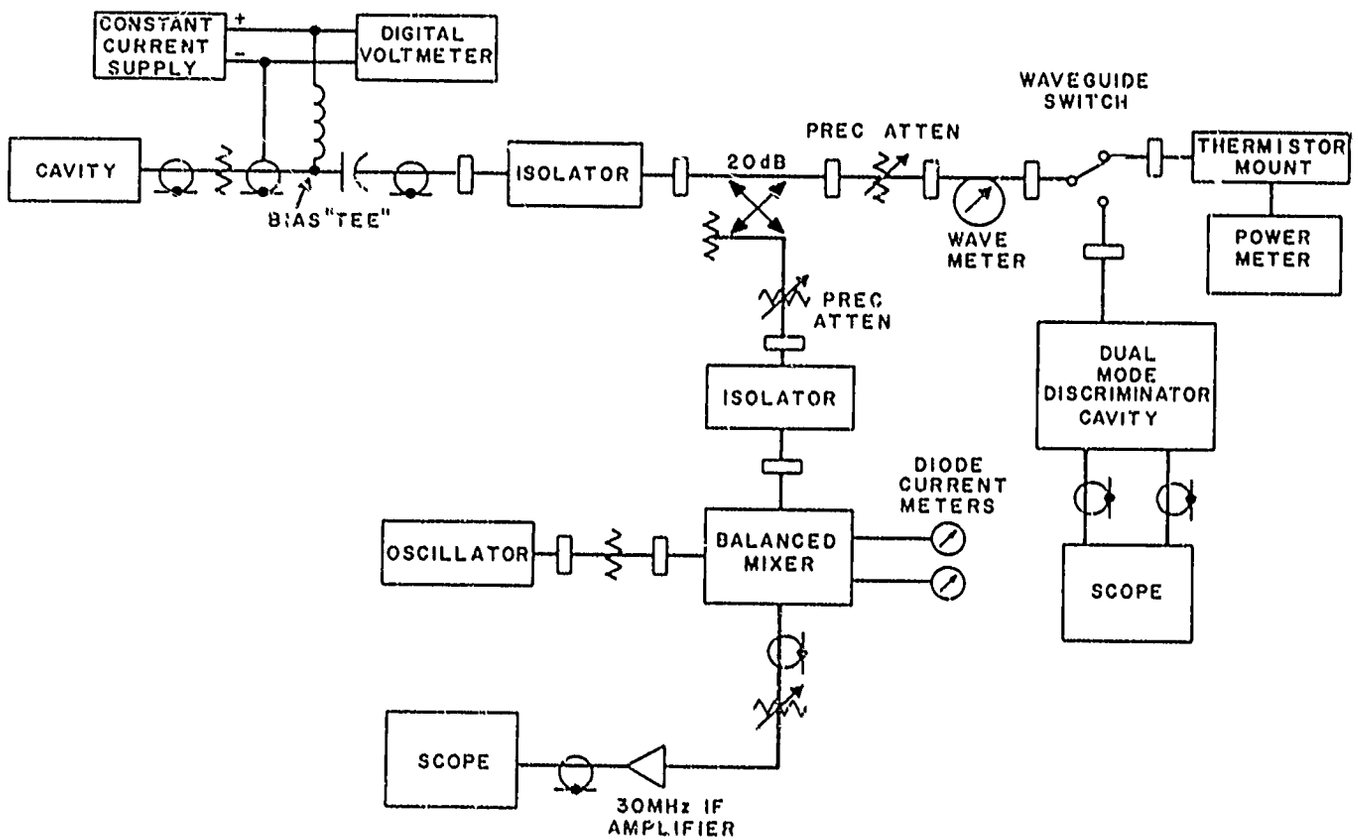

Figure 63. Microwave test circuit.

sampled power is applied to a balanced mixer while the main power is fed through a precision attenuator to an absorption type wavemeter and then to a waveguide switch. One arm of the waveguide switch is connected to a thermistor power head while the other arm is connected to a dual-mode discriminator cavity.

4. Measurement Procedure

(a) DC Bias and Cooling. All measurement of RF power level, frequency, and AM and FM noise was made at a bias of 50 mA, well below the burnout current of about 110 mA. The current density at 50 mA is roughly 500 A/cm^2. Since the junction temperature was found to increase at a rate of about 15 °C per watt of applied bias power, the junction temperature could be maintained at about 80°C based on a cooling water temperature of 20°C. The bias voltage was measured using a digital voltmeter. Since the fixed 10-dB attenuator had a series resistance of 120Ω, 6V had to be subtracted from the voltmeter reading.

(b) Cavity Tuning. Before microwave measurements are made, the cavity must be tuned for maximum power output. Tuning of the cavity is achieved by means of three metallic tuning sleeves placed within the cavity. The length of these tuning sleeves is $\lambda/8$ at 10 GHz. The first sleeve is brought near the diode which effectively matches the reactance component of the diode. With this arrangement, a small power level will be read on the power meter. Fine tuning for maximum power is then achieved by moving the remaining two sleeves, with only slight readjustment of the first sleeve. Spacing of the sleeves should be approximately $\lambda/2$ or about 0.6 in. The movement of the sleeves is done through an access slot along the length of the cavity.

(c) Measurement of Threshold Current. Measurement of threshold current, the minimum avalanche current at which the diode will oscillate, is made by reducing the bias current in small steps until oscillation stops. Readjusting the tuning sleeves at the lower current level will again bring the diode into oscillation. The current level is then further reduced, and the tuning adjusted until the diode no longer oscillates. At the lower current settings the precision attenuator is set to zero and the power meter is set to its lowest power range (-20 dBm setting).

(d) RF Power and Frequency Measurement. Measurement of RF power level was made using a Hewlett-Packard model 431B power meter with a model X486a thermistor mount. The power level is determined by first setting the power-meter range switch to the 0-dBm position. The precision attenuator is then adjusted to give full-scale deflection on the power meter. The power output in dBm from the diode cavity may then be determined by adding 10 dB (the value of the fixed coaxial attenuator) to the reading of the precision attenuator.

Measurement of RF frequency was made using a Hewlett-Packard model X532B absorption-type wavemeter. The RF frequency is read directly from the scale on the wavemeter. This point may be seen by a dip in the power-meter reading.

The oscillation frequency and the FM noise discussed in the next paragraph were found to be primarily controlled by the tuning and Q of the coaxial cavity rather than by characteristics of the avalanche diode. They were monitored during this experiment to determine if any sudden frequency or noise shifts might occur due to radiation. No dramatic changes of consequence were observed during the study.

(e) FM-Noise and AM-Noise Measurements. FM-noise measurements were made using a dual-mode discriminator cavity. In the discriminator cavity, two right-angle modes tuned to slightly different frequencies are generated, the center frequency being tunable from 9 GHz to 10 GHz continuously. The detected signals from the two modes are applied to the inputs of a Tektronix — Type D differential plug-in unit. The peak-to-peak FM noise voltage as a function of frequency can then be read directly from the oscilloscope display. The measurement is only intended to show relative changes in the FM noise level.

Measurement of AM noise was made using heterodyne detection. In this method, a portion of the main power is sampled through a 20-dB directional coupler and applied to a LEL model XCH low-noise mixer circuit. Local oscillator power for the mixer is provided from a LFE model 814A ultrastable oscillator. The power from the local oscillator is adjusted to give 0.5-mA current from the diodes in the mixer circuit while the frequency is adjusted to be 30 MHz above the microwave frequency. The 30-MHz signal from the mixer is attenuated by a 40-dB attenuator and then applied to the input of a LEL IF amplifier. A negative 3-V bias is applied to the amplifier to reduce any noise generated. The dc-output voltage from the IF amplifier is adjusted to 4V. The peak-to-peak noise voltage is read from the scope display.

5. Irradiations. The diodes were exposed to fast neutrons at the WSFBR up to a total fluence of 10^{15} n/cm^2 (E > 10 keV). The reactor was operated in a steady-state mode. Additional exposures with total fluence up to 10^{16} n/cm^2 (E > 10 keV) were made at the Pennsylvania State University TRIGA reactor also operated in the steady-state mode. In the latter radiations, the samples were wrapped in 0.020-in. Cd foil to reduce the thermal neutron fluence. Neutron fluences were measured with sulfur foil dosimeters and are accurate to within ±20 percent.

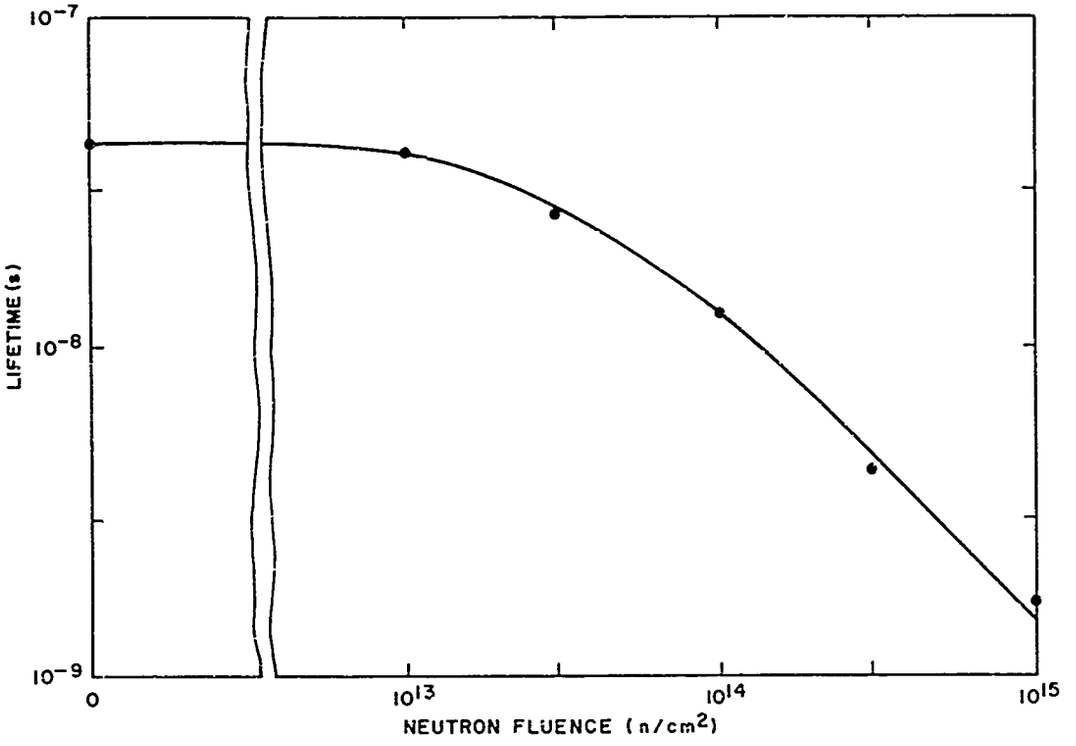

Figure 64. Lifetime versus neutron fluence for I_f = 10 mA.

e. Experimental Results

1. DC Measurements

(a) Lifetime. Minority carrier lifetime in the epitaxial layer was obtained from stored charge measurements as a function of neutron fluence. The average lifetime up to an integrated fluence of 10^{15} n/cm^2 is shown in Figure 64. At higher fluences, the stored charge measurement is subject to significant error and was not used to characterize lifetime. The results shown can be fitted with an expression of the form $1/\tau = 1/\tau_o + K\phi$ with a lifetime damage constant $K = 0.7 \times 10^{-6}$ cm^2/n-s. This value for the damage constant is quite similar to that obtained by other investigators on silicon diodes.

Lifetime measurements were repeated after a complete set of dc and ac measurements were made to estimate the amount of annealing which took place. In no case did more than 10 percent of the damage anneal during the subsequent measurements.

(b) Reverse DC Measurements. Reverse V-I measurements below the breakdown voltage were found not to be relevant in this study because the reverse

current was dominated by a surface leakage and was relatively insensitive to radiation level.

Reverse saturation current (I_s) was estimated by extrapolation of the forward V-I characteristic to zero bias. I_s was found to increase roughly linearly with neutron fluence up to 10^{15} n/cm^2. Above this fluence there was a more rapid increase. The cause of this rapid increase will be discussed further in the next paragraph.

(c) Forward DC Measurements The forward characteristics of the initial sample lot of ten fell into two groups: one having a forward series resistance of the order of 1Ω, the other having a series resistance of the order of 10Ω. The series resistance of the first group agrees with that calculated for the unswept epitaxial layer of the avalanche diodes. The large series resistance of the second group is apparently due to contact resistance between the titanium-gold contact and the boron diffused P-layer. The high-resistance group has a low-surface concentration of boron diffusant while the low-resistance group has a high-surface concentration. The high-series resistance in the one group is shunted by a large parallel capacitance so that it does not affect the electrical measurements of either a pulse or high-frequency nature, but it does seriously degrade the forward characteristics in the dc measurements. Since the forward V-I behavior was masked in the case of the one group by the series resistance, in the following discussion, the forward characteristics discussed will be those of the low-resistance group only.

The decrease in lifetime under radiation causes the forward I-V characteristic to shift toward a lower voltage as a result of the increase in the saturation current. Figure 65 shows the average forward voltage at forward currents of 0.01, 1, and 100 mA. At low-forward currents, the forward voltage decreased linearly as the log of neutron fluence increases up to an integrated fluence of 2×10^{15} n/cm^2. Above this level, the forward voltage decreases abruptly. At 1 mA, the linear decrease in forward voltage with the log of neutron fluence is observed up to $\sim 4 \times 10^{15}$ n/cm^2, but above this level there is a marked increase in the forward voltage. At 100 mA, there is a gradual decline in the forward voltage with a sudden increase for fluence above 4×10^{15} n/cm^2.

At both 1 mA and 100 mA, there is a considerable spread in the measured values for the voltage as indicated in the figure. A better idea of what is occurring is shown in Figure 66 which gives forward V-I characteristics with neutron fluence as a parameter. Up to forward currents of 10 mA, the log I versus V characteristic is a straight line with a slope qV/(nkT) characterized by an n value of 1.5. Above 10 mA, series resistance causes the characteristic to deviate from a straight line. At neutron fluences up to 10^{15} n/cm^2, the characteristic shifts to lower forward voltages with the slope remaining constant and with an increase in the forward series resistance. In the neighborhood of 2×10^{15} n/cm^2, a sharp increase in the

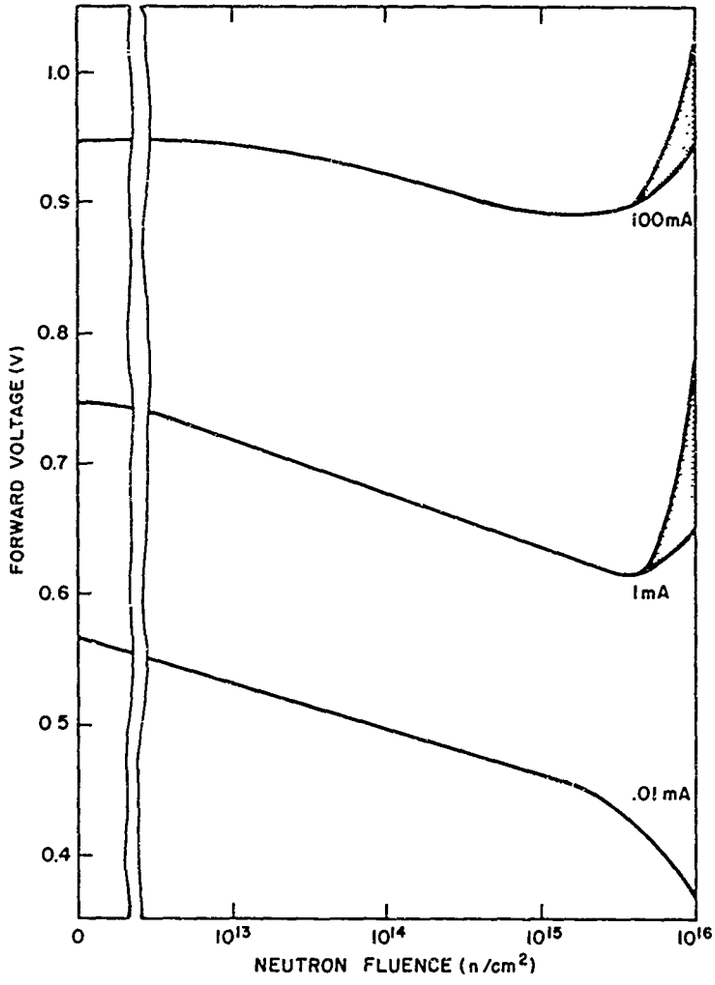

Figure 65. Forward voltage changes with neutron fluence.

forward current at low forward voltages occurs. However, at higher forward currents, the characteristic is displaced to higher forward voltages, again with the same slope. The magnitude of the displacement varies for individual devices from less than 0.1V to more than 0.2V.

We believe that the changes in the forward characteristic are due to the formation of a very narrow intrinsic region in the neighborhood of the metallurgical PN junction. Compensation of the chemical doping by radiation-produced deep traps will tend to produce such a region. At low currents where the generation current by recombination centers in the depletion region dominates the characteristic, the increase in the volume of the generating region by formation of an I layer

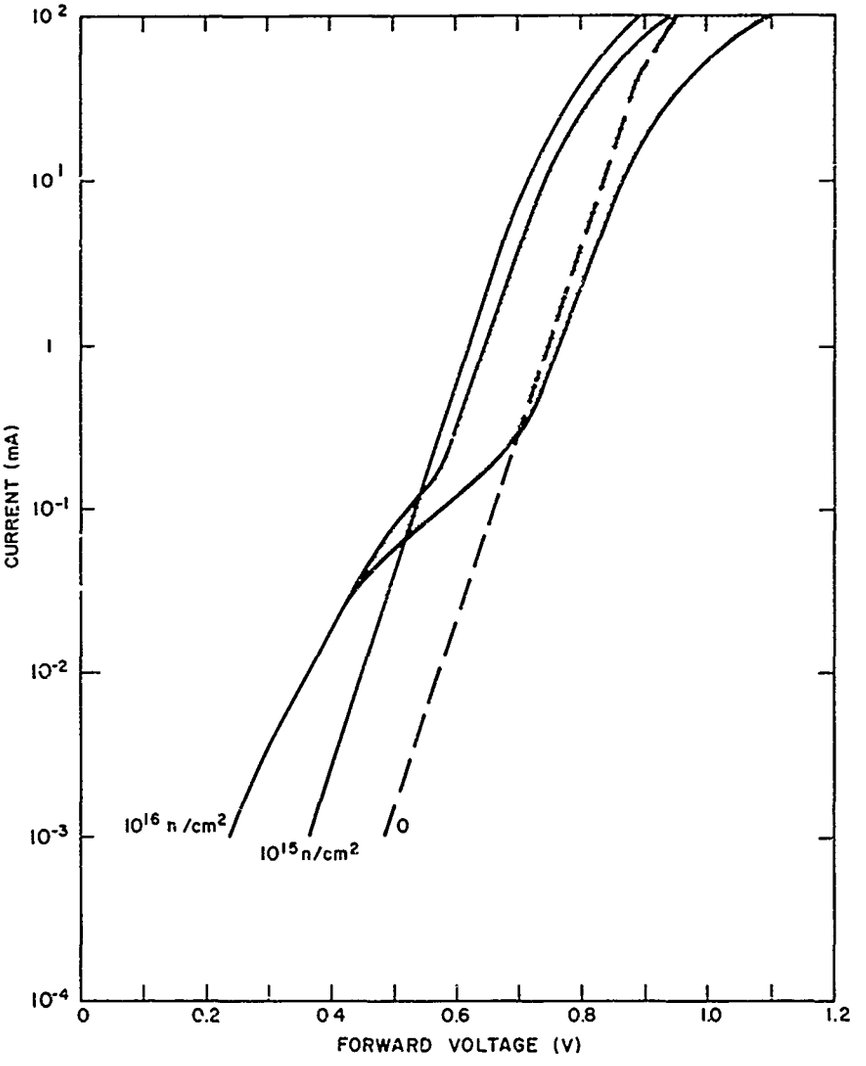

Figure 66. Typical forward V-I behavior.

would give rise to a significant increase in the forward current. At low temperatures this generation current contribution in the I region was found to disappear because of its exponential temperature dependence. At high forward currents where the space-charge region current is less important, a voltage drop will appear across the I layer such that both the minority and majority carriers drift across the layer without recombining. The voltage drop that is required rises exponentially with the ratio of the width of this intrinsic region to a diffusion length. At 10^{16} n/cm^2, the diffusion length is estimated to be 0.3 μm; hence, a significant voltage drop would appear across this intrinsic region if the width of the region were comparable. We

will show later that the intrinsic region also affects the junction capacitance values obtained at very low reverse biases. It is worthwhile to point out that this intrinsic region affects the forward characteristics quite significantly but it will subsequently be shown to have little or no effect upon the behavior of the avalanche microwave characteristics of the diode.

(d) Avalanche Breakdown Characteristics. DC measurements of the avalanche breakdown region were made as a function of neutron fluence. Up to 10^{15} n/cm^2 there was little effect of the radiation on the breakdown characteristics. Above this level, the concentration of active defects approaches the bulk impurity concentration and the breakdown voltage increased significantly. The average breakdown voltage as a function of neutron fluence is shown in Figure 67. The initial breakdown voltage is characteristic of a doping level of 10^{16} cm^{-3}. At 10^{16} n/cm^2 the breakdown voltage is characteristic of the doping level of 5×10^{15} cm^{-3}. One concludes that approximately 0.5 donors/n-cm are removed. However, since there is a significant widening of the space-charge region that accompanies this reduction in the effective doping level it is possible that punch-through to the epitaxial region

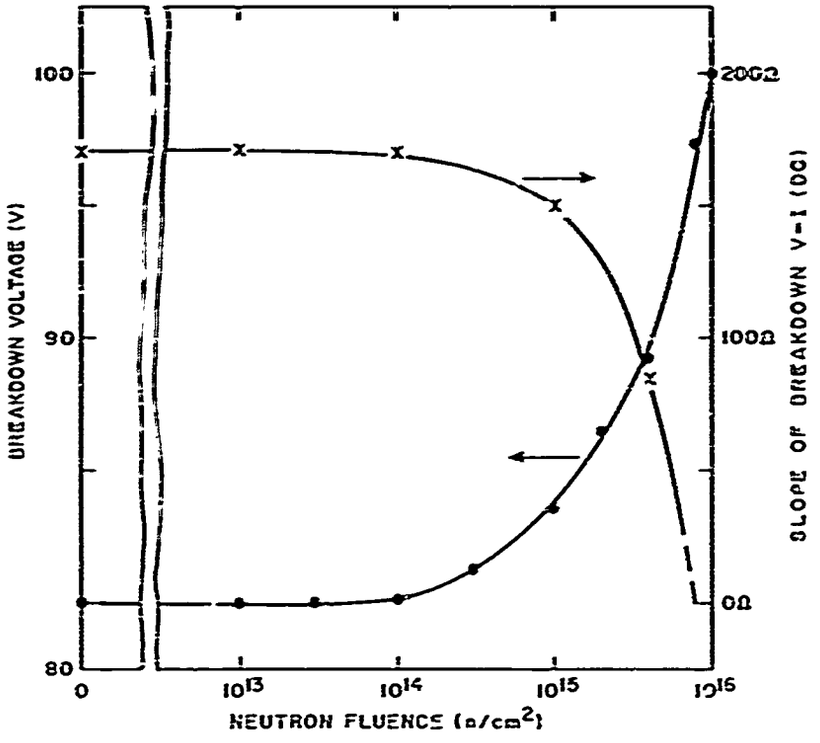

Figure 67. Typical avalanche diode breakdown voltage and dc breakdown slope as functions of neutron fluence for I_R = 50 mA.

has occurred and that the breakdown is characteristic of the PIN structure rather than a P⁺N structure.

From the V-I measurements in the avalanche region the slope of the breakdown region $\Delta V/\Delta I$ was determined. This dc breakdown resistance is largely controlled by the temperature dependence of the breakdown voltage which prior to irradiation is of the order of +0.12 V/°C. From the initial dc resistance of these devices which is of the order of 170Ω, one estimates that the temperature rise in the device at a reverse current of 50 mA must be approximately 70°C.

During the irradiation it is observed that the slope of the breakdown characteristic decreases rapidly above 10^{15} n/cm^2, and in fact becomes negative in the neighborhood of 10^{16} n/cm^2. Thus, there is a dc negative-resistance characteristic following high levels of radiation. The negative resistance may be a result of the large concentration of generation centers formed in the depletion layer. The temperature dependences of the avalanche process and the generation process have opposite effects on the breakdown voltage. If there is a large generation current contribution, its temperature dependence could dominate. Negative resistance may also arise at large current densities from changes in the field profile. The negative resistance may have serious consequences for the device both in terms of the operating behavior and in terms of reliability since thermal runaway is very liable to occur under these circumstances. It is possible also that isolated current filaments could develop. Filamentary conduction is favored since the breakdown voltage across an isolated filament with high-current density and severe local heating will be lower than that across neighboring low-current-density and low-temperature regions.

It should be pointed out that in the course of making the microwave measurements on radiated diodes nearly half of the original devices were lost during the process of the measurements. Generally, these failures occurred after a large integrated dose of neutrons had been accumulated. In normal testing of avalanche diodes, a certain number of devices are lost through burnout and excessive heating of the devices. This loss usually occurs because of stored charge in the measurement apparatus which is discharged very rapidly through the avalanche resistance. Failure could also be due to secondary breakdown. However, there is reason to believe that a number of our failures resulted from the dc negative-resistance behavior produced by radiation. Unfortunately we cannot say that failure specifically followed either thermal runaway or filament formation. It was found that more devices burned out of the low-forward resistance type than of the high-forward resistance type. This might be expected since the high-series forward resistance does provide some protection against thermal runaway and filament formation.

Dynamic resistance measurements were also made in the avalanche region using 50-mA, 50-ns pulses. In these pulse measurements the large forward-spreading resistance in half of our samples does not appear because of the shunt capacitance. The remaining series resistance due to contacts and unswept epitaxial region is of the order of 1Ω or less. Therefore, the observed measured ac resistance of approximately 20Ω is attributed primarily to space-charge resistance of the avalanche region. This resistance is given by the low-frequency space-charge resistance term in Equation (1), i.e.,

$$R_{sc} = \frac{\ell_d^2}{2\epsilon v_d A}$$

For the avalanche diodes under investigation the calculated space-charge resistance is of the order of 20Ω in good agreement with the observed values. During irradiation it was found that the dynamic resistance increased as shown in Figure 68. Presumably, the increase is due to a widening in the space-charge drift region ℓ_d.

The observed increases in R_{sc} are greater than expected from the increase in ℓ_d. In some of the irradiated devices the waveform of the voltage pulse across

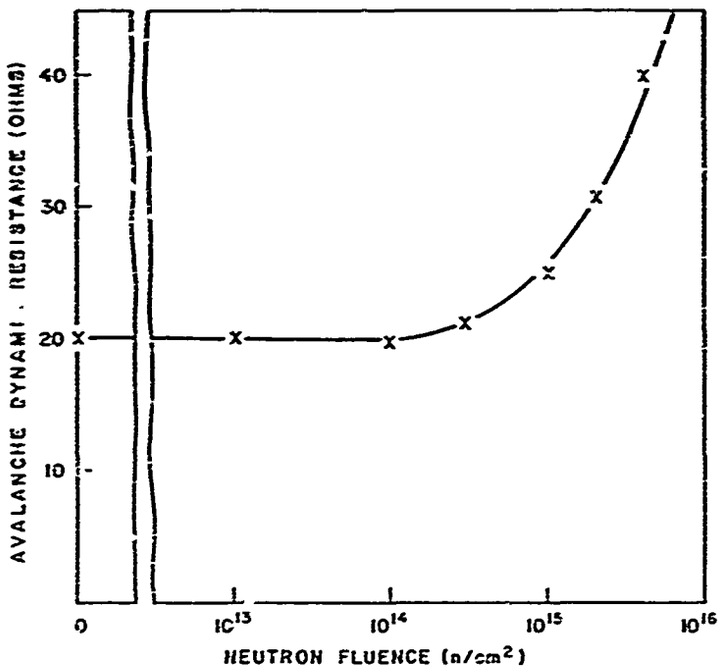

Figure 68. Change in avalanche dynamic resistance with neutron radiation for 50-ns, 50-mA pulse.

the diode indicated a significant drop in the thermal time constant. Before irradiation, the thermal time constants were all greater than 1 μsec so that the temperature rise during a 50-nsec pulse was small. After irradiation, some of the irradiated devices had time constants as short as 0.2 μsec and the temperature rise during a 50-nsec pulse was appreciable. The resulting temperature rise provides an additional voltage change which causes the R_{sc} to appear larger. The decrease in time constant could be attributed to filamentary avalanche conduction in the irradiated devices since the rate of temperature rise in small cross-section filaments would be much greater than in the bulk semiconductor.

(e) Junction Capacitance Measurements. Typical changes in junction capacitance as a function of reverse voltage with increasing neutron fluence are shown in Figure 69. Relatively little change occurs in the junction capacitance up to a neutron fluence of 10^{15} n/cm^2. Above this level a displacement in the curve occurs. The magnitude of the displacement indicates a compensation of a majority carrier dopant of about 0.5 carrier/n-cm in agreement with the value deduced from changes in breakdown voltage.

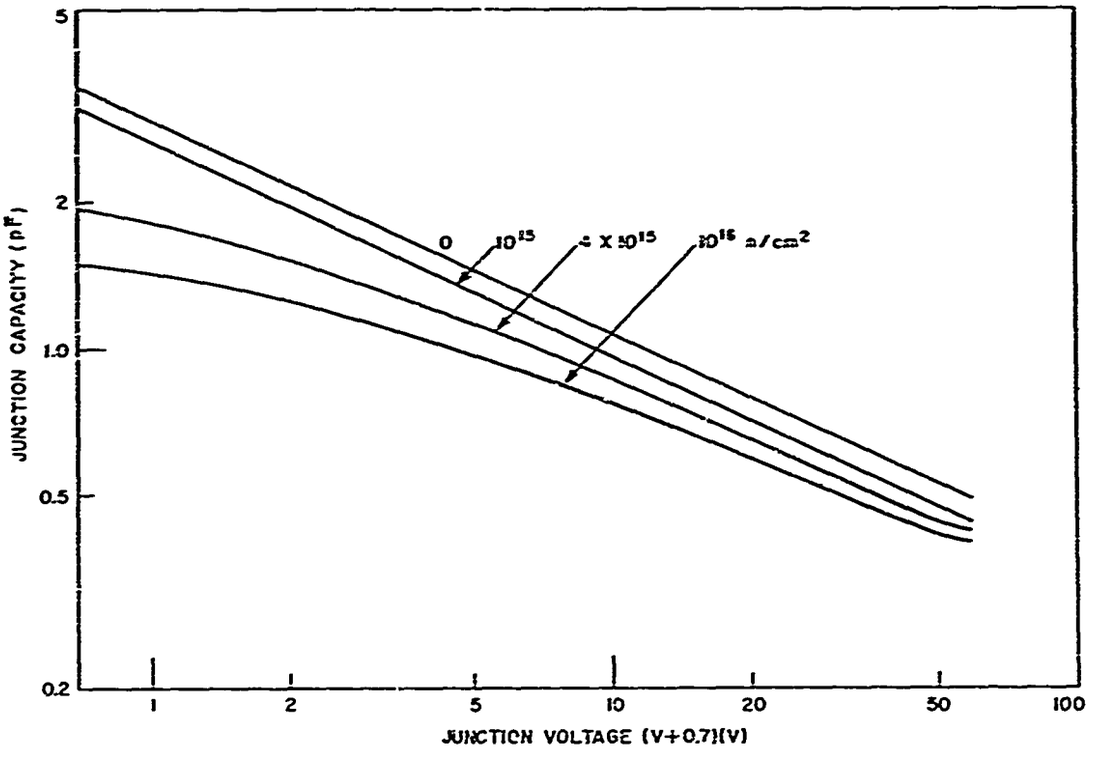

Figure 69. Effect on neutron radiation on C-V characteristics of silicon avalanche diodes.

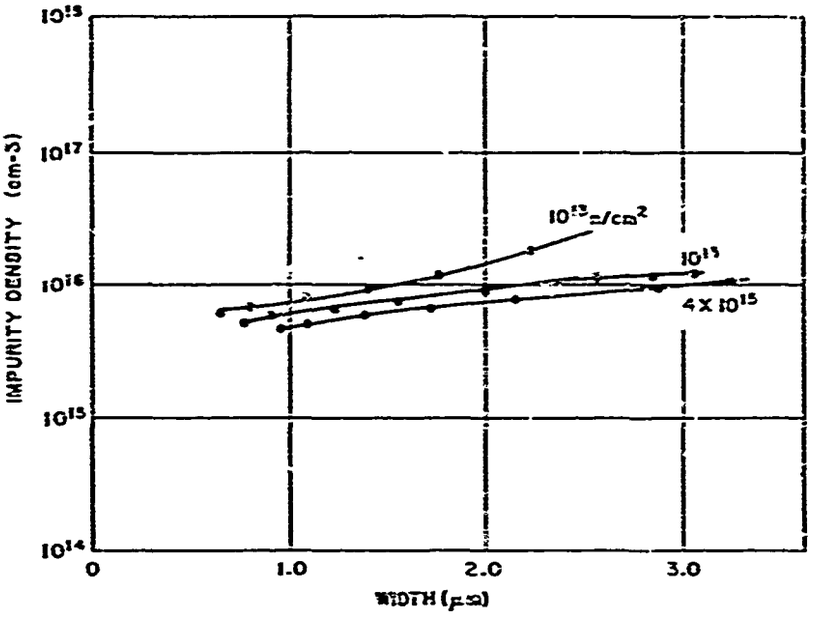

Figure 70. Impurity profile with neutron fluence as parameter.

At fluences $>10^{15}$ n/cm^2, further displacement occurs which indicates further compensation. These changes in effective doping level are shown in Figure 70. In addition to the bulk compensation, a large decrease in the capacitance occurs at very low bias voltages. This large decrease in capacitance at low voltage is attributed to the formation of a narrow intrinsic region at the metallurgical PN interface. The effects of this intrinsic region on the forward V-I characteristics have already been discussed. From the junction capacitance characteristics we have determined that the width of this intrinsic region at 10^{16} n/cm^2 is roughly 0.6 μm.

The capacitance measurements not only show a change in the compensation and in the formation of an intrinsic region but are also useful in deducing the shape of the field profile. The field profile is important in determining the operating characteristics of the avalanche microwave oscillator. The changes in the field profile with radiation are shown in Figure 71. Since the field not only widens but decreases in maximum intensity, we expect that both the drift region width ℓ_d and the avalanche region width ℓ_a will decrease with radiation. The effects of these changes will be discussed later.

2. AC Measurements

(a) RF Frequency. During the course of this study, it was determined that the oscillation frequency was determined primarily by the tuning of the

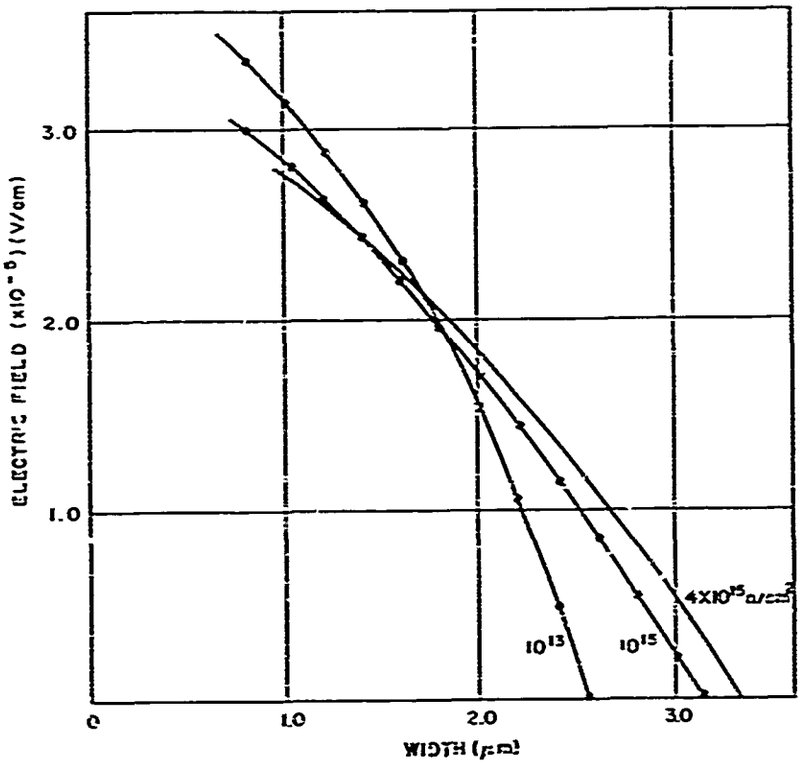

Figure 71. Field profile with neutron fluence as parameter.

microwave cavity and was not affected generally by the specific characteristics of the device under study. Since the devices had to be removed from the cavity to be irradiated, frequency changes between irradiations, which were of the order of 1.0 percent, were probably due to cavity returning. At the completion of the study of the device, several of the radiated devices were subsequently annealed to remove the radiation damage. The annealing was done with the devices mounted in the microwave cavity under conditions where they were continuously oscillating. During the anneal, the oscillation frequency was monitored without readjustment of the tuning slugs. In the course of annealing out more than 50 percent of the observed damage the frequency changes were of the order of 0.2 percent. This change in frequency could be easily corrected by a small readjustment of the current through the diode.

(b) FM and AM Noise. The FM and AM noise measurements were intended to show relative changes in noise level as a result of radiation. However both measurements were largely dependent on the tuning and Q of the coaxial cavity. Hence only general trends in the noise behavior could be determined.

No significant changes in the AM noise levels were observed up to the maximum dose of 10^{16} n/cm^2. The relative FM noise roughly doubled at a dose of 10^{15} n/cm^2 but did not increase further between 10^{15} n/cm^2 and 10^{16} n/cm^2.

(c) Oscillation Threshold and Power Output. The threshold current for oscillation and the power output under CW oscillation conditions at a continuous current of 50 mA were found to be relatively unchanged by neutron irradiation up to a total integrated flux of 10^{15} n/cm^2. The average characteristics for threshold current and output power as functions of the neutron fluence for all ten units are shown in Figure 72. At 10^{15} n/cm^2, the lot of ten was subdivided into two lots, one with a high-average output power, the other with a low-average output power. Subsequent power and threshold measurements were made on three units each of the two lots. The results on these devices are also shown in Figure 72. At neutron levels from 10^{15} n/cm^2 to 4×10^{15} n/cm^2, the threshold current decreased in value and the output power increased in value for both lots. However, the low average power lot showed the greatest improvement. At 10^{16} n/cm^2, the threshold current for both lots returned to nearly its original value. The output power, on the other hand,

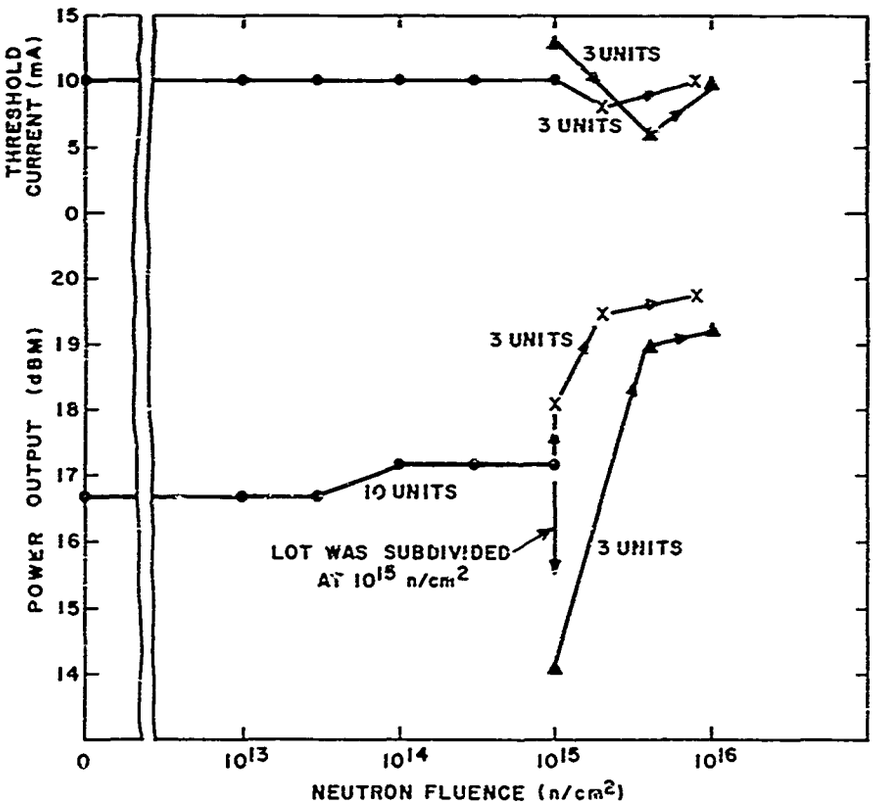

Figure 72. Threshold current and output power as functions of neutron fluence.

continued to increase very slightly in the range up to 10^{16} n/cm^2. The power efficiency of the diodes also increased with the output power although not as drastically because of a small (10 percent) increase in the breakdown voltage at the same time.

The decrease in threshold and the increase in oscillation output are results of the compensation of majority carrier doping in the epitaxial material although the specific mechanism by which the power is increased and the threshold decreased is not clear. More will be said of this topic in the discussion which follows.

f. Discussion

1. DC Characteristic of Neutron Irradiated Avalanche Diodes. The dc characteristics of the nearly-abrupt structure have been studied in order to determine its capabilities for diode applications in a radiation environment. The narrow-base moderately-doped structure should exhibit improved forward characteristics because of the very low series resistance, which has been estimated at roughly 1Ω. At neutron fluences up to 2×10^{15} n/cm^2, excellent forward characteristics were maintained. At higher fluences, however, the forward behavior degraded abruptly. This degradation has been attributed to the formation of a thin I region at the position of the metallurgical PN junction; this formulation resulted from compensation of both donors and acceptors by radiation produced defects. From the observed carrier removal rate of 0.5 carriers/n-cm, the width of the I region for a junction depth of 3 μm and a surface concentration of 10^{18} cm^{-3} is estimated to be approximately 0.5 μm.

The voltage drop across such an I region in the forward direction has been calculated by Herlet and Spenke[19] as:

$$\Delta V_I = 2\,kT/q \sinh W_I/2L \left[2 \arctan \left(e^{W_I/2L - \pi/2}\right)\right]$$

where W_I is the width of the I region and L is the ambipolar diffusion length. From the observed voltage shifts at 1 mA between 10^{15} n/cm^2 and 10^{16} n/cm^2, we estimate the widths of the I regions to vary from 0.7 to 1.0 μm.

The width of the I region has also been estimated from the decrease in the junction capacitance at zero bias. The junction width increases from 0.4 μm in unirradiated devices to 1.0 μm at 10^{16} n/cm^2. This increase in width is in good agreement with the values estimated from the extra forward voltage drop.

The width of the compensated intrinsic region and its consequent effect on device behavior could be reduced by reducing the depth of the diffused junction. Thus it is desirable in radiation-hardened devices to minimize the depth of diffused junctions in addition to the usual constraints on basewidths and doping concentrations.

In the avalanche breakdown region, V-I measurements show that the temperature dependence of the breakdown voltage becomes negative for neutron fluences greater than 4×10^{15} n/cm^2. The negative temperature coefficient gives rise to a negative resistance in the avalanche region and raises serious questions about device reliability in this region. Thermal runaway and filamentary conduction effects have been observed in irradiated avalanche diodes as a result of the negative resistance behavior. Further study of this phenomenon appears desirable.

2. Microwave Behavior of Neutron Irradiated Avalanche Diodes. As expected, lifetime reduction and trapping effects due to neutron bombardment were found to have little or no effect on the microwave behavior of avalanche diodes. On the other hand, carrier removal effects by radiation-induced defects were found to alter significantly the field profile and the performance of the diodes as oscillators. The resultant changes resulted in a decrease of the threshold current and increases in both power output and efficiency. Evidently the original structure was not optimum. However, the reasons for improvement in microwave performance are not clear. From Figure 71 it is apparent that the space-charge region widens and thus shrinks the width of the "unswept" epitaxial region. As already pointed out this can significantly increase the microwave oscillator efficiency. The capacitance data given in Figure 69 shows saturation of the capacitance at high voltages for 10^{16} n/cm^2. This saturation indicates that the space-charge region has reached the substrate region, eliminating the unswept region. In the unirradiated devices, therefore, the unswept region at breakdown is roughly 1 μm thick. The elimination of this region by radiation would not be expected to produce the relatively large improvements observed in oscillator performance.

The increase in space-charge width also increases the width of the drift region and consequently increases the magnitude of the negative space-charge resistance. Indeed, pulse measurements of the space-charge resistance showed a marked increase with neutron radiation. The magnitude of the effect could explain the magnitude of the improvement in the oscillator performance. One would assume that the increase in space-charge width would increase the width of the avalanche region as well as the drift region. This would decrease the critical frequency and reduce the magnitude of the active negative resistance; however, Figure 71 indicates that the width of the avalanche region does not significantly change with radiation and the above conclusion appears valid.

Another possible explanation for the improved oscillator performance is the formation of avalanche current filaments in irradiated diodes. Filamentary conduction would increase the effective current densities, increasing ω_c and in turn the

magnitude of the active negative resistance. However, we find no evidence in the avalanche V-I measurements that filamentary conduction occurs below 4×10^{15} n/cm^2.

g. Summary

The effects of fast neutrons with integrated fluxes up to 10^{16} n/cm^2 on both dc and microwave characteristics of nearly-abrupt X-band avalanche diodes have been studied. Good forward dc characteristics were observed up to 2×10^{15} n/cm^2. At higher doses, the forward characteristics are degraded abruptly by the formation of a thin intrinisc layer at the metallurgical PN junction. The thickness of the intrinsic layer and its effects on device behavior could be significantly reduced by reducing the depth of the diffused junction.

At neutron fluences exceeding 4×10^{15} n/cm^2, the avalanche breakdown voltage has a negative temperature dependence which results in a sharp degradation in device reliability. The negative-temperature coefficient is thought to be a result of an increase in the reverse saturation current by radiation damage or of changes in the field profile.

Microwave oscillator characteristics — including oscillation threshold, power output, frequency, efficiency, and FM and AM noise — were virtually unchanged up to 10^{15} n/cm^2. At neutron fluences greater than 10^{15} n/cm^2, the oscillation threshold fell and power output increased significantly (2 to 6 dB). The improvements are attributed to widening of the drift-field region and to a reduction in width of the unswept epitaxial parasitic resistance region. The greatest improvements occurred for the lowest-output power devices. These results suggest the use of nuclear radiation to tailor the defect concentrations and the field profiles of avalanche diodes to achieve optimal structures.

Lower frequency avalanche diodes which would have lower impurity concentrations and wider space-charge regions will be less tolerant of nuclear radiation. Other types of avalanche diode structures, in particular the PIN structure, could be more tolerant of radiation damage since the field profile would be relatively unaffected by the introduction of defects. Operation of avalanche diodes at higher current densities than used in this study (500 A/cm^2) can be expected to increase the tolerable limit of neutron fluence because of inherent annealing of the neutron damage. Avalanche diode microwave amplifiers should exhibit much the same radiation tolerance as do the avalanche diode oscillators.

BLANK PAGE

IV. CONCLUSIONS

10. CONCLUSIONS

The red luminescence in Zn-and Cd-doped GaP has been studied and, at low temperatures, has been shown to be composed of two overlapping bands whose origins are related. The high-energy band arises from the decay of bound excitons at Zn-O or Cd-O nearest-neighbor complexes, which act as electron traps. The low-energy band arises from transitions in which an electron trapped on a Zn-O or Cd-O complex annihilates a hole trapped on a Zn or Cd acceptor. This recombination mechanism produces a new type of long-lived pair spectrum which is characterized by an absence of any spectral changes in time-resolved spectroscopy. This model is consistent with Zeeman and isotopic-substitution experiments and accounts for the relative positions of the bands. Decay time and absorption measurements yielded the density of Zn-O and Cd-O complexes.

At low temperatures, the intensity ratio of the pair and bound-exciton bands is dependent upon sample preparation and excitation intensity, which can be qualitatively understood. Regardless of the initial value of this ratio, the bound-exciton emission becomes dominant in the temperature range between 60° and 120°K. At room temperature, the emission is almost entirely excitonic. The accompanying large changes in spectral and time-decay characteristics are semiquantitatively explained by a theory based on the assumption of thermal equilibrium of holes amongst the exciton-hole, acceptor, and valence band states.

An analysis of a simple model for radiation-induced space-charge buildup in the SiO_2 layers of MOS structures has been carried out. The model assumes that hole-electron pairs are created in the SiO_2 by the radiation and that some of the electrons created by the radiation drift out of the SiO_2 layer under the action of an applied potential across the oxide, V_G, while the corresponding holes become trapped. The diffusion of electrons is assumed to be negligible. The analysis predicts:

1. A dependence of charge buildup on radiation dose, D, approximately of the form $(1 - e^{-\beta D})$.
2. A linear dependence of the charge buildup on V_G, for both polarities of V_G.
3. The charge buildup depends on the total dose absorbed and not on the rate at which the dose was received.

Experimental observations on the SiO_2 layers found in commercial MOS-FETs show good general agreement with the predictions of the analysis. To obtain quantitative agreement, however, it was necessary to assume that the mobility-lifetime product for electrons in the oxide is much lower at the SiO_2-Si interface than at the SiO_2-metal interface. Other discrepancies were observed but they can be explained as the results of oversimplifications employed in the analysis. In particular, it was necessary to postulate that under some circumstances diffusion of electrons out of the oxide was important and that, in addition to holes, a small number of electrons may be trapped in the oxide in some cases. The space-charge was found to accumulate within ≤ 200Å of the cathode-oxide interface.

Thermoluminescence glow-curve experiments revealed several facts regarding trap levels in simple SiO_2 layers on Si substrates. Fresh, unirradiated layers apparently do not have a very high density of traps in the range 0.8 - 1.2 eV. After a large dose of Co^{60}-gamma radiation, five levels appear in this energy range. The levels do not all appear to belong to the same trap structure. With additional radiation dose and/or high-temperature annealing (~950°C) the five discrete levels change to a continuum of levels with a peak corresponding to a trap depth of ~1 eV.

Thermally stimulated current-glow curves from irradiated commercial MOS-FETs indicate that in addition to a net positive space-charge, radiation also produces a larger compensated trapped charge in the oxide. The space-charge represents the excess of trapped holes over trapped electrons. The electrons are trapped in a continuum of levels ~1 eV below the SiO_2 conduction band while the holes reside in deeper traps. The density of traps in the device oxide layers is inherently very large ($\sim 10^{19}$ cm^{-3}) and does not appear to be altered significantly by quite large doses of Co^{60}-gamma radiation.

A model is proposed for the thermally-stimulated current observed to flow through the irradiated MOS structure. It is postulated that when the trapped electrons are released thermally they recombine with trapped holes producing luminescence. The luminescence is responsible for photoemission of electrons from the electrodes into the oxide layer. The injection efficiency for the metal electrode (Al or Cr) is much greater than for the Si electrode so that a net flow of electrons through the oxide from the gate to the silicon is observed.

Studies were made of the effects of Co^{60}-gamma and fast-neutron irradiations on I-V and C-V characteristics of platinum-silicide/silicon Schottky barrier diodes with a "guard-ring" structure. The forward and reverse characteristics, as well as C-V characteristics, indicate that the metal-semiconductor interface is virtually insensitive to irradiation up to 10^8-rad gamma or 10^{15}n/cm^2. These results open the way to the use of Schottky barrier diodes both as radiation-resistant devices and

as a means of studying the changes in the bulk semiconductor and in the metal-semiconductor interface states caused by energetic radiation.

Open-circuit forward-voltage recovery (OCFVR) measurements were made on neutron-irradiated P$^+$N and P$^+$N silicon diodes. No large dependence of lifetime on injection level was observed in contrast to results obtained on bulk semiconductor samples. In the absence of injection-level dependence, these studies are not useful in characterizing the recombination mechanism. OCFVR measurements made on diodes exposed to bursts of fast neutrons show that diffusion length recovery after fast neutron irradiation is solely due to lifetime recovery and does not involve changes in carrier mobility.

C-V measurements on silicon diodes exposed to neutrons at 77°K show carrier removal rates several times greater than room-temperature irradiations. Following minority carrier injection, the carrier removal rates are reduced to the room-temperature values. The capacitance recovery, following injection, appears to be due to minority carrier trapping at the edges of clustered damage regions. Recovery effects in depleted junction devices, such as junction field-effect transistors, are expected to be much larger than in strongly injecting devices.

The effects of fast neutrons with integrated fluxes up to 10^{16} n/cm^2 on both dc and microwave characteristics of "nearly-abrupt" X-band avalanche diodes were studied. Good forward dc characteristics were observed up to 2×10^{15} n/cm^2. At higher doses, the forward characteristics were degraded abruptly by the formation of a thin intrinsic layer at the metallurgical PN junction. The thickness of the intrinsic layer and its effects on device behavior could be significantly reduced by reducing the depth of the diffused junction.

At neutron fluences exceeding 4×10^{15} n/cm^2, the avalanche breakdown voltage shows a negative temperature dependence which results in a sharp degradation of device reliability. The negative temperature coefficient is thought to be a result of either the increase in the reverse saturation current or the change in field profile.

Microwave oscillator characteristics including oscillation threshold, power output, frequency, efficiency, and FM and AM noise were virtually unchanged up to 10^{15} n/cm^2. At neutron fluences greater than 10^{15} n/cm^2, the oscillation threshold fell and power output increased significantly (2 to 6 db). The improvements are attributed to widening of the drift-field region and to a reduction in width of the "unswept" epitaxial parasitic resistance region. The greatest improvements occurred for the lowest output power devices. These results suggest the use of nuclear radiation to tailor the defect concentrations and the field profiles of avalanche diodes to achieve optimal structures.

V. CONTRIBUTORS, TALKS AND PUBLICATIONS, AND REFERENCES

11. CONTRIBUTORS

The authors of this report and contributors to the research reported herein, are as follows:

List of Authors

D. K. Wilson
J. P. Mitchell
J. D. Cuthbert
H. S. Lee

List of Contributors

D. K. Wilson
J. P. Mitchell
J. D. Cuthbert
H. S. Lee
D. G. DeNure
W. P. Knox
H. E. Noffke

12. TALKS AND PUBLICATIONS

The talks and publications listed below resulted, wholly or in part, from work done under this contract.

a. Talks

1. J. P. Mitchell, "Radiation-Induced Trap Levels in SiO_2 Layers." Presented at the Silicon Interface Specialists Conference, Las Vegas, Nevada, March 4-6, 1968.
2. H. S. Lee, "Effect of Radiation on Silicon Schottky Barrier Diodes." Presented at the Silicon Interface Specialists Conference, Las Vegas, Nevada, March 4-6, 1968.
3. D. K. Wilson and H. S. Lee, "Radiation Effects on Silicon Avalanche Diodes." Submitted to the IEEE Annual Conference on Nuclear and Space Radiation Effects, Missoula, Montana, July 15-18, 1968.
4. D. K. Wilson, "Recovery of Neutron Damage in Silicon PπN and PνN Diodes by Minority Carrier Injection." Submitted to the IEEE Annual Conference on Nuclear and Space Radiation Effects, Missoula, Montana, July 15-18, 1968.

5. J. P. Mitchell, "A Study of Radiation-Induced Trap Levels in SiO_2 Layers Using Thermoluminescence Glow Curve Techniques." Submitted to the IEEE Annual Conference on Nuclear and Space Radiation Effects, Missoula, Montana, July 15-16, 1968.

b. Publications

1. C.H. Henry, P.J. Dean and J.D. Cuthbert, "New Red Pair Luminescence from GaP." Phys. Rev. 166 (1968) p 754.
2. J.D. Cuthbert, C.H. Henry, and P.J. Dean, "Temperature Dependent Recombination Mechanisms in GaP (Cd, O) and GaP (Zn, O)." To be published in Phys. Rev. (1968).
3. W.D. Knox and J.D. Cuthbert, "A Variable Temperature Dewar for Cathodoluminescence Studies." To be published in Rev. Sci. Inst. (1968).
4. J.P. Mitchell, "Radiation-Induced Space-Charge Buildup in MOS Structures." IEEE Trans. Electron Devices ED-14, (1967) p 764.
5. H.S. Lee, and S.M. Sze, "Effects of Radiation on Silicon Schottky Barrier Diodes." To be published.

13. REFERENCES

a. Section I

1. Yu. L. Ivanov and A. V. Yukhnevich, Sov. Phys. - Solid State 6 (1965) p 2965.
2. F. L. Vook, Proceedings of the Santa Fe Conference on Radiation Effects in Semiconductors Oct. 1967 (Plenum Press, New York, 1968) p 421.
3. J. D. Cuthbert, Scientific Report No. 2, Contract AF-19(628)4957, AFCRL 67-0293 (December 1966).
4. T. N. Morgan, B. Welber, and R. N. Bhargava, Phys. Rev. 166 (1968) p 751.
5. J. J. Hopfield, D. G. Thomas, and R. T. Lynch, Phys. Rev. Letters 17 (1966) p 312.

b. Section II

1. J. P. Mitchell and D. K. Wilson, B.S.T.J. 46 (1967) pp 1-80.
2. E. Kooi, IEEE Trans. on Electron Devices ED-13 (1966) pp 238-245.
3. A. J. Speth and F. F. Fang, Appl. Phys. Letters 7 (1965) pp 145-146.
4. A. S. Grove and E. H. Snow, Proc. IEEE 54 (1966) pp 894-895.
5. K. H. Zaininger, Appl. Phys. Letters 8 (1966) pp 140-142.
6. A. G. Stanley, IEEE Trans. on Electron Devices ED-14 (1967) pp 134-138.
7. E. H. Snow, A. S. Grove, and D. J. Fitzgerald, Proc. IEEE 55 (1967) pp 1168-1184.
8. A. M. Goodman, Phys. Rev. 152 (1966) pp 780-784.
9. K. H. Zaininger, "Irradiation of MOS capacitors with High Energy Electrons," paper presented at IEEE Conference on Nuclear and Space Radiation Effects, Palo Alto, July 1966.
10. B. W. Schumacher and S. S. Mitra, "Measuring Thickness and Composition of Thin Surface Films by Means of an Electron Probe," Proc. Electron Components Conference, Washington, D. C. (1962) pp 152-161.
11. For a summary of glow-curve techniques, see K. H. Nicholas and J. Woods, Brit. J. Appl. Phys., 15 (1964) pp 783-795.
12. G. F. J. Garlick and A. F. Gibson, Proc. Phys. Soc. 60 (1948) pp 574-590.
13. C. H. Haake, J. Opt. Soc. Am. 47 (1957) pp 649-652.
14. L. I. Grossweiner, J. Appl. Phys, 24 (1953) pp 1306-7.
15. W. L. Medlin, J. Chem Phys. 38 (1963) pp 1132-1143.
16. R. Yokota, Phys. Rev. 91 (1953) pp 1013-4.
17. E. N. Batrak, Sov. Phys.-Crystal 3 (1958) pp 102-4.
18. J. R. Hensler, Nature 183 (1959) pp 672-673.
19. G. W. Arnold, J. Phys. Chem. Solids 13 (1960) pp 306-320.
20. M. Schlesinger, Phys. Lett 10 (1964) pp 49-50.

21. M. Schlesinger, J. Phys. Chem. Solids 26 (1965) pp 1761-6.

22. W. H. Turner and H. A. Lee, J. Chem. Phys. 43 (1965) pp 1428-1429.

23. T. Kikuchi, J. Phys. Soc. Jap. 13 (1958) pp 526-531.

24. H. Frölich, Proc. Roy. Soc. 188 (1947) p 521.

25. D. K. Wilson, J. P. Mitchell, J. D. Cuthbert, and R. R. Blair, Final Report - AFCRL-67-0068, Contract No. AF19(628)-4157, (31 December 1966).

26. A. M. Goodman and J. J. O'Neill, Jr., J. Appl. Phys. 37 (1966) pp 3580-3583.

27. B. E. Deal, E. H. Snow, and C. A. Mead, J. Phys. Chem. Solids 27 (1966) pp 1873-1879.

28. R. Williams, J. Appl. Phys. 37 (1966) pp 1491-1494.

29. R. Williams, Phys. Rev. 140 (1965) pp 569-575.

30. G. A. Katrick and O. G. Sarbii, Sov. Phys. - Solid State 3 (1961) pp 1181-1187.

31. M. P. Lepseter and S. M. Sze, B.S.T.J 49 (1968) p 195.

32. D. Kahn and M. P. Lepseter, B.S.T.J. 44 (1965) p 1525.

33. A. M. Cowley and S. M. Sze, J. Appl. Phys. 36 No. 10 (October 1965) p 3212.

34. C. K. Crowell and S. M. Sze, Solid State Electronics 9 (November 1966) p 1035.

35. H. J. Stein, Phys. Rev. 163 No. 3 (November 1967) p 801.

36. H. K. Henisch, Rectifying Semiconductor Contacts, (Oxford: Clarendon Press, 1957) p 214.

37. A. S. Grove and D. J. Fitzgerald, Solid State Electronics 9 (1966) pp 783-806

38. A. M. Goodman, J. Appl. Phys. 34 No. 2 (February 1963) p 329.

c. Section III

1. R. N. Hall, Proc. Inst. Radio Engineers 40 (1952) p 1512.

2. A. Herlet and E. Spende: Z. Angew Phys. 7 (1955) p 99; 7 (1955) p 149; 7 (1955) p 195.

3. W. Shockley and W. T. Read, Phys. Rev. 87 (1952) p 835.

4. R. H. Hall, Phys. Rev. 87 (1952) p 387.

5. L. W. Davies, Proc. IEEE 51 (1963) p 1637.

6. P. G. Wilson, Solid-State Electronics 10 (1967) pp 145-154.

7. B. R. Gossick, J. Appl. Phys. 26 (November 1955) pp 1356-1366.

8. O. L. Curtis, R. F. Bass, and C. C. Germano, Harry Diamond Laboratories Report 235-3 (November 1967).

9. B. R. Gossick, J. Appl. Phys. 30 (1959) p 1204.

10. D. K. Wilson, J. P. Mitchell, J. D. Cuthbert, and R. R. Blair, Final Report - AFCRL-67-0068, Contract No. AF19(628) 4157 (December 1966).

11. C. T. Sah and V. G. K. Reddi, IEEE Trans. Electron Devices 11 (1964) p 345.

12. G. Rupprecht and C. A. Klein, Phys. Rev. 116 (1959) p 342.

13. T. Misawa, IEEE Trans. Electron Devices, ED-14 (September 1967) p 580.

14. W. T. Read, Bell Sys. Tech. J. 37 (March 1958) p 401.

15. B. C. De Loach and R. L. Johnston, IEEE Trans. Electron Devices ED-13 (January 1966) p 181.

16. M. Gilden and M. E. Hines, IEEE Trans. Electron Devices ED-13 (January 1966) p 169.

17. S. R. Koval and G. Gibbons, Proc. IEEE (Lett) 56 (November 1967) p 2065.

18. D. E. Iglesias, Proc. IEEE (Lett) 56 (November 1967) p 2065.

19. A. Herlet and E. Spenke, Z. Angew. Phys. 3 (1955) p 149.

APPENDIX A

GLOSSARY FOR SECTION II

A^{**}	effective Richardson constant
C	constant of proportionality
C_{ox}	capacitance of the oxide layer (per unit area) $= \varepsilon\varepsilon_o/X_o$
D	radiation dose (Mrads)
E	electric field
E_t	trap depth
I(T)	luminescence intensity as a function of temperature
J	current density
N_c	effective density of states in the conduction band
N_t	density of electron traps
P(x, t)	density of trapped holes
Q_R	radiation-induced space-charge in SiO_2 layer
Q_M	charge induced on metal gate by Q_R
Q_S	charge induced in Si surface by Q_R
S_t	capture cross section of trap
T	absolute temperature
T_o	initial temperature
V	potential
V_f	forward voltage
V_G	potential difference across SiO_2 layer
ΔV	voltage shift of MOS capacitance-voltage curve caused by Q_R
X_o	oxide thickness
b	linear heating rate
c	characteristic length for an exponential distribution of Q_R
d	width of Q_R
f	attempt-to-escape frequency = $N_c S_T v$
g	generation rate of radiation-produced hole-electron pairs in SiO_2 layer
h	Planck's constant
k	Boltzmann's constant
m*	effective mass of electron
nt_o	initial density of trapped electrons
n(x)	density of free electrons
p	probability of escape
q	magnitude of electronic charge
t	time
v	thermal velocity of an electron in the conduction band
x	transverse distance in SiO_2 layer measured from the SiO_2 - Si interface
δ	Dirac delta function
ϵ	dielectric constant of Si
ε	dielectric constant of SiO_2
ε_o	permittivity of free space
μ	mobility of free electrons in SiO_2
τ	lifetime of free electrons in SiO_2
ϕ_{Bn}	Barrier height

A^{**}	effective Richa
C	constant of pro
C_{ox}	capacitance of (per unit area)
D	radiation dose
E	electric field
E_t	trap depth
I(T)	luminescence i function of tem
J	current density
N_c	effective densi the conduction
N_t	density of elec
P(x, t)	density of trap
Q_R	radiation-induc in SiO_2 layer
Q_M	charge induced by Q_R
Q_S	charge induced by Q_R
S_t	capture cross
T	absolute tempe
T_o	initial tempera
V	potential
V_f	forward voltage
V_G	potential differ SiO_2 layer
ΔV	voltage shift of voltage curve c
X_o	oxide thickness

APPENDIX A

GLOSSARY FOR SECTION II

ting rate	A^{**}	effective Richardson constant	b	linear heating rate
istic length for an l distribution of Q_R	C	constant of proportionality	c	characteristic length for an exponential distribution of Q_R
R	C_{ox}	capacitance of the oxide layer (per unit area) = $\varepsilon\varepsilon_o/X_o$	d	width of Q_R
-escape frequency =	D	radiation dose (Mrads)	f	attempt-to-escape frequency = $N_c S_T v$
rate of radiation-hole-electron pairs yer	E	electric field	g	generation rate of radiation-produced hole-electron pairs in SiO_2 layer
onstant	E_t	trap depth	h	Planck's constant
's constant	I(T)	luminescence intensity as a function of temperature	k	Boltzmann's constant
nass of electron	J	current density	m*	effective mass of electron
sity of trapped	N_c	effective density of states in the conduction band	nt_o	initial density of trapped electrons
free electrons	N_t	density of electron traps	n(x)	density of free electrons
of escape	P(x, t)	density of trapped holes	p	probability of escape
of electronic charge	Q_R	radiation-induced space-charge in SiO_2 layer	q	magnitude of electronic charge
elocity of an electron uction band	Q_M	charge induced on metal gate by Q_R	t	time
e distance in SiO_2 sured from the nterface	Q_S	charge induced in Si surface by Q_R	v	thermal velocity of an electron in the conduction band
a function	S_t	capture cross section of trap	x	transverse distance in SiO_2 layer measured from the SiO_2 - Si interface
constant of Si	T	absolute temperature	δ	Dirac delta function
constant of SiO_2	T_o	initial temperature	ϵ	dielectric constant of Si
ty of free space	V	potential	ε	dielectric constant of SiO_2
f free electrons in	V_f	forward voltage	ε_o	permittivity of free space
free electrons in	V_G	potential difference across SiO_2 layer	μ	mobility of free electrons in SiO_2
ight	ΔV	voltage shift of MOS capacitance-voltage curve caused by Q_R	τ	lifetime of free electrons in SiO_2
	X_o	oxide thickness	ϕ_{Bn}	Barrier height

B.

APPENDIX B*

INITIAL EQUILIBRIUM FREE ELECTRON DENSITY

Consider the situation shown in Figure 2. Since there is initially no space-charge present in the oxide, E is uniform throughout the oxide and of magnitude V_G/X_o ($V_G/X_o \gtrsim 10^5$ V/cm). At any point x in the oxide, the free electron density, n(x), is given by the continuity equation

$$\frac{\partial n}{\partial t} = \left(g - \frac{n}{\tau}\right) + \mu \frac{\partial En}{\partial x} + D \frac{\partial^2 n}{\partial x^2} \tag{1}$$

Since the electric field in the oxide is quite large it will be assumed that diffusion is negligible compared to drift, i.e., $D \sim 0$. It will also be assumed that no space-charge accumulates and hence E remains constant during the time required for n to reach equilibrium, $(\partial n/\partial t) = 0$. Using (1) the initial distribution of the free electron density is given by

$$\mu E \frac{dn}{dx} - \frac{n}{\tau} = -g, \tag{2}$$

where $E = -\dfrac{V_G}{X_o}$

Since the Si cannot supply electrons to the oxide, $n(0) = 0$. Using this boundary condition the solution of (2) is easily found to be

$$n(x) = g\tau \left[1 - \exp\left(-\frac{ax}{X_o}\right)\right] \tag{3}$$

where $a = \dfrac{X_o^2}{\mu \tau V_G}$

*This appendix supplement Part 4 of Section II.

APPENDIX C*

ELECTRIC FIELD IN THE OXIDE AT $x = X_o$ AT ANY TIME

Figure 3 illustrates the situation in the MOS structure at any time t. The purpose of this Appendix is to derive an expression for the field, E, in the oxide at $x = X_o$ in terms of the space-charge $Q_R(t)$. E is uniform for $d \le x \le X_o$ since there is no space-charge in this region. In the region $0 \le x \le d$ Poisson's equation gives

$$\frac{d^2V}{dx^2} = \frac{-q}{\varepsilon\varepsilon_o} P(x,t) \tag{1}$$

Integration of (1) yields

$$\frac{dV}{dx} = \frac{-q}{\varepsilon\varepsilon_o} \int_0^x P(x,t)dx - A \tag{2}$$

where $A = \left.\frac{dV}{dx}\right|_{x=0} = -E(0)$

It is easily shown by using Gauss' Law and (1) that

$$E(0) = -\left[\frac{Q_R(t) + Q_M(t)}{\varepsilon\varepsilon_o}\right] \tag{3}$$

Now $Q_M(t)$ will be the sum of the charge on the metal electrode at $t = 0$, namely $C_{ox}V_G$, and the charge induced by $Q_R(t)$, i.e.,

$$Q_M(t) = C_{ox}V_G - q\int_0^d \frac{x}{X_o} P(x,t)dx \tag{4}$$

Combining (3) and (4) we have

$$A = -E(0) = \frac{q\int_0^d P(x,t)dx + C_{ox}V_G - q\int_0^d \frac{x}{X_o} P(x,t)dx}{\varepsilon\varepsilon_o}$$

*This appendix supplements Part 4 of Section II.

Substituting for A in (2) we obtain

$$E(X_o) = E(d) = -\left.\frac{dV}{dx}\right|_{x=d}$$

$$E(X_o) = -\frac{V_G}{X_o} - \frac{q}{\varepsilon\varepsilon_o}\int_0^d \frac{x}{X_o}\, P(x,t)dx$$

APPENDIX D
GLOSSARY FOR SECTION IV

A	cross sectional area	n	density of free electrons	A
C	capacitance of the total depletion zone	n_i	density of intrinsic carriers	C
ϵ	electric field	n_o	initial density of free elections	ϵ
E_c	energy of conduction band edge	p	density of free holes	E_c
E_F	Fermi level energy	p_o	initial density of free holes	E_F
E_g	energy band gap	q	electronic charge	E_g
E_i	intrinsic Fermi level energy	t	time	E_i
E_t	energy of trap level	v_d	drift velocity	E_t
E_v	energy of valence band edge	v_n	electron thermal velocity	E_v
I_{rg}	reverse current space-charge generation term	v_p	hole thermal velocity	I_{rg}
I_s	reverse saturation current	α	ionization coefficient	I_s
J	dc current density	ϵ	dielectric constant	J
K	lifetime damage constant	λ	wavelength	K
L	ambipolar diffusion length	ϕ	neutron fluence	L
N_A	acceptor concentration	μ_p	hole mobility	N_A
N_D	donor concentration	μ_n	electron mobility	N_D
N_c	density of states in conduction band	σ_n	electron capture cross section	N_c
N_t	density of traps	σ_p	hole capture cross section	N_t
R_s	series resistance	τ	lifetime	R_s
R_{sc}	space-charge resistance	τ_o	initial lifetime	R_{sc}
T	temperature	τ_h	high-level-injection lifetime	T
W/L	base width-to-diffusion length ratio	τ_l	low-level-injection lifetime	W/L
W_I	width of intrinsic region	τ_n	electron lifetime	W_I
Z	total impedance	τ_p	hole lifetime	Z
j	$\sqrt{-1}$	τ_{no}	electron lifetime in heavily doped P-type material	j
k	Boltzmann's constant	τ_{po}	hole lifetime in heavily doped N-type material	k
l_a	avalanche region width	ω	frequency of operation	l_a
l_d	drift region width	ω_c	critical resonance frequency	l_d

A

APPENDIX D
GLOSSARY FOR SECTION IV

A	cross sectional area
C	capacitance of the total depletion zone
ϵ	electric field
E_c	energy of conduction band edge
E_F	Fermi level energy
E_g	energy band gap
E_i	intrinsic Fermi level energy
E_t	energy of trap level
E_v	energy of valence band edge
I_{rg}	reverse current space-charge generation term
I_s	reverse saturation current
J	dc current density
K	lifetime damage constant
L	ambipolar diffusion length
N_A	acceptor concentration
N_D	donor concentration
N_c	density of states in conduction band
N_t	density of traps
R_s	series resistance
R_{sc}	space-charge resistance
T	temperature
W/L	base width-to-diffusion length ratio
W_I	width of intrinsic region
Z	total impedance
j	$\sqrt{-1}$
k	Boltzmann's constant
l_a	avalanche region width
l_d	drift region width
n	density of free electrons
n_i	density of intrinsic carriers
n_o	initial density of free elections
p	density of free holes
p_o	initial density of free holes
q	electronic charge
t	time
v_d	drift velocity
v_n	electron thermal velocity
v_p	hole thermal velocity
α	ionization coefficient
ϵ	dielectric constant
λ	wavelength
ϕ	neutron fluence
μ_p	hole mobility
μ_n	electron mobility
σ_n	electron capture cross section
σ_p	hole capture cross section
τ	lifetime
τ_o	initial lifetime
τ_h	high-level-injection lifetime
τ_l	low-level-injection lifetime
τ_n	electron lifetime
τ_p	hole lifetime
τ_{no}	electron lifetime in heavily doped P-type material
τ_{po}	hole lifetime in heavily doped N-type material
ω	frequency of operation
ω_c	critical resonance frequency

B.

ATTACHMENT I

NEW RED PAIR LUMINESCENCE FROM GaP*

by

C. H. Henry
P. J. Dean
J. D. Cuthbert

* This article appeared in the Physical Review 166, No. 3 (15 February 1968) pp. 754-756.

Reprinted from THE PHYSICAL REVIEW, Vol. 165, No. 3, 754-756, 15 February 1968
Printed in U. S. A.

New Red Pair Luminescence from GaP†

C. H. HENRY AND P. J. DEAN
Bell Telephone Laboratories, Murray Hill, New Jersey

AND

J. D. CUTHBERT
Bell Telephone Laboratories, Whippany, New Jersey

(Received 31 August 1967)

We report optical experiments showing that the low-temperature red luminescence in GaP doped with Cd (or Zn) acceptors arises in two ways: (a) from the recombination of electrons bound to neutral complexes involving Cd (or Zn) and O, with holes trapped at distant Cd (or Zn) acceptors producing pair spectra with novel properties; (b) from the decay of an exciton bound at these complexes, as recently reported by Morgan *et al.* Zeeman and isotopic shift experiments which provide information about the symmetry axis, electronic structure, and chemical identity of the exciton-impurity complex are also discussed. The concentrations of the neutral complexes in Zn- and Cd-doped GaP have been estimated from absorption measurements using oscillator strengths derived from the measured decay time of the exciton luminescence.

IN the past several years there has been an intensive effort to understand the origin of the red luminescence in GaP. Gershenzon *et al.*[1,2] and Nelson[3] have attributed this luminescence to pair recombination involving the deep donor oxygen and the shallow acceptors Cd and Zn. In a recent paper, Morgan, Welber, and Bhargava[4] (MWB) reported a structured red luminescence in Cd- and O-doped GaP. This spectrum is characteristic of the recombination of an electron and hole trapped on a single site (bound exciton), rather than their recombination at donor-acceptor pairs distributed on different sites. They have attributed this decay to an exciton bound to Cd and O nearest neighbors. We have independently discovered this exciton luminescence and in this paper report (a) experiments determining the symmetry, level structure, lifetimes, and concentration of the exciton site, and verification that the center binding the exciton involves both Cd and O; (b) experiments showing that a second relatively featureless band, at slightly lower energies, exhibits a decay characteristic of recombination at electron trap-acceptor pairs of variable separations. We present strong evidence that this pair luminescence results from the recombination between holes at isolated Cd (or Zn) acceptors and electrons at the complex described above which behaves as a deep neutral electron trap. Unlike previously reported pair transitions,[5] the pair spectrum does not contain a Coulomb shift [see Eq. (1), below].

The exciton luminescence at 20°K [Fig. 1(a), curve I] shows a zero-phonon line A, followed by phonon replicas. The A transition is frozen out on cooling from 20 to 1.6°K, and a new transition B appears. Transition B is forbidden and can only be observed if strain or magnetic field are present, as shown in Figs. 2(a) and 2(b). Lines A and B both split anisotropically in a magnetic field. The splittings of the B line are shown in Fig. 2(d). The data were fitted by the solid theoretical curve assuming the site binding the exciton has a ⟨111⟩ symmetry axis, that the excited states can be split into two levels, that the ground state is a singlet, and that the levels only split when a component H is parallel to the symmetry axis [see Fig. 2(c)]. The magnitude of the splitting was adjusted to fit the data for H along [100]. The magnetic splittings, the fact that the B transition is forbidden, and the dependence of the intensity of the B transition on H can be predicted on the basis of a simple model which assumes that the exciton is formed from an electron with $J_z=\pm\frac{1}{2}\hbar$ and a hole with $J_z=\pm\frac{3}{2}\hbar$, where J_z is the angular momentum along the symmetry axis. From this analysis, we find $g_e=1.82\pm0.20$ and $g_h=0.98\pm0.05$, in agreement with values obtained from Zeeman studies of much shallower bound exciton complexes in GaP.[6] These level assignments differ from those of MWB, which could not explain our data.[7]

The most striking features of the exciton spectrum are the narrow vibrational sidebands spaced by 7.0 meV. In crystals doped with Cd^{110} and Cd^{116} we have found an isotope shift for this vibrational energy of $(1.36\pm0.20)\%$, i.e., $\frac{3}{4}$ as large as the shift expected for Cd vibrating alone. We also observe a shift of the zero-

† Research sponsored in part by the Cambridge Research Laboratory, Office of Aerospace Research, under Contract No. AF19628-67-C-0147.

[1] M. Gershenzon, F. A. Trumbore, R. M. Mikulyak, and M. Kowalchik, J. Appl. Phys. 36, 1528 (1965).
[2] M. Gershenzon, F. A. Trumbore, R. M. Mikulyak, and M. Kowalchik, J. Appl. Phys. 37, 483 (1966).
[3] D. F. Nelson and K. F. Rodgers, Phys. Rev. 140, A1667 (1965).
[4] T. N. Morgan, B. Welber, and R. N. Bhargava, preceding paper, Phys. Rev. 166, 751 (1968), hereafter referred to as MWB.
[5] See, e.g., J. J. Hopfield, D. G. Thomas, and M. Gershenzon, Phys. Rev. Letters 10, 162 (1963), F. M. Ryan and R. C. Miller, Phys. Rev. 148, 858 (1966).
[6] D. G. Thomas, M. Gershenzon, and J. J. Hopfield, Phys Rev. 131, 2397 (1963).
[7] MWB assign level A to be a triplet and level B to be a quartet. We find experimentally that these levels are each doublets. For $H=0$, MWB's assignments predict five nondegenerate transitions. We find only two transitions (A and B), each of which are 0.2-meV wide at 4°K. The no-phonon lines observed by MWB were 0.75 meV broad, because of instrumental broadening.

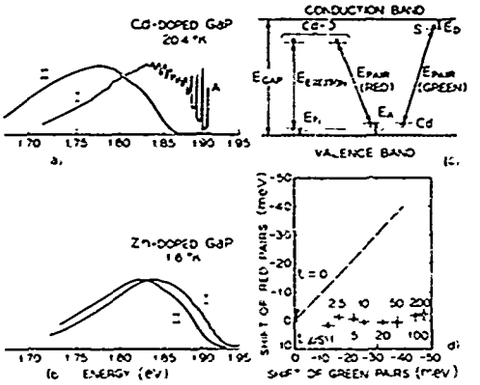

FIG. 1. (a) Curve I (Cd-O) exciton luminescence, curve II (Cd-O)-Cd pair luminescence. These bands were of comparable intensity; (b) curve I (Zn-O) exciton luminescence, curve II (Zn-O)-Zn pair luminescence; (c) level diagram showing the exciton and pair decays for Cd-doped GaP; (d) shift of the (Cd-O)-Cd pair luminescence versus the shift in the Cd-S pair luminescence with time after pulse excitation. The shifts were measured at the high-energy side half-maximum of each band. If the electron trap giving rise to the red pair luminescence was an ordinary ionized donor such as O^-, both the red and green pair bands would have shifted by comparable amounts as indicated by the dashed line.

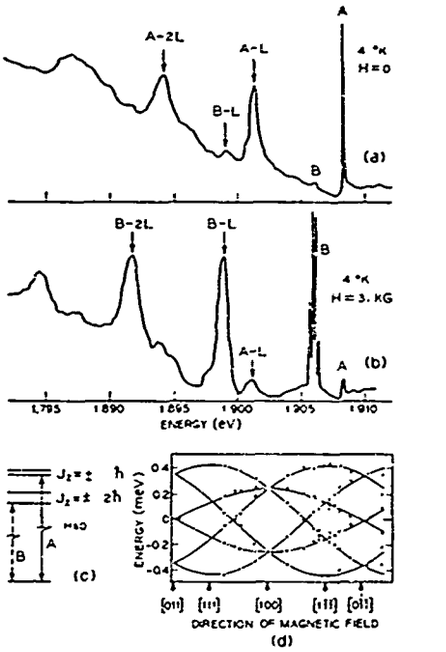

FIG. 2. (a) (Cd-O) exciton luminescence at 4°K with $H=0$; (b) (Cd-O) exciton luminescence at 4°K with $H=31$ kg. The six components result from the center having different orientations with respect to H. Transition B is forbidden for $H=0$ and has an intensity proportional to the square of the component of H perpendicular to the [111] symmetry axis of the Cd-O complex, (c) level diagram; (d) splittings of transition B versus direction of H as H was rotated in a plane perpendicular to the [011] direction.

phonon line A of 0.65 meV to higher energy in samples containing O^{18}. This result agrees with the oxygen-isotope experiment performed originally by MWB.[8] No shifts were observed in the other phonon replicas. This is not consistent with phonon assignments of MWB, who take the 48-meV mode to be a vibration involving the O atom.

The exciton decays exponentially with a decay time of 90 nsec from level A and 560 nsec from level B. From these lifetime measurements and from the measurement of the exciton absorption spectrum[9] (not shown), we find a maximum concentration of about 2×10^{16} cm^{-3} for the complexes in Cd-doped crystals.

Spectrum II in Fig. 1(a)[8] is long lived and decays nonexponentially in a way that is characteristic of pair spectra.[10] We have followed its decay to 10 msec. The band has a shape and half-width that are very similar to the exciton spectrum if the phonon fine structure in the latter is smoothed out.

We are also able to distinguish exciton and pair bands in the Zn-doped crystals, as shown in Fig. 1(b). The luminescence was excited with 4880 Å light of an argon ion laser beam having a power of 40 mW. By focusing the laser beam, we were able to saturate the pair band and observe the exciton band. The exciton spectrum has weak vibrational sidebands on the high-energy side, with a spacing of 6.0 meV. The zero-phonon line is not observable, presumably because of large phonon coupling. The exciton and pair bands are even more clearly distinguishable in time-resolved spectra and are then separated by 25±2 meV. Optimally, Zn- and O-doped crystals[11] contain up to 5×10^{16} cm^{-3} of the Zn-O complexes.

The relative positions of the pair bands and exciton bands, shown in Figs. 1(a) and 1(b), can be explained by the level diagram in Fig. 1(c). If the Cd-O complex only traps an electron, pair decay can occur in which this electron recombines with a hole on a distant Cd acceptor. The exciton band and the pair band should have roughly the same shape (as observed), because the phonon coupling will be determined primarily by the deeply trapped electron. The energy separation between the pair band and the exciton band is E_A-E_A [see Fig. 1(c)]. We measure this separation to be

[8] We were motivated to repeat this experiment because the zero-phonon line reported by MWB was broad, making it difficult to check for O isotope-induced shifts in the phonon replicas. (See Ref. 7.)

[9] This spectrum was most easily observed in crystals cooled rapidly from 800°C after growth. Such crystals contain relatively high concentrations of free Cd acceptors.

[10] D. G. Thomas, J. J. Hopfield, and W. M. Augustyniak, Phys. Rev. 140, A202 (1965).

[11] Optimum doping condition for the red luminescence in Zn-doped GaP are discussed in Ref. 1.

60±6 meV for Cd-doped crystals and 25±2 meV for Zn-doped crystals. The acceptor binding energies are known to be $E_A(\mathrm{Cd})=95\pm2$ meV and $E_A(\mathrm{Zn})=62\pm2$ meV.[12] Thus for the Cd-O exciton $E_A=35\pm8$ meV and for the Zn-O exciton $E_A=37\pm4$ meV. We expect the hole to be bound to the trapped electron by an effective-mass binding energy, reduced by about 5 meV because the hole is not bound to a point charge and in addition by 5–10 meV because of the repulsion produced by the same short-range (non-Coulomb) potential that attracts the electron. If we take the effective-mass energy to be the same as the binding energy of the weakly bound Si acceptor, $E_A(\mathrm{Si})=46$ meV,[12,13] we would predict $E_A\approx31$–36 meV, close to our experimental values.

The Zn pair band is more than 48±4 meV higher in energy than the Cd pair band (at 20°K).[14] If the electron were trapped on the same site in both cases, we would expect the pair bands to be separated by $E_A(\mathrm{Cd})-E_A(\mathrm{Zn})=33$ meV. We must conclude that the binding energy of the electron giving rise to the pair spectra changes in going from Zn-doped crystals to Cd-doped crystals. This result is consistent with the model and weighs against the idea that the electron is trapped on the neutral donor oxygen,[1,2,3,15] or at *any* electron trap which is independent of the nature of the acceptor.

We have heated Cd-doped crystals at 1000°C for several minutes and then cooled them rapidly to room temperature. This treatment caused a reduction of 3–10 in both the exciton and red pair luminescence relative to the green pair luminescence. This is further evidence that the pair and exciton luminescence involve a common site which dissociates upon heating the sample to 1000°C.

In ordinary donor-acceptor pair recombination, the decay energy $h\nu$ is given (aside from phonon cooperation) by

$$h\nu=E_{\mathrm{exp}}-E_A-E_D+e^2/\epsilon r \qquad (1)$$

for pairs of sufficiently large separation r.[14,16] This dependence on r causes the more closely spaced pairs, which decay first, to have higher energy. As a result, after pulse excitation, the high-energy side of the pair spectrum shifts with time to lower energies. In our case, the electron is trapped at a neutral complex and the equation for the decay energy does not contain the Coulomb term. This is conclusively verified by the data in Fig. 1(d). No shift with time was observed for the red pair band within the experimental error of ±3 meV, while the green (Cd-S) pair band shifted by 47 meV under identical experimental conditions. A similar result was observed in Zn-doped crystals.

The deep electron trap has been shown to involve both Cd (or Zn) and O, has ⟨111⟩ symmetry, and is neutral with no unpaired spin. A possible model is a nearest-neighbor Cd (or Zn)-O substitutional pair, as proposed by MWB. The exciton transitions are equivalent to the recombinations at nearest-neighbor O-Cd (or Zn) donor-acceptor pairs. The model proposed by MWB has been further strengthened by the recent observation of discrete transitions, accurately described by Eq. (1), at remote pairs of these donors and acceptors.[15]

We wish to thank C. J. Frosch, R. T. Lynch, and F. A. Trumbore for sample preparation; R. A. Faulkner, D. G. Thomas, and J. J. Hopfield for helpful discussions; and E. I. Gordon for providing an Ar^+ laser tube. We are grateful to T. N. Morgan for providing the MWB paper prior to publication.

[12] P. J. Dean, J. D. Cuthbert, D. G. Thomas, and R. T. Lynch, Phys. Rev. Letters 18, 122 (1967).

[13] Evidence will be presented in a forthcoming paper that the shallow acceptor attributed to Si in Ref. 12 is in fact due to C.

[14] Since the phonon interaction is stronger in the Zn pair band, the observed separation of 48±4 meV between the pair bands tends to *underestimate* the difference in E_A+E_T between the two spectra and therefore underestimates the discrepancy with the model in which the ionization energy E_T of the electron trap is invariant.

[15] Remote pair transitions involving isolated deep O donors have recently been discovered in the near infrared (~1.5 eV); P. J. Dean, C. H. Henry, and C. J. Frosch (unpublished).

[16] D. G. Thomas, M. Gershenzon, and F. A. Trumbore, Phys. Rev. 133, A269 (1964).

ATTACHMENT II

TEMPERATURE DEPENDENT RADIATIVE RECOMBINATION MECHANISMS IN GaP (Zn,0) and GaP (Cd,0)*

by

J. D. Cuthbert
C. H. Henry
P. J. Dean

* The contents of this Attachment will be published in the Physical Review (June 1968).

TEMPERATURE DEPENDENT RADIATIVE RECOMBINATION MECHANISMS in GaP(Zn,O) and GaP(Cd,O)

Abstract

Henry et al. have shown that the low-temperature red luminescence in both GaP(Zn,O) and GaP(Cd,O) is composed of a bound-exciton band overlapped at lower energies by a new type of long-lived pair band. This paper describes a study of the temperature dependence of the spectral positions and time-decay characteristics of these red bands. The samples were excited with electrons from a pulsed accelerator, and the bands were studied by time-resolved spectroscopy in the range 1.7° to 300°K. At low temperatures, the intensity ratio of the pair and bound-exciton bands is dependent upon sample preparation and excitation intensity. Regardless of the initial value of the ratio, the exciton emission becomes dominant in a transitional temperature range between 60° and 120°K. At room temperature the emission is almost entirely excitonic. The accompanying large changes in the spectral and time-decay characteristics are semiquantitatively explained by a theory based on the assumption of thermal equilibrium of holes amongst the exciton-hole, acceptor, and valence band states. Luminescence excitation measurements in GaP(Zn,O) were used to estimate the concentrations of Zn-O complexes which were correlated with relative luminescence efficiencies and melt compositions.

1. INTRODUCTION

Recent studies[1,2,3] of the low-temperature red luminescence in gallium phosphide doped with Zn and O or Cd and O [GaP(Zn,O) and GaP(Cd,O), respectively] revealed that, in both cases, the emission is composed of two overlapping bands. Previous investigators were unaware of this major complication.[4,5,6] The recent experiments established that the red bands arise from the formation of nearest-neighbor Zn-O or Cd-O donor-acceptor pair complexes. The concentration of these

[1] C. H. Henry, P. J. Dean, and J. D. Cuthbert, Phys. Rev. 166, (Feb. 1968) pp. 754-756.

[2] T. N. Morgan, B. Welber, and R. N. Bhargava, Phys. Rev. 166, (Jan. 1968) p. 751.

[3] P. J. Dean, C. H. Henry, and C. J. Frosch Phys. Rev. (to be published).

[4] M. Gershenzon, F. A. Trumbore, R. M. Mikulyak, and M. Kowalchik, J. Appl. Phys. 36 (1965) p. 1528 and J. Appl. Phys. 37 (1966) p. 483.

[5] D. F. Nelson and K. F. Rodgers, Phys. Rev. 140 (1965) p. A1667.

[6] J. A. W. Van der Does de Bye, Phys. Rev. 147 (1966) p. 589.

nearest-neighbor substitutional complexes is much greater than anticipated for a random distribution of donors and acceptors and indicates that preferential pairing occurs on the nearest-neighbor sites.[7] The Cd-O and Zn-O complexes act as deep electron traps. After trapping an electron at low temperatures, the complex becomes negatively charged and can trap a hole by coulomb attraction. The electron and hole then decay as a bound exciton and produce the "bound-exciton band." If a hole is not trapped, the electron will eventually recombine with a hole on a distant acceptor. This recombination results in the "pair band" lying somewhat lower in energy than the bound exciton band. The energy levels and transitions are indicated in Figure 1.

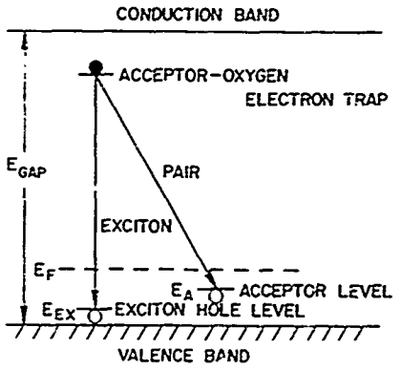

Figure 1. Energy level diagram showing the transitions that give rise to the bound exciton and pair luminescence bands in GaP(Cd,O) or GaP(Zn,O). Electrons are trapped at Cd-O or Zn-O complexes. Holes are trapped either at free Cd or Zn atoms (level E_A) or at negatively charged Cd-O or Zn-O complexes (exciton-hole level E_{ex}).

In contrast with the bound exciton luminescence, the pair luminescence persists for long times after pulse excitation and, in this respect, resembles the well-known "green" donor-acceptor pair recombination in GaP.[8] In the red pair bands, however, there is no electrostatic energy contribution $e^2/\epsilon r$ to the photon energy, so that the distinctive series of sharp lines normally present in donor-acceptor pair spectra is missing.

---

[7]From the intensity of the Zn-O infrared pair band and the saturation of this band it is estimated that the concentration of isolated oxygen is less than 5×10^{17} atoms/cm^3. Therefore the concentration of 5×10^{16} Zn-O nearest-neighbor pairs, reported later in this paper, must be due to preferential pairing.

[8]D. G. Thomas, M. Gershenzon, and F. A. Trumbore, Phys. Rev. 133, (1964) p. A269.

The pair band and the bound-exciton band are broadened primarily by the phonon coupling of the deeply trapped electron, so that both bands have approximately the same shape and ~135-meV half-width. They are separated by the difference in the binding energies of a hole trapped on an exciton or on an acceptor. The small energy separations, 25 meV for GaP(Zn,O) and 60 meV for GaP(Cd,O) result in extensive overlap of the bands.

This paper describes a detailed study of the temperature dependence of the spectral position and time-decay characteristics of the red luminescence. At low temperatures, the intensity spectrum is quite sample dependent. Whether the red luminescence is dominated by the pair band or bound-exciton band depends upon the number of neutral acceptors available for pair decay. In general, low acceptor concentrations favor the bound-exciton band and high concentrations, the pair band. Because the density of exciton-hole states is proportional to the excitation intensity, the intensity spectrum at any acceptor concentration depends on the excitation intensity. Therefore, intense excitation favors the bound-exciton band and weak excitation, the pair band. In heavily p-type GaP(Zn,O) it is believed that hole-tunnelling effects cause the bound exciton decay to dominate the luminescence even for weak excitation.

At high temperatures, up to 300°K, the time-decay characteristics and spectral position of the red luminescence show that the bound-exciton band dominates the emission of both GaP(Cd,O) and GaP(Zn,O) crystals regardless of acceptor concentration and excitation intensity. This is explained by the much larger transition probability for exciton over pair decay and by the assumption of a thermal equilibrium distribution of holes among the hole states at elevated temperatures.

Also discussed are absorption spectra of the bound-exciton transitions obtained by luminescence excitation and measurements of the red-luminescence efficiency. These measurements have provided information on the densities of Cd-O and Zn-O complexes and insight into the doping conditions for optimal luminescence efficiency.

2. EXPERIMENTAL TECHNIQUES

Time-resolved spectra and luminescence decay times in the liquid hydrogen and helium ranges were recorded in the following manner:[9] The samples were repetitively excited in the refrigerants by 100-nsec electron pulses from a Van de Graaff accelerator operating at 300 keV. The maximum current density at the sample was about 0.1 A/cm^2. The luminescence pulses were dispersed by a Spex f/6.8 scanning spectrometer and detected at the output slit by an RCA 7102

[9] J. D. Cuthbert and D. G. Thomas, J. Appl. Phys. (Feb. 1968).

photomultiplier. The S-1 photocathode and blaze of the grating provided a spectral response constant to within 10 percent over the red wavelength range. The photomultiplier output was displayed on a Tetronix 564 Sampling Oscilloscope triggered coincidentally with the arrival of the electron pulses at the sample. For time-resolved spectra, the analog output of the oscilloscope, proportional to the luminescence intensity I(t) at a time t defined by the setting of the sampling window, provided the Y deflection and the wavelength analog voltage from the spectrometer provided the X axis deflection of an X-Y recorder. Luminescence decay curves for a given spectrometer wavelength setting were obtained by using the same arrangement but with the time analog voltage from the sampling oscilloscope applied to the X axis of the recorder.

Although the overall luminescence efficiency of the samples was usually high, the large breadth of the red bands compared with the 7Å resolution used for recording the spectra resulted in relatively weak photomultiplier signals. The necessity of using a photomultiplier detector with an S-1 photocathode having a quantum efficiency of less than 1 percent accentuated this problem. It was therefore found desirable to sometimes reduce the bandwidth of the system to provide more sensitivity by using a cathode follower and variable load resistors at the photomultiplier output. Care was exercised not to distort the pulse shape in the time interval of interest.

The study of samples at temperatures in the range between 20° and 300°K was facilitated by a specially constructed variable temperature dewar. The samples were again excited by energetic electrons which passed into the dewar through a stainless steel window. The samples were maintained at a given temperature by forced convection of helium gas at the appropriate temperature. Pilot experiments showed that this scheme enabled the heat dissipated in the sample to be effectively removed.

3. CRYSTAL DATA

The crystals of GaP(Cd,O) and GaP(Zn,O) were grown by cooling Ga-rich solutions in sealed evacuated vitreous silica tubes.[10] The acceptor concentration was varied by changing the percentage of acceptor added to the melt. The O content was varied by adding Ga_2O_3 to the melt. Invariably O is also present as a natural impurity in the starting materials, so that the total O concentration is incompletely

[10]See, for example, J. F. Miller in "Compound Semiconductors," edited by R. K. Willardson and H. L. Goering, Vol. 1, Chap. 23, Reinhold Publishing Corp., N.Y. (1962).

controlled. Although the distribution coefficient for Cd between Ga and GaP is unknown, the solubility of Cd is much smaller than Zn in GaP. Barrier capacitance measurements show that the amount of Cd was not greatly in excess of the donor contaminants; sulphur is the major inadvertant donor impurity.

When the Cd-doped crystals were slowly cooled to room temperature after growth, bound-exciton decay dominated the low-temperature red luminescence. On the other hand, when the Cd-doped samples were rapidly cooled after growth from 800°C to room temperature, the pair recombination dominated the red luminescence. It is believed that slow cooling reduces the number of isolated Cd acceptors. At present the fate of these acceptors is uncertain. It might be theorized that this reduction in the acceptor concentration results from an increased pairing with O donors, but absorption measurements did not confirm this. Decreasing the number of Cd acceptors decreases the pair luminescence relative to the bound-exciton luminescence. Although observable, these effects are less prominent in Zn-doped samples, especially at high acceptor concentration, probably because Zn is much more soluble in the GaP lattice than Cd.

4. RESULTS

a. Bound-Exciton Decay Times in GaP(Cd,O) and GaP(Zn,O)

The decay time of the bound exciton was studied in several slow-cooled crystals of GaP(Cd,O). Slow cooling emphasizes the bound-exciton band relative to the pair band. Further discrimination against the pair band was obtained by choosing a spectrometer wavelength setting corresponding to the prominent zero-phonon line or first phonon replica. Figure 2 shows that the decays are exponential and have values of 560 and 330 nsec at 1.7° and 20°K, respectively. Many of the crystals showed a small post-excitation increase in luminescence lasting about 15 nsec. The luminescence efficiency remains constant in this temperature interval, so it is concluded that the change in decay time results from thermalization between the bound-exciton A and B states[i] which are separated by an energy of 2.1 meV. A straightforward calculation, based on these experimental values and Equation (1) in reference of footnote 11, yields the decay time values τ_A = 0.1 μsec and τ_B = 0.6 μsec.

For GaP(Zn,O) it is not possible to discriminate spectrally against the pair decay because of the overlap of the pair and bound-exciton bands and because of the absence of sharp lines in the latter. Slow-cooled, rather strongly excited crystals

[11] J. D. Cuthbert and D. G. Thomas, Phys. Rev. 154 (1967) p. 763.

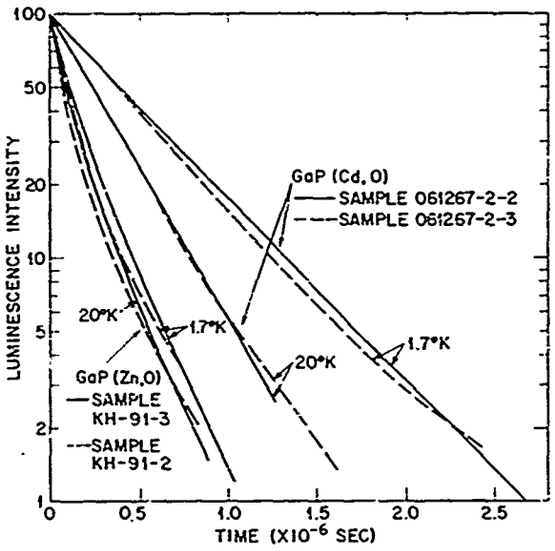

Figure 2. Fluorescence time-decay characteristics for two slow-cooled crystals of GaP(Cd,O) and GaP(Zn,O). For GaP(Cd,O) the zero of time is taken 15 nsec after the end of the exciting electron pulse. For GaP(Zn,O) the zero of time is at the end of the exciting pulse.

afford the best chance of observing the true excitonic decay time. Under such conditions the density of exciton-hole states is high, thereby enhancing the bound exciton band.

Figure 2 shows that the decays at 1.7°K and 20°K are similar and reasonably exponential. No post-excitation increase in luminescence occurred in these crystals. Assuming that the j-j splitting of the A and B states is roughly equal to that in GaP(Cd,O), the lack of any temperature dependence due to thermalization between A and B states implies a large degree of mixing between these states. The data indicate a value for τ_A of about 100 nsec.

For both GaP(Cd,O) and GaP(Zn,O) the slight sample dependence of the time-decay characteristics is attributed to the variable contribution of the long-lived pair luminescence.

b. Temperature Dependence of Luminescence Decay Curves and Time-Resolved Spectra for GaP(Cd,O)

Figure 3 shows the temperature dependence of the time-resolved spectra from a fast-cooled sample of GaP(Cd,O). It may be assumed that the bands have the same change in energy with temperature as the indirect band gap. According to this assumption, the arrows in the figure indicate where the peaks of the bound-exciton band would be expected to lie at high temperatures. As explained in the previous

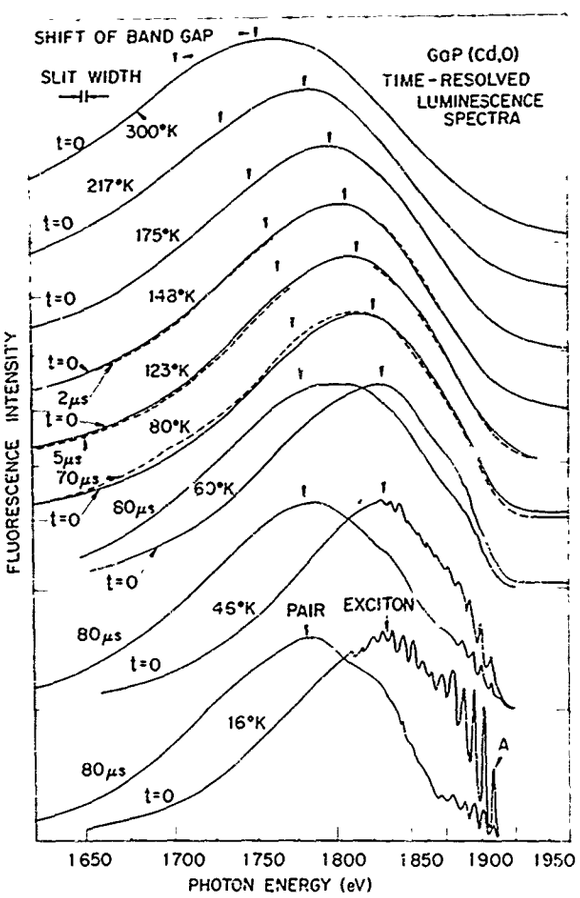

Figure 3. Normalized time-resolved spectra as a function of the temperature of a fast-cooled crystal of GaP(Cd,O). The exciting-electron beam-current density was about 0.05 A/cm^2. At 16°K the arrows show the energies of the clearly resolved pair and bound exciton bands. The arrows at higher temperatures show the expected energy position of these peaks after the variation in band gap energy is allowed for.

section, fast-cooled crystals have a larger fraction of pair luminescence, which was desirable here. At temperatures up to 46°K the pair and bound-exciton bands are clearly resolved. At 60°K the bound-exciton band appears almost unchanged in energy although the sharp phonon sidebands have become thermally broadened to the extent that they are almost unresolved. The pair peak, however, has shifted distinctly to higher energy. Between 60° and 80°K the two bands have merged into a single spectrum located at an intermediate energy. Between 80° and 148°K the spectrum moves to higher energy relative to the band gap until it coincides with the position predicted for the bound-exciton band alone.

The relative contributions of the bound exciton and pair bands to the total luminescence can be inferred from Figure 4 which shows the spectra formed by integrating the single pulses from the photomultiplier. A careful comparison of the normalized spectra in Figures 3 and 4 shows that up to approximately 80°K, where

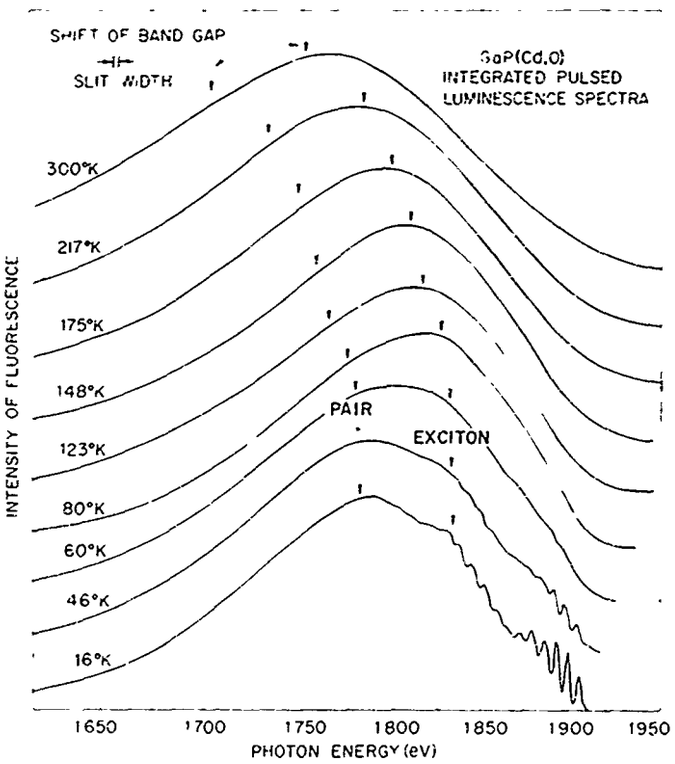

Figure 4. Normalized spectra obtained by integrating the photomultiplier response to the light from the same pulse-excited crystal of GaP(Cd,O) used for Figure 3. The excitation conditions were identical with those in Figure 3. The arrows show the expected energy positions of the bound-exciton- and pair-band peaks at the various temperatures. Up to about 60°K the pair band is dominant. Above the transitional temperature range (approximately 70° - 100°K) the bound-exciton band dominates.

the time-resolved spectra coalesce, the integrated and pair bands are identical. Above 80°K the spectra in the two figures must be, and are, identical, and correspond mainly to bound-exciton recombination. The total red luminescence efficiency was found to change with temperature in much the same way as previously reported for GaP(Zn,O).[4]

The time-decay characteristics of the total red emission as a function of temperature for the same crystal are presented in Figures 5 and 6 for the time ranges 0 to 2.8 μsec and 0.1 to 100 μsec, respectively. At all temperatures, it was noticed that the build-up time of the luminescence was equal to the length (100 nsec) of the exciting pulse (see Reference 6). It is seen in Figure 5 that up to about 70°K there is an initial fast decaying luminescence followed by a very long-lived component, which considering the results in Figure 3 must be associated with the bound-exciton and pair-luminescence bands respectively. The 1/e decay times ($\tau_{1/e}$) taken from Figure 5 are plotted in Figure 7. Thermalization of excitons from the B into the A state causes the temporary decline in $\tau_{1/e}$ as the temperature is raised from 1.7°K (see paragraph 4a. of this attachment). Figure 5 shows that between 70° and 90°K the pure bound-exciton component becomes much less noticeable; Figure 6 shows that in this same temperature range, the long-lived luminescence begins to decay much faster. These results corroborate the results in Figures 3 and 4 by showing that near 70°K the pair and bound-exciton systems have a similar time decay. As the temperature is increased beyond this point, the luminescence decay rate gets progressively faster and becomes more nearly exponential in form. These changes are clearly reflected by the parameter $\tau_{1/e}$ in Figure 7.

In the temperature range ($\lesssim$ 50°K) where thermal equilibrium is not attained, it is observed that the intensity of the bound-exciton band increases rapidly relative to the pair band for exciting-beam current densities in the range 0.01 to 0.1 A/cm^2, corresponding to carrier injections of 10^{16} to 10^{17} electron-hole pairs/cm^3 per pulse. In terms of the model for the luminescence, this variation is reasonable, since the density of exciton-hole states is always equal to the number of occupied Cd-O$^-$ states and the latter is proportional to pumping power. Hence, low pumping intensity ($< 10^{16}$ electron-hole pairs/cm^3) favors pair recombination because the density of exciton-hole states is small in comparison to the density of free Cd acceptor states, estimated to be $\sim 10^{17}$/cm^3. When the carrier injection per pulse is approximately equal to this acceptor density, the probability for the capture of holes into the isolated acceptor and exciton-hole states will be comparable and the bound-exciton band will grow relative to the pair band.

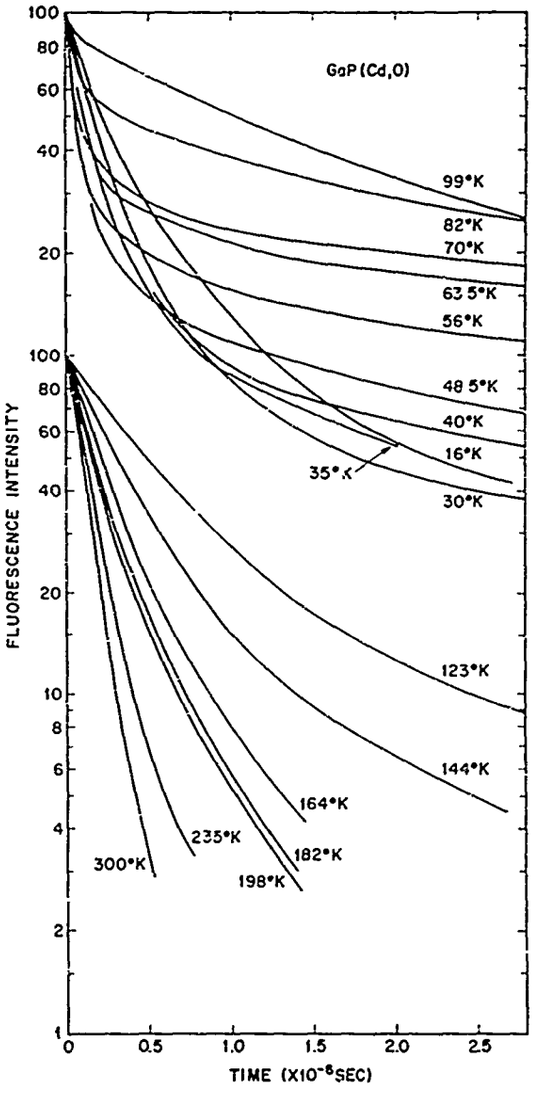

Figure 5. Total luminescence time-decay characteristics of the red band from the same GaP(Cd,O) crystal and with the same excitations used for Figure 3. At low temperatures the decays show the fast exciton decay followed by the long pair decay. Between 80°K and 100°K the bound-exciton decay lengthens and merges with the long-lived component. Above 100°K the decay rate increases and becomes more nearly exponential.

c. Temperature Dependence of Luminescence Decay Curves and Time-Resolved Spectra for GaP(Zn,O)

The temperature dependence of the time-resolved spectra for GaP(Zn,O), shown in Figure 8, is qualitatively the same as that in Figure 3 for GaP(Cd,O). For this crystal there is little change in the spectra up to 30°K. At 40°K the pair band has moved significantly to higher energies, whereas the bound-exciton band has

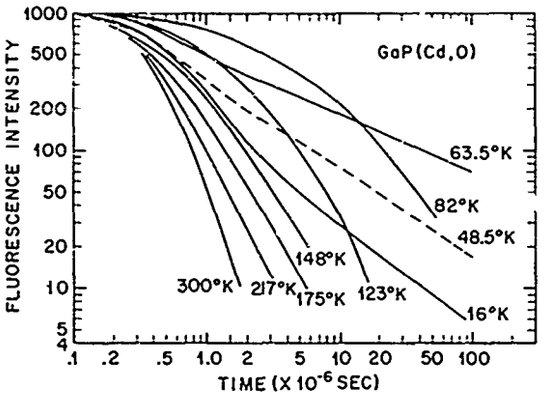

Figure 6. Total time-decay characteristics of the long-lived luminescence from the same GaP(Cd,O) crystal and with the same excitation conditions used for Figure 3. At temperatures up to 63°K the long-lived luminescence obeys a power low characteristic of pair decay. At 83°K and above, the decay rate of the long-lived luminescence increases rapidly.

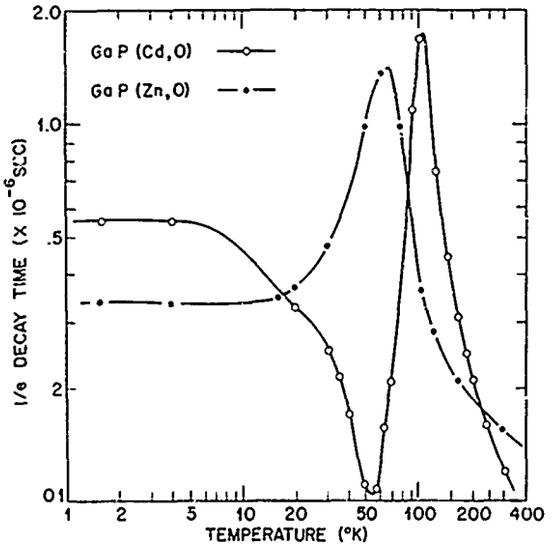

Figure 7. Plots of the 1/e decay times ($\tau_{1/e}$) taken from Figures 5 and 10. For GaP(Cd,O) the initial decrease in $\tau_{1/e}$ is caused by the thermal redistribution of the bound-exciton population between the A and B exciton states. The changes in $\tau_{1/e}$ at temperatures above 60°K are due to the onset of thermal equilibrium of holes among the hole states. A similar situation holds for GaP(Zn,O) although, for reasons discussed in the text, no initial decrease in $\tau_{1/e}$ is observed.

hardly changed in position. By 60°K it has become impossible to distinguish the individual emissions through time-resolved spectroscopy; this indicates that the two bands now have similar time decays. At this temperature the location of the

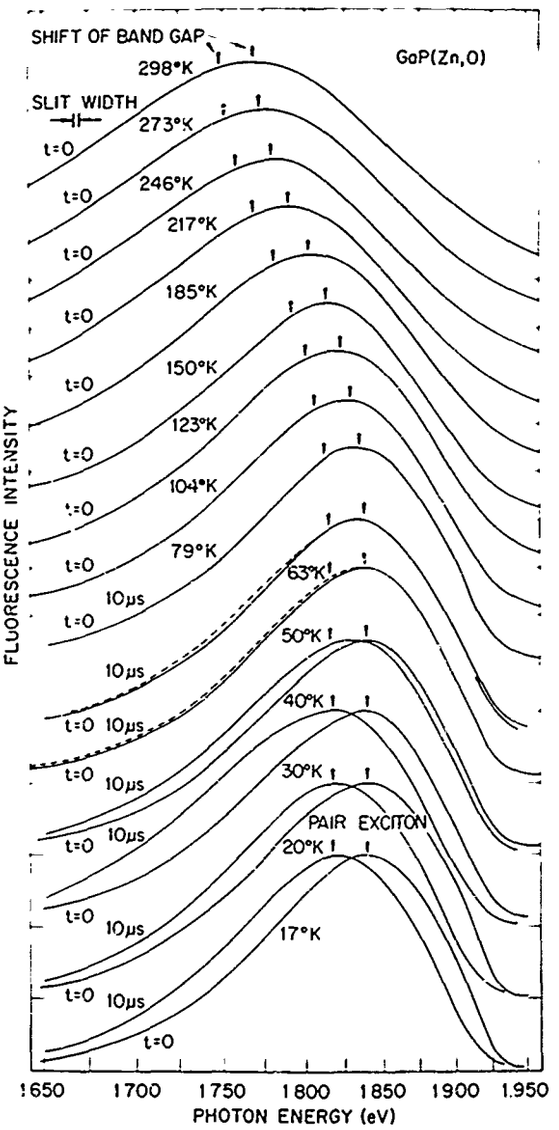

Figure 8. Normalized time-resolved spectra as a function of the temperature of a fast-cooled crystal of GaP(Zn,O). The exciting-electron-beam current density was about 0.05 A/cm^2. At 1.7°K the arrows show the peaks of the resolved pair and bound exciton bands. The arrows at higher temperatures show the expected energy position of these peaks after allowing for the variation in band gap energy.

composite band is slightly shifted to lower energies from the position that the bound exciton band alone would occupy. From 60° to 100°K, the composite band shifts a little further to higher energies relative to the band gap energy to become coincident with the exciton band. At still higher temperatures the shifts are accounted for by band-gap variation alone.

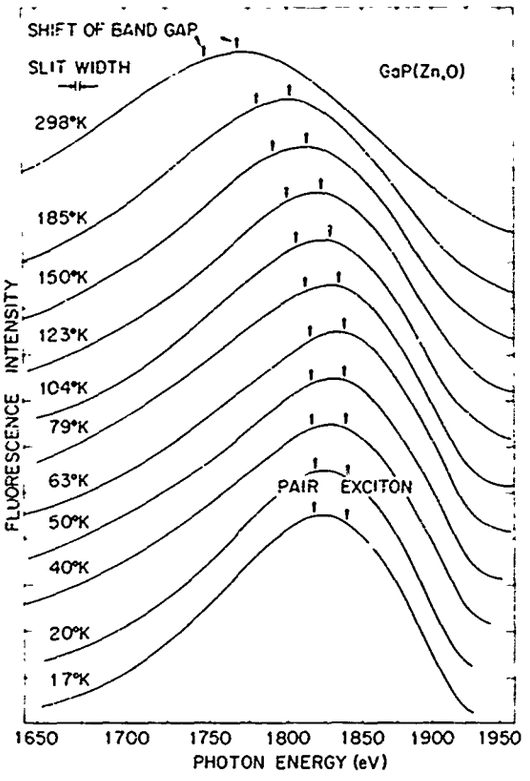

Figure 9. Normalized spectra obtained by integrating the photomultiplier response to the light from the same pulse-excited crystal of GaP(Cd,O) and with the same excitation conditions used for Figure 8. The arrows show the expected energy positions of the bound-exciton- and pair-band peaks at the various temperatures.

Figure 9 shows the integrated spectra for the same excitation intensity and temperatures. Detailed comparison of the spectra in Figures 8 and 9 shows that the integrated spectra fall nearer the 10-μsec time-resolved pair spectra at temperatures up to 30°K. At higher temperatures the emission becomes progressively more heavily weighted towards bound exciton emission. The total red luminescence intensity altered with temperature in the way previously described.[4]

Figures 10 and 11 show the corresponding temperature dependence of the luminescence time-decay characteristics of the total red emission for the same crystal. The $\tau_{1/e}$ decay times are plotted versus temperature in Figure 7. Comparison with GaP(Cd,O) in the low temperature region up to 30°K shows the initial fast decay due to the bound exciton is not as easily distinguished from the slow decay of the pairs in this crystal. However, other crystals were examined in which the bound exciton was very dominant at the lowest temperatures, and in such cases the faster decaying bound exciton was readily distinguished. Nevertheless, it is easily

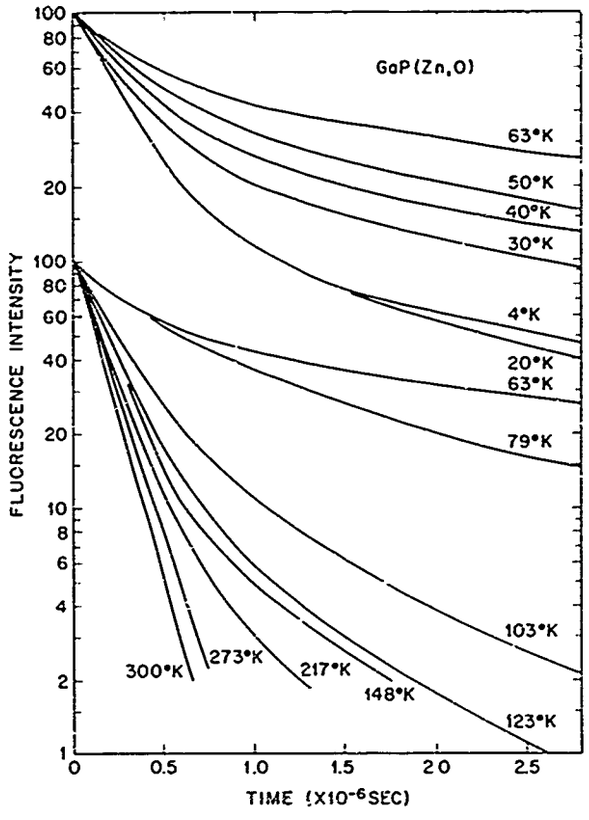

Figure 10. Total luminescence time-decay characteristics of the red band from the same crystal and with the same excitation conditions used for Figure 8.

seen from Figures 7 and 10 that as the tempera raised to about 60°K the initial excitonic decay becomes increasingly long after . ich it decreases. Note that in agreement with the results of paragraph 4a. of this attachment an initial decrease in $\tau_{1/e}$, due to excitons thermalizing from the B state into the A state as the temperature is raised above 1.7°K, is not observed for GaP(Zn,O).

The decay rate of the luminescence at longer times due to the pairs (Figure 11) exhibits little change with temperature up to 50°K. Between 60° and 100°K the decay rate of the long-lived component increases very rapidly and at still higher temperatures continues to increase but more slowly. This behavior is consistent with the data in Figures 8 and 9 which show a sizable contribution from pair emission up to about 60°K and an increasingly dominant bound-exciton emission above the transitional temperature range 50° to 70°K.

Some evidence of low temperature tunnelling between hole states was obtained from a series of experiments in which an argon ion laser was used to excite GaP(Zn,O) crystals containing Zn concentrations in the range from 2×10^{17} to

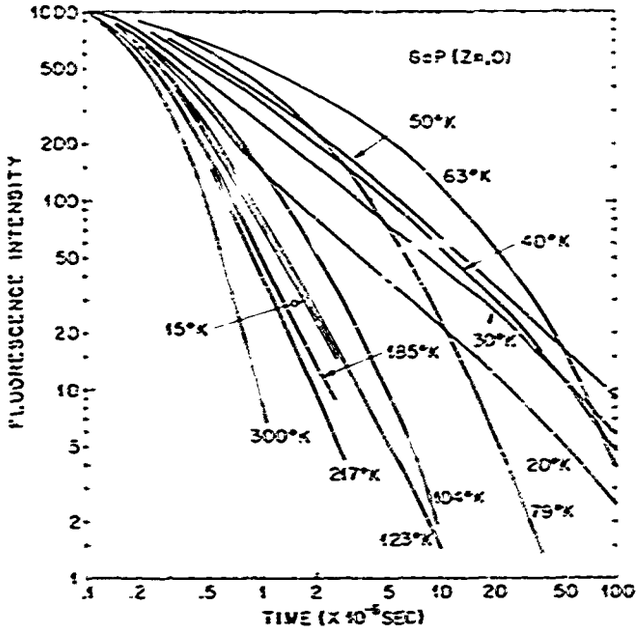

Figure 11. Total time-decay characteristics of the long-lived luminescence from the same GaP(Zn,O) crystal and with the same excitation conditions used for Figure 8.

5×10^{18} atoms/cm^3 at 1.7°K. When the Ar ion laser was focused, the bound-exciton band dominated the emission for all crystals. In the unfocused condition (pumping intensity down by a factor of 10^{-4}), the pair band was dominant at Zn concentrations in the range from 2 to 5×10^{17} atoms/cm^3 while for higher concentrations the bound-exciton band intensity increased with concentration. This result is attributed to an increased probability of tunnelling between hole states at high acceptor concentrations.

d. Exciton Absorption Spectra of Cd-O and Zn-O Complexes

The exact shapes of the absorption bands due to the creation of excitons bound to nearest-neighbor donor-acceptor pair complexes were difficult to determine by direct means, since the bands are very broad and the absorption is weak. The absorption spectra were more conveniently obtained from measurements of the intensity of the bound-exciton luminescence as the energy of the exciting radiation, corrected to constant excitation intensity, was scanned through the absorption bands. These spectra will be called LE (luminescence excitation) absorption spectra.

The low-temperature Cd-O LE absorption spectrum obtained in this way is considerably broader than the bound-exciton luminescence spectrum, and the phonon

structure is much weaker.[12] The Zn-O exciton luminescence spectrum is almost devoid of structure so it is not surprising that the corresponding LE absorption spectrum shown in Figure 12 is broad and quite featureless. The no-phonon transition energy of excitons decaying at Zn-O complexes is located near the arrow labelled E_{cent} at 2.01 eV, a point midway between the low-energy half maximum of the LE absorption spectrum and the high-energy half maximum of the luminescence spectrum.[13]

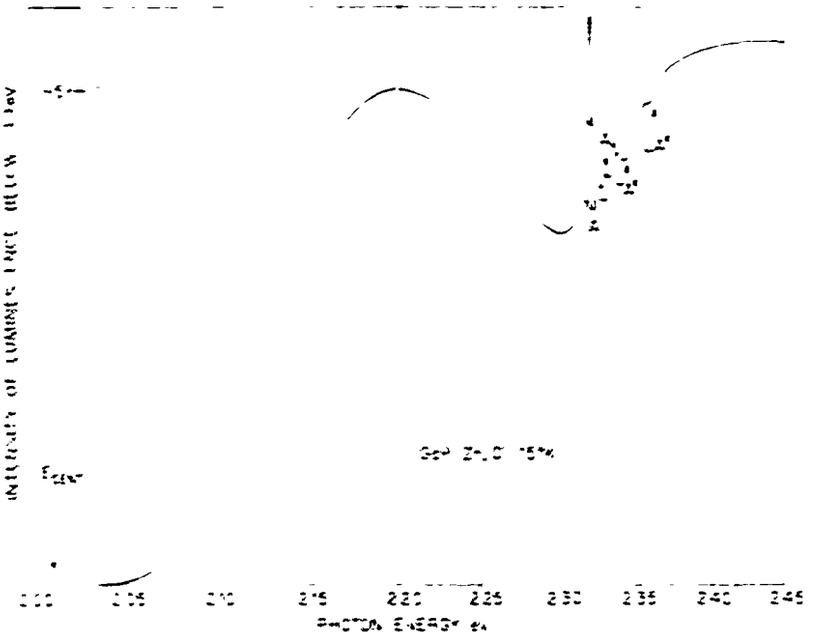

Figure 12. Luminescence excitation spectrum for a slow-cooled crystal of GaP(Zn,O).

The absorption scale in Figure 12 is relevant only to the Zn-O absorption band below 2.30 eV. The structure above this energy is due to the photo-creation of excitons at isoelectronic N impurities (lines A and A_X)[14] and to intrinsic absorption processes (indirect absorption threshold TA^E and LA^E).[15] These absorption

[12] C. H. Henry, P. J. Dean, D. G. Thomas, and J. J. Hopfield, Proceedings of the International Conference on Localized Excitations in Solids, Irvine, California (1967) (to be published).

[13] The exact relationship between E_{cent} and the no-phonon transition energy of the Zn-O exciton is unknown, but the latter probably lies a little below the former since the half bandwidths of the two spectra suggest that the Huang-Rhys factor is larger in the absorption spectrum.

[14] D. G. Thomas and J. J. Hopfield, Phy. Rev. 150, 680 (1966).

[15] P. J. Dean and D. G. Thomas, Phys. Rev. 150, 690 (1966).

processes contribute relatively weakly to the Zn-O exciton luminescence and are therefore lightly weighted in the LE absorption spectrum. The peak absorption of the Zn-O exciton band is ~5 cm^{-1} in GaP crystals optimally doped for the red luminescence measured at 80°K or 300°K, shown in this paper to be due mainly to Zn-O exciton recombinations. When we use the oscillator strength f ~0.07 of the Zn-O exciton transition derived from the decay time measurements of the luminescence, the absorption coefficient corresponds to a Zn-O concentration of ~5 x 10^{16} atoms/cm^3.

It has previously been reported that maximum red luminescence is obtained in solution-grown crystals from Ga containing 0.1 at .% Zn and 0.01 at .% Ga_2O_3.[4] Figure 13 shows that for the series of crystals examined in the present work, the

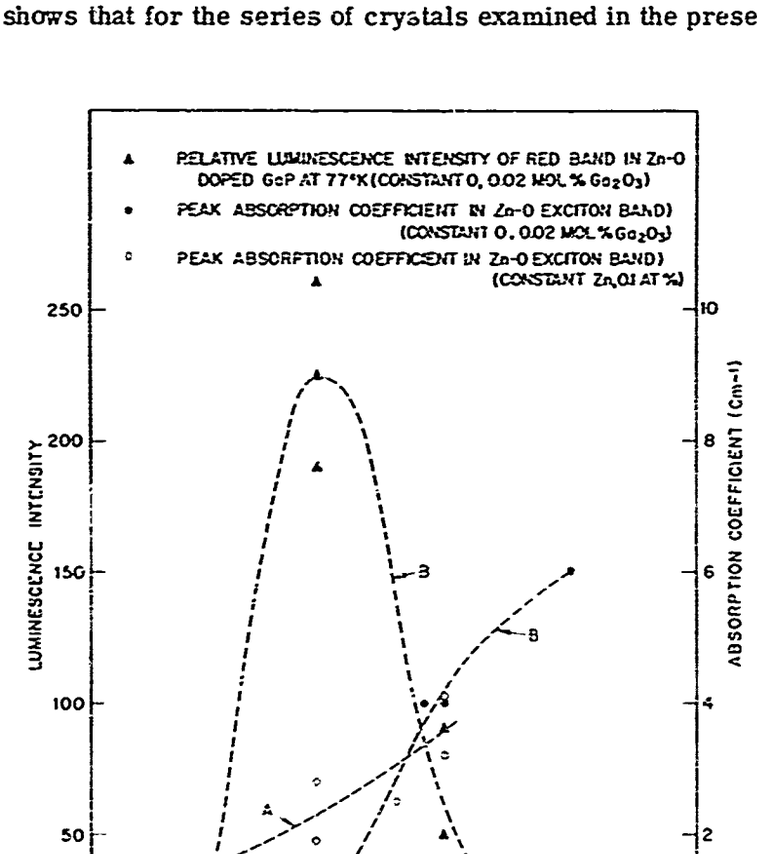

Figure 13. Dependence of the relative red-luminescence intensity and of the peak absorption coefficient in the Zn-O exciton band on the melt composition.

red fluorescence intensity was a maximum for Ga solutions containing close to 0.01 at .% Zn. The concentrations of free Zn acceptors in crystals grown from Ga solution containing 0.01, 0.1, and 1 at .% Zn are respectively 0.5, 1.5, and 5 x 10^{18} atoms/cm^3. It is interesting to note that the Zn-O exciton absorption of these crystals continues to increase up to 1 at .% Zn-doped Ga solution although the luminescence efficiency falls rapidly in this region. It has been shown recently[16] that Auger recombination causes a rapid decrease in the low-temperature luminescence efficiency of the relatively tightly-bound Bi exciton transition in GaP above a neutral donor concentration of ~$10^{18}/cm^3$. Impurity banding sets in at this donor concentration and promotes the interaction of a third electronic particle with the bound exciton. It is very likely that a similar effect is responsible for the quenching of the Zn-O bound-exciton luminescence at the higher Zn concentrations, shown in Figure 13. According to this model, the onset of concentration quenching is expected to be insensitive to temperature changes in the range where isolated Zn acceptors become thermally unstable, in agreement with experiment.

Figure 13 also shows that the Zn-O exciton absorption increases with the amount of Ga_2O_3 in the Ga solution. While there is no background of Zn, there is a significant background concentration of O in these crystals. Recent experiments[3] using the O^{18} isotope shift of the Cd-O bound-exciton no-phonon line as an indicator have shown that it is very difficult to obtain an increase in the concentration of these complexes by more than a factor of 4 or 5. The residual concentration of Cd-O sites is about 0.5 x 10^{+16} cm^{-3} in slow-cooled crystals grown in sealed-off quartz tubes from Ga solution containing 10 at .% Cd, even when rigorous measures are taken to exclude O. Possible sources of this O are the quartz tubes and the GaP source material.

5. DISCUSSION

The time-resolved spectra and luminescence time-decay characteristics of the red luminescence exhibit the following principle features.

(1) At low temperatures there is a rapid bound exciton decay followed by a slow pair decay and two distinct spectra are recorded in time-resolved spectroscopy corresponding to the pair and bound-exciton bands. The crystals chosen for the study had prominent pair bands at low temperatures at the excitation levels used.

(2) As the temperature is raised above ~60°K for GaP(Zn,O) and above ~80°K for GaP(Cd,O) the initial fast excitonic component in the total time decay

[16] J. C. Tsang, P. J. Dean, and P. T. Landsberg (to be published).

lengthens to become substantially longer than the bound-exciton lifetime. Also, the long pair decay shortens, so that the combined time-decay characteristics eventually approximate a single exponential. At the same time, the intensity spectra alter and show that the bound-exciton band begins to dominate the total emission.

(3) As the temperature is raised still further, the time-decay characteristics of the total luminescence get significantly more rapid. Apart from broadening and a shift due to the band gap variation with temperature, no further changes in the intensity spectra are seen.

These effects can be accounted for semiquantitatively by assuming that the holes in acceptor states, in bound-exciton hole states, and in the valence band are in thermal equilibrium at the higher temperatures. It is also assumed that in the temperature range 1.7° to 300°K the electron remains trapped at the acceptor O complex. Let p_A and p_{ex} be the occupation probabilities for a hole to be in an acceptor state and in a bound exciton hole state. If the holes are in thermal equilibrium, the occupation probabilities are given by Fermi-Dirac statistics as[17]

$$p_A = \left[1 + D_A^{-1} \exp\left\{\left(E_F - E_A\right)/kT\right\}\right]^{-1} \tag{1}$$

$$p_{ex} = \left[1 + D_{ex}^{-1} \exp\left\{\left(E_F - E_{ex}\right)/kT\right\}\right]^{-1} \tag{2}$$

where E_F, E_A, and E_{ex} are the energies of the quasi-Fermi level governing the hole distribution, the acceptor level, and the level corresponding to a hole in a bound-exciton hole state. These energies are measured relative to the valence-band maximum. D_A and D_{ex} are the degeneracies of the hole on the acceptor and in the bound exciton. The acceptor ground state is four-fold degenerate, while the hole in the bound exciton is two-fold degenerate.[18] Let τ be the lifetime of an electron trapped on the acceptor-oxygen complex. The trapped electron decay rate τ^{-1} is given by

$$\tau^{-1} = W_{ex} p_{ex} + \sum_r W(r) p_A \tag{3}$$

[17] See, e.g., J. S. Blakemore, "Semiconductor Statistics," Pergmagon Press (1962).

[18] The zone center-valence-band hole states are four-fold degenerate. These states are split into two Kramers doublets by the crystal field of the acceptor-oxygen site.[1,12] In calculating p_{ex} we should take into account both doublets; this is done by changing D_{ex} in Equation (2) from 2 to 2 + 2 exp (- $\Delta E/kT$) where ΔE is the splitting between the states and is taken to be 10 meV. We can not justify this noice, but other reasonable value of ΔE would not substantially alter the results of the calculation.

where W_{ex} is the exciton decay rate and W(r) is the decay rate for the electron to recombine with a hole located on an acceptor a distance r from the trapped electron. The transition rate W(r) is taken to be[19]

$$W(r) = W_{max} \exp(-2r/a) \tag{4}$$

where a is the Bohr radius of the hole on the shallow acceptor. This formula is only valid when either the hole or the electron is tightly bound. It is applicable in our situation because the electron is very tightly bound compared to the hole. W_{max} is the transition rate for r = 0 (that is, when the electron and hole wave functions have maximum overlap). W_{max} is estimated to be equal to W_{ex} multiplied by the ratio of the maximum hole density on the acceptor to the maximum hole density in the bound exciton. These densities are inversely proportional to the cube of the ratio of the Bohr radii of the holes on the acceptor (a) and in the bound exciton (a_{ex}) so that

$$W_{max} \approx W_{ex} \left(a_{ex}/a \right)^3 \tag{5}$$

The total rate of pair decay is given by

$$\sum_r W(r) = \left(N_A - N_D\right) W_{ex} \left(\frac{a_{ex}}{a}\right)^3 \int_0^\infty 4\pi r^2 \exp(-2r/a)\, dr$$

$$= \left(N_A - N_D\right) W_{ex} \left(a_{ex}\right)^3 \pi \tag{6}$$

where N_A is the acceptor density, N_D is the donor density, and $(N_A - N_D)$ is the density of neutral acceptors. The ratio of the bound-exciton intensity to the pair-band intensity is given by

$$I_{ex}/I_{pair} = W_{ex} p_{ex} \Big/ \sum_r W(r) p_A \approx p_{ex}/p_A \left(N_A - N_D\right) \left(a_{ex}\right)^3 \pi \tag{7}$$

The Boltzmann factors appearing in Equations (1) and (2) may be calculated using standard semiconductor statistics.[17] They depend upon N_A, N_D, the binding energy of the acceptor E_A, and the density of states effective mass of the hole, which is taken to be 0.37 times the free electron mass.[20]

[19] D. G. Thomas, J. J. Hopfield, and W. M. Augustyniak, Phys. Rev. 140, 202 (1965).
[20] R. A. Faulkner (private communication).

For the case of GaP(Zn,O), we take $N_A = 10^{18}$ atoms/cm^3 and $N_D = 2 \times 10^{17}$ atoms/cm^3. The binding energy of the Zn acceptor is known to be 62 meV.[21] These estimates of N_A and N_D for the Zn-doped samples are based on the solubility measurements of Trumbore et al.[22] The Cd-doped samples are less heavily doped and more highly compensated than the Zn-doped samples, and we estimate that $N_A = 10^{17}$ atoms/cm^3 and $N_D = 4 \times 10^{16}$ atoms/cm^3. We are much less certain of the latter parameters than of the parameters for the Zn-doped samples. The binding energy of the Cd acceptor is known to be 95 meV.[21] For both Zn and Cd we take W_{ex} to be 10^7 sec^{-1} (see paragraph 4a.), the binding energy of the hole in the bound exciton to be 36 meV, and the Bohr radius of the hole in the bound exciton to be 16.9Å. The predicted lifetime τ and ratio I_{ex}/I_{pair} are plotted versus temperature in Figure 14.

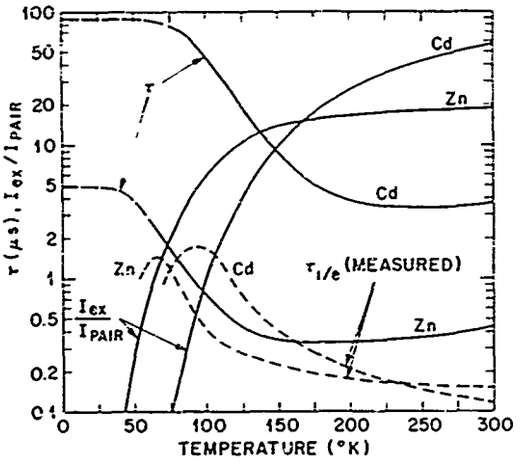

Figure 14. Comparison of the calculated decay times with the experimentally-determined decay times of the red emission. A comparison is only meaningful at temperatures where thermal equilibrium conditions approximate, namely above ~80°K for GaP(Cd,O) and above ~ 60°K for GaP(Zn,O).

If true thermal equilibrium were achieved, the red luminescence would decay exponentially, giving straight lines in Figures 5 and 10. The deviation from an exponential decay gives some indication of the deviation from thermal equilibrium.

[21] P. J. Dean, J. P. Cuthbert, D. G. Thomas and R. T. Lynch, Phys. Rev. Letters 18, 122 (1967).

[22] F. A. Trumbore, H. G. White, M. Kowalchik, R. A. Logan, and C. L. Luke, J. Electrochem. Soc.

Clearly, at low temperatures there is very little thermalization. Because thermal equilibrium is only approximately achieved even at the higher temperatures, only qualitative agreement is expected between theory and experiment.

The ratio I_{ex}/I_{pair} is predicted to be unity at 65°K for the Zn-doped sample and at 100°K for the Cd-doped sample and to increase rapidly with temperature. Experimentally, it is found that the bound exciton becomes dominant above 60°K in Zn-doped samples and above 80°K in Cd-doped samples in good agreement with theory. It is predicted that the ratios of I_{ex}/I_{pair} are 19 for Zn-doped samples and 57 for Cd-doped samples at 300°K.

At room temperature, the densities of free holes in the valence band and holes in the acceptor states are of the same order of magnitude so that the intensity of the recombination luminescence due to free holes annihilating the trapped electrons is expected to be of the same order of magnitude as the pair luminescence intensity. Therefore the bound-exciton luminescence is predicted to dominate both the pair luminescence and the free-to-bound luminescence at room temperature, in agreement with experiment.

The calculated and measured lifetimes are compared in Figure 14. The experimental lifetimes peak at 65°K in Zn-doped crystals and at 95°K in Cd-doped crystals. Theory and experiment can only be compared at these temperatures and at higher temperatures. Below these temperatures little thermalization of the holes has taken place. The agreement between theory and experiment is fairly good for the case of GaP(Zn,O). The maximum experimental lifetime $\tau_{1/e}$ (measured at the e^{-1} intensity point) is 1.5 μsec at 65°K. The predicted value at this temperature is 2.3 μsec. At higher temperatures both the predicted and the experimental lifetimes decrease. The experimental lifetime decreases faster, however, presumably because nonradiative processes shorten the experimental lifetime and these processes become increasingly important at higher temperatures.

For the Cd-doped crystals, the agreement is much worse. While the experimental lifetime at 100°K of 1.7 μsec is long compared to the exciton lifetime (0.1 μsec), in agreement with our ideas, this lifetime is small compared to the predicted lifetime of 45 μsec. The agreement remains poor at higher temperatures. At present the reason for this disagreement is not understood. It may result because thermalization is less likely in Cd-doped samples because of the large Cd binding energy (95 meV) and because the assumed concentration of Cd acceptors is rather low. It is also possible that nonradiative processes, which shorten the measured lifetime, are more important in the Cd-doped material.

6. CONCLUSIONS

It was previously established by Henry, Dean, and Cuthbert[1] that the low-temperature red luminescence in GaP(Zn,O) and GaP(Cd,O) is due to the near superposition of a pair band and a bound-exciton band. In this paper, the red luminescence has been studied by electron beam excitation in the temperature range from 1.7° to 300°K. Above about 50°K the bound holes in the acceptor and exciton-holes states tend to come into thermal equilibrium. The thermalization appears to be only partially achieved, becoming more effective at higher temperatures. The result of this thermalization is to cause the red luminescence to be dominated by bound-exciton decay above 60°K in Zn-doped crystals and above 80°K in Cd-doped crystals. As thermalization is achieved, the time-decay characteristic of the red luminescence becomes more nearly exponential. Although the red luminescence is dominated by exciton decay above 80°K, the decay time of the luminescence is much longer than the bound exciton decay time between 80° and 150°K, because the processes promoting thermal equilibrium cause holes to be continuously transferred from the acceptor to the bound-exciton hole states. The decay time becomes shorter with increasing temperature as the bound-exciton decay becomes increasingly dominant. Bound-exciton decay is the principal source of red luminescence at room temperature. These results can be explained semiquantitatively by the theory of thermal equilibrium among the hole states presented in this paper. The agreement between theory and experiment is much better for Zn than for Cd. Measurement of the luminescence excitation spectra in GaP(Zn,O) shows that although the concentration of Zn-O complexes continues to rise as the Zn acceptor concentration is increased above that corresponding to maximum luminescence efficiency, the onset of concentration quenching of the luminescence, probably by nonradiative Auger processes, offsets any possible increase in luminescence efficiency. The absolute concentrations of the Zn-O and Cd-O complexes have been estimated from measurements of the exciton absorptions and luminescence decay times.

Acknowledgements

The authors are indebted to R. T. Lynch for the crystals and to W. P. Knox for constructing the variable temperature irradiation dewar. Discussions with R. A. Faulkner, D. G. Thomas, and D. K. Wilson were most helpful and encouraging.

ATTACHMENT III

A VARIABLE TEMPERATURE DEWAR FOR CATHODOLUMINESCENCE STUDIES

by

W. P. Knox
J. D. Cuthbert

* This article will appear in the Review of Scientific Instruments.

A VARIABLE TEMPERATURE DEWAR FOR CATHODOLUMINESCENCE STUDIES

Abstract

We describe a single refrigerant variable-temperature dewar employing the forced convection of cold gas to obtain sample temperatures in the range 12° to 300°K. Although the dewar was developed for cathodoluminescence studies using 100- to 400-KeV electrons, the design permits easy modification for other uses. The dewar features quick cool-down time, the option of fast thermal cycling, the efficient removal of heat from small irregularly shaped samples mounted strain free, the ability to change samples quickly at all temperatures, and thermometry isolated from the sample irradiation chamber.

1. INTRODUCTION

This paper describes a variable-temperature dewar which employs the forced convection of an exchange gas to obtain sample temperatures in the range from 12° to 300°K. The forced convection of gas at the desired temperature effectively removes the heat generated in a sample and maintains its temperature very close to that of the gas. In our experiments the heat is produced in semiconductor samples by a high-energy electron beam used to excite recombination luminescence. The dewar affords the following advantages:

(1) The over-all time required to reduce the sample (and dewar) temperature from 300°K to low temperatures (~12°K) is less than 30 minutes.

(2) The usual liquid nitrogen shield is eliminated.

(3) Several hundred milliwatts of power can be effectively removed from the sample at temperatures potentially as low as 4.2°K.

(4) Since the sample is directly cooled by the gas, thermal contact of the sample with the mount is not necessary so that irregularly shaped samples can be studied and strain-free mounting achieved.

(5) Samples can be changed very conveniently during an experiment without disturbing the experimental setup.

(6) Isolation of the temperature sensors from the vicinity of the irradiation chamber prevents their deterioration by X-ray and electron irradiation.

Several variable temperature dewars have been discussed in the literature,[1] including one by Maeda[2] which also uses purely convective cooling, and variable temperature dewars which are now commercially available. To date, the latter have utilized either forced convective cooling plus electrical heating of the sample to obtain a given temperature or the usual cold finger arrangement — both arrangements require good thermal conduction across the mount-sample interface. None of the designs possess the combination of advantages cited for the dewar described here.

2. DEWAR DESCRIPTION

The dewar is shown in Figure 1. A helium transfer tube, A, is hermetically connected to the cooling-gas input tube, C, by a quick-disconnect coupling, B. The exit nozzle of the transfer tube terminates approximately 2 in. above the sieve of the gas heat exchanger, K.

The heat exchanger, K, consists of a german-silver rod, about 1-in. long and 0.5-in. in diameter, through which are longitudinally drilled sixteen 0.030-inch diameter capillaries. The rod is soldered into a copper block that houses a 40-watt cartridge heater, J. For a typical gas flow of 2100 liters/hr through the sieve, the rate of heat transfer from the heater to the gas is sufficient to cause rapid temperature changes within the range 12° to 80°K when the power supplied to the heater is altered.

Electron excitation of the crystal occurs in the irradiation chamber, N, which adjoins the gas distribution manifold, P. Electrons enter the irradiation chamber by penetrating a 0.0005-in. stainless-steel window, Q, mounted in the face of the irradiation chamber opposite the electron accelerator.

The gas from the heat exchanger, K, enters the distribution manifold, P, which directs the gas flow into the sample tube, D, and thermometer tube, E. The gas distribution manifold has a large flat-bottom surface which mates with the inside bottom surface of an aluminum cup which forms the inner heat shield, M. The two are firmly attached by pressure washers and screws so that the inner heat shield

---

[1] For example:
E. W. Williams, D. V. Parham, and J. Knox, J. Sci. Instr. 44 (1967) p. 271.
L. P. Potapov: Cryogenics (1963) p. 240.
L. F. Lowe, C. Jimenez and E. A. Burke, Rev. Sci. Instr. 34 (1963) p. 1348.
R. L. Chaplin and P. E. Shearin, Rev. Sci. Instr. 33 (1962) p. 459
A. Sosin and H. H. Neely, Rev. Sci. Instr. 32 (1961) p. 922.
J. M. Flourney, L. H. Baum, and S. Siegel, Rev. Sci. Instr. 31 (1960) p. 1133.

[2] K. Maeda, J. Phys. Chem. Solids 26 (1965) p. 595.

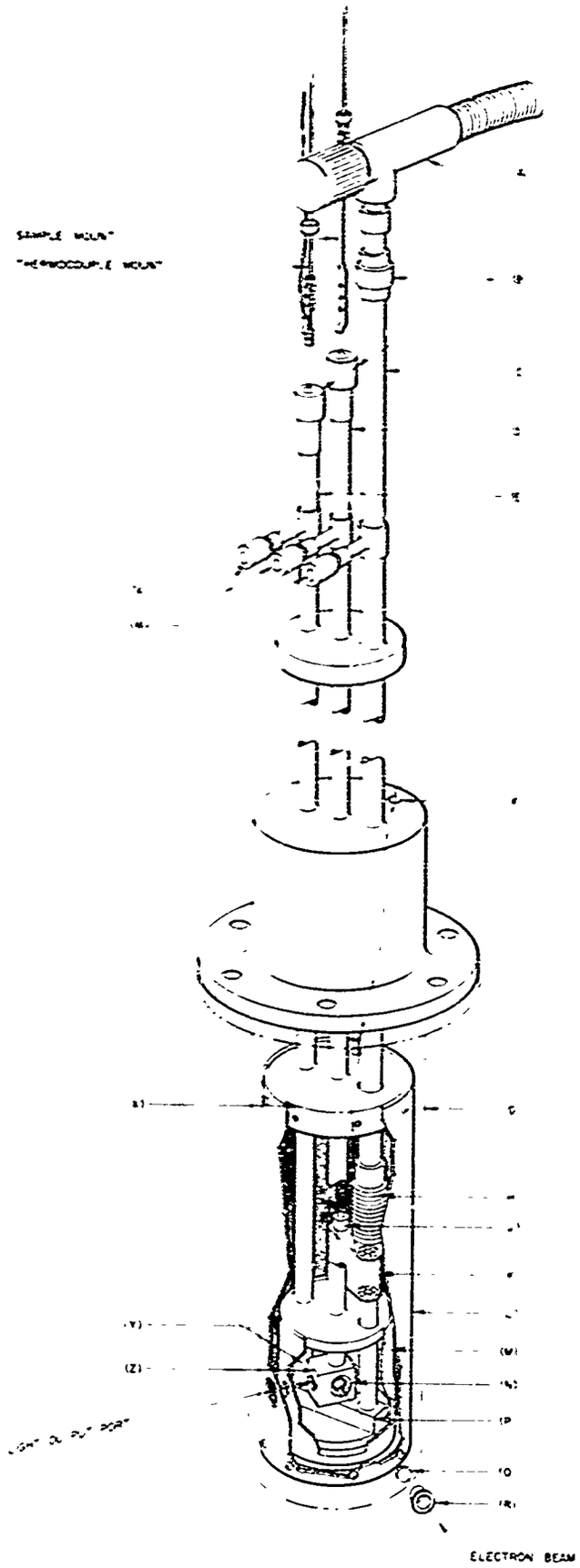

Figure 1. Variable temperature dewar for cathodo luminescence studies.

is cooled by heat conduction across the interface. Additional radiation shielding is provided by the outer radiation shield, I, which is attached to the heat exchanger, X. This is a copper disc soldered to tubes D and E. It provides mechanical rigidity and is cooled by the gas as it leaves the lower sections of these tubes. Tube C passes freely through X and is connected to the heat exchanger, K, by a stainless steel bellows, H. The bellows is required to relieve the stress created by the unequal thermal contractions of tube C relative to tubes D and E whose common temperature may not be the same as that of tube C.

The intermediate stainless-steel window mount, R, serves:

(1) to decouple thermally the stainless-steel window, Q, from the brass chamber, N so that the window can be readily unsoldered and replaced;

(2) to locate the stainless-steel window in the flow of the cooling gas so that the heat generated by electrons stopped in the window is removed; and

(3) to facilitate mounting the sample in the flow of gas and close to the window where the divergence of the focused electron beam is minimal.

The brass irradiation chamber N also houses a quartz window which is sealed in position with an epoxy cement. In spite of repeated thermal cycling and long exposure to X-rays (from which it is partially shielded by the chamber itself), the epoxy window seal has proved to be very durable.

The thermometer mount, S, is attached to the bottom of a thin-walled stainless-steel, sealed tube. Brass spacers, U, stabilize the tube within the access tube E. The spacers have many holes drilled in them to permit the easy flow of gas along the tube and to provide protected paths to the exterior for the fine thermocouple and carbon resistor leads which are threaded through them. The leads are passed through small holes in the termination at the top of the stainless-steel tube, and the holes are filled with epoxy cement. The termination fits into tube E and is hermetically sealed with a quick-disconnect coupling. The thermometers, V, are externally calibrated as situated on the thermometer mount. Once in place in the dewar, they are not normally disturbed again.

An arrangement similar to the thermometer mounting is used for the sample mounting T. Several samples may be mounted at one time. By loosening the quick-disconnect coupling and raising or lowering the sample mount, any one of several samples may be selected for study.

3. OPERATION AND CHARACTERISTICS

Cold exchange gas is obtained by boiling off liquid refrigerant from a storage dewar. Depending on the temperature required for the experiment, any of the

standard refrigerants can be used. To conserve helium, the dewar is normally precooled to liquid-nitrogen temperatures with gaseous nitrogen from a liquid-nitrogen storage dewar. Then the transfer tube is switched to a liquid-helium supply to reduce the sample temperature to approximately 12°K. This procedure can be completed in 30 minutes. Heat losses in the transfer syphon presently result in 12°K, which is the lowest temperature attainable with a helium consumption of ~3 liters/hour. By using a short liquid-nitrogen shielded transfer syphon, it is expected that an ultimate temperature closer to 4.2°K can be obtained.

Because of the small specific heats of materials at low temperatures, excessive heating can result during intense sample excitation. It is therefore necessary to provide maximum cooling to carry away the heat dissipated in the sample, and, for the temperature range 12° to 70°K, the gaseous flow rate is usually maintained at that corresponding to a consumption of 3 liters of liquid helium per hour. Temperatures in this range are maintained by supplying power to the heater, J, in the heat exchanger, K. In this temperature range, the gas temperature responds rapidly to changes in power input to the heater, so there is little difficulty in manually correcting for small temperature drifts.

At temperatures higher than 70°K, the heat exchanger begins to lose its effectiveness and temperature changes are made by reducing the flow of cold helium gas and mixing with it a controlled stream of warm helium gas which enters at input, F. Mixing of the warm and cold gases is aided by the capillaries in K. Since a relatively small amount of warm gas can change the temperature of the gaseous mixture by many degrees, a fine metering valve is used in the warm gas supply line. Two thermally insulated valves located at the outputs, W, are used to control the relative gas flow rates past the samples and thermometer.

The performance of the dewar was tested by placing two identical, calibrated thermocouples in the dewar, one located in the normal temperature monitoring location Y, the other in the sample irradiation location. Both thermocouples were soldered to pieces of copper approximately the size of a typical sample (2. mm x 2. mm x 0.5 mm). In the absence of an electron beam, it was found that the thermometers indicated equal temperatures to within ±0.5°K for both locations over a wide range of temperatures. Equalization of flow rates is not necessary; therefore, to obtain optimum convective cooling of the irradiated samples, a larger flow is normally passed through the irradiation chamber. To test the effectiveness of the cooling gas, 200 mW was dissipated in the copper sample by electron-beam irradiation. At 12°K, there was less than a 1°K temperature rise, registered as a difference in the thermometer readings. At 28.5°K, no change in temperature could be detected. At any selected temperature it was found possible to maintain the temperature constant to within ±1°K for long periods with a minimum of attention.

The dewar has proven very useful in recent studies of Zn- and Cd-doped GaP crystals in which the red cathodoluminescence spectra were recorded as a function of temperature between 12° and 300°K. The advantages of rapid temperature changes, the easy interchange and assessment of small, brittle samples, and the ability to strongly excite samples without troublesome heating effects were invaluable in reducing the time to obtain results.

UNCLASSIFIED
Security Classification

DOCUMENT CONTROL DATA - R & D

(Security classification of title, body of abstract and indexing annotation must be entered when the overall report is classified)

1 ORIGINATING ACTIVITY (Corporate author)	2a. REPORT SECURITY CLASSIFICATION
Bell Telephone Laboratories, Incorporated on behalf of Western Electric Company, Incorporated 83 Maiden Lane, New York, New York 10038	UNCLASSIFIED 2b. GROUP

3 REPORT TITLE

EFFECTS OF RADIATION ON SEMICONDUCTOR MATERIALS AND DEVICES

4 DESCRIPTIVE NOTES (Type of report and inclusive dates)

Final Scientific Report. Period covered. 1 Jan 67 thru 30 Dec 67. Approved: 23 May 68

5 AUTHOR(S) (First name, middle initial, last name)

D. K. Wilson J. D. Cuthbert
J. P. Mitchell H. S. Lee

6 REPORT DATE	7a. TOTAL NO OF PAGES	7b. NO OF REFS
30 April 1968	189	99

8a. CONTRACT OR GRANT NO	9a. ORIGINATOR'S REPORT NUMBER(S)
b. PROJECT NO Project, Task, Work Unit Nos. 4608-01-01	
c. DoD Element 62405274 d. DoD Statement 634608	9b. OTHER REPORT NO(S) (Any other numbers that may be assigned this report) AFCRL-68-0250

10 DISTRIBUTION STATEMENT

1 - DISTRIBUTION OF THIS DOCUMENT IS UNLIMITED. It may be released to the Clearinghouse, Department of Commerce, for sale to the general public.

11 SUPPLEMENTARY NOTES	12 SPONSORING MILITARY ACTIVITY
TECH, OTHER	Air Force Cambridge Research Laboratories (CRW) L. G. Hanscom Field, Bedford, Mass. 01730

13. ABSTRACT

Results of investigation on the effects of nuclear radiation on semiconductor materials, device surface layers, and devices are discussed.

Optical studies revealed that low-temperature red luminescence in GaP doped with (Zn,O) or (Cd,O) arises either from recombination of electrons at neutral Cd-O (or Zn-O) complexes with holes trapped at Cd (or Zn) acceptors, or from decay of excitons at Cd-O (or Zn-O) complexes. The temperature dependence of intensity and time-resolved spectra of the red luminescence was investigated and showed that bound-exciton emission becomes dominant between 60° and 120°K. An explanation is offered for the accompanying large changes in the spectral and time-decay characteristics.

An analysis of the model for radiation-induced positive space-charge buildup in SiO_2 layers is presented and the predictions compared with results obtained on commercial MOS-FETs. Trap levels in SiO_2 layers were investigated using thermoluminescence thermally stimulated glow curve techniques. Co^{60}-gamma radiation introduces five trap levels in SiO_2 layers. Oxide layers in commercial MOS-FETs showed a high density of inherent electron traps. Platinum-silicide/silicon Schottky barrier diodes with "guard-rings" were found to be unaffected by up to 10^8 rads of ionizing radiation and 10^{15} n/cm^2.

Recombination and trapping mechanisms in neutron-irradiated silicon diodes were studied using open-circuit forward-voltage recovery and reverse-bias capacitance-voltage characteristics. The results are interpreted in terms of isolated defect and clustered damage models.

The effects of fast neutrons on the dc and microwave characteristics of "nearly-abrupt" X-band avalanche diodes are reported. Above 10^{15} n/cm^2 significant improvement in device behavior was observed.

DD FORM 1 NOV 65 1473

UNCLASSIFIED
Security Classification

UNCLASSIFIED
Security Classification

14 KEY WORDS	LINK A		LINK B		LINK C	
	ROLE	WT	ROLE	WT	ROLE	WT
Defect Properties						
Radiation Damage						
Semiconductors						
GaP						
Luminescence						
New Pair Luminescence						
Bound Exciton Luminescence						
Recombination Mechanisms						
Zeeman Studies						
Luminescence Excitation						
Isotope Shifts						
Doping Dependence						
Election Beam Excitation						
Decay Times						
Time Resolved Spectroscopy						
Van de Graaff Accelerator						
Variable Temperature Dewar						
Space-Charge Accumulation						
MOS-FET						
SiO_2						
Thermoluminescence						
Glow Curve						
Thermally Stimulated Current						
Trap Levels						
Co^{60}-Gamma Radiation						
Photoinjection						
Guard-Ring Schottky Barrier Diode						
Metal-Semiconductor Barrier						
Semiconductor Devices						
Silicon Diodes						
Clustered Neutron Damage						
Lifetime Dependence on Injection Level						
Junction Capacitance						
Injection-Induced Recovery						
IMPATT Diodes						
Radiation Resistant Microwave Sources						

Security Classification